

Thermostatistical theory of plastic deformation in metals

Enrique I. Galindo-Nava



The research in this thesis has been financially supported by the Mexican Council of Science and Technology (CONACYT) and the Roberto Rocca Education Program.

Thermostatistical theory of plastic deformation in metals

Proefschrift

ter verkrijging van de graad van doctor
aan de Technische Universiteit Delft,
op gezag van de Rector Magnificus prof. ir. K.C.A.M. Luyben,
voorzitter van het College voor Promoties,
in het openbaar te verdedigen op vrijdag 30 augustus 2013 om 15:00 uur

door
ENRIQUE I. GALINDO NAVA

Bachelor of Science in Mathematics
National Autonomous University of Mexico, Mexico
geboren te, Mexico-stad, Mexico

Dit proefschrift is goedgekeurd door de promotoren:

Prof.dr.ir. J. Sietsma

Prof.dr. P.E.J. Rivera Díaz-del-Castillo

Samenstelling promotiecommissie:

Rector Magnificus, voorzitter

Prof.dr.ir. J. Sietsma, Technische Universiteit Delft, promotor

Prof.dr. P.E.J. Rivera Díaz-del-Castillo, University of Cambridge, promotor

Prof. F.P.E. Dunne, Imperial College London, United Kingdom

Prof.dr.ir. T.J.H. Vlugt, Technische Universiteit Delft

Prof.dr. J.Th.M. de Hosson, University of Groningen, the Netherlands

Dr. R. Arróyave, Texas A&M University, United States

Dr. A. Perlade, ArcelorMittal, France

Prof.dr. I.M. Richardson, Technische Universiteit Delft, reservelid

Keywords: Dislocation evolution, statistical thermodynamics, plastic deformation, modelling, recovery, recrystallisation

Cover designed by Daniela López and Enrique Galindo-Nava

Copyright ©2013 by Enrique I. Galindo-Nava

All rights reserved. No part of the material protected by this copyright notice may be reproduced or utilised in any form or by any means, electronic or mechanical, including photocopying, recording or by any information storage and retrieval system, without permission from the author.

Printed in The Netherlands

ISBN: 978-94-6191-860-4

To my parents and wife

Contents

1	Introduction	1
1.1	Deformation mechanisms in metals	1
1.1.1	Deformation by slip	2
1.1.2	Deformation twinning	2
1.1.3	Grain boundary sliding	3
1.2	Modelling plastic deformation in metals	4
1.3	Scope and outline of the thesis	5
2	Background	7
2.1	Basic dislocation theory	7
2.1.1	Partial dislocations and stacking faults	10
2.1.2	Dislocation cross-slip	11
2.1.3	Vacancies and dislocation climb	12
2.2	Entropy and dislocation thermodynamics	13
2.3	Dislocation arrangements	15
2.3.1	Low angle grain boundaries: Tilt boundaries	15
2.3.2	Dislocation cells	16
2.3.3	Nano-twin boundaries	17
2.4	Modelling techniques	18
2.4.1	Molecular dynamics	18
2.4.2	Discrete dislocation dynamics	18
2.4.3	Crystal Plasticity/ Finite Element Method	19
2.4.4	Mesoscale approaches	21
2.4.5	Multiscale modelling	22
2.5	Kocks-Mecking equation	23
3	A thermostatistical theory for plastic deformation	27
3.1	Introduction	27
3.2	Dislocation kinetics: Statistical entropy	29
3.2.1	Vacancy-dislocation kinetic contribution	32

3.2.2	Transition temperatures	34
3.3	Dislocation annihilation: Dynamic recovery and cell formation . .	36
3.3.1	Dynamic recovery coefficient	40
3.3.2	Dislocation cell size	42
3.3.3	Cell misorientation angle	44
3.3.4	Work hardening evolution: Stage IV	49
3.3.5	Results	50
3.4	Nanotwinning	55
3.4.1	Results	56
3.5	Conclusions	57
4	Plastic deformation theory for body-centred cubic metals	59
4.1	Introduction	59
4.2	Kocks–Mecking formulation	60
4.2.1	Statistical entropy	60
4.2.2	Number of microstates for BCC	62
4.2.3	Dynamic recovery coefficient	62
4.2.4	BCC <i>vs.</i> FCC	63
4.3	Results	64
4.4	Conclusions	69
5	Deformation twinning in hexagonal close packed metals	71
5.1	Introduction	71
5.2	Twinning formulation	75
5.2.1	Twin nucleation strain	78
5.2.2	Twinning growth coefficient	80
5.2.3	Twin mode transition temperatures	82
5.2.4	Orientation effect	84
5.2.5	Twin volume fraction	86
5.3	Results	86
5.4	Discussion	91
5.4.1	Orientation effects and twin volume fraction	92
5.4.2	Summary of the current approach	94
5.5	Conclusions	94
6	Hot deformation in metals: Dynamic recrystallisation	97
6.1	Introduction	97
6.2	Theory	99
6.2.1	Dynamic recrystallisation coefficient	100
6.2.2	Critical shear strain for grain nucleation	102
6.2.3	Results	103
6.2.4	Discussion	105

6.2.5	Condition for the occurrence of dynamic recrystallisation	107
6.2.6	Grain boundary mobility	108
6.3	Conclusions	111
7	Application of the theory to multicomponent metals	113
7.1	Introduction	113
7.2	Dislocation generation: $d\rho^+/d\gamma$	115
7.2.1	Substitutional atoms	115
7.2.2	Interstitial atoms	116
7.3	Dislocation annihilation: $d\rho^-/d\gamma$	117
7.3.1	Multicomponent dynamic recovery	119
7.3.2	Multicomponent dynamic recrystallisation	120
7.3.3	Multicomponent critical strain for grain nucleation	122
7.3.4	Condition for the occurrence of dynamic recrystallisation	122
7.3.5	Physical parameters estimation	123
7.4	Results	125
7.4.1	Design for dynamic recrystallisation	128
7.5	Dilute concentrations: Application to low alloy steels	130
7.5.1	Experimental procedure	131
7.5.2	Results	132
7.6	Combined effects: Twinning induced plasticity of high Mn steels	140
7.6.1	Model	140
7.6.2	Results	141
7.7	Discussion	143
7.8	Conclusions	145
	Summary	147
	Samenvatting	155
	Appendix A Physical parameters	163
	Bibliography	169
	Acknowledgements	193
	List of publications	195
	Curriculum Vitae	197

Chapter 1

Introduction

Dislocations are linear defects in the crystal structure of metals, they are largely responsible for the material's permanent deformation via their motion and multiplication. Elaborate interactions between the defects in the crystal structure lead to complex forms of mechanical behaviour, often a reminder of a phrase attributed to Frank: "Crystal defects are like people, it is the defects in them that make them interesting" [1]. In spite of the scientific interest and technological importance, a single formulation describing plasticity phenomena from nanometric to macroscopic scales is lacking, even for pure metals. As early as 1953, Cottrell pointed out that "work hardening was the first problem to be attempted by dislocation theory and may well prove to be the last to be solved" [2].

Modern industrial applications demand the design and optimisation of new alloys, improving their mechanical performance during plastic deformation. Different microstructures are introduced to achieve these requirements. However, the complexity of their interrelations also increases, posing a challenge to our understanding.

1.1 Deformation mechanisms in metals

The most important deformation mechanisms occurring in metals are deformation by dislocation slip and twinning [3]. They can occur for different processing conditions and crystal structures. Another important deformation mechanism in fine-grained alloys is grain boundary sliding, where displacement of adjacent grains occurs. These mechanisms determine the material's mechanical behaviour.

1.1.1 Deformation by slip

Plastic deformation on a microscopic scale consists of the movement of large numbers of atoms in response to an applied stress. Dislocations allow materials to deform without disturbing their crystal structure at stresses below that at which the atomic planes would slip if they were not present [4]. They accumulate and slip in the material to accommodate strain as plastic deformation continues. The Burgers vector \mathbf{b} describes the magnitude and direction of the lattice distortion induced by a dislocation. Dislocations can attract or repel each other depending on their orientation. If two dislocations with opposite Burgers vector encounter in the same slip plane, they will annihilate each other [5]. This process is defined as recovery.

Dislocation annihilation occurs more frequently when a dislocation can switch from one slip plane to another; two mechanisms occurring at various temperatures are responsible: at low temperatures ($T < 0.3T_m$, where T_m is the absolute melting temperature), the governing dislocation annihilation process is cross-slip, driven by thermally activated glide [6, 7]; at high temperatures ($T > 0.6T_m$), annihilation is driven by vacancy-assisted dislocation climb [8]; and at intermediate temperatures ($0.3T_m < T < 0.6T_m$) both processes take place, exhibiting a mixed behaviour. These limits are only an estimate for face-centred cubic metals, but their presence is well established from experiments in other crystal structures.

The balance between dislocation storage and annihilation determines the material's work hardening behaviour. Deformation by slip occurs in face-centred cubic (FCC) metals with medium and high stacking fault energy (χ); body-centred cubic (BCC) metals at medium and high temperatures, and at low strains for low temperatures; and hexagonal-closed packed (HCP) metals at low strains or high temperatures [3].

1.1.2 Deformation twinning

Deformation twinning occurs when dissociation of dislocations into partials occurs due to localised stress concentrations in the material [9]; dislocation dissociation can be induced by dislocation pile-up at crystal defects (including themselves and solute atoms) or at grain boundaries [10], or by homogeneous lattice shear in a region of high stress concentrations [9]. Stress accumulation arise around them, becoming energetically favourable for dislocations to split into partials and nucleate twin boundaries [3]. Twinning has been recognised to be an important deformation mechanism in recent years for technological applications [11, 12].

Twinning takes place in several crystalline materials for various reasons: HCP metals have fewer slip systems¹, leading to earlier pile-up saturation [9]; when

¹See table 2.1

BCC and FCC metals with low stacking fault energy are deformed at low temperatures, dislocation cross-slip is more difficult to occur, limiting the material capacity to change its shape (through dislocation motion), and the pile-up concentration rate is increased [3]. Figure 1.1 shows the twinning evolution in pure magnesium under compression at room temperature. Twin density (volume fraction) and thickness increase with strain [13].

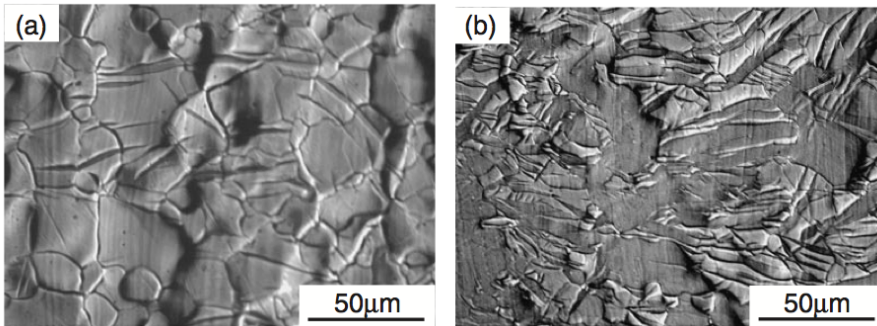


Figure 1.1: *Microstructure of pure magnesium after deformation at (a) strain of 0.5% and (b) strain of 5.0% shows the increase of both twin density and size (dark plates) with the increase of strain. Adapted from Li and Enoki [13].*

The formation of coherent nanoscaled twins (boundaries) in relatively large grain sizes prior to deformation has been possible in pure copper [11]; nanotwin boundaries increase the material’s yield strength by 7–10 times with respect to their coarse-grained version, while preserving good ductility limits. These microstructures are obtained by employing a pulsed electrodeposition technique [11].

1.1.3 Grain boundary sliding

Plastic deformation in ultra-fine-grain materials (with grain sizes of a few microns or less) is usually controlled by grain boundary sliding (GBS) [14], where adjacent grains displace with respect to each other to accommodate strain. Deformation by slip is hindered by the reduced space for dislocation generation in the grain interiors. Grain boundary sliding usually occurs at relatively elevated temperatures ($\sim 0.5T_m^2$ and above, with T_m being the melting point). This process is particularly important for superplastic forming of metals and ceramics, where high tensile elongations can be reached, ranging from 200 up to a few thousands percent [15].

²These limits are only an estimate from experimental observations.

Two major mechanisms are involved in GBS [15, 16]: The first mode is driven by the movement of intragranular dislocations, facilitating boundary displacement; the second mode involves grain elongation through stress-directed vacancy diffusion. The former usually takes place at medium temperatures ($T \leq 0.6T_m$), whereas the latter is present above them.

Meyers *et al.* [14] have pointed out that grain boundary sliding can play a significant role in the development and exhibition of novel properties of UFG and nanostructured materials. Moreover, Van Swygen *et al.* [17, 18] have shown that GBS is the primary deformation mechanism in nanocrystalline materials and that such sliding mechanism results in a build-up of stress across neighbouring grains. This deformation mechanism will not be considered in this thesis. However, it can be shown that the main outputs from this work can be applied to describe cavitation kinetics and grain boundary sliding behaviour in superplastic alloys [19].

1.2 Modelling plastic deformation in metals

Materials modelling has emerged as a field of research with unique features, most notably the ability to analyse and predict a wide range of physical phenomena [20]. Stemming from atomic interaction descriptions up to macroscopic stress distributions in a deformed specimen, many approaches have been proposed to describe and understand the material's mechanical properties. Some of the most common modelling techniques are discussed in Chapter 2.

Engineering alloys often display an elaborate composition and undergo sophisticated thermal processing schedules. Their ability to withstand load stems from the combination and interaction of elements in their internal microstructure. Dislocations are central to determine alloy mechanical properties during plastic deformation. Their evolution and interactions with other crystal defects determine the material's ability to accommodate strain. For instance, at high temperatures, dislocation annihilation (reduction in material's strength) is mainly controlled by the climb of dislocations, a process controlled by the diffusion of vacancies; deformation twinning requires the dissociation of dislocations into partials and the formation of twin boundaries³.

Developing a theoretical tool for describing dislocation evolution and concomitant interactions with other defects in terms of composition, loading conditions and microstructure can be crucial for designing new alloys with improved mechanical properties. Isolated contributions of dislocation interactions with other crystal defects, such as vacancies [8] or twins [21, 22], have been considered in

³A consequent increase in the material's strength is driven by twin growth and their interaction with dislocations.

previous work. However, several parameters, such as the critical stress for twin nucleation or the critical resolved shear stress for slip, are difficult to estimate from experiments. A number of constitutive or phenomenological relations are introduced for each material at different loading conditions. These relations usually remain valid for limited loading and compositional ranges, impeding their extension to predict new scenarios. Moreover, various interactions between crystal defects and microstructural features are difficult to isolate for characterising their contribution; for instance, quantitative analysis to solid solution effects in HCP alloy's twinning behaviour and work hardening is not clear yet, as simultaneous twin nucleation and grow, and dislocation accumulation occurs during straining. Thus, developing a theoretical tool able to incorporate all these effects into a single formulation represents a major challenge for material scientists.

1.3 Scope and outline of the thesis

This work aims to describe plastic deformation and microstructure evolution of metals at various scales in terms of dislocation behaviour. The theory is based on statistical thermodynamics, where the entropy ΔS is proposed to incorporate the possible paths for dislocation motion. Other than estimating the velocity gradients a dislocation may reach, the number of possible paths (configurations) that are *favourable* in terms of free energy at a given temperature and strain rate are considered in ΔS .

It will be demonstrated that ΔS features strongly in plasticity: 1) Its description supplies a physical foundation to the Kocks–Mecking formulation across the scales at a variety of deformation conditions for FCC, BCC and HCP metals, by identifying the activation energy for dislocation annihilation. 2) The transitions from low, medium and high temperature dislocation annihilation mechanisms are physically explained. 3) It aids in describing the conditions for the formation of dislocation cells and their average size, as well as the work hardening behaviour at large strains in FCC and BCC metals. 4) Deformation twinning in HCP, FCC and nano-twinned copper can be described. 5) The transition temperatures where different twin modes predominate in HCP metals are predicted. 6) The dynamic recrystallisation behaviour in pure and multicomponent FCC systems can be described; the critical conditions for recrystallisation occurrence are obtained in terms of alloy's composition and deformation parameters. 7) Solid solution effects in work hardening can be identified. All these results allow to describe various plasticity phenomena in terms of a single parameter: the average dislocation density.

Succinct expressions for the dislocation generation, dynamic recovery and recrystallisation rates in the dislocation evolution equation are obtained with this approach. These terms are expressed in terms of a number of physical parameters

(such as shear modulus, stacking fault energy, vacancy formation and migration energy), temperature, strain rate, and chemical composition. This aids to reduce the number of constitutive relations and parameters to be identified for each material during deformation, by thermodynamic-based descriptions that can be employed in several systems.

The outline of this thesis is as follows: in **Chapter 2**, basic dislocation properties are reviewed, some of the most relevant dislocation arrangements in metals are described, the entropy of a dislocation and modern modelling techniques describing plastic deformation and dislocation behaviour at various scales are discussed. Special emphasis is made on the Kocks–Mecking equation.

Chapter 3 presents the main body of the theory for FCC metals; statistical entropy is defined in terms of dislocation kinetics at various temperatures. This allows to describe: 1) Dynamic recovery (DRV) at low and high temperatures, which is obtained by performing an analysis on a dislocation segment undergoing annihilation. 2) Dislocation cell formation and misorientation, where entropy accounts for the dislocation displacement energy to form cells. 3) Nanotwinning, where twin and grain boundaries act as barriers for dislocation motion. The model results are applied to pure copper, nickel, aluminium and silver.

The theory is extended in **Chapter 4** to describe plasticity in body-centred cubic (BCC) metals, where additional crystallographic features are present.

Deformation twinning in pure hexagonal-cubic (HCP) metals (Ti, Mg and Zr) is described in **Chapter 5**.

In **Chapter 6** the theory is extended to model dynamic recrystallisation (DRX) in FCC pure metals, where grain nucleation and growth occurs from high-angle (sub)grain boundaries (due to strong dislocation accumulation).

Multicomponent effects in the theory are introduced in **Chapter 7**; high temperature deformation (DRV+DRX) in FCC single phase multicomponent systems is reviewed; an application to the hot forming of low alloy steels is presented; work hardening of twinning-induced plasticity (TWIP) steels is also delineated. Following this, concluding remarks and a summary of this thesis are presented.

The theory is able to describe plastic deformation in 12 pure elements (Cu, Ni, Al, Ag, Fe, Mo, Ta, V, W, Ti, Mg and Zr) and 28 alloys (including more than 20 steels). This thesis covers dislocation evolution in temperature ranges from very low up to near-melting point, and for up to 7 orders of magnitude in strain rates.

Chapter 2

Background

General properties of dislocations are presented in this chapter. The strain energy induced by a dislocation segment is defined; the dislocation dissociation process and stacking fault formation are discussed. Basic characteristics for dislocation motion are introduced; dislocation cross-slip and vacancy-assisted dislocation climb are briefly summarised. Dislocation thermodynamics and entropy effects on dislocation formation are discussed. The dislocation arrangements that are analysed throughout this thesis are defined: Low-angle grain boundaries, dislocation cells and nano-twins. The most relevant modelling techniques for describing dislocation motion and population evolution at various scales are presented. Special emphasis is made on the Kocks–Mecking equation, as modifications of this approach will be employed in the following chapters for describing several deformation mechanisms.

2.1 Basic dislocation theory

A dislocation is defined as a crystal defect with atoms being misaligned around the dislocation line. The misalignment is with respect to the otherwise perfect crystal structure, smaller than one interatomic distance, and vanishes with distance from the dislocation line. There are two main dislocation types: edge and screw. An edge dislocation can be described as the result of an extra half-plane of atoms inducing planar distortion around it. A screw dislocation can be seen as the result of an atomic plane being sheared, inducing a spiral distortion on its surroundings. In real crystals, dislocations form in many different ways. For example, they can appear by shearing along crystal planes, or by condensation of interstitials (extra atoms in the lattice) or vacancies (empty atomic sites) [5]. The Burgers vector \mathbf{b} of an edge and screw dislocation are normal and parallel to the dislocation line, respectively. Figure 2.1(a) and (b) shows the atomic arrangement around an edge

and screw dislocation in a simple-cubic crystal, respectively; the Burgers vector orientation is also show for both cases. In real materials, dislocations are usually found of mixed mode. Figure 2.1(c) schematically shows a curved dislocation with an edge orientation at one end (on the left) and a screw orientation at the other end (on the right).

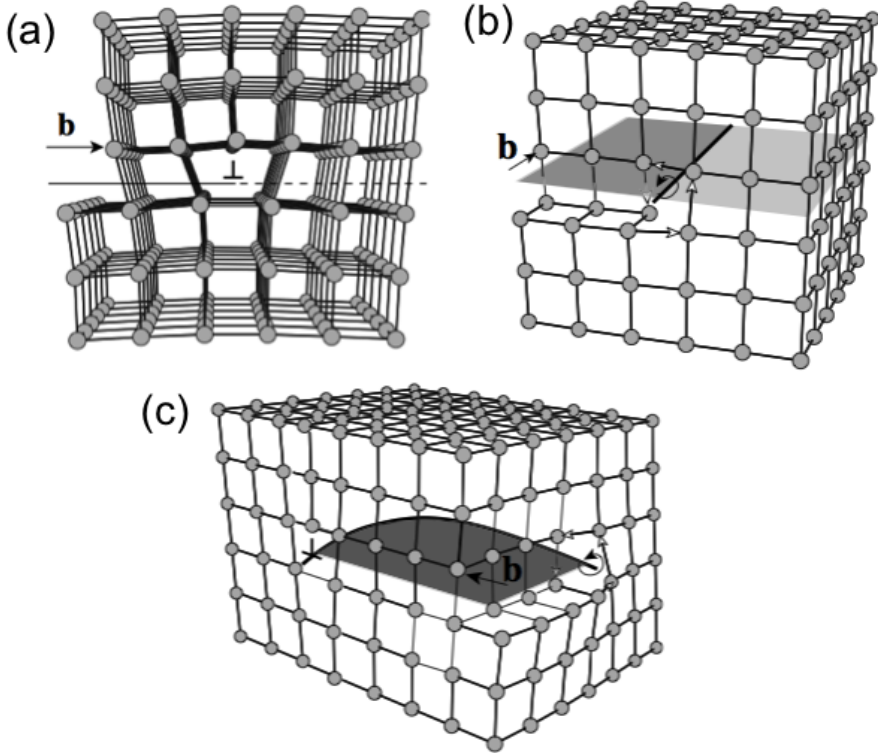


Figure 2.1: Schematic representation of the atomic arrangement around an (a) edge and (b) screw dislocation, with their respective \mathbf{b} orientation; and a (c) curved dislocation with mixed modes. Adapted from [23].

The strain energy per unit length induced around a screw dislocation is described by [5]

$$E = \frac{\mu b^2}{4\pi} \ln \left(\frac{R_{core}}{r_{core}} \right), \quad (2.1)$$

where μ is the material's shear modulus and b is the magnitude of the Burgers vector, R_{core} and r_{core} are the upper and lower cut-off radii that define the

limit of the dislocation's elastic zone, respectively. The strain energy of an edge dislocation is similar to the previous equation, but an additional factor $1/(1-\nu)$ is introduced, where ν is the Poisson ratio. r_{core} is usually taken between b and $5b$ [3], and R_{core} depends on the presence of other dislocations. If only an approximate value of the dislocation energy is required, the previous equation can be simplified to [3]:

$$E_d = \frac{1}{2}\mu b^2. \quad (2.2)$$

This equation is expressed in terms of the energy per unit length. The dislocation density in a material, ρ is expressed as the total dislocation length per unit volume.

Dislocations glide if an applied force reaches a critical resolved shear stress. They slip along preferred planes and directions. The planes spanned throughout a dislocation line and \mathbf{b} are called the *slip planes*; and the direction of movement is called the *slip direction*. The combination of slip plane and direction define a *slip system* [5]. Table 2.1 shows the most common slip systems observed for several FCC, BCC and HCP metals [5]; it is worth noting that different systems may operate as well, as will be introduced in the following chapters.

Table 2.1: Slip systems for FCC, BCC and HCP metals.

Metal	Crystal structure	Slip plane	Slip direction	Number of slip systems
Cu, Al, Ni, Ag, Au	FCC	{111}	$\langle\bar{1}\bar{1}0\rangle$	12
Fe, Mo, W, Ta	BCC	{110}	$\langle\bar{1}\bar{1}1\rangle$	12
Fe, W, Ta, V	BCC	{112}	$\langle\bar{1}\bar{1}1\rangle$	12
Fe, Cr	BCC	{123}	$\langle\bar{1}\bar{1}1\rangle$	24
Ti, Zr	HCP	{10 $\bar{1}$ 0}	$\langle 11\bar{2}0\rangle$	3
Mg, Zn, Co	HCP	(0001)	$\langle 11\bar{2}0\rangle$	3
Ti, Mg	HCP	{10 $\bar{1}$ 1}	$\langle 11\bar{2}0\rangle$	6

Plastic deformation results from the motion of dislocations, and the average dislocation velocity $\langle v \rangle$ can be related with the macroscopic axial strain rate $\dot{\epsilon}$, via the Orowan equation [5, 24]:

$$\dot{\epsilon} = b\rho_m \langle v \rangle. \quad (2.3)$$

where ρ_m is the mobile dislocation density. $\langle v \rangle$ depends on the deformation conditions [25], however it is not possible to obtain a specific velocity distribution, as dislocation motion is highly erratic [26], as will be discussed in Chapter 3.

2.1.1 Partial dislocations and stacking faults

Closed-packed structures (*e.g.* FCC and HCP metals) are formed by stacking atomic planes in specific periodic structures. For instance, a FCC structure is formed by periodically stacking three different atomic planes (A, B and C); Figures 2.2a-c show a schematic representation of the stacking process [25]. The stacking sequence for this structure is ABCABCABC.

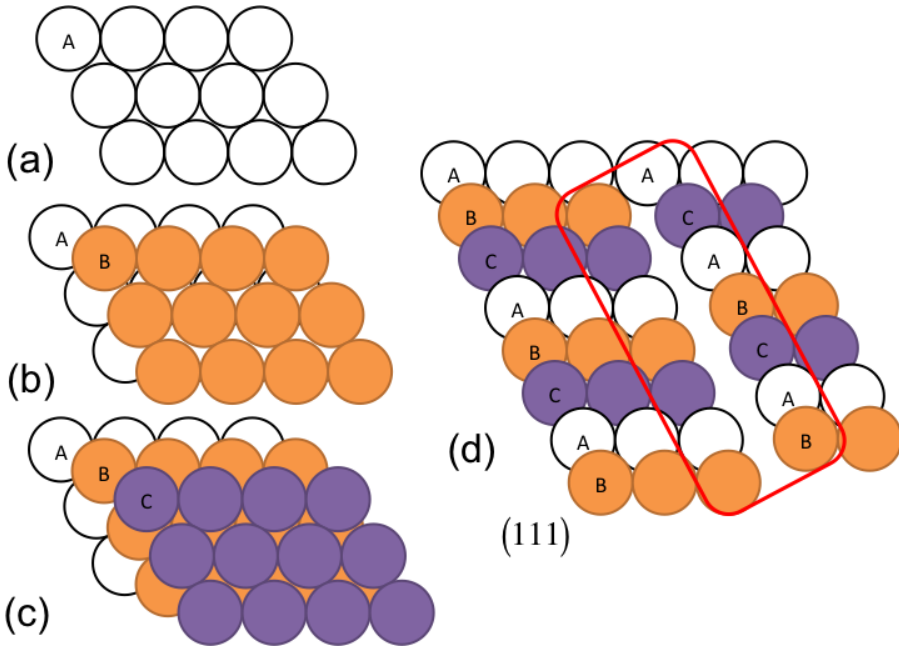


Figure 2.2: *FCC stacking process: (a) a reference atomic plane A is defined, (b) an additional plane B is placed on top of the interatomic spaces of A, and (c) a plane C is added on top of the interatomic spaces of B, being not coincident with atoms of A. (d) Typical stacking fault sequence is formed on a FCC structure by shifting atoms from B to C position.*

Stacking faults originate from shifting the atomic arrangements in the sequence, or by a swapping the stacking order. For instance, the sequence ABCACABC carries a fault by the omission of a B plane (by shifting B to C atom positions). Figure 2.2d shows a schematic representation of this fault in the FCC lattice projected on the (111) plane.

The modified stacking sequence is delimited by a pair of partial dislocations with Burgers vector that does not equal a lattice vector, and a lower strain energy (equation 2.2) [5, 27]. The width of the fault is a consequence of the balance

between the repulsive force between the partial dislocations and the stacking fault energy χ . The stacking fault energy per unit area is inversely related to r_{part} [27]

$$\chi = \frac{(2 + \nu)\mu b^2}{24\pi(1 - \nu)r_{part}}, \quad (2.4)$$

where r_{part} is the equilibrium distance between partials. The stacking fault energy determines the extent to which perfect dislocations dissociate into partials to lower the strain energy around the dislocation.

2.1.2 Dislocation cross-slip

In general, dislocations glide on a unique slip plane. However, screw dislocations can switch from one slip plane into another with relative ease, as their Burgers vector is parallel to the dislocation line [25]. In contrast, edge dislocations require the addition or disappearance (through diffusion) of atoms at the core, making this process energetically less favourable than in screw dislocations [25]. This mechanism is called cross-slip.

Cross-slip frequently occurs when dislocations split into partials, as they propagate along the most densely packed planes, which are at a certain angle adjacent to the primary slip plane. Figure 2.3 shows a schematic representation of this process.

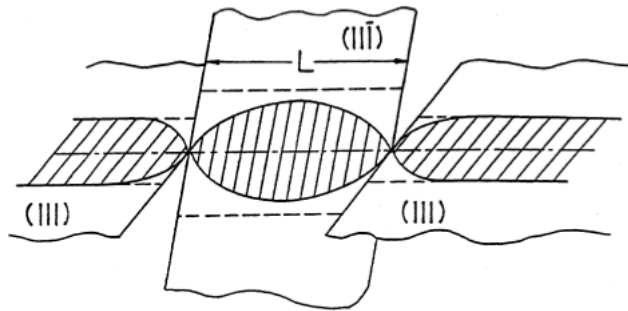


Figure 2.3: *Elementary cross-slip process in a FCC metal. A dislocation partial switches from (111) to (11 $\bar{1}$) plane. Adapted from W. Puschl [7].*

Cross-slip is thermally activated and its frequency decreases with temperature [7, 25, 28]. It is one of the most important dislocation mechanisms of plastic deformation; it strongly features in dislocation generation, annihilation (dynamic recovery), and pattern (cell) formation [7]. This mechanism is more difficult to

activate in metals with low stacking fault energy, as dislocation dissociation is less favourable (equation 2.4).

2.1.3 Vacancies and dislocation climb

Point defects affect the performance of several material properties, such as thermal conductivity, creep and work hardening [28]. Particularly, vacancies have a major importance in dislocation theory, as their mutual interaction provokes dislocations to undergo climb from one slip plane into another, increasing the number of dislocation encounters for annihilation [8].

A vacancy can be formed by thermal fluctuations in the lattice, inducing atom vibrations and local displacements; “empty” sites result from this process, whose concentration increases with temperature. Vacancies undergo diffusion [28], hence following a random walk. They move through the crystal structure from one atomic site to the next at an average frequency ϑ

$$\vartheta = \vartheta_D \exp\left(-\frac{E_m}{k_B T}\right), \quad (2.5)$$

where $\vartheta_D = 10^{13} \text{ s}^{-1}$ is the Debye frequency, and E_m is the vacancy migration energy. The vacancy concentration at equilibrium c_{eq} equals [4]:

$$c_{eq} = \exp\left(-\frac{E_f}{k_B T}\right), \quad (2.6)$$

where E_f is the vacancy formation energy.

The chemical potential μ_v induced by the formation of a number of vacancies is [4]

$$\mu_v = k_B T \ln \frac{c_{conc}}{c_m}, \quad (2.7)$$

where c_{conc} is the actual vacancy concentration, c_m is a reference vacancy concentration at the melting point, k_B is the Boltzmann constant, and T is the temperature.

Vacancies are easily adsorbed around a neighbouring edge dislocation. The “empty” site formed by a vacancy is filled by an atom at the dislocation’s core; this cancel’s the dislocation’s local distortion, shifting the distortion by half atomic plane (up or down). Thus, the dislocation “climbs” to an adjacent slip plane. Argon and Moffatt [8] have developed a hard sphere model to visualise the climb mechanism of an edge dislocation. From this analysis, they proposed a model for the dislocation climb velocity v_c , being controlled by vacancy emission around a dislocation. Under an applied stress σ , v_c equals:

$$v_c = 2b\vartheta_D n_{coord} \left(\frac{b}{d}\right)^2 \exp\left(-\frac{Q_{self}}{k_B T}\right) \left(\exp\left(\frac{\sigma\Omega}{k_B T}\right) - 1\right), \quad (2.8)$$

where n_{coord} is the crystal structure's coordination number (this model was developed for FCC metals), d is the stacking fault width, Q_{self} is the atomic self diffusion energy ($Q_{self} = E_f + E_m$) and Ω is the atomic volume. This equation shows that dislocation climb mainly occurs at high temperatures due to an increased vacancy concentration and motion.

2.2 Entropy and dislocation thermodynamics

In Cottrell's classical work [29], the free energy for dislocation formation ΔG_{dis} is estimated. ΔG_{dis} contains the strain energy ΔU_{dis} induced by atomic displacements when a dislocation is introduced and entropy contributions from the possible locations (configurations) of a dislocation in the material ΔS_{config} , and from atom vibrations due to thermal oscillations ΔS_{vib} :

$$\Delta G_{dis} = \Delta U_{dis} - T\Delta S_{config} - T\Delta S_{vib}. \quad (2.9)$$

A configurational entropy exists because the dislocation can be arranged in the crystal in various ways. By assuming the dislocation line to be straight, the number of possible positions n_{dis} of a dislocation in the crystal (if the specimen's area normal to the line is A) is $n_{dis} \simeq A/a^2$, where a is the atomic spacing. The configurational entropy of a dislocation *per atomic plane* along the line of length L equals [29]

$$\Delta S_{config} = -\frac{a}{L}k_B \ln n_{dis} = -\frac{a}{L}k_B \ln \left(\frac{A}{a^2} \right). \quad (2.10)$$

This value was found to be in the range of $\sim 10^{-6}k_B$ (8.6×10^{-11} eV/K)[29, 30, 31]. The vibrational entropy ΔS_{vib} is obtained by combining a linear oscillator model for N atoms with the total atomic displacement (due to the presence of a dislocation). ΔS_{vib} was found to be in the range of $\sim 3k_B$ per atom plane. Cottrell concluded that entropy contributions to the free energy of formation are very low with respect to the strain energy.

This analysis was employed for dislocation formation *only*, and was not extended for the possible configurations for dislocation glide. ΔS_{vib} is not expected to change significantly when a dislocation glides, passing through the atom lattice [5, 32]. However, the configurational entropy contribution when dislocations glide can become relevant, as ΔS_{config} will account for the energy (dissipation) at every moment, continuously increasing the number of possible paths during the glide process. Thus, if it is desired to model plastic deformation when strain increases, this term has to be taken into account.

The use of thermodynamics for describing dislocation evolution in plastic deformation has been widely employed by different methods. For instance, Ryu *et al.* [33] have recently revisited the entropy effect on dislocation nucleation via

molecular dynamics simulation (Section 2.4.1). They have compared the nucleation rate when a constant strain γ and stress σ are considered, respectively. The dislocation nucleation rate I_{dis} at a given strain γ is

$$I_{dis} = \nu_0 \exp\left(-\frac{F_c(T, \gamma)}{k_B T}\right), \quad (2.11)$$

where F_c is the activation free energy, and $\nu_0 = k_B T/h$ is a frequency, and h is Planck's constant. F_c is defined as $F_c(T, \gamma) = E_c(\gamma) - T S_c(\gamma)$, where E_c and S_c are the activation energy and entropy, respectively. On the other hand, the activation free energy for a constant stress σ can also be obtained by applying the Legendre transform $G_c = F_c - \sigma \gamma V$, where V is the volume of the ensemble. They found large activation entropy values for both scenarios: The activation entropy contribution at constant strain is caused by thermal expansion, with negligible contribution from the vibrational entropy, whereas the activation entropy at constant stress is significantly larger than that at constant strain, as a result of thermal softening and vibrational effects. They concluded that entropy effects are important for describing dislocation nucleation rate at an atomic scale. Langer *et al.* [34] have postulated a thermodynamics-based approach to describe dislocation evolution by writing equations of motion for the flow of energy and entropy associated with dislocations. They propose an equation of motion for the average dislocation density ρ that is based on the second law of thermodynamics and energy conservation. An effective temperature \tilde{T} defined as the stored energy (due to dislocations) variation with respect to the configurational entropy (of atomic displacements and rearrangements). The second law requires ρ to relax towards its most probable (equilibrium) value at the steady state ρ^{SS} depending on the effective temperature \tilde{T} . The evolution equation has the form: $\frac{d\rho}{d\varepsilon} = k\left[1 - \frac{\rho}{\rho^{SS}}\right]$, where k is a constant depending on material type and deformation conditions. More importantly, they concluded that dislocation entropy is an essential ingredient of a theory of dislocation-mediated deformation. However, no dislocation arrangements nor additional crystal defects are taken into account (*e.g.* vacancies at high temperatures). Although the flow stress response is recovered for various temperatures and strain rates in pure copper, a considerable number of parameters (six) were fitted.

Rivera and Huang [35] have employed irreversible thermodynamics theory as a framework to describe plastic deformation in pure metals and alloys. In their approach, the total entropy production equals the contribution of the entropy generation of the system of all irreversible processes (dislocation generation, glide and annihilation) and the entropy flux rate between the system and the surroundings. Expressions describing the average dislocation density at various deformation conditions are obtained, as is presented in Section 2.4.4.

2.3 Dislocation arrangements

2.3.1 Low angle grain boundaries: Tilt boundaries

Grain boundaries are interfacial defects created between two grains that have different crystallographic orientation. When the misorientation between adjacent grains is small, typically below $10\text{--}15^\circ$ [3], it is customarily referred to as a *low-angle grain boundary* (LAGB). When the angle of misorientation is large (above 15°), the boundary is referred to as a *high-angle grain boundary* (HAGB).

The simplest LAGB is a *tilt boundary*; this structure can be described in terms of dislocation arrays, consisting of a wall of parallel dislocations stacked perpendicular to the slip plane as illustrated in Figure 2.4.

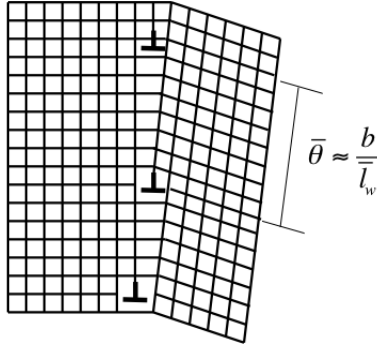


Figure 2.4: *Schematic description of a tilt boundary.*

The average misorientation angle ($\bar{\theta}$) equals [4]:

$$\bar{\theta} = \sin\left(\frac{b}{\bar{l}_w}\right) \approx \frac{b}{\bar{l}_w}, \quad (2.12)$$

where \bar{l}_w is the average dislocation spacing at the boundaries. If $\bar{\theta}$ is small, the energy of a tilt boundary per unit area can be approximated by [3]:

$$\gamma_s \approx \frac{\mu b^2}{2\bar{l}_w} = \frac{1}{2}\mu b\bar{\theta}. \quad (2.13)$$

HAGBs have a higher energy content; dislocations cannot traverse the boundaries during deformation, provoking dislocations to pile-up and stack around them. However, their effect on dislocation behaviour and plasticity is less understood [3, 36].

2.3.2 Dislocation cells

In early stages of deformation, dislocations multiply and gather to form networks. In such process, dislocations glide, slip and undergo cross-slip, intersecting each other and forming cellular structures [7, 37]. Experimental results show that dislocation cells are formed under specific circumstances: FCC metals with medium and high stacking fault energy, as well as BCC metals at medium and high temperatures, due to the high cross-slip rate [38, 7].

Compared with a dislocation forest, cellular structures represent an effective means to reduce the stored energy due to deformation [3, 39]. Figure 2.5 shows an example of dislocation cell arrangements in copper at room temperature initially strained to 10% at different strain rates [40].

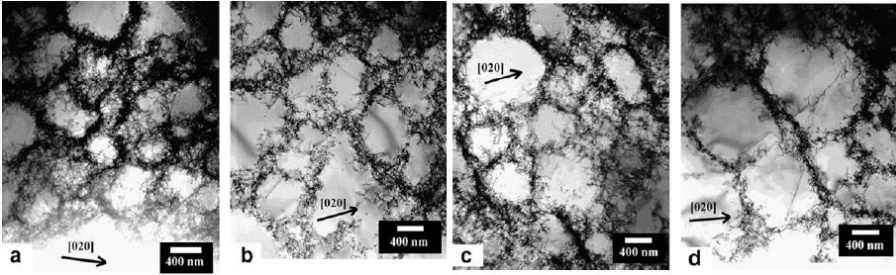


Figure 2.5: Dislocation cell morphology (dark regions) after 1 day at room temperature of tensile test specimens initially strained to 10% at different strain rates: (a) 0.05 s^{-1} , (b) 0.005 s^{-1} , (c) 0.0005 s^{-1} and (d) 0.00005 s^{-1} . Adapted from Kuo and Lin [40].

Determining the conditions for the formation and evolution of cells and subgrains in engineering alloys remains a topic of fundamental importance in the theory of metallurgy. Cell size and misorientation are highly dependent on temperature, strain and strain rate. Such parameters are at the centre of metal processing conditions in the advanced alloys industry, and their prediction can have a great influence in the control and improvement of mechanical properties. An eloquent example is the formation of subgrain boundaries in high temperature alloys, when grain nucleation and growth occurs from HAGB containing an elevated density of dislocations [3], triggering recrystallisation and causing microstructural degradation (such as grain coarsening), decreasing service life [3, 27].

Many authors have pointed out that the average cell size (d_c) is inversely proportional to the square root of the average dislocation density (ρ) [41, 42, 43, 44, 45]: $d_c = \kappa_c / \sqrt{\rho}$, and the average misorientation angle ($\bar{\theta}$) follows a power-law dependence of the applied strain (γ) [46]: $\bar{\theta} = \kappa_\theta \gamma^{2/3}$. The proportionality coefficients κ_c and κ_θ are obtained by fitting to experimental data to describe the behaviour

under specific deformation conditions. On the other hand, it has also been found that the cell size and misorientation angle distributions follow a master function characterised only by their *average* values [46, 47, 48]. Such relations simplify the problem of finding the actual distributions across the material by focusing on their average values *only*. There is no theory able to predict the kinetics of cell size and misorientation evolution during processing and operation.

2.3.3 Nano-twin boundaries

In recent years, nanocrystalline materials have been developed aimed at enhancing the strength and ductility of alloys. The introduction of coherent nanoscaled twins (TB), typically between 15 and 100 nanometers, for ultra-fine grained copper of grain size typically between 400 and 1500 nanometers, has shown to induce excellent properties in both strength and ductility [11]. Figure 2.6 shows transmission electron microscopy (TEM) images of pure copper composed of nanoscale twin lamellae of different thickness [49].

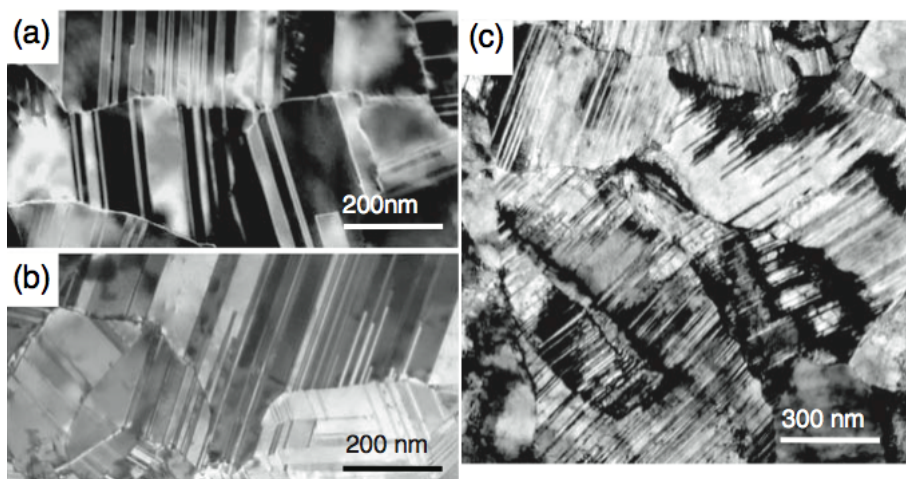


Figure 2.6: TEM images of as-deposited Cu samples with various mean twin thicknesses: (a) 96 nm, (b) 15 nm, and (c) 4 nm. Average grain size ~ 450 nm. Adapted from Shen et al. [49].

Nanotwins in fine grains are synthesised in high-purity copper by using a pulsed electrodeposition technique from an electrolyte of CuSO_4 [11]. The incorporation of nanotwins and microscopic grains allows the material to increase in ductility, with respect to its nanograined version. Coherent twin boundaries are as effective

as grain boundaries in material strengthening. Moreover, nanotwinned structures are energetically more stable than nanograined counterparts. Their mechanical response improves when the strain rate increases [50]; however, You *et al.* [51] have observed that microhardness decreases when the material is rolled at 77 K with respect to a specimen rolled at room temperature. This effect suggests the effect of different underlying deformation mechanisms.

2.4 Modelling techniques

2.4.1 Molecular dynamics

Molecular dynamics (MD) simulations reproduce atomic interactions employing classical Newton equations with semiempirical potentials that describe atomic interactions [52, 23]. A method to generate a dislocation is by deviating lattice positions of adjacent atoms. The characteristic velocity (or mobility) of such dislocation segments has been studied for very short time periods, typically in the range of 1 ps [53, 54, 55, 56].

Several microstructural features can also be examined with these simulations. For instance, the vacancy formation and migration energy is obtained by removing atoms in the arrangement [57, 58]; the stacking fault energy is reproduced by modifying the stacking sequence in the lattice [59]; grain boundary migration can be described [60, 61]. Dislocation interactions with other defects can also be reproduced. However, MD simulations are limited to short time deformation periods (up to $\sim 10^{-6}$ s) and number of atoms in the arrangement due to the prolonged computing times. Thus, their application is limited to problems at a small length scale and few crystal defects. Atomic potentials have to be developed for different alloys.

2.4.2 Discrete dislocation dynamics

Discrete dislocation dynamics (DDD) describes the collective behaviour of a set of dislocations under an external stress σ_{app} [20, 62]. Each dislocation line is represented explicitly; it is composed by a succession of elementary segments of straight edge or screw type dislocations. Long-range interactions are determined from elasticity theory (equation 2.1), and constitutive rules are introduced for their nucleation, mobility, annihilation and short-range interactions [23].

The force per unit length \mathbf{F} acting locally on a dislocation is given by the Peach-Koehler equation [28]

$$\mathbf{F} = ((\sigma_{\text{int}} + \sigma_{\text{app}}) \cdot \mathbf{b}) \otimes \xi, \quad (2.14)$$

where σ_{int} is the stress induced by other dislocations, \otimes is the vector product, and ξ is the unit vector of the dislocation line direction. Most of the computing

time of the simulation is employed to solve this equation. A relation between the dislocation velocity and the applied stress is usually represented by an Arrhenius [63], or by a proportionality relation (drag–force type) [64, 65]. Some authors also employ a differential equation for the velocity vector \mathbf{v} that accounts for an inertia term, a drag term and a driving force vector [20]

$$m_s \dot{\mathbf{v}} + \frac{1}{M_s} \mathbf{v} = \mathbf{F}_s, \quad (2.15)$$

where m_s is the effective dislocation segment mass, M_s is the dislocation mobility that depends on the temperature and applied stress, and \mathbf{F}_s represents the external forces acting on a dislocation. The Orowan equation (2.3) is applied to obtain the strain rate effect on each slip plane.

The dislocation generation and annihilation rate is obtained by estimating the dislocation density on each slip system ρ^i with the equation [66]:

$$\frac{d\rho^i}{d\gamma} = \frac{1}{b} \left(\frac{\sqrt{\sum_j k_j \rho^j}}{K_{ddd}} \right) - y\rho^i, \quad (2.16)$$

where ρ^j is the dislocation density of other slip planes; k_j and K_{ddd} are dislocation generation constants that depend on the specimen orientation, applied stress and dislocation interactions; and y is the dynamic recovery term. These constants are fitted for each slip system, temperature and material.

Discrete dislocation dynamics aim at describing microstructure formation, dislocation interactions, density, stored energy and local stresses in the material. However, the evolution of discretised segments requires long computing times, and singularities in the elastic equations may occur. This method can describe low dislocation densities only, due to long computing times for equation solving; thus, the deformation conditions tackled by this method are usually far from those for industrial applications [20, 23].

2.4.3 Crystal Plasticity/ Finite Element Method

Crystal Plasticity (CP) modelling is based on continuum mechanics and variational principles; an equilibrium solution is obtained between the applied external forces and the compatibility of internal displacements (depending on the material's mechanical resistance) in a volume element (polycrystal) to undergo plastic deformation. This volume is discretised into finite elements (FE) and their equations of motion are solved [67]. A dimensionless strain tensor \mathbf{F} is defined by comparing element displacements induced by an external force with respect to the unstrained material. Plastic flow evolves according to the velocity gradient [68]: $\mathbf{L} = \dot{\mathbf{F}}\mathbf{F}^{-1}$ [s⁻¹], where $\dot{\mathbf{F}}$ is the derivative of \mathbf{F} with respect to time. This

tensor is composed by an elastic \mathbf{L}_e and a plastic \mathbf{L}_p response. The former is related to the elastic elongation that is restored once the external stress is removed. \mathbf{L}_p is induced by dislocations provoking an irreversible distortion. \mathbf{L}_p is equal to the sum of shear rates on all slip systems:

$$\mathbf{L}_p = \sum_{\mathbf{i}} \dot{\gamma}^{\alpha} \mathbf{m}^{\alpha} \otimes \mathbf{n}^{\alpha}, \quad (2.17)$$

where \mathbf{m}^{α} and \mathbf{n}^{α} are unit vectors describing the slip direction and the normal direction to the slip plane in the slip system α , respectively; and $\dot{\gamma}^{\alpha}$ is the shear rate on that same system. Finite Element Method (FEM) is employed to solve these equations.

Phenomenological equations are defined to relate $\dot{\gamma}^{\alpha}$ with an applied shear stress τ^{α} (on the slip system α) and critical resolved shear stress τ_c^{α} to activate the slip system α : $\dot{\gamma}^{\alpha} = f(\tau_c^{\alpha}, \tau^{\alpha})$, where f is usually a power-law expression. A number of parameters are fitted for each system.

The variation of τ_c^{α} in time ($\dot{\tau}_c^{\alpha}$) depends on the shear strain contribution and critical resolved shear stress of other slip systems. Empirical relations are fitted to capture micromechanical dislocation interaction in different slip systems.

Equation 2.17 describes plasticity in terms of the critical resolved shear stress for each slip plane only, and it lacks microstructural information. An extension can be made to relate the dislocation evolution to the effective stress on every slip system. For instance, mesoscale methods describe the average dislocation density evolution of each slip plane with simple relations¹ [69, 70, 71]; on the other hand, discrete dislocation dynamics have been employed to describe specific dislocation arrangements [72, 73].

Deformation twinning can be directly incorporated into this methodology by inserting an additional twinning distortion term in equation 2.17 [74, 75]. Once again, additional phenomenological relations are required to describe twin evolution with deformation.

Another approach at the continuum scale is based on combining the von Mises criterion for plastic flow, and postulating the stress tensor variation $\dot{\sigma}$ in terms of the strain rate tensor [76]: $\dot{\sigma} = \mathbf{C}(\dot{\epsilon} - \dot{\epsilon}^p)$, where \mathbf{C} is a constant tensor, and $\dot{\epsilon}$ and $\dot{\epsilon}^p$ are the total and plastic strain rate tensors, respectively. This approach is widely employed in industry for describing the macroscopic flow stress response in various directions.

These methodologies incorporate orientation effects in plasticity and are able to describe the macroscopic material response. However, a number of semiempirical or phenomenological relations for the critical resolved shear stress, strain rate and temperature are introduced with several fitting parameters. Additional techniques are required to describe microstructure evolution.

¹See Section 2.5.

2.4.4 Mesoscale approaches

Several approaches at the mesoscale (typically accounting for microstructure evolution occurring between 10^{-8} – 10^{-5} m) have been proposed. These methods focus on describing plasticity as a function of one or more internal state variables. One of the most employed phenomenological models at the mesoscale is the Kocks–Mecking (KM) formulation, which accounts for the competition between dislocation generation and annihilation, describing the evolution of the average dislocation density ρ during deformation [6]. This formulation is further analysed in Section 2.5.

Another approach has been proposed by Huang *et al.* [77, 35], where plasticity is described by means of an irreversible thermodynamics framework. Dislocation motion is considered as the main energetic contributor to plastic deformation.

This theory is based on Prigogine’s concept of entropy S in irreversible processes [78]. It is postulated that the total entropy change dS is null in a stationary state and all state variables are independent of time: the entropy production rate in the system d_iS is compensated by the entropy flux of the system to the surroundings d_eS

$$\frac{dS}{dt} = \frac{d_iS}{dt} + \frac{d_eS}{dt} = 0. \quad (2.18)$$

Three major irreversible processes take place during deformation: dislocation generation, glide and annihilation. d_iS is expressed in terms of these effects as:

$$d_iS = \frac{dW_{gen}}{T} + \frac{dW_{gl}}{T} + \frac{dW_{an}}{T}, \quad (2.19)$$

where dW_{gen} , dW_{gl} and dW_{an} are the mechanical work required for the generation, glide and annihilation of dislocations, respectively. The instantaneous dislocation–density variation $d\rho$ equals the difference between the instantaneous generation $d\rho^+$ and annihilation $d\rho^-$: $d\rho = d\rho^+ - d\rho^-$. dW_{gen} and dW_{an} are assumed to be proportional to $d\rho^+$ and $d\rho^-$, respectively: $dW_{gen} = \frac{1}{2}\mu b^2 d\rho^+$ and $dW_{an} = \frac{1}{2}\mu b^2 d\rho^-$. The energy dissipated due to dislocation glide dW_{gl} is expressed as [35]: $dW_{gl} = \tau b \bar{l} d\rho^+$, where τ is the applied shear stress and \bar{l} is the average dislocation spacing.

The external entropy d_eS is related to the heat loss dQ to the surroundings by: $d_eS = \frac{dQ}{T}$. According to the energy conservation law dQ is approximated by the difference between the internal energy increase $dU = \frac{1}{2}\mu b^2 d\rho$ (due to the dislocation storage) and the mechanical work conducted into the metal by the external loading $dW = \tau d\gamma$ [35], where $\tau = \alpha \mu b \sqrt{\rho}$ is the applied stress, and α is a constant:

$$d_eS = \frac{dQ}{T} = \frac{dU - dW}{T} = \frac{\frac{1}{2}\mu b^2 d\rho - \alpha \mu b \sqrt{\rho} d\gamma}{T}. \quad (2.20)$$

The total entropy variation with time has been proposed to be proportional to the work hardening rate [35]:

$$\frac{dS}{dt} = \dot{\gamma} \frac{dS}{d\gamma} = \dot{\gamma} \frac{C}{T} \frac{b}{l} \frac{d\tau}{d\gamma}, \quad (2.21)$$

where $\dot{\gamma}$ is the strain rate, and C is a proportionality constant. Combining the previous equations, the evolution of the dislocation density with strain can be obtained:

$$\frac{d\rho}{d\gamma} = \left(\frac{2\alpha}{2+2\alpha-C\alpha} \right) \frac{1}{b} \sqrt{\rho} - \frac{2+2\alpha}{2+2\alpha-C\alpha} \frac{d\rho^-}{d\gamma}, \quad (2.22)$$

where $\frac{d\rho^-}{d\gamma}$ is the dislocation annihilation rate. As the annihilation of individual dislocations is a thermally activated process (driven by dislocation glide), Rivera and Huang express this rate as [35]:

$$\frac{d\rho^-}{d\gamma} = \frac{\nu_0}{\dot{\gamma}} \exp\left(-\frac{\Delta G}{k_B T}\right) \rho, \quad (2.23)$$

where ν_0 is the atomic vibration frequency, and ΔG is the activation energy for dislocation annihilation. Inserting this expression into equation 2.22, the dislocation evolution equation becomes:

$$\frac{d\rho}{d\gamma} = \left(\frac{2\alpha}{2+2\alpha-C\alpha} \right) \sqrt{\rho} - \left(\frac{2+2\alpha}{2+2\alpha-C\alpha} \right) \frac{\nu_0}{\dot{\gamma}} \exp\left(-\frac{\Delta G}{k_B T}\right) \rho. \quad (2.24)$$

Grain boundary and precipitation hardening effects can be incorporated in this formulation by including additional stress terms in τ [35, 79].

A very interesting aspect of this approach is the ability to recover the Kocks–Mecking equation [35]. The previous equation was derived on a thermodynamics basis. Moreover, Rivera and Huang [35] have demonstrated that the energy barrier for dislocation annihilation ΔG is the key parameter strongly controlling plasticity via $\frac{d\rho^-}{d\gamma}$; however it was fitted for each specific material and the model showed to be very sensitive to ΔG variations, also the model is very sensitive to strain rate variations. A more fundamental description of ΔG (and the dislocation annihilation rate) is required.

2.4.5 Multiscale modelling

The combination of different modelling approaches allows to describe plastic deformation at various scales. For instance, Zhu *et al.* [80] have combined MD with Finite Element Methods (FEM) to model nanoindentation in copper single crystal; short-range interactions are described around the indenter, whereas FEM

is employed for the long-range effects at higher length scales. Groh *et al.* [81] have combined MD, DDD and CP to describe plasticity at various scales in aluminium single crystals; MD is employed to describe dislocation mobility; DDD determines the work hardening rate on each system; and CP incorporates the previous results to describe the macroscopic material response. Other interesting contributions include CP coupled with DDD only [82, 83]. Lee *et al.* [70] have combined CP with the evolution of a single dislocation density, but a number of fitting parameters are incorporated for various orientations. Sundararaghavan and Zabaras [84, 85] have combined the FEM and CP to forging; in their work the macroscopic deformation gradient is represented purely in terms of the motion of the exterior boundary; strain rate effects are incorporated in the form of an Arrhenius equation, to account for dislocation slip to be thermally activated process. Sundararaghavan and Kumar [86] have further added a probability density function to prescribe the most likely crystal orientations.

All in all, these approaches are able to describe plasticity at various scales. They demand *ad hoc* relationships between dislocation motion and evolution due to dissimilar scales in length and time; these are usually fitted and phenomenologically determined, particularly as a function of strain, strain rate and temperature. However, incompatibilities due to the lack a unique variable become present, leading to a limited range of applications. Moreover, as stated by McDowell [87], the transition and hierarchy between methods describing different scale ranges needs further examination, as incompatibilities due to the lack of a unique variable become present.

2.5 Kocks-Mecking equation

The Kocks-Mecking equation accounts for the evolution rate of the average (homogeneous) dislocation density ρ with strain γ . It is composed of a dislocation storage ($\frac{d\rho^+}{d\gamma}$) and annihilation ($\frac{d\rho^-}{d\gamma}$) rate, respectively:

$$\frac{d\rho}{d\gamma} = \frac{d\rho^+}{d\gamma} - \frac{d\rho^-}{d\gamma}. \quad (2.25)$$

This approach has been directly applied to obtain the flow stress during plastic deformation or it is incorporated into more complex techniques such as the methods previously described, providing the material's hardening behaviour via the average dislocation density [88, 89], the dislocation development on different slip systems [70, 69, 71, 90], and the temperature and strain rate effects on plasticity [21, 91]. Examples of the use of KM approach as input to other modelling techniques are listed in Table 2.2.

Table 2.2: Modelling approaches employing Kocks-Mecking (KM) formulation as input: crystal plasticity (CP), finite-element method (FEM), discrete dislocation dynamics (DDD), and mesoscale/internal-state-variable (ISV).

Modelling technique	Physical Phenomena	Reference
CP	Deformation in single crystals	[70]
CP	Pyramidal indentation in FCC metals	[69]
CP	Softening kinetics in polycrystalline nickel with different sample thicknesses and grain sizes	[71]
FEM	Multiscale modelling of nanocrystalline materials	[88]
FEM	Static and dynamic recrystallisation in copper	[92]
FEM	Twinning-induced plasticity in steels	[89]
DDD	Thin-film plasticity	[90]
ISV	Temperature effects of twinning in zirconium	[21]
ISV	Twinning hardening in magnesium	[91]
ISV	Dynamic recrystallisation in a two-phase Ti alloy	[93]

A number of fitting parameters are introduced in this equation to describe the behaviour of specific alloys and deformation phenomena (temperature, strain rate, orientation and microstructure), thereby lacking a generalised formulation that would provide more information on how to improve the alloy properties by modifying material parameters. These could be achieved with a physics-based approach that would be able to incorporate microstructural and processing effects on the dislocation generation and annihilation rates.

Estrin and Mecking [94] have shown that dislocation storage involves the additions of the inverse dislocation mean free path Λ , accounting for 1) dislocation-dislocation interactions (Λ_{dis}^{-1}), and 2) microstructural obstacles impeding dislocation motion. The effect of grain boundaries, twins and solute atoms on dislocation evolution are described in this thesis. The storage contribution of each barrier then equals the inverse mean free path of the respective obstacle:

$$\frac{d\rho^+}{d\gamma} = \frac{1}{b} \left(\frac{1}{\Lambda_{dis}} + \frac{1}{\Lambda_T} + \frac{1}{\Lambda_{SS}} + \frac{1}{\Lambda_{GB}} \right), \quad (2.26)$$

where Λ_T is the average twin thickness, Λ_{SS} is the average dislocation mean free path in the presence of solute strengtheners, and Λ_{GB} is the average grain boundary spacing. Λ_{dis} has been obtained by Kocks and Mecking [6]: $\Lambda_{dis} = \frac{1}{k_1\sqrt{\rho}}$, where

$$k_1 = \frac{1}{30} \left(\frac{\mu}{\mu_0} \right)^2 \quad (2.27)$$

is a constant, and μ_0 is the shear modulus at 0 K. The temperature dependence of k_1 is implicitly described in μ . Although only a phenomenological description of this equation is available, it will be shown that it is valid for several crystal structures and deformation conditions.

The dislocation annihilation term accounts for the contributions of 1) dynamic recovery (DRV), due to dislocation interactions and interactions with other crystal defects; and 2) dynamic recrystallisation (DRX), where grain nucleation and growth occurs. DRX occurs at high temperatures and/or low strain rates, and a critical (incubation) strain is required. $\frac{d\rho^-}{d\gamma}$ equals [6, 77, 95]:

$$\frac{d\rho^-}{d\gamma} = f_{DRV}\rho + f_{DRX}\rho_{DRX}, \quad (2.28)$$

where f_{DRV} is the dynamic recovery coefficient, f_{DRX} is the dynamic recrystallisation coefficient, and ρ_{DRX} is the dislocation density in the growing grains. Kocks and Mecking obtained an empirical relation for the dynamic recovery coefficient in pure FCC metals that incorporates temperature and strain rate effects [6]:

$$f_{DRV}^{KM} = \frac{\mu}{\mu_0} \frac{1}{100\tau_{\nu 0}} \left(1 - \sqrt{\frac{1}{g_0} \frac{k_B T}{\mu b^3} \ln \frac{\dot{\epsilon}_0^{KM}}{\dot{\epsilon}}} \right)^{-2}, \quad (2.29)$$

where $\tau_{\nu 0}$ and g_0 are material-dependent constants, and $\dot{\epsilon}_0^{KM}$ is a constant generally considered to be equal to 10^7 s^{-1} for FCC crystals. However, these constants are identified for different materials and remain valid for a limited temperature range [6].

Combining equations 2.26, 2.27 and 2.28, the Kocks–Mecking equation becomes:

$$\frac{d\rho}{d\gamma} = \frac{1}{b} \left(\underbrace{k_1\sqrt{\rho}}_{(A)} + \underbrace{\frac{1}{\Lambda_T}}_{(B)} + \underbrace{\frac{1}{\Lambda_{SS}}}_{(C)} + \underbrace{\frac{1}{\Lambda_{GB}}}_{(D)} \right) - \underbrace{f_{DRV}\rho}_{(E)} - \underbrace{f_{DRX}\rho_{DRX}}_{(F)}. \quad (2.30)$$

It is worth noting that each term features under specific circumstances: (B) is only considered for HCP metals, FCC with low stacking fault energy and nano-twinned copper; (C) is not present for pure materials; (D) is neglected for single crystals and coarse-grain polycrystals; and (F) is active only at high temperatures. $k_1\sqrt{\rho}$ and $f_{DRV}\rho$ are present for all plasticity scenarios, but their values change for different deformation conditions and crystal structures. Analytical expressions for these terms are provided in this thesis. This offers a physical basis of the parameters involved in the Kocks–Mecking equation.

Finally, the Taylor relation depicts the macroscopic (axial) stress σ with the average dislocation density [6]:

$$\sigma = \sigma_0 + \alpha M \mu b \sqrt{\rho}, \quad (2.31)$$

where σ_0 is the friction stress induced by lattice resistance, grain boundary or solid solution strengthening [96]; $\alpha = 0.3$ is a constant; and M is the Taylor orientation factor. M is generally considered to equal 3 [6], except for HCP metals where orientation severely affects the material's work hardening behaviour, and a relationship in terms of the deformation orientation is introduced in Chapter 5.

Chapter 3

A thermostatistical theory for plastic deformation

A new theory for describing dislocation evolution in metals is presented in this chapter. The novelty of the approach stems from obtaining an expression for the dynamic recovery term in the Kocks–Mecking equation. A thermodynamic analysis on an annihilating dislocation segment is performed to determine the energy barrier for dislocation annihilation. The statistical entropy associated to energy dissipation of energetically favourable dislocation paths during deformation is introduced. It is demonstrated that statistical entropy features strongly in modelling plasticity at low and high temperatures. This approach is successful in quantifying: (1) The transition between low to intermediate, and intermediate to high temperature dislocation annihilation regimes are delimited by transitions in the number of microstates. (2) The average dislocation cell size and misorientation angle evolution as a function of strain, strain rate and temperature, which are obtained by performing an energy balance between the dislocation forest and the cellular structure formation, expressing the slip energy to form the latter in terms of the statistical entropy. Employing only input parameters obtained from experiments, the new theory is able to reproduce the experimental saturation stress, stress-strain relationships, and average cell size evolution at wide temperature ranges for pure FCC metals at a variety of strain rates.

3.1 Introduction

Quantitative understanding of dislocation motion is essential to describe plasticity in crystalline materials. Dislocation mobility controls the material's ability to accommodate strain and modify its microstructure [25]. The velocity of a disloca-

tion segment (at a given time) depends on several parameters such as the crystal structure, the resolved shear stress, the interaction with other crystal defects, temperature and strain rate [25, 76, 97].

Every modelling approach requires the introduction of specific relations to describe dislocation kinetics; these relations or “constraints” depend on the model scale and variables. For instance, molecular dynamics describes the interaction of atoms, where interatomic potentials constrain the lattice distortion (dislocation) behaviour. Discrete dislocation dynamics require the introduction of a velocity vector for every dislocation segment (variable) in two or three dimensions, by the presence of a constraining driving force and their motion is limited to specific slip planes (when pure slip occurs). In contrast to the former techniques, average dislocation density descriptions present no constraints on the dislocation average velocity or spatial distribution; however, this leads to loss of microstructural information. The Orowan equation (2.3) is a relation between the average velocity $\langle v \rangle$ and the macroscopic strain rate that may represent an additional physical constraint.

Only approximations have been obtained for $\langle v \rangle$, such as power-law equations in terms of the applied stress [25, 98, 99, 100], or Arrhenius-type equations with energy barrier descriptions [101, 26]. Cai and Bulatov [54, 23] have expressed the dislocation velocity in terms of a mobility term M_{dis} and an applied (driving) force P_{dis} on the segment for discrete dislocation dynamics $\langle v \rangle = M_{dis}P_{dis}$. The former is usually fitted to an Arrhenius equation. Some discrete dislocation dynamics approaches employ a first order differential equation for the velocity vector evolution in time (similar to a Newton equation of motion) [20], a number of parameters are fitted for specific deformation conditions (see equation 2.15). Although a velocity (probability) distribution for a single dislocation (or a group of them) is required, describing the effects involved in the dislocation velocity evolution poses a big challenge.

If it is wished to assign probabilities to different dislocation velocities that are subjected to specific model constrains (*e.g.* atom interactions, slip planes, number of dislocations, applied stress, etc.), the probability distribution p that best describes this problem should maximise the information content by the given model relations [102, 103], *i.e.* it is able to *predict* the dislocation velocity values for the given model characteristics. Such is obtained when the function

$$H(p) = - \sum_i p_i \ln(p_i) \quad (3.1)$$

reaches its maximum value, where p_i is the probability of a dislocation to reach a (discrete) velocity v_i ; H is called the information entropy [102]. The entropy is a measure of the average uncertainty in the dislocation velocity. This criterion is called the maximum entropy principle; it aids to provide the best probability

distribution that reflects the model *constraints* associated to a problem. If no constraints are defined, the events are assigned equal probabilities and a uniform (velocity) distribution is able to describe dislocation kinetics [102, 104].

This approach suggests more attention is to be paid to mesoscale approaches, where less constraints are defined. However, there is no physics-based approximation able to link dislocation kinetics with the average dislocation density evolution yet. Although the Orowan equation relates the macroscopic strain rate with the mobile dislocation density, it does not provide further description on the dislocation density evolution with strain.

Nevertheless, a natural correspondence between the maximum entropy principle and statistical thermodynamics is arguable [105, 106]: the statistical entropy can be explained in terms of the possible states a physical system can reach. Thus, describing dislocation kinematics in a thermostatistical framework allows to estimate the energy loss due to different migration paths of a dislocation, instead of describing its instantaneous velocity at every moment. This allows to incorporate dislocation kinematics into the energy barrier for dislocation annihilation, cell formation, misorientation, grain nucleation and growth. These cases are explored in the following sections.

In a recent review, McDowell [87] stated that, in the context of plasticity, “thermodynamic and kinetic relations are at the core of evolution equations for microstructure”. On the other hand, Cottrell’s seminal work [29] on dislocation nucleation estimates a small effect from the configurational entropy (due to the possible initial dislocation locations); this term has been usually neglected in modern literature. However, configurational effects become important when considering dislocation glide configurations; at every moment (time step) a dislocation can move any number of atoms (limited by the speed of sound [29, 5]), increasing the number of possible configurations as deformation evolves. This effects are considered for modelling dislocation behaviour during deformation.

3.2 Dislocation kinetics: Statistical entropy

When a dislocation glides, the magnitude of its velocity v is limited by the speed of sound c in the material [5]; it can also remain immobile for a given time ($v = 0$). Thus, v can take values in the range $0 \leq v < c$ [5].

A microstate, or a specific configuration j , is defined as the number of interatomic distances n_j a dislocation glides during an arbitrary time step Δt (given in multiples of the magnitude of the Burgers vector) along the slip direction [104]

$$n_j = \left[\frac{v_j}{b} \Delta t \right], \quad (3.2)$$

where $[\]$ is the integer-part function and v_j is the dislocation instantaneous

velocity during Δt . Note that, to simplify the analysis, the values of v_j are discrete. It is worth noting that the microstate definition is made in terms of atomic displacements to preserve the thermostatics formalism [107], however this analysis can be modified by defining a microstate in terms of the dislocation velocity, obtaining the same result.

The microstates dictate the slip possibilities for a dislocation segment. If a dislocation would glide at the speed of sound (c), the equivalent number of subunits it moves is

$$N = \left[\frac{c}{b} \Delta t \right]. \quad (3.3)$$

It is worth noting that $0 \leq n_j < N$ for all j . This microstate ensemble defines a set of

$$\{n_j\}_{j=1}^{M_{vel}} \quad (3.4)$$

possible distances a dislocation can glide during Δt , where M_{vel} is an arbitrary number that depends on the scale of the description (atomic, mesoscale, or microscopic) and its constrains. Figure 3.1 shows a schematic representation of this ensemble. Equation 3.4 represents the set of possible distributions for dislocation displacement (velocity) during Δt . This analysis is consistent with the microcanonical formalism in statistical mechanics [107, 104].

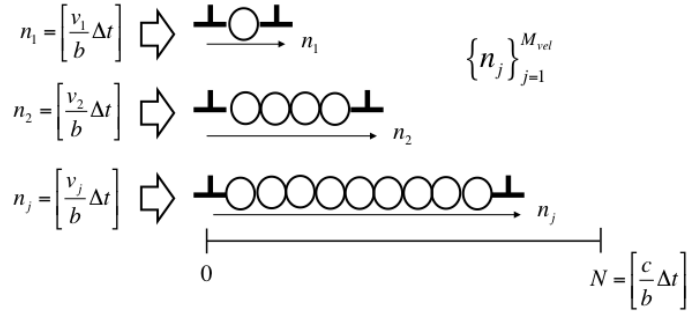


Figure 3.1: Schematic representation of the possible dislocation atomic displacements. Atoms are represented by circles. The arrows represent the trajectory from the initial state (prior to deformation) to the possible atomic displacements for the given velocities.

When the average dislocation density is considered and no restrictions are imposed, the previous ensemble (equation 3.4) is reduced to a set containing multiples of the average dislocation displacements [104]

$$\langle n \rangle = \left[\frac{\langle v \rangle}{b} \Delta t \right] \quad (3.5)$$

that is limited by N and it contains $M_{vel} = \left[\frac{N}{\langle n \rangle} \right]$ elements.

The total number of microstates Ω_{dis} is then equal to [102, 104, 107]

$$\Omega_{dis} = M_{vel} = \left[\frac{N}{\langle n \rangle} \right] \approx \frac{c}{\langle v \rangle}. \quad (3.6)$$

This result remains valid only when average displacements are considered; however this formalism can be extended to other scales with their respective constraints. For instance, molecular dynamics requires the use of statistical mechanics to express microscopic information in terms of macroscopic observables, by introducing additional energy constraints [20].

The previous equation can be expressed in terms of strain rate via the Orowan equation. The value of ρ_m in equation 2.3 is obtained from the dislocation density consistent with yield point (ρ_Y), as this determines an equivalent dislocation population at the onset of plastic deformation [104]. Note that $\langle v \rangle$ accounts for mobile and immobile ($v = 0$) dislocations, as no distinction between dislocation types is being considered. Equation 3.6, in terms of the strain rate, becomes:

$$\Omega_{dis} = \frac{c}{\langle v \rangle} = \frac{b\rho_m c}{\dot{\epsilon}} \approx \frac{b\rho_Y c}{\dot{\epsilon}} = \frac{\dot{\epsilon}_0}{\dot{\epsilon}}, \quad (3.7)$$

with

$$\dot{\epsilon}_0 = b\rho_Y c. \quad (3.8)$$

$\dot{\epsilon}_0$ estimation

The temperature range where additional crystal defects such as vacancies only moderately alter dislocation slip is $0 < T < 0.6T_m$ [6], where T_m is the melting point temperature. Figure 3.2 shows a) the values of $\dot{\epsilon}_0$ in terms of the homologous temperature $T_h = T/T_m$ for Cu, Al, Ni and Ag, and b) the average values of $\dot{\epsilon}_0$ as a function of the temperature in the range of application, via the mean value theorem: $\dot{\epsilon}_0^{avg} = \frac{1}{0.6T_m} \int_0^{0.6T_m} (bc\rho_Y(T))dT$ (in the case of Ni, the lower limit of integration was taken as 250 K to avoid a critical point as $T_h \rightarrow 0$ and the formula for σ_Y diverges, see Appendix A). The dislocation density consistent with the yield point is approximated by employing the Taylor relation (equation 2.31) with $\sigma_0 = 0$ [6]: $\rho_Y = (\sigma_Y/(\alpha bM\mu))^2$. The material parameters are shown in Appendix A.

The fitted value employed originally by Kocks and Mecking $\dot{\epsilon}_0^{KM} = 10^7 \text{ s}^{-1}$ to describe the experimentally observed saturation stress of Cu, Ni, Al and Ag is shown with a dotted line (equation 2.29), and a value employed by Follansbee [108] $\dot{\epsilon}_0 = 10^8 \text{ s}^{-1}$ for Fe is shown to be an upper bound. It is remarkable to notice that all the average values computed here, and stemming from the speed of sound assumption, approach the value for $\dot{\epsilon}_0$ employed by Kocks and Mecking

(equation 2.29). Thus, the model is able to provide physics-based justification for this constant.

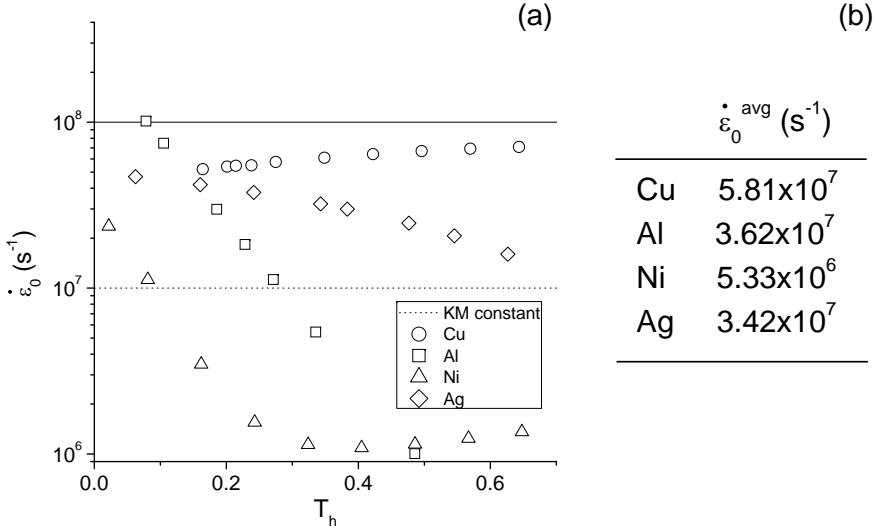


Figure 3.2: (a) Values for $\dot{\epsilon}_0$ as function of temperature and (b) average values of $\dot{\epsilon}_0$ for Cu, Al, Ni and Ag.

3.2.1 Vacancy-dislocation kinetic contribution

When temperature increases, vacancy–dislocation interaction becomes prominent, provoking dislocations to undergo climb, increasing dislocation displacement events, including those leading to annihilation. Consequently, an additional term in equation 3.7 is required. A microstate is defined in terms of dislocation slip paths; however vacancies migrate through the material via diffusion [4], being this mechanism of a different nature [5], consequently they cannot be directly combined and a common reference system has to be defined [107, 109].

Both mechanisms are compared with the average distance between two dislocations $\bar{l} = 1/\sqrt{\rho}$ to define a common migration length. The number of interatomic distances between two dislocations is defined as \bar{l}/b . The additional number of microstates due to the vacancy–dislocation interaction Ω_{v-d} is the ratio between the average maximum vacancy occupancy \hat{n}_v in \bar{l} , and the average slip fraction

n_d a dislocation glides with respect to \bar{l} [109].

Analogous to the speed of sound for dislocation slip in equation 3.7, \hat{n}_v defines an upper boundary for vacancy–assisted climb. Figure 3.3 shows a schematic representation of the vacancy–dislocation interaction system. Although vacancy–dislocation interaction takes place in three dimensions, this involves complex calculations and the inclusion of additional equations; to simplify the analysis, the average interaction effect is assumed to occur in one dimension.

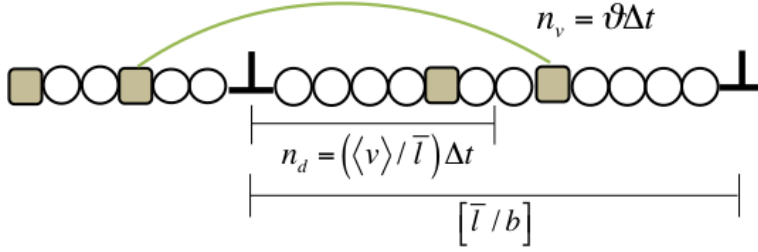


Figure 3.3: One–dimensional representation of the vacancy–dislocation interactions. Vacancies are represented by squares and atoms by circles. During a time step Δt , n_v is the number of interatomic distances a vacancy can move, and n_d is the number of interatomic distances a dislocation can glide. The curved line represents the number of atomic jumps.

A vacancy can migrate an average of $n_v = \vartheta \Delta t$ sites during Δt , where ϑ is the migration frequency (equation 2.5); the units of ϑ is atomic sites per unit time. Note that n_v is proportional to the total vacancy migration length path ($\vartheta \Delta t$) to measure all possible vacancy–dislocation encounters.

The maximum number of vacancies that can migrate within two average dislocations separated by a distance \bar{l} is $[\frac{\bar{l}}{b}]$. Thus, the maximum vacancy occupancy during Δt becomes:

$$\hat{n}_v = n_v \left[\frac{\bar{l}}{b} \right] = \vartheta \Delta t \left[\frac{\bar{l}}{b} \right] \simeq \vartheta \Delta t \frac{\bar{l}}{b}. \quad (3.9)$$

On the other hand, when a dislocation glides at $\langle v \rangle$ during Δt , the reduced glide length within \bar{l} is $n_d = \frac{\langle v \rangle}{\bar{l}} \Delta t$. Combining the previous expressions, Ω_{v-d} leads to [109]

$$\Omega_{v-d} = \frac{\hat{n}_v}{n_d} = \frac{\vartheta \Delta t (\bar{l}/b)}{\langle v \rangle \Delta t / \bar{l}} = \frac{\vartheta \bar{l}^2}{b \langle v \rangle} = \frac{\vartheta}{b \langle v \rangle \rho} = \frac{\vartheta}{\bar{\epsilon}}, \quad (3.10)$$

where the mobile dislocation density has been equated with the total dislocation density to account for both mobile and immobile dislocations. Ω_{v-d} is a measure of the weighted contribution of the ability of a vacancy to drift as a response to

thermal activation, with respect to the migration of a dislocation as a response to strain.

The total number of microstates Ω_{pure} for dislocation motion becomes

$$\Omega_{pure} = \Omega_{dis} + \Omega_{v-d} = \frac{\dot{\epsilon}_0}{\dot{\epsilon}} + \frac{\vartheta}{\dot{\epsilon}}. \quad (3.11)$$

Finally, the statistical entropy equals [107]

$$\Delta S = k_B \ln \Omega_{pure} = k_B \ln \left(\frac{\dot{\epsilon}_0}{\dot{\epsilon}} + \frac{\vartheta}{\dot{\epsilon}} \right). \quad (3.12)$$

This equation incorporates the effect of dislocation glide and vacancy–assisted climb only; additional effects altering dislocation motion, such as solute atoms, grain boundaries and nanotwins are introduced in the following sections.

The Orowan equation is employed to describe dislocation kinetics for dynamic plastic deformation, however this methodology can be applied to static conditions such as static recovery, static recrystallisation or creep by introducing the respective relations for $\langle v \rangle$.

3.2.2 Transition temperatures

It is possible to obtain the transition points where different dislocation annihilation mechanisms prevail (Section 1.1.1) with equation 3.11 [109]:

1. If $\Omega_{v-d} < 1$, $\vartheta < \dot{\epsilon}$ and no microstates are available for vacancy–dislocation interaction, leading to cross–slip domination.
2. If $\Omega_{v-d} > \Omega_{dis}$, $\vartheta > \dot{\epsilon}$ and the vacancy–dislocation interaction is dominant over dislocation slip as there are more microstates available for dislocation motion due to the presence of vacancies, dislocation climb becoming the prevailing migration mechanism.
3. If $1 < \Omega_{v-d} < \Omega_{dis}$, both processes are present and a mix of cross–slip and climb take place.

The transition boundaries can be described as $\Omega_{v-d} = \frac{\vartheta}{\dot{\epsilon}} = 1$, and $\Omega_{v-d} = \Omega_{dis} \Rightarrow \vartheta = \dot{\epsilon}_0$. Such limits are expressed in terms of temperature and strain rate (equations 2.5 and 3.8) [109]:

$$\begin{aligned} T_0 &= \frac{E_m}{R \ln \left(\frac{\vartheta_D}{\dot{\epsilon}} \right)}, \\ T_f &= \frac{E_m}{R \ln \left(\frac{\vartheta_D}{\dot{\epsilon}_0} \right)}, \end{aligned} \quad (3.13)$$

where T_0 and T_f are the transition temperatures for the low, medium and high regimes, respectively.

Tables 3.1 and 3.2 show a comparison of these values with the experimental ranges obtained from the literature where transitions occur for Cu, Al, Ni and Ag. The homologous temperature $T_h = T/T_m$ is also shown. As experimental measurements usually do not show a sharp transition point, results are shown within the ranges where the transitions occur. The experimental values for Al are estimated when the charts for the activation energy for creep and activation area for glide change their curvature, respectively; for pure Cu the values are obtained when the shape of the shear stress plot at the stage V of deformation (approximately 40% of strain) is changed. For Ni and Ag, no experimental values were found. For T_0 , a strain rate of $4 \times 10^{-4} \text{ s}^{-1}$ is assumed when no experimental data were found.

Table 3.1: Lower limit temperature. E stands for experimentally determined and M for model results.

Material	$\dot{\epsilon}$ (s^{-1})	T_0^E (K)	Ref	T_0^M (K)	T_h
Cu	4×10^{-4}	-		276	0.20
Al	2×10^{-5}	250-290	[110]	176	0.18
Ni	4×10^{-4}	-		430	0.24
Ag	4×10^{-4}	-		255	0.2

Table 3.2: Upper limit temperature. E stands for experimentally determined and M for model results.

Material	$\dot{\epsilon}_0$ (s^{-1})	T_f^E (K)	Ref	T_f^M (K)	T_h
Cu	7.1×10^6	773-900	[111]	882	0.65
Al	2.6×10^6	450-520	[110]	474	0.5
Ni	1.3×10^6	-		1025	0.6
Ag	1.8×10^7	-		728	0.58

The results show good agreement with the experimental ranges. The lower and upper limits lay within the ranges of $0.2 - 0.24T_m$ for T_0 , and $0.5 - 0.65T_m$ for T_f , which are consistent with the ranges usually reported in the literature. T_0 is lower than $0.3T_m$; this can be due to the vacancy concentration at these temperatures is very low, and the transition becomes observable at higher temperatures when vacancy concentration increases.

To confirm that the theory is consistent with microstructural observations (vacancy–dislocation interactions), the vacancy accumulation at T_f is compared against the effective dislocation interaction length. At a given temperature there are c_{eq}/b^3 vacancies per unit volume in the material, where c_{eq} is the vacancy concentration at equilibrium, so that the mean spacing of neighbouring vacancies is $\Lambda_{vac} = b/c_{eq}^{1/3}$ (equation 2.6) [25]. On the other hand, as explained in Section 3.3, the interaction range of a dislocation with other crystal defects is given by its distortion length $l^* = 12.5b$. In the framework of this theory, l^* accounts for the effective distance for a dislocation to ensure its interaction with other defects such as vacancies or solute atoms. Furthermore, the initial dislocation population (in terms of their average spacing) can be approximated by the average dislocation spacing at the yield point ($\bar{l}_Y = 1/\sqrt{\rho_Y}$). Thus, an effective interaction length Λ_{v-d} can be defined as the distortion field length of the initial dislocation spacing: $\Lambda_{v-d} = l^* \bar{l}_Y/b$. Table 3.3 shows a comparison between Λ_{vac} and Λ_{v-d} for Cu, Al, Ni and Ag. Both lengths have the same order of magnitude at this temperature, implying that above T_f at least one vacancy may jump within a dislocation’s distortion field length to interact and undergo climb. Although these results are consistent with the experimentally observed transition points, σ_Y variations may cause fluctuations in Λ_{v-d} .

Table 3.3: Vacancy mean spacing (Λ_{vac}) vs. initial dislocation interaction length (Λ_{v-d}).

Material	E_f (kJ mol ⁻¹)	T_f (K)	Λ_{vac} (nm)	Λ_{v-d} (nm)
Cu	97	882	21	9
Al	67	474	81	59
Ni	135	1025	49	77
Ag	106	728	99	16

3.3 Dislocation annihilation: Dynamic recovery and cell formation

An expression for the dynamic recovery coefficient (f_{DRV}) in equation 2.30 is presented for pure FCC single crystals, where dislocation slip is the main deformation mechanism and no dynamic recrystallisation is present (only terms (A) and (E) are present in equation 2.30).

Dislocation annihilation due to dynamic recovery occurs by the encounter of dislocations with opposite signs. This rate is related to the characteristic (average) velocity $\langle v \rangle$ of a dislocation [35]. The derivations in this section rest on three

assumptions [104]:

- i*) The displacement (velocity) of a dislocation segment leading to annihilation is thermally activated.
- ii*) Once dislocations are in close proximity to each other, their strain fields screen their neighbours' and impinge on each other; this alters $\langle v \rangle$.
- iii*) The energy necessary for a dislocation segment to migrate in a cross-slip annihilation event is proportional to the macroscopic yield stress of the material (σ_Y). For uniaxial loading conditions, σ_Y is directly related to the critical resolved shear stress to initiate dislocation slip [76].

Assumption *i*) leads to an expression for the average velocity of a dislocation segment such that annihilation takes the form of an Arrhenius law [26, 104]

$$\langle v \rangle = c \exp \left(- \frac{\langle \Delta G \rangle}{k_B T} \right), \quad (3.14)$$

where $\langle \Delta G \rangle$ is the energy barrier to overcome in order to reach $\langle v \rangle$. The velocity is a function of several parameters such as temperature, strain rate and chemical composition, which dependency is incorporated into $\langle \Delta G \rangle$.

Consider a dislocation segment of length l that undergoes annihilation under an applied stress. The volume of this (thermodynamic) system is delimited by the dislocation segment length (l) multiplied by the distortion field length (l^*) and the magnitude of the Burgers vector, *i.e.* the volume of substance per dislocation that is not dislocated after a certain strain increment

$$V_{sys} = l^* b l. \quad (3.15)$$

l^* delimits the boundaries within which annihilation occurs, and it is determined by the point beyond which more than 98% of the strain vanishes away from the dislocation core. It was found to be $l^* \simeq 12.5b$ for different metals [112, 113, 114]. $\langle \Delta G \rangle$ is composed by [104]: (1) a dislocation formation energy term, U_{form} , this is approximated by the strain energy around the segment; (2) a dislocation migration energy term, U_{mig} , that initiates glide towards annihilation; (3) a vacancy energy contribution at higher temperatures ($T > T_0$), U_{vac} , induced by the vacancy chemical work around the segment; and (4) the entropy, $T\Delta S_{DRV}$, that dictates the degree of disorder in the system due to the different dislocation velocities:

$$\langle \Delta G \rangle = \frac{b}{l} (U_{form} + U_{mig} + U_{vac} - T\Delta S_{DRV}), \quad (3.16)$$

where the factor b/l scales the energy contributions to the number of atoms along the dislocation line participating in the annihilation process [104].

The strain energy around the segment is approximated by equation 2.2:

$$U_{form} = \frac{1}{2}\mu b^2 l. \quad (3.17)$$

The migration energy term (assumption *ii*) is considered to be the product of the yield stress σ_Y (mechanical work), which is the initial point for slip, the activation area $A_{act}b^2$ for cross-slip [7], where A_{act} is a dimensionless, multiplied by the length of the segment:

$$U_{mig} = \sigma_Y A_{act} b^2 l. \quad (3.18)$$

The chemical stress σ_v induced in the crystal structure by the inclusion of a vacancy is equal to the chemical potential (equation 2.7) divided by its volume:

$$\sigma_v = \frac{\mu_v}{b^3}. \quad (3.19)$$

The chemical work induced on the dislocation segment (V_{sys}) becomes:

$$W_v = -\sigma_v V_{sys} = -\frac{l^* l}{b^2} \mu_v. \quad (3.20)$$

W_v increases with temperature (equation 2.7), however the contribution of vacancies to dislocation annihilation below T_0 is null and consequently their energy contribution as well. To incorporate such behaviour, a function $\delta(T)$ is defined [109]:

$$\delta(T) = \begin{cases} 0 & \text{if } T < T_0 \\ \frac{T-T_0}{T_f-T_0} & \text{if } T_0 \leq T < T_f \\ 1 & \text{if } T_f < T, \end{cases} \quad (3.21)$$

and combined with equation 3.20 to incorporate the energy contribution U_{vac} of vacancies for dislocation annihilation

$$U_{vac} = \delta(T) W_v = \frac{l^* l}{b^2} \delta(T) (E_f + k_B T \ln c_m), \quad (3.22)$$

where the vacancy concentration in the chemical potential has been approximated by the equilibrium concentration (equation 2.6).

When vacancies are included in the system, the average annihilation velocity is increased and equation 3.14 is modified to include this effect, which in terms of the strain rate and vacancy migration frequency (equations 2.3 and 2.5) becomes

$$\left(\frac{\langle v \rangle}{c + c_{int}} \right) = \left(\frac{\dot{\epsilon}}{\dot{\epsilon}_0 + \vartheta} \right) = \exp \left(-\frac{\langle \Delta G \rangle}{k_B T} \right), \quad (3.23)$$

where c_{int} is an equivalent increase in the annihilation velocity due to the presence of vacancies ($\vartheta = b\rho_Y c_{int}$) [109]. Equation 3.23 offers an expression for the microstates, which can be readily input to equation 3.12 to obtain the statistical entropy. The role of dislocation impingement, however, needs first to be examined.

Dislocation impingement

When dislocations are in the proximity of each other they screen the deformation field of their neighbours. The impingement length is defined as the maximum distance between two dislocations when their strain fields screen each other. Once dislocation impingement takes place, the average annihilation velocity is altered along with the total number of microstates in the system. By defining $i = 1, 2, \dots, N_d - 1$ as the dislocations impinging with a reference dislocation $i = 0$, where N_d is the number of dislocations within an interaction volume, then the *additional* number of microstates introduced by impingement, considering independent events, is determined by a multiplication factor [104]

$$\Omega_{imp} = (\Omega_1 \cdot \Omega_2 \dots \Omega_{N_d-1})^{1/3} = (\Omega_{pure})^{\frac{1}{3}(N_d-1)} \quad (3.24)$$

where the exponent 1/3 in the equation is due to the fact that the number of microstates can only increase unidimensionally: an annihilating dislocation segment can only “see” neighbours along its slip direction. Note that if dislocations are far away from each other, impingement will not occur and $N_d = 1$, $\Omega_{imp} = 1$. The number of microstates then becomes

$$\Omega = \Omega_{pure} \cdot \Omega_{imp} = (\Omega_{pure})^{\mathcal{N}}, \quad (3.25)$$

where $\mathcal{N} = 1 + \frac{1}{3}(N_d - 1)$ when $N_d > 1$ and $\mathcal{N} = 1$ when $N_d \leq 1$. The modified entropy for dynamic recovery becomes

$$\Delta S_{DRV} = k_B \ln \Omega = k_B \ln \left(\frac{\dot{\epsilon}_0}{\dot{\epsilon}} + \frac{\vartheta}{\dot{\epsilon}} \right)^{\mathcal{N}}. \quad (3.26)$$

On the other hand, if impingement takes place, the number of microstates in equation 3.25 is modified; this alters also the value of $\langle v \rangle$ in equation 3.23 [109]:

$$\left(\frac{\langle v \rangle}{c + c_{int}} \right)^{\mathcal{N}} = \left(\frac{\dot{\epsilon}}{\dot{\epsilon}_0 + \vartheta} \right)^{\mathcal{N}} = \exp \left(- \frac{\langle \Delta G \rangle}{k_B T} \right). \quad (3.27)$$

Combining equations 3.16, 3.17, 3.18, 3.22, 3.26 and 3.27 leads to

$$\left(\frac{\dot{\epsilon}}{\dot{\epsilon}_0 + \vartheta} \right)^{\mathcal{N}} = \exp \left(- \frac{\langle \Delta G \rangle}{k_B T} \right)$$

$$\langle \Delta G \rangle = \frac{b}{l} \left(\frac{1}{2} \mu b^2 l + \sigma_Y A_{act} b^2 l + \frac{l^* l}{b^2} \delta(T) (E_f + k_B T \ln c_m) - T \Delta S_{DRV} \right).$$

l is obtained with the previous equations:

$$l = b \frac{\overbrace{T\Delta S_{DRV}}^{(1)}}{\underbrace{\frac{1}{2}\mu b^3}_{(2)} + \underbrace{\sigma_Y A_{act} b^3}_{(3)} + \underbrace{\frac{l^*}{b} \delta(T)(E_f + k_B T \ln c_m) - k_B T \ln \left(\frac{\dot{\epsilon}_0 + \vartheta}{\dot{\epsilon}}\right)^{\mathcal{N}}}_{(4)}}, \quad (3.28)$$

where l is the decrease in the dislocation length per dislocation at a given temperature and strain rate. This expression incorporates the effects of dislocation (1) kinetics (via the entropy term), (2) formation, (3) migration and (4) interactions with vacancies. These terms allow to describe temperature, strain and strain rate variations in the dislocation annihilation rate, providing a physical basis for this process during plastic deformation.

3.3.1 Dynamic recovery coefficient

The dynamic recovery coefficient can be defined as the fraction of substance undergoing dislocation annihilation per dislocation [104]: $f_{DRV} = \frac{N_A}{w_a} (\rho_a V_{sys})$, where N_A is Avogadro's number, w_a is the atomic weight of the material, and ρ_a is the density of the material. The dynamic recovery coefficient equals

$$f_{DRV} = \frac{N_A \rho_a b^2 l^*}{w_a} \frac{T\Delta S_{DRV}}{\frac{1}{2}\mu b^3 + \sigma_Y A_{act} b^3 + \frac{l^*}{b} \delta(T)(E_f + k_B T \ln c_m) - k_B T \ln \left(\frac{\dot{\epsilon}_0 + \vartheta}{\dot{\epsilon}}\right)^{\mathcal{N}}}. \quad (3.29)$$

Number of impinging dislocations

The number of dislocations N_d impinging with a reference dislocation will be the ratio of the critical distance for impingement r^* divided by half distance between dislocations when impingement is ignored $r_{NI} = 1/(2\sqrt{\rho_{NI}})$, where ρ_{NI} is the average dislocation density in the absence of impingement:

$$N_d = \frac{r^*}{r_{NI}}. \quad (3.30)$$

If $r^* < r_{NI}$, N_d is less than 1, implying that $\mathcal{N} = 1$ [104].

Impingement takes place when the strain field of the annihilating dislocation segment screens its neighbours'. The minimum radius for such screening is considered to be that at which it can dissociate into partials, which is determined by the stacking fault energy. Based on the treatment by Howie and Swann [115] to obtain the stacking fault energy, a formula to estimate whether the impingement

reaction becomes energetically favourable by directly comparing the line tension of a dislocation against the stacking fault energy χ is given by [104]

$$\chi = \frac{1}{l^*} \frac{\mu b^2}{4\pi} \ln \left(\frac{r^*}{r_0} \right), \quad (3.31)$$

where r_0 is the distance between partials in the cross-slip plane and r^* is the critical radius between dislocations that will favour dislocation dissociation over impingement. From this equation, the critical radius for impingement equals

$$r^* = r_0 \exp \left(\frac{l^* 4\pi \chi}{\mu b^2} \right). \quad (3.32)$$

On the other hand, in the absence of impingement, equation 2.30 (terms (A) and (E)) can be solved for $\mathcal{N} = 1$ in the dynamic recovery coefficient (equation 3.29) to obtain the equivalent average dislocation density. This is denoted by the subscript “NI” (not impinged) in:

$$\frac{d\rho_{NI}}{d\gamma} = \frac{k_1}{b} \sqrt{\rho_{NI}} - f_{NI} \rho_{NI}, \quad (3.33)$$

where f_{NI} has the value (equation 3.29):

$$f_{NI} = \frac{N_A \rho_a b^2 l^*}{w_a} \frac{k_B T \ln \left(\frac{\dot{\epsilon}_0 + \vartheta}{\dot{\epsilon}} \right)}{\frac{1}{2} \mu b^3 + \sigma_Y A_{act} b^3 + \frac{l^*}{b} \delta(T) (E_f + k_B T \ln c_m) - k_B T \ln \left(\frac{\dot{\epsilon}_0 + \vartheta}{\dot{\epsilon}} \right)}. \quad (3.34)$$

Activation area for annihilation

The activation area A_a for cross-slip is assumed to be the region where the distortion field of a dislocation is present, multiplying the distance r_0 between partials in the cross-slip plane by the half distortion distance:

$$A_a = A_{act} b^2 = \frac{l^*}{2} r_0. \quad (3.35)$$

Figure 3.4 shows a schematic representation of this area.

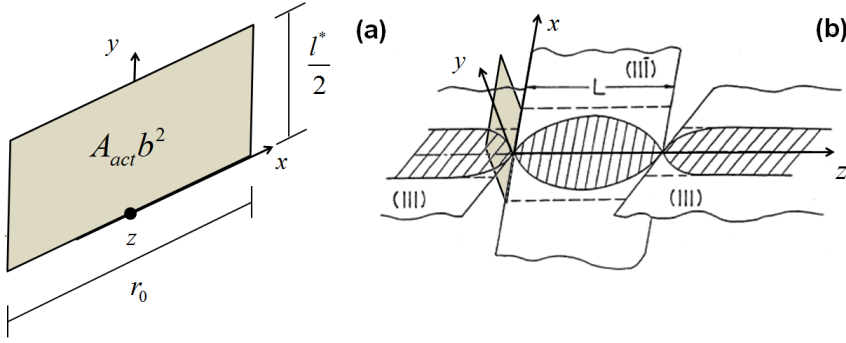


Figure 3.4: a) Schematic representation of the activation area for annihilation. b) Activation area in cross-slip process. Figure adapted from Puschl [7].

3.3.2 Dislocation cell size

Dislocation cell structures are formed when metals of medium to high stacking fault energies are moderately deformed; this results in the reduction of energy stored in the material and further plastic deformation can be undertaken [3, 39]. Taking this into consideration, this section is developed under an additional assumption [116]:

- iv)* The formation of dislocation cells occurs when the energy of the dislocation forest (E_{forest}), plus the energy required for the glide of dislocations towards the cell walls (E_{disp}), equal the energy of dislocations arranged in the cell walls (E_{cell}).

This leads to the energy balance equation:

$$E_{forest} + E_{disp} = E_{cell}, \quad (3.36)$$

from which the cell size can be obtained.

Consider a forest of n homogeneously distributed dislocations $\rho = 1/\bar{l}^2$. The average value of the volume delimited by the forest is:

$$V_{forest} = n\bar{l}^3. \quad (3.37)$$

The strain energy per unit volume of a dislocation population equals (equation 2.2):

$$E_{dis} = \frac{1}{2}\mu b^2 \rho = \frac{1}{2} \frac{\mu b^2}{\bar{l}^2}. \quad (3.38)$$

Combining equations 3.37 and 3.38, the average energy value for a forest of n dislocations is expressed by:

$$E_{forest} = E_{dis}V_{forest} = \frac{n}{2}\mu b^2\bar{l}. \quad (3.39)$$

E_{disp} represents the energy absorption to form the cell walls from gliding dislocations. From Section 3.2, the energy per unit volume associated to the glide of a dislocation is taken to equal the statistical entropy per unit volume (equation 3.12) multiplied by T [116]:

$$E_{slip} = \frac{1}{b\bar{l}^2}T\Delta S. \quad (3.40)$$

Combining equations 3.37 and 3.40, the displacement energy for a forest of n dislocations leading to cell formation is

$$E_{disp} = E_{slip}V_{forest} = \frac{n\bar{l}}{b}T\Delta S. \quad (3.41)$$

According to Puschl [7], cross-slip triggers the formation of cellular structures as dislocations dissociate into partials on the cross-slip planes. By approximating the cell shape to be cylindrical, the area surrounding the walls is equal to its perimeter (composed by $2n$ partials) multiplied by its length (d_c):

$$A_{cell} = 2nr_{part}d_c, \quad (3.42)$$

where r_{part} is the distance between partials. The energy of the cell (E_{cell}) equals the energy around A_{cell} (equation 2.4). Combining equations 2.4 and 3.42, the average energy value in the forming cell becomes:

$$E_{cell} = \frac{1}{2}\chi A_{cell} = \frac{n(2+\nu)\mu b^2}{24\pi(1-\nu)}d_c, \quad (3.43)$$

where the factor $1/2$ accounts for the shared effect of the walls in adjacent cells. Combining equations 3.36, 3.39, 3.41 and 3.43, the energy balance becomes

$$\frac{n}{2}\mu b^2\bar{l} + \frac{n\bar{l}}{b}T\Delta S = \frac{n(2+\nu)\mu b^2}{24\pi(1-\nu)}d_c, \quad (3.44)$$

which leads to the average size of a cell to be

$$d_c = \frac{24\pi(1-\nu)}{(2+\nu)}\left(\frac{1}{2} + \frac{T\Delta S}{\mu b^3}\right)\bar{l} = \frac{\kappa_c}{\sqrt{\rho}}, \quad (3.45)$$

with

$$\kappa_c = \frac{24\pi(1-\nu)}{(2+\nu)} \left(\frac{1}{2} + \frac{T\Delta S}{\mu b^3} \right). \quad (3.46)$$

Equation 3.45 recovers the form of the classical relation reported in the literature (Section 2.3.2) and supplies an expression for κ_c . Table 3.4 shows a comparison of the values of κ_c obtained from equation 3.46, and the experimental values reported in the literature. The physical parameters employed in the computations are shown in Appendix A. The model displays mixed agreement. However, cell size and dislocation density measurements were obtained from microscopy experiments where error bars are usually wide (in the range of 0.5 to 2 times the size measurement [117, 41], hence the experimental values for κ_c can differ, as it shown for Ni and Al results. Nevertheless, the model results are in the same order of magnitude.

Table 3.4: Comparison of the constant in the cell size evolution. E stands for experimentally determined and M for model results.

Metal	Ref	T (K)	$\dot{\epsilon}$ (s ⁻¹)	κ_c (E)	κ_c (M)
Cu	[42]	298-973	10 ⁻⁴	16	14.2-26
Al	[43]	298	10 ⁻³	14	14.5
Al	[44]	298	6.6 × 10 ⁻²	20	14.2
Ni	[44]	298	10 ⁻²	20	12.4
Ni	[45]	298	3.3 × 10 ⁻⁴	13	12.7

Once cells have formed, the misorientation across the cell boundaries increases with strain as deformation continues (stages III and IV) [3].

3.3.3 Cell misorientation angle

Consider two adjacent cells C_1 and C_2 and define a cartesian reference system fixed to C_1 (Figure 3.5a). These cells are misoriented an angle θ and are brought into coincidence by rotating C_2 an angle θ about the z axis. For the purposes of this work, the orientation of C_1 with respect to the xyz reference system is assumed to be fixed, and the geometrical misorientation is assumed to equal the crystallographic misorientation¹. Symmetry along z axis is assumed, so that misorientation is defined on the xy plane. As strain is increased, the misorientation angle between the adjacent cells increases due to the slip and storage of dislocations within the walls.

¹This assumption is explained in the following sections.

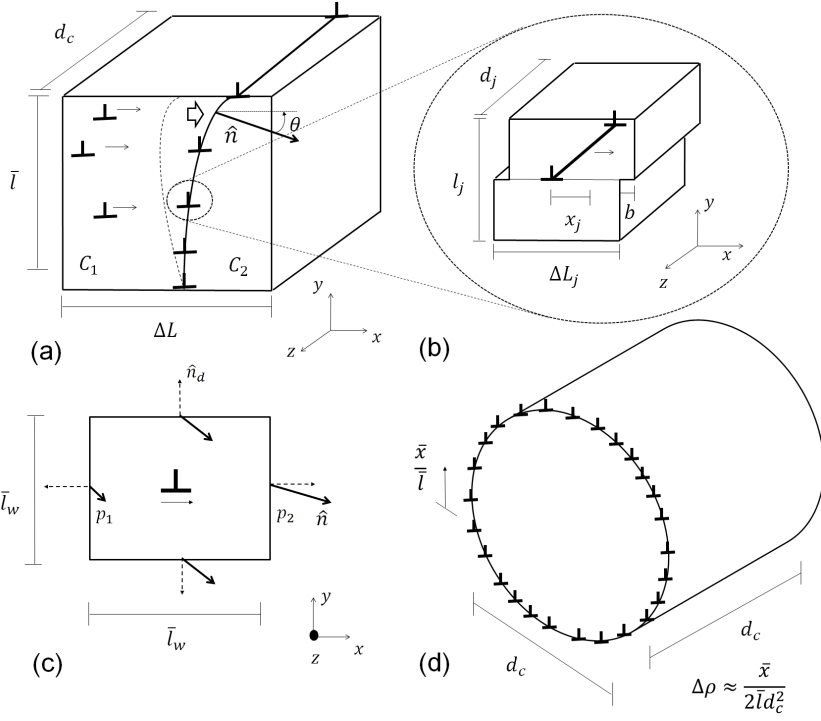


Figure 3.5: Schematic representation of (a) two adjacent cells with a misorientation angle θ ; (b) a dislocation j gliding in a volume V_j located at the wall; (c) the projection of \mathbf{n} onto the surface ∂V_d ; the solid arrows represent \mathbf{n} and the dashed arrows represent \mathbf{n}_d ; (d) variation of the total dislocation density at stage IV, where the ratio \bar{x}/\bar{l} represents the strain localisation at the wall due to dislocation slip.

The Young–Laplace equation describes the pressure build-up (ΔP) across the interface (cell walls) between two curved surfaces [118]

$$\Delta P = -\gamma_s \nabla \cdot \mathbf{n}, \quad (3.47)$$

where γ_s is the interfacial energy per unit area and \mathbf{n} is a vector normal to the surface. The equation can be applied to describe the residual stress (ΔP) across subgrain/cell boundaries. γ_s is approximated by equation 2.13: $\gamma_s = \frac{\mu b^2}{2\bar{l}_w} = \frac{1}{2}\mu b\bar{\theta}$, where $\bar{\theta}$ and \bar{l}_w are the average misorientation angle and dislocation spacing on the walls, respectively.

The vector normal to the walls can be expressed as (Figure 3.5a)

$$\mathbf{n} = (\hat{n}_x, \hat{n}_y) = \left(1, -\frac{dx_w}{dy_w}\right) / \sqrt{1 + \left(\frac{dx_w}{dy_w}\right)^2}, \quad (3.48)$$

where $\frac{dx_w}{dy_w}$ measures the shape change along the walls (y_w direction). The mis-orientation angle is defined as

$$\tan \theta = \frac{dx_w}{dy_w}. \quad (3.49)$$

If θ is small, $\tan \theta \approx \theta = \frac{dx_w}{dy_w}$ and $\nabla \cdot \mathbf{n} \approx -\frac{d^2 x_w}{dy_w^2} = -\frac{d\theta}{dy_w}$. In order to avoid the inclusion of specific orientations across the microstructure, the divergence term is expressed in terms of average angle values ($\bar{\theta}$), which leads to the approximation [116]

$$\nabla \cdot \mathbf{n} \approx -\frac{d\bar{\theta}}{d\bar{y}_w} = -\frac{d\bar{\theta}}{d\bar{x}_w} \frac{d\bar{x}_w}{d\bar{y}_w} \approx -\frac{d\bar{\theta}}{d\bar{x}_w} \bar{\theta}. \quad (3.50)$$

Turning our attention to a smaller scale, and considering a cell-wall dislocation j to be confined within a volume $V_j = \Delta L_j l_j d_j$ that may glide a distance x_j as shown in Figure 3.5b. The strain ε_j induced by that dislocation is

$$\varepsilon_j = \frac{x_j b}{\Delta L_j l_j}. \quad (3.51)$$

The total strain induced in the walls is then

$$\varepsilon_w = b \sum_j \frac{d_j}{\Delta L_j l_j d_j} x_j = b \sum_j \rho_j x_j = b \rho_w \bar{x}_w, \quad (3.52)$$

where ρ_j is the length of a dislocation segment per unit volume (within V_j , Figure 3.5b), ρ_w is the average dislocation density on the walls and \bar{x}_w is the average dislocation displacement in the walls. This formula is analogous to the Orowan equation but accounts for glide effects produced by dislocations on the walls.

Considering small changes of ρ_w along x_w ($\bar{\theta}$ is small), equation 3.47 is approximated in terms of the strain induced in the walls (equations 3.50 and 3.52) by

$$\Delta P \approx \gamma_s \bar{\theta} \frac{d\bar{\theta}}{d\bar{x}_w} \approx \gamma_s \bar{\theta} \frac{d\bar{\theta}}{d\varepsilon_w} b \rho_w. \quad (3.53)$$

Accompanied by a macroscopic strain, dislocations glide towards the cell walls and pressure builds up across them. Similar to the cell formation balance (equation 3.36), the energy produced by dislocation slip is equal to the statistical entropy multiplied by T . Thus, the pressure difference ΔP per dislocation around

the walls becomes [116]:

$$\Delta P = \frac{T\Delta S}{\Delta V}, \quad (3.54)$$

where ΔV is the volume surrounding a cell–wall dislocation (Figure 3.5a) and is defined as the volume delimited by the average cell size d_c , the average dislocation spacing in the walls \bar{l}_w , and ΔL the average length for dislocation interaction approaching one side of the wall:

$$\Delta L = \frac{\bar{l}_w \bar{l}}{2 \bar{x}}, \quad (3.55)$$

where \bar{l}/\bar{x} represents the range of interaction for a dislocation in the slip direction. From the Orowan equation² $\varepsilon = b\rho\bar{x}$ and equations 3.45 and 3.55, ΔV equals³

$$\Delta V = d_c \bar{l}_w \Delta L = \frac{\kappa_c \bar{l}^2 \bar{l}_w^2}{2 \bar{x}} = \frac{\kappa_c b}{2 \rho_w \varepsilon}. \quad (3.56)$$

Combining equations 3.54 and 3.56 the pressure difference becomes

$$\Delta P = \frac{2\rho_w \varepsilon}{\kappa_c} \frac{T\Delta S}{b}. \quad (3.57)$$

Finally, combining equations 2.13, 3.53 and 3.57 leads to the equation

$$\bar{\theta}^2 \frac{d\bar{\theta}}{d\varepsilon_w} = \frac{4T\Delta S}{\kappa_c \mu b^3} \varepsilon = \alpha_\theta \varepsilon, \quad (3.58)$$

where $\alpha_\theta = \frac{4T\Delta S}{\kappa_c \mu b^3}$. In order to relate ε_w and ε , Gauss' theorem [119] is applied on the normal vector to the cell walls over the volume $V_d = \bar{l}_w^2 d_c$ containing one dislocation as illustrated in Figure 3.5c

$$\int_{V_d} \nabla \cdot \mathbf{n} dV = \oint_{\partial V_d} (-\mathbf{n} \cdot \mathbf{n}_d) dS_d, \quad (3.59)$$

where ∂V_d is the surface enclosing the volume V_d , and \mathbf{n}_d is the vector normal to ∂V_d . The negative sign is due to the normal vector being defined in the clockwise direction while the integration path is defined in the counterclockwise direction. The variation of \mathbf{n} in V_d is produced by dislocation glide on the horizontal direction, remaining unchanged in the y and z directions (see Figure 3.5c). Thus, the dot product on the right hand side of the previous equation is approximated by

$$\mathbf{n} \cdot \mathbf{n}_d \approx \|\mathbf{n}_{p_2} - \mathbf{n}_{p_1}\| \approx \left(\frac{\partial \mathbf{n}}{\partial x_w} \right) \Delta x_w, \quad (3.60)$$

²The average dislocation displacement and macroscopic strain are considered instead of the average velocity and strain rate.

³ ΔV accounts for the average value of ΔV_j .

where $\frac{\partial \mathbf{n}}{\partial x_w} = \left(\frac{\partial \hat{n}_x}{\partial x_w} + \frac{\partial \hat{n}_y}{\partial x_w} \right)$. Differentiating equation 3.48 with respect to x_w and neglecting the second order terms it follows that:

$$\frac{\partial \hat{n}_x}{\partial x_w} + \frac{\partial \hat{n}_y}{\partial x_w} \approx -\frac{\partial \theta}{\partial x_w}. \quad (3.61)$$

If average variations are considered in V_d and with the definition of $\bar{\theta} = b/\bar{l}_w$ the previous expression is simplified: $\frac{\partial \theta}{\partial x_w} \approx \frac{\partial \bar{\theta}}{\partial x_w} \approx b/\bar{l}_w^2$ and Δx_w is approximated by the average dislocation displacement in the walls \bar{x}_w . Combining these expressions with equations 3.60 and 3.61 results

$$\mathbf{n} \cdot \mathbf{n}_d \approx \left(\frac{\partial \mathbf{n}}{\partial x_w} \right) \Delta x_w \approx -\frac{\partial \bar{\theta}}{\partial x_w} \Delta x_w = -\frac{b}{\bar{l}_w^2} \bar{x}_w = -b\rho_w \bar{x}_w = -\varepsilon_w. \quad (3.62)$$

Note that the integration path on the right hand side of equation 3.59 features only on the xz plane. Combining these results with equations 3.47 and 3.59 leads to the relation

$$\frac{\Delta P}{\gamma_s} \bar{l}_w^2 d_c = \frac{\Delta P}{\gamma_s} V_d \approx \int_{V_d} \nabla \cdot \mathbf{n} dV = \oint_{\partial V_d} (-\mathbf{n} \cdot \mathbf{n}_d) dS_d \approx \int_{p_1}^{p_2} \varepsilon_w dS_d = \varepsilon_w (\bar{l}_w d_c). \quad (3.63)$$

This equation is combined with equations 2.13 and 3.57 to relate ε_w and ε :

$$\varepsilon_w = \frac{4T\Delta S}{\kappa_c \mu b^3} \varepsilon = \alpha_\theta \varepsilon. \quad (3.64)$$

Applying the chain rule to equation 3.58 and using the previous expression, the evolution of the average misorientation angle in terms of the total strain is described by

$$\bar{\theta}^2 \frac{d\bar{\theta}}{d\varepsilon} = \alpha_\theta^2 \varepsilon. \quad (3.65)$$

The previous equation is expressed in terms of the shear strain by using the Taylor relation $\gamma = M\varepsilon$ [6] and it is integrated with respect to γ . Setting the initial conditions $\bar{\theta} = 0$ when $\gamma = 0$ results in

$$\bar{\theta} = \left(\frac{3}{2} \right)^{1/3} \left(\frac{\alpha_\theta \gamma}{M} \right)^{2/3} = \kappa_\theta \gamma^{2/3}, \quad (3.66)$$

with $\kappa_\theta = \left(\frac{3}{2} \right)^{1/3} \left(\frac{4T\Delta S}{\kappa_c \mu b^3 M} \right)^{2/3}$. Note that initial conditions may in actuality be different from zero, as prior misoriented cells may be present due to earlier forming processes [27].

3.3.4 Work hardening evolution: Stage IV

As deformation continues, dislocation generation or annihilation reach equilibrium and only dislocation rearrangement is occurring. Variations in cell size and misorientation become the main contributors to the dislocation density evolution [120, 121]. At this stage, Kocks–Mecking equation fails to describe such evolution and a new formulation is required. Such situation is referred to as stage IV, where the evolution of the dislocation density can be obtained from the Young–Laplace equation. The expression for divergence in equation 3.50 is modified by applying the chain rule in terms of the vertical axis direction \bar{y}_w :

$$-\nabla \cdot \mathbf{n} = \frac{d\bar{\theta}}{d\bar{y}_w} = \frac{d\bar{\theta}}{d\rho_{IV}} \frac{d\rho_{IV}}{d\bar{y}_w} \approx \frac{d\bar{\theta}}{d\rho_{IV}} \frac{\Delta\rho_{IV}}{\Delta\bar{y}_w}. \quad (3.67)$$

The variation of dislocation density along a single direction is approximated by (Figure 3.5d) [116]:

$$\Delta\rho_{IV} = \frac{\bar{x}}{2\bar{l}d_c^2}, \quad (3.68)$$

where a factor of 2 divides the distribution of dislocations between the adjacent cells. The ratio \bar{x}/\bar{l} is proportional to the accumulation of strain at the cell wall only, and the factor $1/d_c^2$ distributes the strain within the area contained by each cell. The variation $\Delta\bar{y}_w$ is approximated by the average dislocation spacing in the walls: $\Delta\bar{y}_w \approx \bar{l}_w$. Combining this result with equations 3.55 and 3.67, the divergence of the normal vector becomes:

$$-\nabla \cdot \mathbf{n} = \frac{d\bar{\theta}}{d\rho_{IV}} \frac{\bar{x}}{2\bar{l}d_c^2\bar{l}_w} = \frac{d\bar{\theta}}{d\rho_{IV}} \frac{1}{4d_c^2\Delta L}. \quad (3.69)$$

The evolution of the dislocation density for stage IV is obtained by combining equations 3.47, 2.13, 3.54, 3.56 and 3.69

$$\frac{d\rho_{IV}}{d\bar{\theta}} = \frac{1}{4d_c b} \frac{\frac{1}{2}\mu b^3}{T\Delta S} = \frac{\sqrt{\rho_{IV}}}{8\kappa_c b} \frac{\mu b^3}{T\Delta S} = \frac{k_{IV}}{b} \sqrt{\rho_{IV}}, \quad (3.70)$$

where $k_{IV} = \frac{1}{8\kappa_c} \frac{\mu b^3}{T\Delta S}$. The solution is

$$\rho_{IV} = \underbrace{\left(\sqrt{\rho_0^*} + \frac{k_{IV}}{2b} (\bar{\theta} - \theta_0^*) \right)^2}_{(A')}, \quad (3.71)$$

where ρ_0^* and θ_0^* are the dislocation density and misorientation angle at the onset of stage IV respectively. The initial conditions $(\gamma_0^*, \theta_0^*, \rho_0^*)$ for the transition to the stage IV are obtained when equations 2.30 and 3.71 are equal

$$\frac{d\rho_{III}}{d\gamma} = \frac{d\rho_{IV}}{d\gamma}. \quad (3.72)$$

3.3.5 Results

Results for copper single crystals (terms (A) and (F) in equation 2.30) at different temperatures and strain rates are shown in Figure 3.6 for (a) the saturation shear stress ($d\rho/d\gamma = 0$) in terms of the homologous temperature $T_h = T/T_m$, and (b) the shear stress–shear strain curves for different temperatures and shear strain rates ($\dot{\gamma} = M\dot{\epsilon}$), and their comparison with experimental data obtained from [122, 123, 124, 125]. The physical parameters employed in the model are shown in Appendix A. c_m equals 2.1×10^{-4} , 4.2×10^{-4} , 9.4×10^{-4} and 1.7×10^{-4} for Cu, Ni, Al and Ag, respectively; these values are obtained from [97]. It is worth noting that the additional softening behaviour shown in the experiments at 673 K is due to dynamic recrystallisation [123], an effect that is introduced in Chapter 6. Figure 3.6(c) and (d) shows the model results for the average cell size in polycrystalline copper as a function of temperature and shear strain; the experimental results were obtained from [42] and [126], respectively. The average dislocation density is calculated using equations 2.30 and 3.71 for stages I–III, and IV ((A') in equation 3.71), respectively. Large deformation behaviour of polycrystalline copper is shown in Figure 3.6(e) for the shear stress–shear strain curves when deformed at room temperature, showing the transition between stage III and IV [126]. The experimental measurements are plotted in dots, whereas the model results are shown as lines. The dotted line shows the error to be incurred had stage IV been ignored. This curve is the corresponding stress response to the cell size evolution shown in Figure 3.6(d). Figure 3.6(f) shows the evolution of the average misorientation angle at different temperatures obtained from [127]. A low initial dislocation density $\rho_0 = 10^{11} \text{ m}^{-2}$ is employed for all cases as no previous deformation is assumed in the bulk. ρ_0 modifications do not display a clear variation in the results as long as $\rho_0 \leq 10^{11} \text{ m}^{-2}$. The model results show remarkable accuracy in the flow stress as well as the average cell size and misorientation for various deformation conditions.

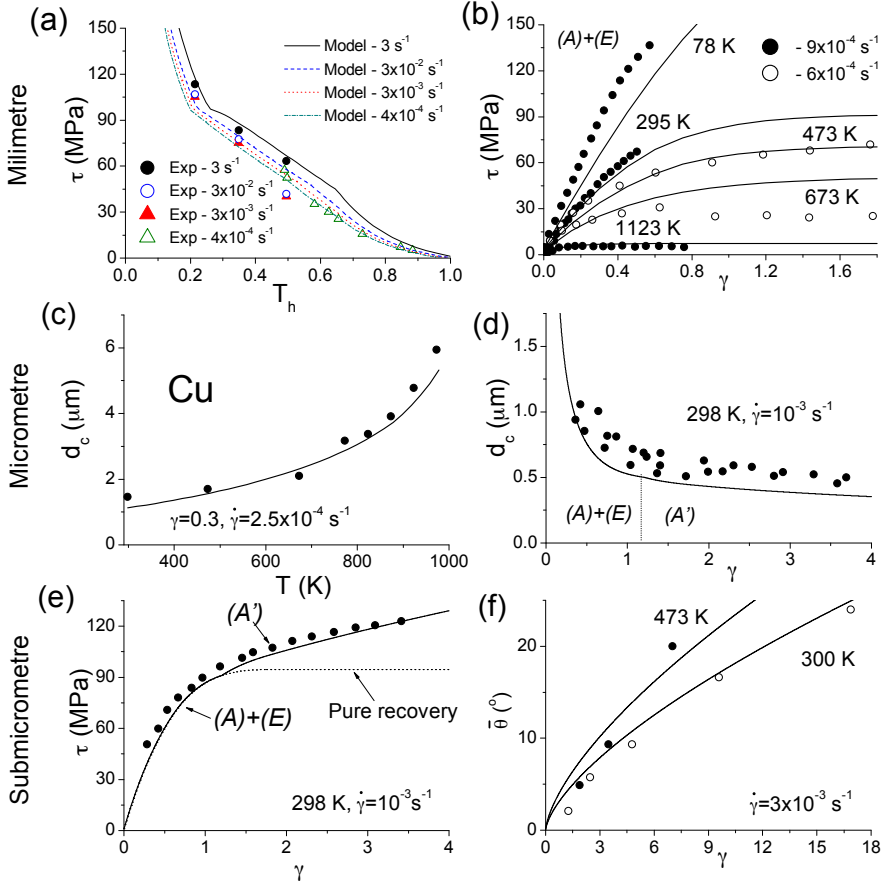


Figure 3.6: *Deformation phenomena at various scales in copper. Millimetre: (a) single crystals saturation shear stress, (b) shear stress–shear strain curves. Micrometre: average dislocation cell size variation with (c) temperature and (d) shear strain. Submicrometre: (e) Severe deformation strains and (f) their corresponding cell misorientation angles [109, 116].*

Figure 3.7 shows additional results for pure nickel for (a) the saturation shear stress in terms of the homologous temperature and its comparison with experimental data obtained from [122, 128]; (b) the shear stress–shear strain curves for different temperatures and shear strain rates and experimental measurements for $\langle 111 \rangle$ Ni single crystals and for coarse grained Ni (225–230 μm) that were obtained from [129] and [128, 130], respectively; (c) the average cell size in nickel and the experimental measurements of the average boundary spacing of geomet-

rically necessary (cell) boundaries in cold rolled polycrystalline Ni with average grain size $100\ \mu\text{m}$, where the data was obtained from [131]. Figure 3.7(d) shows the model shear stress–strain curves for large strains where stage IV occurs and the comparison with polycrystalline Ni with average grain sizes between $80\text{--}100\ \mu\text{m}$, data obtained from [132]. Figure 3.7(e) shows the average cell misorientation angle evolution in cold rolled Ni [46]. The model displays good accuracy in the flow stress for various deformation conditions; the cell size shows an initial value lower than the experimental measurements, however, at higher strains the model approximates well the experimental cell size; a lower misorientation angle is predicted at large strains, with a maximum discrepancy of 8° ; this difference can be ascribed to the high strain rate conditions from the experimental data.

It is interesting to understand how the misorientation angle described by equation 3.66 varies with strain, strain rate and temperature. Figure 3.7(f) shows the variation of temperature with strain rate at which misorientation angles of $\bar{\theta} = 5, 6, 7^\circ$ are formed for $\gamma = 0.9$ in pure Ni. An experimental value obtained from [133] for a nickel superalloy with an induced misorientation angle of 8° that crept at $1223\ \text{K}$ with a steady state rate approximately of $2 \times 10^{-5}\ \text{s}^{-1}$ is included in the Figure showing a difference of approximately 1.5° at the same conditions for pure nickel.

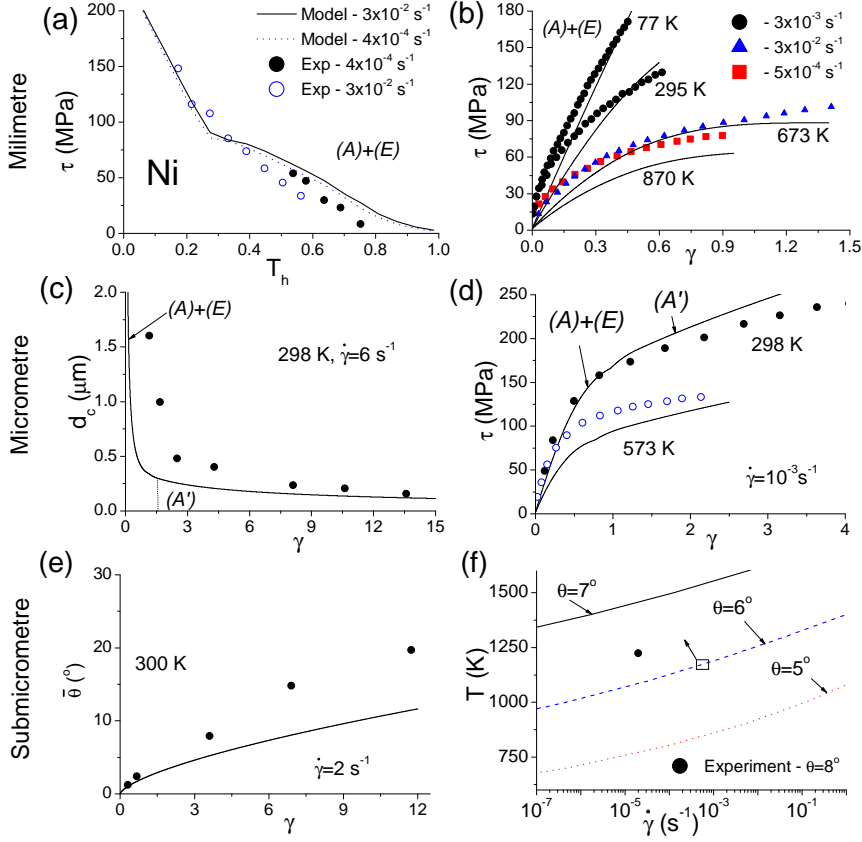


Figure 3.7: Deformation phenomena at various scales in nickel: (a) polycrystals saturation shear stress, (b) shear stress–shear strain curves, (c) average dislocation cell size variation with shear strain (d) severe deformation strains (refining the microstructure to submicrometric scales) and (e) cell misorientation angle; (f) variation in temperature and strain rate at different misorientation angles [109, 116].

The model is also applied to describe the deformation behaviour in pure Al and Ag. Figure 3.8(a) shows the saturation shear stress and its comparison with experimental measurements for Al and Ag single crystals; the experimental data were obtained from [122, 134] for Al, and from [122, 135] for Ag. The shear stress–strain response is shown in Figure 3.8 for (b) Al and (c) Ag single crystals; the experimental points are obtained from [136] for $\langle 111 \rangle$ Al single crystals, and [135] for Ag polycrystals (20 μm). Figure 3.8 also shows (c) the average dislocation

cell size variation with shear strain, (e) flow stress response at stage IV and (f) cell misorientation angle evolution in pure Al. The model results show good agreement with the experimental data; however, the saturation shear stress shows lower values than experimental observations in Ag at low temperatures, this discrepancy can be due to deformation twinning, as silver undergoes twinning due to its low stacking fault energy [3]; Al presents a higher work-hardening rate in stage IV than the one observed in experiments at 77 K.

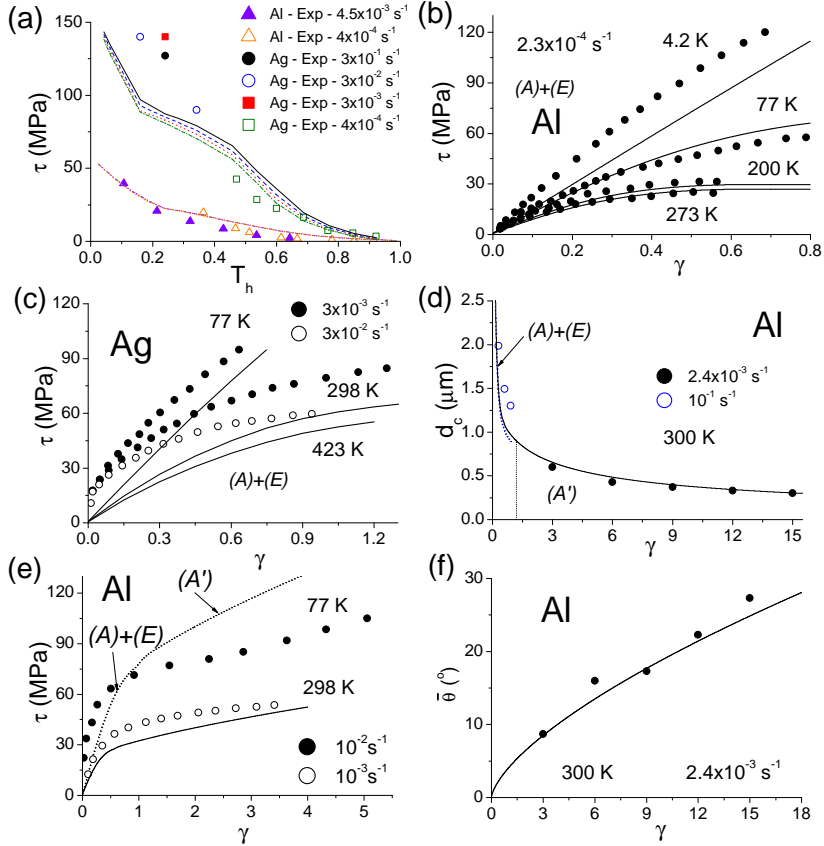


Figure 3.8: Deformation phenomena at various scales in aluminium and silver: (a) polycrystals saturation shear stress, (b) (c) shear stress–shear strain curves, (d) average dislocation cell size variation, (e) severe deformation strains, and (f) cell misorientation angles [109, 116].

3.4 Nanotwinning

When nano twinning is present on deformation, dislocations laterally expand within the twin boundary (TB) when piling up, reducing the sites available for further dislocation storage [137]. An additional term (B) accounting for dislocation storage if nanotwins are present impeding dislocation's motion is considered in equation 2.30 [94, 138, 139]:

$$\frac{1}{\Lambda_T} = \frac{N_{nT}}{bD_{TB}}, \quad (3.73)$$

where D_{TB} is the average nanotwin–boundary thickness and N_{nT} is the dislocation storage term due to the presence of nanotwins.

The storage coefficient N_{nT} is the product of the average number of effective slip sites available for dislocation pile up in the TB (n_{slip}) [139], multiplied by the fraction of dislocations not stored in the twin and grain boundaries ($1 - d_{frac}$):

$$N_{nT} = n_{slip}(1 - d_{frac}). \quad (3.74)$$

The variation of n_{slip} with respect to the TB thickness depends on the perimetrical fraction per grain available for TBs to form, dictating their density distribution within the grains; if the grains are assumed to have a two dimensional hexagonal shape with diameter D_{GS} (average grain size), this fraction equals to $P_{GS}/A_{GS} = 8/(\sqrt{3}D_{GS})$, where $P_{GS} = 3D_{GS}$ and $A_{GS} = 3\sqrt{3}D_{GS}^2/8$ are the perimeter and area of a grain, respectively. The evolution equation is proposed to be [139]

$$\frac{dn_{slip}}{dD_{TB}} = 2 \frac{8}{\sqrt{3}D_{GS}} n_{slip}, \quad (3.75)$$

where the factor of 2 accounts for the parity of the TB.

The ability of boundaries to store dislocations depends on the slip plane distribution per grain, which is delimited by a circular region around each slip plane $2\pi\lambda_{sp}$ where dislocations approach the boundaries on the perimetrical fraction, where λ_{sp} is the mean spacing between slip planes at the boundaries [140]. Following the treatment by Bouaziz *et al.* for dislocation storage at grain boundaries [138], d_{frac} is described by the equation [139]

$$\frac{dd_{frac}}{d\gamma} = 2\pi\lambda_{sp} \frac{2P_{GS}}{A_{GS}} = 2\pi\lambda_{sp} \frac{16}{\sqrt{3}D_{GS}} (1 - d_{frac}). \quad (3.76)$$

It has been found experimentally that the maximum strength of nanotwinned copper is reached when the average twin thickness is equal to $D_0=15$ nm [141]; below this critical value the work hardening rate is reduced as there is less space available for dislocations to pile up at the boundaries; in light of this result, n_{slip}

reaches its minimum when the TBs reach this value ($n_{slip}(D_0) = 1$). Assuming that no dislocations are initially at the TBs ($d_{frac}(0) = 0$), N_{nT} is equal to [139]:

$$N_{nT} = \exp\left(\frac{16}{\sqrt{3}D_{GS}}(D_{TB} - D_0)\right) \exp\left(-\frac{32\pi\lambda_{sp}}{\sqrt{3}D_{GS}}\gamma\right). \quad (3.77)$$

On the other hand, a nano-TB can absorb dislocations letting them glide with more freedom [137] increasing the average number of possible dislocation slip paths as its thickness is increased. Moreover, if the grain size is increased, the absorption rate is lowered. These effects are incorporated in equation 3.11 via an additional number of microstates Ω_{TB} , which depend on the TB thickness (D_{TB}/b), and grain size (λ_{sp}/D_{GB} , where λ_{sp} incorporates the slip plane multiplicity on the grain) [139]:

$$\Omega_{TB} = \Omega_{pure}^{D_{TB}\lambda_{sp}/4bD_{GB}}, \quad (3.78)$$

where the factor of 4 is to reduce the multiplicity of adjacent twin boundaries (2) and to project the two-dimensional spread of the TB onto one dimension (2). Combining equations 3.12 with 3.78, the entropy for nano twinning takes place equals [139]

$$\Delta S_{TB} = k_B \ln(\Omega_{pure} \cdot \Omega_{TB}) = k_B \ln \Omega_{pure} \cdot \Omega_{pure}^{n_{nT}} = k_B \ln\left(\frac{\dot{\epsilon}_0 + \vartheta}{\dot{\epsilon}}\right)^{(1+n_{nT})\mathcal{N}}, \quad (3.79)$$

where $n_{nT} = \frac{D_{TB}\lambda_{sp}}{4bD_{GS}}$. Note that dislocation impingement is also affected, as twins are present prior deformation and imply modifications in the dislocation velocity effect [139]; term (B) in equation 2.30 is included in equation 3.33. Nanotwinning also affects the average velocity formula (equation 3.27), by replacing $(1 + n_{nT})\mathcal{N}$ in the velocity exponent (instead of \mathcal{N}) [139]. Equation 3.79 is combined with 3.12 to obtain the dynamic recovery coefficient with nanotwin and grain boundaries:

$$f_{DRV}^{TB} = \frac{N_A \rho_a b^2 l^*}{w_a} \frac{T \Delta S_{TB}}{\frac{1}{2} \mu b^3 + \sigma_Y A_{act} b^3 + \frac{l^*}{b} \delta(T) (E_f + k_B T \ln c_m) - k_B T \ln\left(\frac{\dot{\epsilon}_0 + \vartheta}{\dot{\epsilon}}\right)^{(1+n_{nT})\mathcal{N}}}, \quad (3.80)$$

which can be compared with equation 3.29.

Finally, a friction stress (σ_0) is inserted in equation 2.31 to account for twin and grain boundary strengthening [77, 139]: $\sigma_0 = 0.3 \frac{d_{frac}}{D_{TB}} \mu b$, where the 0.3 is a geometry constant depending on the grain shape and grain size distribution.

3.4.1 Results

Figure 3.9 shows the twinning deformation model results for the axial stress-strain curves for pure copper deformed at room temperature, in this case also

featuring the term (B) in equation 2.30 for (a) TBs of different average thickness with $D_{GS}=420$ nm and for the case of coarse grain (CG) polycrystals⁴ (terms (A) and (E) are only present in equation 2.30), and (b) at different average grain sizes and TBs thickness, and their comparison with experimental values obtained from [11, 142]. The yield stress variation with the TB thickness was obtained from [143], and was fitted to the formula $\sigma_Y = 113043/\sqrt{D_{TB}}$ [MPa] to simplify calculations. $\lambda_{sp} = 150$ nm was obtained from [140]. The model shows good agreement in the stress-strain response for different average twin boundary's thicknesses and grain sizes.

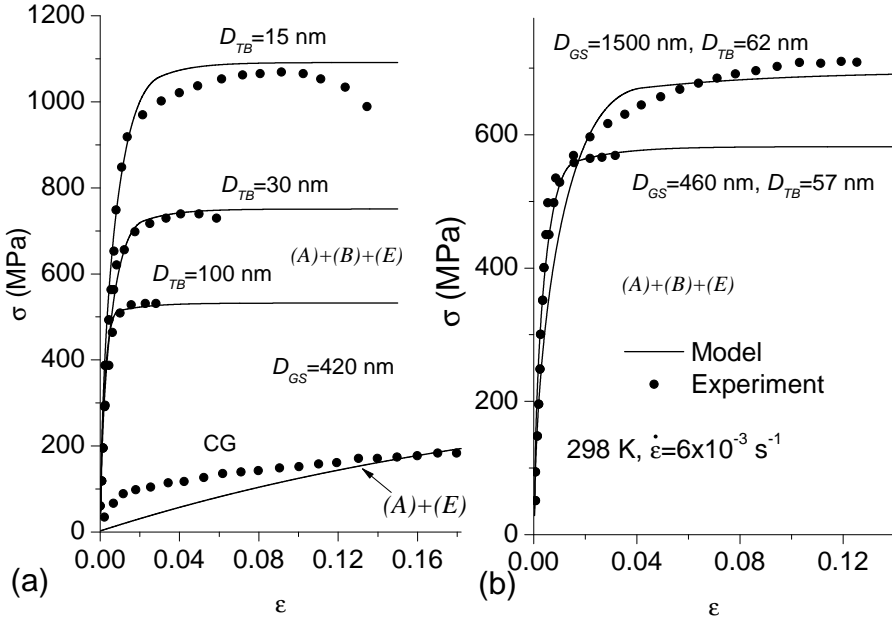


Figure 3.9: Stress-strain curves of pure copper for different average (a) twin boundary thickness and coarse grain polycrystal, and (b) grain sizes with different twin boundaries thickness.

3.5 Conclusions

The “classical” approaches to the modelling of multiscale plasticity demand *ad hoc* relationships between dislocation motion and evolution, usually fitted and phenomenologically determined, particularly as a function of strain, strain rate

⁴Equation 3.29 is employed for the dynamic recovery coefficient.

and temperature. Moreover, as stated by McDowell [87], the transition and hierarchy between methods describing different scale ranges in plasticity modelling needs further examination, as incompatibilities due to the lack of a unique variable become present. The interplay between dislocation storage and annihilation describes the progress in dislocation density with strain, which can be employed as a unique parameter for describing multiscale plasticity.

Shortcomings of this theory include that only average values are described, and the model cannot reproduce microstructural development in two- or three- dimensional systems displaying texture. It does not provide more detailed information on dislocation interactions with other crystal defects, and only energy contributions are accounted for. The statistical entropy describing the energy loss due to possible dislocation slip and climb paths does not predict the actual velocity distribution of a dislocation. This analysis is defined under the assumptions that the dislocation velocity is limited by the speed of sound, and that the dislocation density consistent with the yield point represents an equivalent dislocation population when dislocation slip commences. Other effects occurring at high rates, such as phonon-drag effects are not considered [144]. The total number of microstates can be related to the macroscopic strain rate (via the Orowan equation). However, for static cases, such as creep and static recovery and recrystallisation, additional modifications have to be made.

Dislocation entropy features strongly in plasticity across the scales, and has an essential effect when temperature and strain rate effects are included. Expressions for the entropy for dislocation annihilation and rearrangement (in the form of cells) are derived from statistical mechanics concepts. The characteristic microstates associated to the possible dislocation velocities, and their interaction with vacancies and twins are accounted for. The exceptional stress-strain behaviour displayed by nanotwinned materials is recovered by incorporating the parameters describing its progressive refinement with strain, increasing the number density of barriers for dislocation glide by the presence of nanotwin boundaries, and the capacity to store dislocations at the grain boundaries without undergoing failure. The progressive refinement of the microstructure as dislocations are formed with strain, combined with the increase in the number of microstates due to the twinning process of dislocation absorption are responsible for such unique behaviour. It is demonstrated that complex properties may be described without a detailed description of the slip systems participating in plasticity, but by thermostatically describing their energetically favourable paths instead.

Chapter 4

Plastic deformation theory for body-centred cubic metals

This chapter extends the theory presented in Chapter 3 for describing plastic deformation in body-centred cubic (BCC) metals. The distinctions between FCC and BCC stem primarily from the possible directions and planes for dislocation slip and cross-slip, as well as from the presence of the kink-pair mechanism for dislocation migration in BCC, which are incorporated to the mathematical formulation of the model. The theory presented in this chapter is unique in describing the stress-strain response for pure iron, molybdenum, tantalum, vanadium and tungsten employing physical parameters as input; the description is made for wide ranges of temperature and strain rate. Additionally, succinct equations to predict dislocation cell size variation with strain, strain rate and temperature are provided and validated for pure iron.

4.1 Introduction

Plastic deformation of body-centred cubic (BCC) metals occurs by dislocation slip driven by thermally activated kink-pair migration [5, 26], leading to dislocation cross-slip for both generation [145] and annihilation [7]. Moreover, the presence of vacancies aids the annihilation of dislocations via their segregation around the dislocation's core enhancing dislocation mobility and climb [142]. At higher temperatures vacancy-assisted dislocation climb becomes the dominant annihilation mechanism [5, 146]. A modified version of the FCC model for work hardening and dislocation cell evolution for single crystal/coarse grained BCC

metals at low and medium temperatures is presented in this chapter. Section 4.2.4 outlines the main differences between BCC and FCC deformation. Dynamic recovery is the main dislocation annihilation mechanism, and only terms (A) and (E) are present in the Kocks–Mecking equation (2.30) presented in this chapter for BCC metals.

4.2 Kocks–Mecking formulation

Owing to the multiplicity of slip systems, dislocation cross-slip rate is increased in BCC materials compared to FCC [5]; dislocations with $\langle 111 \rangle$ Burgers vector may undergo cross-slip on 48 slip planes¹ (Table 2.1): 12 $\{110\}$, 12 $\{112\}$, and 24 $\{123\}$ planes, whereas for FCC metals there are only 12 planes for the most likely cross-slip direction, it follows that cross-slip events are more frequent in BCC than in FCC metals. Moreover, the number of possibilities for dislocation interaction in BCC metals is lower than for FCC materials as their coordination number (number of possible dislocation interaction directions) is 8 and 12, respectively. These crystallographic characteristics modify the capabilities of BCC materials for dislocation storage and annihilation, increasing the dislocation’s mean free path and dislocation annihilation rate by a factor of $\underbrace{(48/12)}_{(1)} \cdot \underbrace{(8/12)}_{(2)} = 8/3$ [147],

where (1) incorporates the additional dislocation cross-slip rate, and (2) the variation in dislocations self interactions. Therefore, it is proposed that in order to describe dislocation evolution for BCC materials, the (Kocks–Mecking) equation 2.30 is modified by increasing the dislocation mean free path (inverse dislocation storage term) and the dislocation annihilation rate by a factor of 8/3 [147]:

$$\frac{d\rho}{d\gamma} = \frac{3}{8} \frac{d\rho^+}{d\gamma} - \frac{8}{3} \frac{d\rho^-}{d\gamma} = \underbrace{\frac{3k_1}{8b}}_{(A)} \sqrt{\rho} - \underbrace{\frac{8}{3} f_{DRV}^{BCC}}_{(E)} \rho. \quad (4.1)$$

4.2.1 Statistical entropy

A key feature in this theory is the introduction of the statistical entropy ΔS (from previous chapter) that incorporates the possible paths for dislocation motion in terms of the total number of microstates: $\Omega_{pure} = \Omega_{dis} + \Omega_{vac}$ (equation 3.11), where $\Omega_{dis} = \frac{\dot{\epsilon}_0}{\dot{\epsilon}}$ and $\Omega_{v-d} = \frac{\dot{\nu}}{\dot{\epsilon}}$ are the number of microstates due to dislocation slip and to vacancy–dislocation interactions, respectively; $\dot{\epsilon}$ is the axial strain rate; $\dot{\epsilon}_0 = cb\rho_Y$ is the limiting value for the strain rate, a constant related to the

¹Although dislocations have preferred slip planes for gliding, cross-slip may take place in any closed-packed direction.

speed of sound in the material (c); $\rho_Y = (\sigma_Y/\alpha M\mu b)^2$ is the dislocation density consistent with the yield point σ_Y , $\alpha = 0.3$ is a constant, M is the Taylor factor; and $\vartheta = \vartheta_D \exp(-\frac{E_m}{RT})$ is the vacancy migration frequency, and $\vartheta_D = 10^{13} \text{ s}^{-1}$ is the Debye frequency and E_m is the vacancy migration energy.

The transition temperatures where different dislocation annihilation mechanisms prevail are obtained by comparing Ω_{dis} and Ω_{vac} (equations 3.13): For deformation temperatures below $T_0 = \frac{E_m}{R \ln(\vartheta_D/\dot{\epsilon})}$ no vacancy effect is present; at deformation temperatures higher than $T_f = \frac{E_m}{R \ln(\vartheta_D/\dot{\epsilon}_0)}$, vacancy-assisted dislocation climb prevails and becomes fully present, and at temperatures between T_0 and T_f , vacancy-dislocation interaction enhances the kink-pair mechanism for dislocation motion.

T_0 values for pure iron, molybdenum, tantalum, vanadium and tungsten are shown in Table 4.1 for different strain rate conditions; they are compared with experimental values where the curvature of the flow stress (Fe, Mo), yield stress (Ta, V) and critical resolved shear stress (W) charts significantly change with temperature, decreasing the stress value with increasing temperature, with a corresponding increase in the dislocation annihilation rate. As experimental measurements usually do not show a sharp transition point, some results are shown within temperature ranges where the transitions are observed. Physical input parameter values are listed in Appendix A. The modelled homologous temperature $T_h = T_0/T_m$ is also shown. The values of T_0 are in good agreement with the corresponding experimental values (T_0^E) for Fe, Mo and W; for the case of Ta and V the model predictions are below those experimentally measured by ~ 100 K.

Table 4.1: Lower temperature limit

Material	$\dot{\epsilon}$ (s^{-1})	T_0^E (K)	Ref	T_0 (K)	T_h
Fe	8.5×10^{-4}	250	[148]	245	0.13
Fe	4×10^{-5}	200-300	[149]	226	0.12
Mo	8.5×10^{-4}	400-425	[150]	374	0.13
Ta	1.2×10^{-6}	270-320	[151]	191	0.06
V	2.55×10^{-4}	500-550	[152]	396	0.18
W	7×10^{-6}	550-650	[153]	614	0.16

Table 4.2 shows the estimated values for T_f and the respective homologous temperature. However, no experimental information was found in the literature to compare these values.

Table 4.2: Upper temperature limit.

Material	Fe	Mo	Ta	V	W
T_f (K)	500	1160	685	1625	1260
T_h	0.28	0.4	0.2	0.74	0.34

Christian has pointed out [154] that the flow stress in BCC metals features three regimes with respect to temperature variations, being the transition points between these ranges $\sim 0.15T_m$ and $\sim 0.33T_m$, whereas the model predicts the transition temperatures to be $0.06T_m \leq T_0 \leq 0.16T_m$ and $0.2T_m \leq T_f \leq 0.4T_m$ for the tested metals, except for vanadium where $T_f = 0.74T_m$. This difference can be due to the extrapolation of $\sigma_Y^{T_f}$ (Appendix A), an exponential formula was fitted for $T \leq 293$ K, and its values significantly increase at higher temperatures. This may overestimate the value of $\dot{\epsilon}_0$, increasing T_f value.

4.2.2 Number of microstates for BCC

The motion of a dislocation in a BCC metal is composed of the migration of two thermally activated kinks; this determines the migration rate necessary for a dislocation to glide [5]. If independent events are considered, this behaviour induces a double kinetic effect for a dislocation to slip, *i.e.* the total number of microstates (Ω_{BCC}) for BCC metals is squared [147]

$$\Omega_{BCC} = \Omega_{pure} \cdot \Omega_{pure} = \Omega_{pure}^2. \quad (4.2)$$

This equation incorporates the necessary conditions for kink-pair formation, triggering dislocation glide. The statistical entropy incorporating the dislocation's kinetic effect then becomes [147]:

$$\Delta S_{BCC} = k_B \ln \Omega_{BCC} = k_B \ln \left(\frac{\dot{\epsilon}_0 + \vartheta}{\dot{\epsilon}} \right)^2. \quad (4.3)$$

4.2.3 Dynamic recovery coefficient

The multiplicity of dislocation slip paths discussed previously leads to an expression for the average dislocation velocity $\langle v \rangle$ for annihilation (expressed in terms of the strain rate) equal to (equation 3.23) [147]:

$$\left(\frac{\langle v \rangle}{c + c_{int}} \right)^2 = \left(\frac{\dot{\epsilon}}{\dot{\epsilon}_0 + \vartheta} \right)^2 = \exp \left(- \frac{\langle \Delta G \rangle}{k_B T} \right), \quad (4.4)$$

where $\langle \Delta G \rangle$ is the energy barrier for dislocation annihilation, and $c_{int} = \vartheta/b\rho_Y$ is an equivalent increase in the annihilation velocity due to the presence of vacancies [109]. $\langle \Delta G \rangle$ is obtained by performing a thermodynamic analysis on a dislocation segment l_{BCC} that undergoes annihilation; $\langle \Delta G \rangle$ accounts for (equation 3.16): the formation and migration energy of a dislocation, the vacancy chemical work around a dislocation at higher temperatures ($T > T_0$) and the statistical entropy that accounts for the energy loss due to the variation in the slip(+climb) dislocation paths. The energy for a dislocation to migrate depends on the critical resolved shear stress τ_{CRSS} (for uniaxial loading conditions, σ_Y is directly related to τ_{CRSS}), which barrier increases in BCC metals; this effect is included in $\langle \Delta G \rangle$ (equation 3.18). The same analysis outlined in Section 3.3 is followed to obtain l_{BCC} :

$$l_{BCC} = \frac{bT\Delta S_{BCC}}{\frac{1}{2}\mu b^3 + \sigma_Y A_{act} b^3 + \frac{l^*}{b}\delta(T)(E_f + k_B T \ln c_m) - 2k_B T \ln\left(\frac{\dot{\epsilon}_0 + \vartheta}{\dot{\epsilon}}\right)}. \quad (4.5)$$

The impingement effect that accounts for the favourable conditions of dislocations to split into partials and alters the dislocation velocity is not included for BCC metals.

The dynamic recovery term f_{DRV}^{BCC} is defined as the fraction of substance undergoing dislocation annihilation per dislocation around the volume of substance that is *not* dislocated after a certain strain increment (V_{sys}) [104, 109]. By employing $V_{sys} = bl^*l_{BCC}$ (equation 3.15), the recovery coefficient equals

$$\begin{aligned} f_{DRV}^{BCC} &= \frac{N_A \rho_a V_{sys}}{w_a} \\ &= \frac{w_a^{-1} N_A \rho_a b^2 l^* T \Delta S_{BCC}}{\frac{1}{2}\mu b^3 + \sigma_Y A_{act} b^3 + \frac{l^*}{b}\delta(T)(E_f + k_B T \ln c_m) - 2k_B T \ln\left(\frac{\dot{\epsilon}_0 + \vartheta}{\dot{\epsilon}}\right)}. \end{aligned} \quad (4.6)$$

This formula is similar to the recovery coefficient for FCC metals (equation 3.29), except for the 2 factor multiplying $T\Delta S_{BCC}$ and the logarithmic term in the denominator (coming from equation 4.4).

In addition to the stress contribution from dislocations during deformation, a frictional stress σ_0 due to the lattice resistance (Peierls barrier) is required to ignite dislocation motion in BCC metals [155]; it is assumed to be equal to σ_Y [147]; this term is strongly dependent on temperature and strain rate. The Taylor equation becomes equal to:

$$\sigma = \sigma_Y + \alpha \mu M b \sqrt{\rho}. \quad (4.7)$$

4.2.4 BCC vs. FCC

Table 4.3 summarises the principal differences between both models.

Table 4.3: Differences between FCC and BCC thermostistical models.

Item	FCC	BCC	Eq.	Description
1	1	8/3	4.1	Prefactor to the inverse dislocation storage and annihilation rates
2	1	2	4.3	Exponent in the number of microstates
3	\mathcal{N}	2	4.4	Exponent in the thermally activated average velocity
4	0	σ_Y	4.7	Incorporation of the friction stress in σ

Referring to Table 4.3, item 1 is introduced to account for the increase in the number of cross-slip events, as well as to account for the decrease in number of nearest neighbours for dislocations to interact with each other. Cross-slip is well accepted to be a major dislocation annihilation process, however it also contributes to dislocation generation via a double cross-slip process, as pointed out by Galkin *et al.* [145]. The kink-pair driven dislocation motion requires that the probability (Ω_{pure}^{-1} in equation 3.11 [104]) for each event occurs simultaneously (joint probability), increasing the multiplicity in the number of microstates by a factor of two as shown in item 2. The expected velocity of a dislocation is also affected as the two joint-kink migration events are needed to ignite dislocation motion (item 3). Item 4 incorporates additional frictional stress required to ignite dislocation motion.

4.3 Results

The evolution of the average dislocation density is obtained by solving equation 4.1 with the modified dynamic recovery coefficient (equation 4.7). At large strains, where dislocation generation and annihilation reach equilibrium, additional work hardening takes place due to dislocation rearrangement [121, 116]; this is defined as stage IV and the evolution of the dislocation density is depicted in Section 3.3.4. The evolution of dislocation density at this stage is described by equation 3.71 and it is denoted by term (A'). The model results combine both equations to describe dislocation evolution at large strains. An initial dislocation density ρ_0 is taken to be equal to 10^{11} m^{-2} in all studied cases. The dislocation storage coefficient is obtained from equation 2.27. Figure 4.1 shows the values of the lower-yield stress obtained from the experimental stress-strain curves that were used to compare with the model as a function of the reduced temperature: $k_B T \ln((\dot{\epsilon}_0 + \vartheta)/\dot{\epsilon})/\mu b^3$.

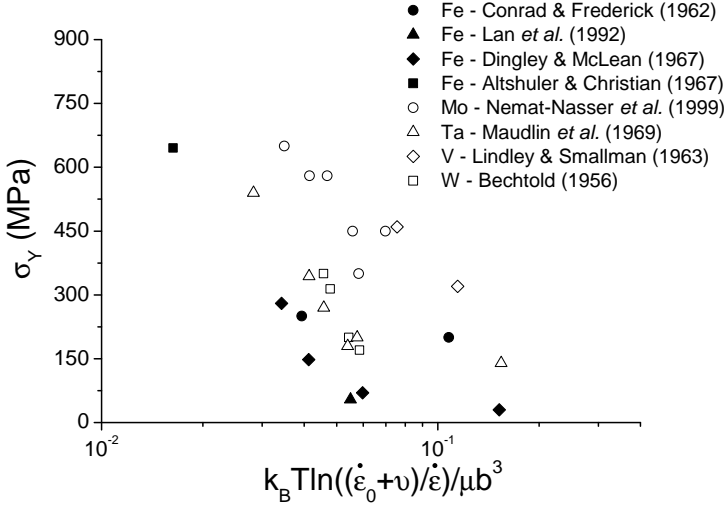


Figure 4.1: Yield stress for pure Fe, Mo, Ta, V and W.

The BCC model is tested against experimental stress–strain results reported in the literature for pure Fe, Mo, Ta, V and W. The physical parameters were obtained from the literature and are listed in Appendix A. The vacancy concentration at the melting point is estimated with the formula

$c_m = \exp(-\Delta S_{form}/R) \exp(-E_f/RT)$, where ΔS_{form} is the vacancy formation entropy, and $\Delta S_{form}/R$ is approximately equal to 1.5 [156], except for Mo where $c_m = 0.000013$ was obtained from [97].

The values of $A_{act}b^2$ for the studied BCC metals are shown in Appendix A. $A_{act}b^2$ is inversely proportional to the stacking fault energy (equation A.1). Assuming that the prevailing slip planes for iron, molybdenum, vanadium, tungsten and tantalum are those present at low temperature, the relevant (close–packed) slip planes respectively become $\{110\}$, $\{123\}$ and $\{112\}$ [5]. A generalised Peierls–Nabarro model can then be applied to determine the values of the stacking fault energies on these planes. Following Watanabe [157], Segall *et al.* [158] and Hartley [159], the associated minimum fault energies are for the systems $\{110\}\langle 111\rangle$ in Fe, $\{110\}\langle 111\rangle$ in Mo, $\{110\}\langle 111\rangle$ in Ta and $\{112\}\langle 111\rangle$ in W, which respective stacking fault energies are listed in Appendix A. For Mo and Ta, the atomic displacement for the formation of the stacking fault was taken as $0.25b$ (maximum theoretical atomic displacement) [155]. For the case of vanadium, no calculations were found in the literature and this value was fitted.

Results of the stress–strain curves for pure iron single crystals deformed at 77

K and $\dot{\epsilon} = 5 \times 10^{-4} \text{ s}^{-1}$ [160], and for coarse-grained pure iron deformed at different conditions [161, 162] are plotted in Figure 4.2(a) (terms (A) and (E) are present in equation 4.1, as can be compared to equation 2.30), and at large strains, equation 3.71 is also incorporated (term (A')). The model shows good agreement for very wide temperature and strain rate ranges. Figure 4.2(b) shows the model predictions for the average cell size evolution and its respective stress-strain curve for pure polycrystalline iron with an average grain size of $150 \mu\text{m}$ deformed at room temperature and $\dot{\epsilon} = 4.2 \times 10^{-4} \text{ s}^{-1}$, and its comparison with the experimental measurements obtained from [163]; additional measurements are shown for the average cell size are shown in pure iron single crystal deformed in the $[110]$ direction at room temperature and at $2 \times 10^{-4} \text{ s}^{-1}$. These values were obtained from [164]. It is worth noting that experimental measurements show discrepancies of $\sim 2 \mu\text{m}$ at low strains ($\epsilon \leq 0.175$), whereas they converge at large strains. This discrepancy can be ascribed to the dislocation density present before the material had been deformed. At low strains the model shows intermediate cell size values with respect to experiments; and the average cell size evolution is successfully recovered after a strain of ~ 0.175 , being in good agreement with the size reduction behaviour, as well as with the respective stress-strain curve exhibiting stage IV of deformation.

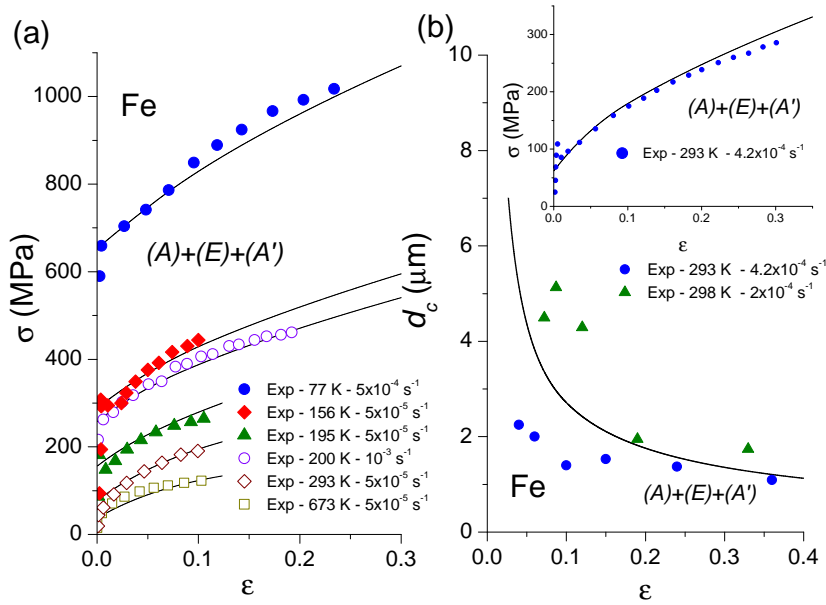


Figure 4.2: Model comparison with experimental data for pure Fe at different conditions: (a) Stress-strain curves and (b) average cell size.

Figure 4.3 shows the model results for different temperatures for pure polycrystalline molybdenum deformed at 10^{-1} s^{-1} and 10^{-3} s^{-1} and its comparison with the experimental data obtained from [165]. The model results show good agreement.

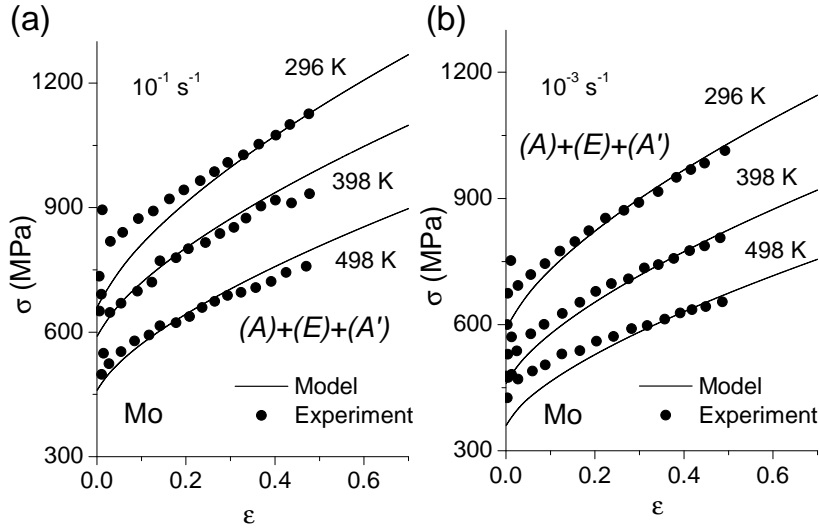


Figure 4.3: *Model comparison with experimental data for pure Mo.*

Figure 4.4 shows a comparison for different deformation conditions of pure polycrystalline tantalum [166], tungsten [167], and vanadium, the latter having an average grain size of $260 \mu\text{m}$ [168]. The model shows good agreement for the three materials when it is compared with experiments at different temperatures and low strain rates (approximately below $\dot{\epsilon} \sim 1 \text{ s}^{-1}$). For the case of Ta, it shows discrepancies for high strain rate values ($\geq 2600 \text{ s}^{-1}$) are observed, this is probably due to other factors limiting dislocation slip [169].

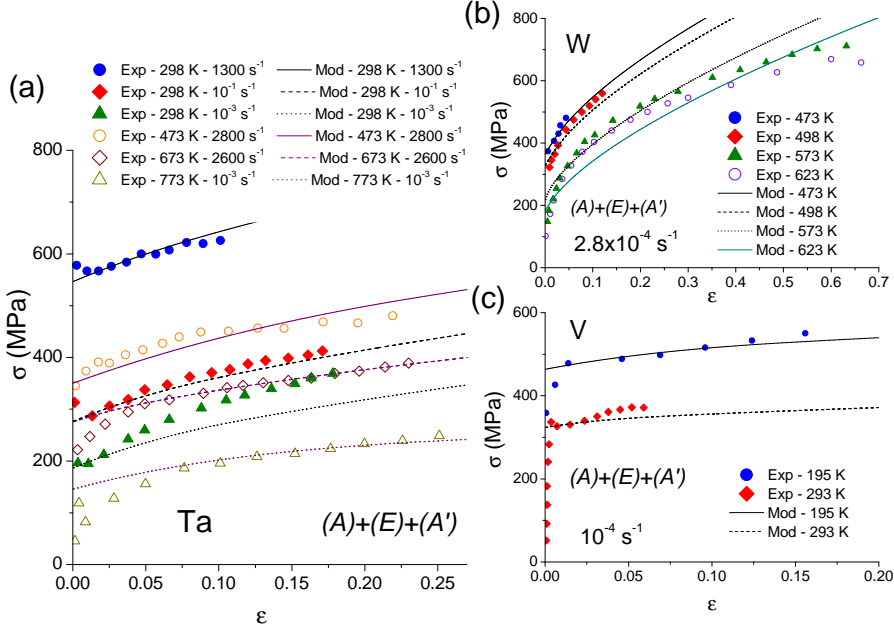


Figure 4.4: Model comparison with experimental data for pure a) Ta, b) W, and c) V.

The modifications incorporated in the present model and summarised in Section 4.2.3 can be regarded as the *compaction* of the non-close-packed structure inherent to BCC metals, leading to an equivalent close-packed counterpart. This also justifies the use of a generalised value of χ (on the close-packed directions), to obtaining the activation energy for cross-slip $A_{act}b^2$ (equation A.1).

4.4 Conclusions

The thermostatical theory describing plastic deformation has been extended in this chapter to describe work hardening and dislocation cell evolution in BCC metals. It has been demonstrated to apply for wide temperature and strain rate ranges. Additional crystallographic features and deformation modes characteristic of BCC metals have been incorporated. Using input physical parameters reported in the literature, such as the shear modulus, the vacancy formation and migration energy, it was possible to accurately describe the stress-strain behaviour for Fe, Mo, Ta, V and W for various temperatures and strain rates, as well as the average cell size evolution for pure Fe.

Vacancies aid the dislocation annihilation process by arranging along the dislocation's core enhancing kink motion, or by aiding dislocation climb at high temperatures. The onset value for vacancy-dislocation interaction T_0 is compared with the transition points (ranges) where the curvature of the flow stress curves with respect to the temperature changes, showing good agreement for iron, molybdenum and tungsten, and fair agreement for vanadium and tantalum.

Other than coefficients accounting for the differences in crystal structure, it is important to note that no additional fitting parameters were introduced in the current formulation, and that the entire stress-strain curve is described via the average dislocation density only. Shortcomings to the model include a strong dependency on the yield stress (friction force), which is the onset for plastic deformation. The value of the high temperature transition T_f could not be validated with experimental measurements as no data were found in the literature. The extrapolation of the fitted yield stress may not describe accurately the material's behaviour at very high temperatures, and its dependence with strain rate has been neglected.

Chapter 5

Deformation twinning in hexagonal close packed metals

Deformation twinning in HCP metals is described in this chapter. The aim of this work is to capture the overall twinning behaviour in terms of a single dislocation density, predicting its occurrence for various temperature and strain rate ranges. Thermodynamic descriptions for the critical conditions for twin nucleation and growth are respectively derived. This is obtained by accounting for the competition between the strain energy in the material from local stress concentrations and dislocation slip. Deformation by dislocation slip, at strains before twinning occurs, is described by the theory derived in Chapter 3 and now applied to HCP materials without additional considerations. An average and homogeneous dislocation density is considered, remaining a pseudo-continuum approach with only one parameter evolution. A dislocation generation term accounting for twin propagation is added to the evolution equation. Such term becomes active once a critical strain for twin nucleation is reached. Only physical parameters are employed as input. The new theory is successful in describing work hardening and twin volume fraction evolution of Ti, Zr and Mg. The transition temperatures where tensile or compressive twin modes dominate in Ti, Zr and Mg are also described.

5.1 Introduction

Hexagonal closed-packed (HCP) alloys are good candidates for modern industrial applications. For instance, automotive industry demands lighter materials while preserving or increasing their strength, leading to an increased interest in Mg-

based alloys; aerospace and nuclear power generation industries require good mechanical performance (strength, creep and corrosion resistance) at elevated temperatures, where Ti and Zr-based alloys display excellent properties.

HCP metals present fewer slip systems in comparison to other crystal structures such as face centred-cubic (FCC) or body centred-cubic (BCC), due to the reduced symmetry in their atomic arrangement. They are highly anisotropic, and their mechanical response variation is stronger under different crystallographic orientations. When they are plastically deformed, slip planes quickly saturate from dislocation glide and cross-slip, leading to the decomposition of dislocations into partials and twin formation. Deformation twinning is one of the principal modes of plastic deformation in crystalline solids [3]. Although HCP metals have been under investigation for many years, specific deformation mechanisms taking place at various temperatures and deformation orientations are not entirely understood yet.

When an HCP specimen is deformed under compression perpendicular to the basal poles, *i.e.* in-plane compression (IP), an additional hardening contribution is observed from twinning in a predominant mode. However, under different compression orientations, various twin and slip modes may take place at different temperatures; under through-thickness (TT) compression in magnesium at room temperature, basal and non-basal slip takes place and the twinning contribution to work hardening is lower with respect to IP compression [170, 171]; although a predominant twin mode is observed, the activity ratio of other twin and slip modes is higher. Figure 5.1 shows a schematic representation of IP and TT compression orientations. Many authors have found that under tensile deformation parallel to the c_{HCP} -axis, these metals exhibit a “normal” work hardening behaviour by dislocation slip, as almost no twin modes are favoured [172, 173, 13]. However, work hardening rate and yield stress are increased.

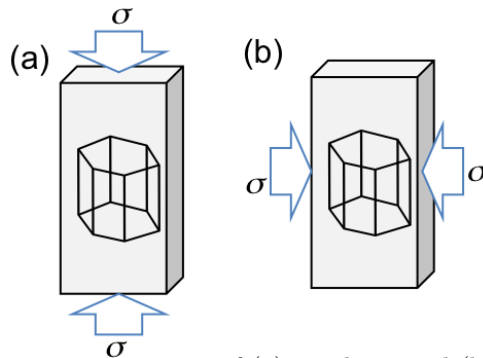


Figure 5.1: Schematic representation of (a) in-plane, and (b) through-thickness compression orientations.

There are two types of twin modes: tensile and compressive; they differ in their ability to accommodate strain during deformation. The interaction of dislocations with tensile $\{10\bar{1}2\}$ twins in Ti, Mg and Zr is repulsive¹, as a local stress concentration is produced due to pile-up at the interfaces [9]. Compressive $\{11\bar{2}2\}$ twins have an opposite effect, as they tend to contract the crystalline structure, and attract additional dislocations [9].

Table 5.1 summarises the experimentally observed predominant slip and twin modes in pure Mg, Ti and Zr at various temperatures and deformation orientations. Tensile twins predominate in pure magnesium at higher temperatures ($T \geq 298$ K); compressive twins in titanium prevail at and below room temperature, Zeng *et al.* [174] observed tensile twins dominate at high temperatures ($T \geq 673$ K) for moderate strains ($\varepsilon \leq 0.36$)². In zirconium, compressive twins prevail at low temperatures ($T \leq 300$ K). However, McCabe *et al.* [175] found that compressive twins dominate at 77 K at medium strains ($\varepsilon = 0.25$), whereas tensile twins are present at room temperature and at 77 K at low strains ($\varepsilon < 0.1$) instead. Note that the work from Song and Gray [176], shows opposite results for Ti and Zr in IP compression, although the compression orientation direction was not specified. Moreover, Morris *et al.* [177] performed atomistic calculations in Ti and Zr, finding that $\{11\bar{2}2\}$ compressive twin nucleation rate is higher at low temperatures, whereas $\{10\bar{1}2\}$ tensile twins are easily nucleated at higher temperatures. However, the transition temperatures where each mode predominates have not been described. For Mg alloys with moderate concentrations in Al and Zn (≤ 3 wt%), the deformation mechanisms are similar to those for pure Mg [178, 179].

¹Same effect occurs for other tensile twins.

²They also found that at large strains ($\varepsilon = 0.96$) $\{10\bar{1}1\}$ compressive twins are formed and almost all tensile twins have been annihilated, however this deformation range lies beyond the scope of the present work.

Table 5.1: Slip and twin modes found in Mg, Ti and Zr for various deformation conditions.

Material	Temp. (K)	Def. mode	Slip mode	Twin mode	Twin system	Ref.
Mg	298-580	IP Comp.	Basal	Tensile	$\{10\bar{1}2\}\langle 10\bar{1}1 \rangle$	[180]
Mg	298-423	IP Comp.	Basal	Tensile	$\{10\bar{1}2\}\langle 10\bar{1}1 \rangle$	[181]
Mg	298-580	Tension	Basal & Non-basal	No twinning	-	[182]
Mg	298	TT Comp.	Basal & Non-basal	Tensile	$\{10\bar{1}2\}\langle 10\bar{1}1 \rangle$	[170]
Mg	77-298	Tension	Pyramidal	No twinning	-	[183]
Ti	76-298	IP Comp.	Prismatic	Compressive	$\{11\bar{2}2\}\langle 11\bar{2}3 \rangle$	[184]
Ti	298	IP Comp.	Prismatic	Compressive	$\{11\bar{2}2\}\langle 11\bar{2}3 \rangle$	[185]
Ti	298	c_{HCP} -axis rolled	Prismatic	Compressive	$\{11\bar{2}2\}\langle 11\bar{2}3 \rangle$	[186]
Ti	673-973	IP Comp.	Prismatic	Tensile	$\{10\bar{1}2\}\langle 10\bar{1}1 \rangle$	[174]
Ti, Zr	76, 300	Compression	Prismatic	Tensile	$\{10\bar{1}2\}\langle 10\bar{1}1 \rangle$	[176]
Zr	4.2-300	IP Comp.	Prismatic	Compressive	$\{11\bar{2}2\}\langle 11\bar{2}3 \rangle$	[187]
Zr	298	IP Comp.	Prismatic	Tensile	$\{10\bar{1}2\}\langle 10\bar{1}1 \rangle$	[175]
Zr	76	IP Comp.	Prismatic	Tensile	$\{10\bar{1}2\}\langle 10\bar{1}1 \rangle$	[175]
Zr	$(0.04 \leq \varepsilon \leq 0.1)$					
Zr	76 ($\varepsilon = 0.25$)	IP Comp.	Prismatic	Compressive	$\{11\bar{2}2\}\langle 11\bar{2}3 \rangle$	[175]
Zr	298	TT Comp.	Prism. & Pyram.	No twinning	-	[175]
Zr	76	TT Comp.	Prismatic	Compressive	$\{11\bar{2}2\}\langle 11\bar{2}3 \rangle$	[175]
Zr	$(0.04 \leq \varepsilon \leq 0.1)$					
Zr	76 ($\varepsilon = 0.25$)	TT Comp.	Prismatic	Tensile	$\{10\bar{1}2\}\langle 10\bar{1}1 \rangle$	[175]

Crystal plasticity and/or finite element modelling have been frequently employed to describe deformation twinning in hexagonal metals [188, 189, 74, 178], as these methodologies can incorporate deformation gradients on specific slip and twin planes, and account for deformation orientation effects. Constitutive relations are introduced for the critical stress to activate each respective slip or twin mode. Texture distributions can be mapped with these approaches. Mesoscale models have been employed in magnesium [190] and titanium alloys [191, 192] to describe temperature and strain rate variations during work hardening. Beylerlein and Tomé [21], and Oppedal *et al.* [22] have developed a dislocation-based thermally-activated hardening model for pure Zr and Mg, respectively, for different temperature and orientation conditions: the evolution of the dislocation density of each slip mode follows a Kocks–Mecking evolution equation; a dislocation–twin hardening constitutive relationship is defined. The previous methods require the definition of empirical or phenomenological relations to account for temperature and strain rate variations, and for the activation conditions of the respective slip and twin modes. Moreover, quantitative analysis on solid solution effects in alloy’s work hardening and twinning behaviour is not clear yet. The objective of this chapter is to present a thermostatics-based description of deformation twinning in HCP metals. Concomitant interactions of dislocations with twins are studied with a single parameter description [193]. The novelty of this approach stems from mapping the critical conditions for twin nucleation and growth by expressing the favourable energy conditions for their occurrence. Central to this analysis is the introduction of a statistical entropy term that

accounts for the possible dislocation migration paths. This allows to postulate thermodynamic descriptions between the strain energy induced by local stress concentrations in the material and the dissipation effect from moving dislocations; the latter is crucial to be considered, as dislocation slip always precedes twin nucleation and growth [194]. As a result from these balances, the transition temperatures for predominant twin modes are successfully described.

This approach aids to reduce the number of parameters to be identified for each material; this is achieved by employing physics-based expressions that can be applied in several systems. This is demonstrated by applying the model (with the same set of equations) to describe work hardening, where pure slip and twinning occur, and twin volume fraction evolution for different temperature, strain rate and orientation conditions in pure Ti, Mg and Zr.

An incentive for introducing this approach is that several parameters, such as the critical stress for twin nucleation or the critical resolved shear stress for slip, are difficult to estimate from experiments [9, 195], and a number of constitutive or semiempirical relations, including several fitting parameters, are introduced for each material at different temperatures and strain rates. Furthermore, continuous dislocation and twin interactions represent a challenge for describing their isolated contributions. This makes difficult to make further predictions or extensions for designing new systems within the same formulation. Such complexities are not required in this theory, as it is based on estimating the energy production rate in the material, rather than characterising the specific mechanics of deformation twinning and dislocation slip.

5.2 Twinning formulation

Based on the previous discussion, the current model is defined on the following assumptions:

- i*) Only uniaxial loading conditions are being considered at moderated strains for pure materials.
- ii*) A single twinning and slip mode predominate for a given temperature and strain rate.
- iii*) An average macroscopic Taylor factor is predominant for a given deformation orientation. In-plane compression is set as the reference deformation orientation.

The introduction of assumption *ii*) is inspired by the experimental observations listed in Table 5.1, where in nearly all cases no more than one twin mode predominates. Table 5.2 shows the slip and twin modes considered in the model³;

³The transition temperatures where each mode predominates are provided in Section 5.2.3.

secondary twin modes are not considered in this work. Assumption *iii*) follows from *ii*), as different slip mode/twin mode combinations lead to different orientation factors [196]. This assumption is also supported by the work from Cáceres and Lukáč [197], where they estimated the Taylor factors from the stress-strain curves of pure magnesium with different texture conditions. These assumptions are valid at a macroscopic level only; at a polycrystalline level, stress variations occur on different orientations. Moreover, the Taylor factor can be defined at a macroscopic level. Solute atom contributions to twinning behaviour are not considered in this thesis, however they can be included in the current formation. This can be found in [193]. Coarse-grained materials are considered, as for relatively large grain sizes ($\geq 15 \mu\text{m}$), material's work hardening behaviour remains constant [198]. An interesting aspect of these observations is that, although twins can be formed at grain boundaries, their possible formation do not contribute to the material's macroscopic behaviour.

Table 5.2: Slip and twin systems considered in the model.

Material	twinning type	Ti, Zr	Mg
Slip system		$\{10\bar{1}0\}\langle 11\bar{2}0\rangle$	$(0002)\langle 1120\rangle$
Twin mode	Tensile	$\{10\bar{1}2\}\langle 10\bar{1}1\rangle$	$\{10\bar{1}2\}\langle 10\bar{1}1\rangle$
Twin mode	Compressive	$\{11\bar{2}2\}\langle 11\bar{2}3\rangle$	$\{11\bar{2}2\}\langle 11\bar{2}3\rangle$

Additional work hardening occurs once twin nucleation and propagation occurs. Twins act as barriers for dislocation slip, inducing an additional dislocation generation term ($\frac{d\rho_T^+}{d\gamma}$) in the Kocks–Mecking equation (term (B) in equation 2.30):

$$\frac{d\rho}{d\gamma} = \frac{d\rho^+}{d\gamma} - \frac{d\rho^-}{d\gamma} = \frac{k_1}{b}\sqrt{\rho} + \frac{d\rho_T^+}{d\gamma} - f_{DRV}\rho = \frac{1}{b} \left(\underbrace{k_1\sqrt{\rho}}_{(A)} + \underbrace{\frac{1}{\Lambda_T}}_{(B)} \right) - \underbrace{f_{DRV}\rho}_{(E)}, \quad (5.1)$$

where γ is the shear strain, k_1 is the dislocation storage coefficient [6], and Λ_T is the average twin boundary spacing of the predominant twin mode. This term becomes active once twin nucleation takes place.

Twin nucleation involves the dissociation of dislocations into partials due to localised stress concentrations [9]. This effect can be induced by dislocation pile-up at crystal defects (these include encountering other dislocations from adjacent slip planes, solute atoms or grain boundaries) [10], or by homogeneous lattice shear in a region of high stress concentrations [9]. Irrespective of the occurring mechanism, a critical strain energy is required to nucleate partial dislocations and drive twin propagation [194]. The twin nucleation and growth process being considered in this work is:

- a) At an initial state ($\gamma = 0$), the material contains a low dislocation density (ρ_0).
- b) Plastic deformation takes place under the critical strain at which twin nucleation occurs ($\gamma < \gamma_{Twin}^*$): dislocations form and slip in the crystal.
- c) Critical stress concentration occurs and partials are formed (by any of the previous mechanisms) at $\gamma = \gamma_{Twin}^*$ to nucleate twins; these twins contain an equivalent very low dislocation density ρ_T (twin boundaries+interiors); it is assumed that $\rho_T \sim \rho_0$.
- d) As plastic deformation continues ($\gamma > \gamma_{Twin}^*$), twin propagation occurs and the dislocation density of the twins ρ_T increases (ρ_T adds more dislocations to ρ).

Figure 5.2 shows a schematic description of this process. Arrows in Figure 5.2(b) point out where critical stress concentrations may occur, leading to twin formation (from dislocation self-interactions). A homogeneous dislocation density is described in equation 2.25: ρ_T at $\gamma > \gamma_{Twin}^*$ equals ρ at $\gamma - \gamma_{Twin}^*$ [95]. Although a number of twins are also nucleated below γ_{Twin}^* , they do not contribute macroscopically to dislocation hardening [191]. This criterion is consistent with the use of a uniform dislocation density.

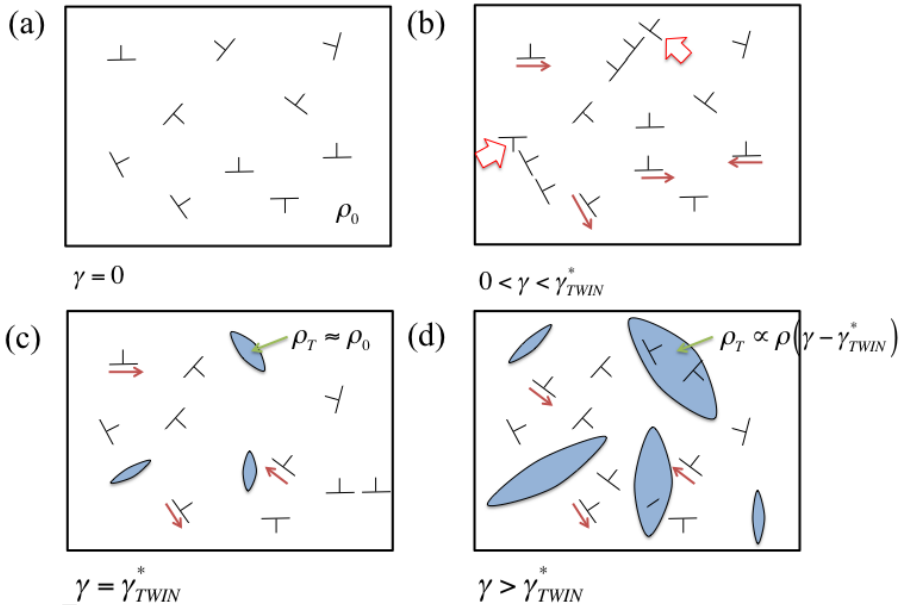


Figure 5.2: Schematic representation of twin nucleation and growth process.

An important aspect of this approach is that, as only the average dislocation density is considered, ρ contains both perfect dislocations and twins. This allows to simplify the number of parameter for identification and physical relations. For instance, no local considerations of the mechanisms driving partial formation are initially required, as the overall critical strain energy is considered for the thermodynamic analysis. Moreover, no critical resolved shear stress for slip and for twin nucleation are needed to be identified for different temperatures. However, further considerations need to be taken into account for orientation effects and for separating twin and dislocation contributions (via obtaining the twin volume fraction). This is addressed in Sections 5.2.4 and 5.2.5, respectively.

5.2.1 Twin nucleation strain

Following the previous considerations, it is proposed that twin nucleation occurs when the dislocation forest energy (E_{forest}), accounting for the overall stress accumulation in the material, equals the strain energy to form a twin boundary embryo (E_{nucl}) and the excess strain energy propagate it (E_{exs}); these terms are reduced by the energy dissipation from dislocation migration (E_{disp}), as dislocation glide tends to reduce local stress accumulation. The balance becomes:

$$E_{forest} = E_{nucl} + E_{exs} - E_{disp}. \quad (5.2)$$

Twin growth is not thermally activated, hence its occurrence is driven by the excess strain accumulation in the material only; E_{exs} accounts for such effect. This thermodynamic analysis for nucleation is similar to the balance employed in Chapter 3 for dislocation cell formation [116], where Arrhenius-type equations are not valid.

The energy of a dislocation forest equals [116, 3]

$$E_{forest} = \frac{n_f}{2} \mu b^2 \bar{l}, \quad (5.3)$$

where n_f is the number of dislocations in the forest and \bar{l} is the average dislocation spacing. In the previous section, the statistical entropy concept has been introduced to account for the energy dissipation from possible dislocation slip paths for given deformation conditions. E_{disp} is approximated by $T\Delta S$ per dislocation [116, 95, 139] (Section 3.3.2),

$$E_{disp} = n_f \frac{\bar{l}}{b} T\Delta S. \quad (5.4)$$

E_{nucl} represents the strain energy around a newly formed twin embryo, inducing n_{nuc}^* dislocations to split into Shockley partials:

$$E_{nucl} = \frac{n_{nuc}^*}{2} \mu b^2 \bar{l}. \quad (5.5)$$

n_{nuc}^* is a fraction of n_f . This number should account for the lattice distortion effects induced by a newly formed twin and for the possible sites for stress concentrations by dislocation self-encounters (no grain boundary or solute atom effects are added). Thus, n_{nuc}^* is approximated by *I*) the ratio between the area surrounded by a twin embryo with an initial boundary length \bar{x}_{Twin} (per dislocation) and thickness b , and the equivalent area of the forest in the absence of twins (\bar{l}^2); and *II*) the ratio between the possible encounters of a twin plane and a dislocation gliding in a given slip plane:

$$n_{nuc}^* = \underbrace{\frac{2\bar{x}_{Twin}b}{\bar{l}^2}}_{I)} \underbrace{\frac{\lambda_{Twin}}{\lambda_{slip}}}_{II)} n_f, \quad (5.6)$$

where the 2 factor accounts for the duplicity in twin boundaries; and λ_{Twin} and λ_{slip} are the number of twin and slip planes on an unit cell, respectively. $\lambda_{Twin}/\lambda_{slip}$ represents the frequency of newly formed twins encountering dislocations on different slip planes. Additional terms can be included in n_{nuc}^* to account for dislocation pinning around solute atoms or grain size variations that increase local stress concentrations [193].

E_{exs} equals the energy fraction of the forest surrounding the embryo (S_T):

$$E_{exs} = S_T E_{forest}. \quad (5.7)$$

If a twin embryo is assumed to have a circular cross-section, with the distance between partials (r_{part}) being its diameter, S_T can be approximated by the perimeter of the embryo per unit area

$$S_T = \frac{3P_T b}{8A_T} = \frac{3\pi r_{part} b}{8\pi r_{part}^2/4} = \frac{3b}{2r_{part}} \quad (5.8)$$

where P_T and A_T are the perimeter and area of the embryo, respectively, and 3/8 is a geometry constant accounting for the coherency between the twin embryo and the forest; this value was adjusted. The latter represents the effective dislocation storage rate as twins propagate in a different direction. Combining equations 5.3–5.8, equation 5.2 becomes

$$\frac{n_f}{2} \mu b^2 \bar{l} = \frac{\lambda_{Twin} \bar{x}_{Twin} b}{\lambda_{slip} \bar{l}^2} n_f \mu b^2 \bar{l} + \frac{3n_f b}{4r_{part}} \mu b^2 \bar{l} - n_f \frac{\bar{l}}{b} T \Delta S \quad (5.9)$$

The distance between partials equals $r_{part} = \frac{(2+\nu)\mu b^2}{24\pi(1-\nu)\chi}$ [27], where χ is the stacking fault energy and ν is the Poisson ratio. Rearranging the previous expressions

and substituting r_{part} , the critical strain γ_{Twin}^* for twin nucleation can be obtained

$$\gamma_{Twin}^* = \bar{x}_{Twin} b \rho = \bar{x}_{Twin} b \frac{1}{\bar{l}^2} = \frac{\lambda_{slip}}{\lambda_{Twin}} \left(\frac{1}{2} + \frac{k_B T \ln \left(\frac{\bar{\epsilon}_0 + \vartheta}{\bar{\epsilon}} \right)}{\mu b^3} - \frac{18\pi(1-\nu)\chi}{(2+\nu)\mu b} \right), \quad (5.10)$$

where $\gamma_{Twin}^* = b\bar{x}_{Twin}\rho$ being an Orowan-type equation. γ_{Twin}^* represents the strain at which twins of an initial length \bar{x}_{Twin} are nucleated. Once γ_{Twin}^* is reached, the twinning deformation term Λ_{Twin}^{-1} in the dislocation density evolution equation is active for the rest of the deformation process.

5.2.2 Twinning growth coefficient

Additional strain accumulation is required to grow twin embryos up to a critical size before commencing propagation [9]; this strain energy must be greater than that for dislocation migration and additional dislocation formation. Moreover, Beyerlein and Tomé [21] have pointed out that dislocations in the twin interiors are highly active and they are responsible for twin growth. Based on this, it is proposed that the stored energy E_{stored} induced in the twin to commence propagation, equals the energy of an additional number n_{prop}^* of dislocations being accumulated at the boundaries [193]:

$$E_{stored} = n_{prop}^* (E_{add} - E_{prop}), \quad (5.11)$$

where E_{add} is the strain energy from dislocations screened into the twin boundaries and E_{prop} is the slip energy from dislocations moving towards twin boundaries [194]. This balance prevails for both twin modes (tensile and compressive), however the energy terms vary for each case. E_{stored} corresponds to the strain energy of n_{TB} twin dislocations:

$$E_{stored} = \frac{n_{TB}}{2} \mu b^2 \bar{l}_T, \quad (5.12)$$

where $\bar{l}_T = 1/\sqrt{\rho_T}$ accounts for an equivalent average dislocation spacing of the twins (interiors+boundaries).

Similar to the previous section, n_{prop}^* represents a factor of n_{TB} . It is approximated by I) the ratio between the average twin spacing of the respective mode $\Lambda_{Twin}^{T/C} \cos \theta_{T/C}$ ⁴ and \bar{l} ⁵, to account for the effective spacing available for twin growth, where $\cos \theta_{T/C}$ is the projection of the dislocation's slip direction (from the forest) onto the twinning growth direction (tensile or compressive); and II)

⁴ Λ_{Twin}^T and Λ_{Twin}^C stand for the average tensile and compressive twin spacing, respectively. A similar case occurs for $\cos \theta_T$ and $\cos \theta_C$, respectively

⁵This length includes both twins and dislocations.

the ratio between the possible encounters of a twin plane and a dislocation gliding in a given slip plane; and:

$$n_{prop}^* = \underbrace{\frac{\Lambda_{Twin}^{T/C} \cos \theta_{T/C}}{3\bar{l}}}_{I)} \underbrace{\frac{\lambda_{Twin}}{\lambda_{slip}}}_{II)} n_{TB}, \quad (5.13)$$

where the 3 factor is a geometry constant accounting for the coherency between the twin embryo and the forest. Term *I*) in the previous equation accounts for the effective fraction of dislocations inducing additional stress concentration at twin boundaries. $\cos \theta_{T/C}$ accounts for the effective dislocation–twin boundary interaction directions. This projection has also been employed by other authors, for instance in the work by Capolungo *et al.* [199].

E_{add} equals the strain energy of a dislocation arriving at the boundaries

$$E_{add} = 4 \cos \theta_{T/C} \frac{1}{2} \mu b^2 \bar{l} \quad (5.14)$$

where the 4 factor accounts for the multiplicity in the twin–dislocation interactions (twin interiors+forest), and $\cos \theta_{T/C}$ accounts for the projection from the twin growth direction onto the slip direction (forest).

Similar to the previous section, the magnitude of E_{prop} equals E_{disp} . However, twins can attract or repel dislocations under compressive or tensile modes, respectively. This can reduce or increase the driving force for twin growth [9]. Thus, a sign function is introduced to account for this effect:

$$E_{prop} = \text{sign}(\text{Twin}) E_{disp} = \text{sign}(\text{Twin}) \frac{\bar{l}}{b} T \Delta S, \quad (5.15)$$

where $\text{sign}(\text{Twin})$ is equal to -1 or 1 if the twin mode is tensile or compressive, respectively. If dislocations are attracted (compressive twins), less energy is required to be overcome, whereas the opposite occurs for tensile twins.

Combining the previous expressions, and rearranging equation 5.11, $1/\Lambda_{Twin}^{T/C}$ equals:

$$\frac{1}{\Lambda_{Twin}^{T/C}} = \frac{\lambda_{Twin} \cos \theta_{T/C}}{3\lambda_{slip} \bar{l}_T} \left(4 \cos \theta_{T/C} - \text{sign}(\text{Twin}) \frac{2k_B T \ln \left(\frac{\dot{\epsilon}_0 + \dot{\vartheta}}{\dot{\epsilon}} \right)}{\mu b^3} \right) = \frac{k_{Twin}^{T/C}}{\bar{l}_T}, \quad (5.16)$$

with $k_{Twin}^{T/C} = \frac{\lambda_{Twin} \cos \theta_{T/C}}{3\lambda_{slip}} \left(4 \cos \theta_{T/C} - \text{sign}(\text{Twin}) \frac{2k_B T \ln \left(\frac{\dot{\epsilon}_0 + \dot{\vartheta}}{\dot{\epsilon}} \right)}{\mu b^3} \right)$, is the twinning coefficient of the tensile (T) or compressive (C) mode. The twinning coefficient

cients for each mode become:

$$\begin{aligned} k_{Twin}^T &= \frac{\lambda_{Twin} \cos \theta_T}{3\lambda_{slip}} \left(4 \cos \theta_T - \frac{2k_B T \ln \left(\frac{\dot{\epsilon}_0 + \dot{\nu}}{\dot{\epsilon}} \right)}{\mu b^3} \right) \\ k_{Twin}^C &= \frac{\lambda_{Twin} \cos \theta_C}{3\lambda_{slip}} \left(4 \cos \theta_C + \frac{2k_B T \ln \left(\frac{\dot{\epsilon}_0 + \dot{\nu}}{\dot{\epsilon}} \right)}{\mu b^3} \right). \end{aligned} \quad (5.17)$$

It is worth noting that if $k_{Twin}^{Ten} \leq 0$, then it is fixed to 0 and no deformation twinning takes place. Following assumption *ii*), the additional hardening effect in equation 2.25 is equal to the predominant twin mode, *i.e.* the twin mode with higher growth rate, induced by a higher number of stored dislocations for twin propagation (equation 5.13). This occurs for the twin mode with higher (lower inverse) average spacing values; Λ_{Twin}^{-1} equals [193]:

$$\frac{1}{\Lambda_{Twin}} = \min \left(\frac{1}{\Lambda_{Twin}^T}, \frac{1}{\Lambda_{Twin}^C} \right) = \min(k_{Twin}^T, k_{Twin}^C) \frac{1}{\bar{l}_T} = k_{Twin} \sqrt{\rho_T}. \quad (5.18)$$

5.2.3 Twin mode transition temperatures

The transition temperatures where each twin mode dominates can be obtained from equations 5.17. The physical parameters are shown in Appendix A. Figure 5.3 shows a comparison of twin predominant modes for (a) Ti, (b) Zr and (c) Mg with the experimental observations summarised in Table 5.1 for IP compression. The black and red curves represent the twinning coefficient for the tensile and compressive twin modes, respectively. The predominant modes are shown in the boxes (the twinning coefficient with lower values). Titanium shows that compressive twins are predominant at temperatures below ~ 350 K; at this point a transition from compressive to tensile twins occurs; above ~ 950 K, deformation twinning is no longer present; these ranges are in good agreement with the experimental data reported in the literature. Compressive twins predominate in zirconium for temperatures up to ~ 320 K; between 320 and 750 K, tensile twins predominate, whereas above this temperature, no deformation twinning is present; Akhtar [200] observed a transition from deformation twinning to pure slip at ~ 800 K; the model shows good agreement for these transition ranges. Tensile twins in magnesium predominate from ~ 180 K up to ~ 570 K, where a transition to pure slip occurs, being in good agreement with experimental observations.

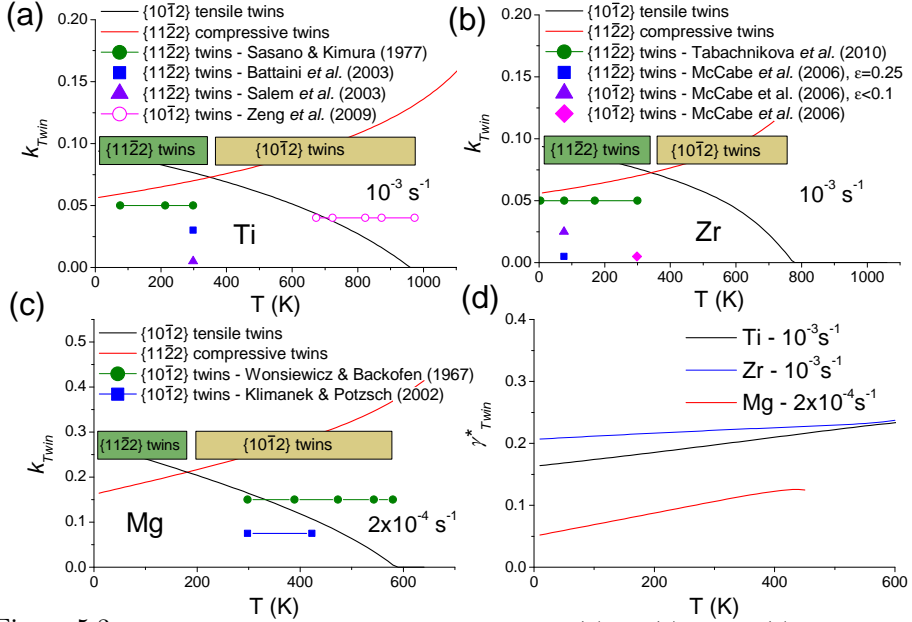


Figure 5.3: Twinning modes transition temperatures for (a) Ti, (b) Zr and (c) Mg and their comparison with experimental observations. The red and black curves represent the twinning coefficient for {1122} and {1012} twin modes, respectively. The model predictions of predominant twin modes are shown in the boxes. (d) Twin nucleation strain for various temperatures.

In order to obtain the projection of the slip and twinning directions, the dot product between the preferred slip and twin directions is obtained⁶: $\cos\theta_{T/C} = \frac{\mathbf{b}_s \cdot \mathbf{b}_T}{|\mathbf{b}_s| |\mathbf{b}_T|}$, where \mathbf{b}_s is the Burgers vector of the slip direction and \mathbf{b}_T is the vector on the twin propagation direction. The c_{HCP} -axis values for Ti, Mg and Zr equal $1.59b$, $1.593b$ and $1.623b$, respectively [25]. Table 5.3 shows the values of the projection effect for Ti, Zr and Mg. Table 5.3 also shows the values of λ_{slip} and λ_{Twin} .

⁶These calculations are displayed to cartesian coordinates

Table 5.3: Twinning-slip orientation parameters. $\cos \theta_T$ and $\cos \theta_C$ stand for the slip projections on tensile and compressive twins, respectively.

Material			Ti	Zr	Mg
Slip system			$\{10\bar{1}0\}$	$\{10\bar{1}0\}$	(0001)
λ_{slip}			6	6	2
Slip direction (\mathbf{b}_s)			$\langle 11\bar{2}0 \rangle$	$\langle 11\bar{2}0 \rangle$	$\langle 11\bar{2}0 \rangle$
Tensile twin	$\{10\bar{1}2\}$	λ_{Twin}	6	6	6
Twin direction (\mathbf{b}_T)	$\langle 10\bar{1}1 \rangle$	$\cos \theta_T$	0.26	0.26	0.26
Compressive	$\{11\bar{2}2\}$	λ_{Twin}	6	6	6
Twin direction (\mathbf{b}_T)	$\langle 1\bar{1}0\bar{3} \rangle$	$\cos \theta_C$	0.2	0.2	0.2

Magnesium displays low ductility due to the early twin activation, whereas titanium and zirconium are considered to be ductile, due to their late twinning activation [9]. Figure 5.3d shows the twin onset strain γ_{Twin}^* for Ti, Zr and Mg at various temperatures. Deformation twinning in magnesium occurs at lower strains in comparison to titanium and zirconium, being this result in good agreement with the twinning activation ranges.

5.2.4 Orientation effect

Specific deformation orientations accommodate strain in different twin modes, inducing different texture distributions. The Schmid factor m is employed to analyse the most likely slip and twin modes taking place at specific deformation orientations [196]. It relates the critical resolved shear stress for slip in a given plane with the applied stress direction. On the other hand, the Taylor factor M is defined as the ratio between the flow stress in a polycrystal and the CRSS in the single crystal [201], and it is used to express the macroscopic strain in terms of the algebraic sum of crystallographic shears. m and M are inversely related, and the Taylor factor can incorporate the macroscopic effect of different deformation orientations. Thus, a function θ_{or} is defined to estimate the orientation variation of M :

$$M = 3\theta_{or}, \quad (5.19)$$

where 3 is a reference value [6]. $\theta_{or} = 1$ when the material is deformed at in-plane compression (reference orientation, assumption *i*) and it is maximum when the material is tension deformed, when no twinning takes place and higher flow stress is observed. θ_{or} accounts for the activity of additional twin and slip modes. Ono *et al.* [182] obtained a Taylor factor of 6.5 for tension in pure magnesium, where various slip modes occur; $\theta_{or} = 2$ is employed in the current calculations. On the other hand, twinning contribution to work hardening is also affected:

When $\theta_{or} = 2$, no deformation twinning is present (tensile deformation) and $\Lambda_{Twin}^{-1} \rightarrow 0$; whereas for $\theta_{or} = 1$, the hardening contribution equals the inverse of the predominant twin spacing (Λ_{Twin}^{-1}) and a single slip mode dominates. Thus, a linear extrapolation of θ_{or} multiplying Λ_{Twin}^{-1} is proposed to account for this effect. Combining these results, the dislocation density evolution becomes [193]⁷:

$$\frac{d\rho[\gamma]}{d\gamma} = \frac{1}{b} \left(\underbrace{k_1 \sqrt{\rho[\gamma]}}_{(A)} + \underbrace{(2 - \theta_{or})k_T \sqrt{\rho[\gamma] - \gamma_{Twin}^*}}_{(B)} \right) - \underbrace{f_{DRV} \rho[\gamma]}_{(E)}. \quad (5.20)$$

For different deformation orientations, $\theta_{or} \leq 2$ displays different values (preferred textures). Table 5.4 shows the values of θ_{or} used for the present calculations. It is worth noting that θ_{or} depends on the slip and twin modes taking place during deformation only, and does not depend on the material type.

Table 5.4: θ_{or} values employed in the model.

Deformation orientation	Twin mode	θ_{or}
IP Compression	Tensile	1
IP Compression	Compressive	1
TT Compression	Tensile	1.75
TT Compression	Compressive	0.7
Tension	-	2

Cáceres and Lukáv [197] have concluded that the Taylor factor in polycrystalline Mg is higher for prismatic and basal slip, whereas it decreases when pyramidal slip is present; from equation 5.19, textural features can be depicted from θ_{or} . For instance $\theta_{or} = 1.75$ in TT compression (tensile twins dominating) represents a mixed activity of basal and prismatic slip, with a low twin activity; these results are in agreement with other modelling results [22]. $\theta_{or} = 0.7$ in TT compression (compressive twins dominating at low temperatures) can represent an increased activity from pyramidal slip, and a higher twin activity from additional compressive twins. Ando *et al.* [202] have found pyramidal slip activity when Mg is deformed at 77 K, where compressive twins dominate, hence θ_{or} for this condition is also consistent with experimental observations. Although this parameter shows good qualitative agreement with experimental and theoretical results, further analysis on texture development by combining other techniques can be implemented to obtain specific values θ_{or} .

⁷[] denotes functional dependence in γ .

5.2.5 Twin volume fraction

Equation 5.20 accounts for the average dislocation density ρ containing both perfect dislocations and twins; if term Λ_{Twin}^{-1} is not considered, the equation describing pure slip behaviour is reduced to:

$$\frac{d\rho_{slip}}{d\gamma} = \frac{k_1}{b} \sqrt{\rho_{slip}} - f_{DRV} \rho_{slip}, \quad (5.21)$$

where ρ_{slip} is the average dislocation density if deformation by slip is the only deformation mechanism. f_v can be obtained by comparing the stress contributions by slip+twinning σ_{T+s} (via ρ) and pure slip σ_s (via ρ_{slip}). This can be obtained by the Taylor relation [6] for pure slip $\sigma_s = \alpha M \mu b \sqrt{\rho_{slip}}$ and for twinning+slip $\sigma_{T+s} = \alpha M \mu b \sqrt{\rho}$, where α is a constant:

$$f_v = \frac{\sigma_{T+s} - \sigma_s}{\sigma_{T+s}} = 1 - \sqrt{\frac{\rho_{slip}}{\rho}}. \quad (5.22)$$

This allows to separate twin and dislocation contributions to material's mechanical response. This relation follows a similar consideration than the softening fraction equation being employed for recrystallisation evolution [203].

5.3 Results

The HCP model is compared to experimental axial-stress strain curves for Ti, Zr and Mg obtained from the literature, at different temperatures and deformation orientations. The dislocation density is obtained by solving equation 5.20, using the value of k_1 from equation 2.27; and the value of f_{DRV} shown in equation 3.29. It is worth noting that no modifications are required for these parameters. Physical parameter values are listed in Appendix A. The vacancy concentration at the melting point equals $c_m = \exp(-\Delta S_{form}/R) \exp(-E_f/RT)$, where ΔS_{form} is the vacancy formation entropy, and $\Delta S_{form}/R$ is approximately equal to 1.5 [156]. The lower (T_0) and higher (T_f) transition temperatures where different dislocation annihilation mechanisms occur are listed in Table 5.5 (see Section 3.2.2); these values are obtained with equations 3.13. An experimental value for T_0 in pure Ti was obtained from [204], when a maximum peak in the flow stress is observed. T_f for Mg was obtained from [205], where the value of the activation energy for plastic deformation changes. The model shows good agreement for these values. However, no experimental data was found for Zr.

Table 5.5: Lower and higher temperature limits. E and M stand for experimental and model values, respectively.

Material	$\dot{\epsilon}$ (s^{-1})	T_0^E (K)	Ref.	T_0^M (K)	T_h^M	T_f^E (K)	Ref.	T_f^M (K)	T_h^M
Ti	10^{-3}	400	[204]	409	0.21			1096	0.56
Mg	10^{-3}	220			0.24	560-620	[205]	555	0.6
Zr	10^{-3}	252			0.11			635	0.3

The axial stress is obtained from the Taylor relation [6] $\sigma = \sigma_Y + \alpha M \mu b \sqrt{\rho}$, where M holds different values, according to the deformation orientation (equation 5.19 and Table 5.4), and σ_Y accounts for the friction stress. Figure 5.4 shows the yield stress values measured from the experimental stress-strain curves at different deformation conditions that were obtained from [191, 21, 206, 207, 13, 208, 182]; the horizontal axis is expressed in terms of the reduced temperature $\frac{k_B T \ln(10^7/\dot{\epsilon})}{\mu b^3}$.

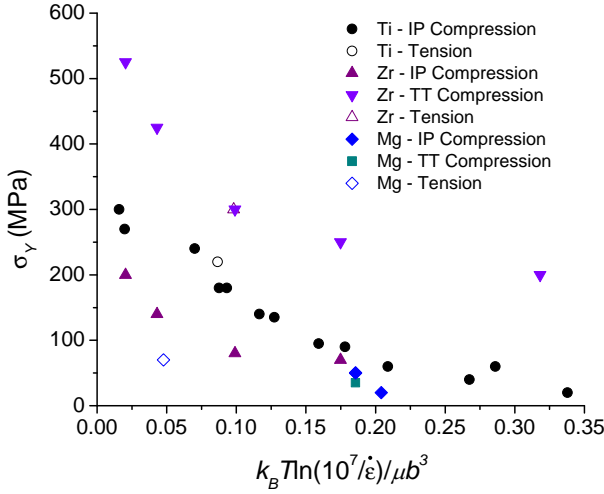


Figure 5.4: Experimental yield stress employed in the model.

Figure 5.5 shows the model results for IP compression ($\theta_{or} = 1$) and their comparison with experimental data at different temperatures and strain rates for (a), (c) commercially pure titanium, previously extruded, with average grain size of $40 \mu\text{m}$ [191], (b) pure rolled zirconium with average grain size of $20 \mu\text{m}$ [21], and (d) commercially pure magnesium (rolled prior deformation) [207], and pure magnesium (previously extruded) with average grain size of $50 \mu\text{m}$ [208]. The

arrows show where the (axial) twin nucleation strain $\varepsilon_{Twin}^* = \gamma_{Twin}^*/M$ occurs. The model results for Ti show good agreement in the twinning onset range and work hardening behaviour; however, at 77 K it shows additional work hardening after $\varepsilon \sim 0.15$; for temperatures above 473 K at 10^{-3} s^{-1} the experiment observations show higher flow stress response at large strains ($\varepsilon > 0.2$); this discrepancy can be due to the presence of impurities in the material as pointed out by Biget and Saada [209]. They observed that the flow stress for various temperatures in a titanium specimen with 50 and 100 ppmw O and Fe, respectively, was $\sim 60 \text{ MPa}$ higher than other specimen with 30 and < 10 ppmw O and Fe, respectively. The experimental samples shown in Figure 5.5(a) and (b) present a concentration of 270 ppmw O, 2 ppm Fe, and additional impurities [191]. The model results for pure zirconium show good agreement with experiments, except at 150 K where at strains above 0.15, the model presents a higher work hardening rate. The results for magnesium show good agreement at room temperature and at 373 K for strains up to 0.04; above this value the experimental stress shows additional work hardening behaviour. This discrepancy may be due to reorientation effects in the specimen.

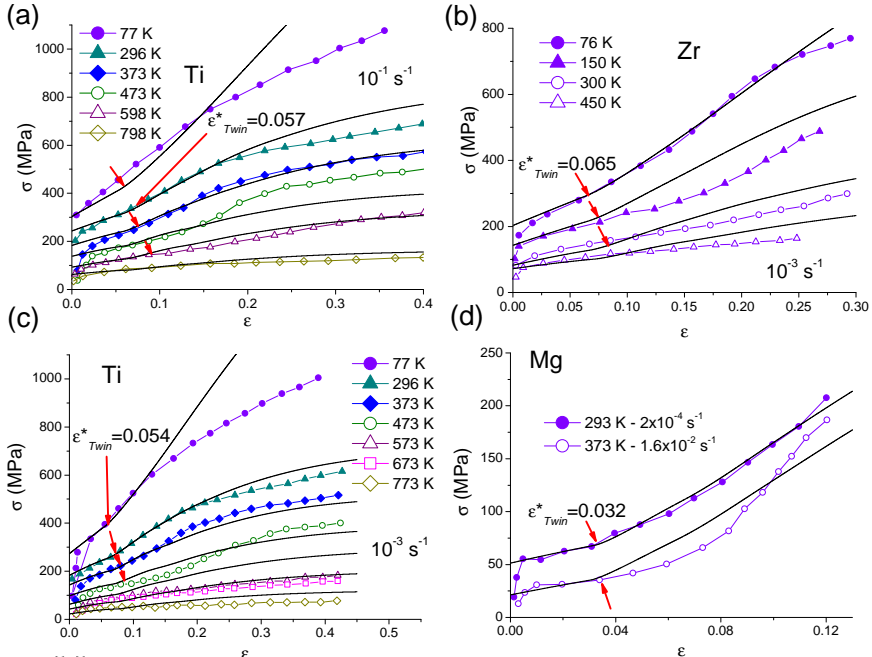


Figure 5.5: IP compression of pure (a), (c) Ti, (b) Zr and (d) Mg. The ε arrows show the strain where twinning begins. Items (A), (B) and (E) are present in the Kocks–Mecking equation.

Figure 5.6 shows the model results for tensile ($\theta_{or} = 2$) and IP ($\theta_{or} = 1$) compressive deformation, and their comparison with experimental data for (a) commercially pure titanium [206, 191]; (b) pure zirconium [21]. Figure 5.6(c) shows the through-thickness (TT) compression behaviour of pure zirconium at different temperatures; the experiment results were obtained from [210, 21] (at 300 K, a value of $\theta_{or} = 1.75$ was employed instead, to consider tensile twins as shown in Table 5.1). Figure 5.6(d) shows the deformation behaviour of pure magnesium deformed in tension, TT and IP compression [13, 208, 207, 182, 22]. The magenta line represents tensile deformation at 77 K. Red arrows show where twin nucleation occurs. The model shows good agreement for these materials at various deformation conditions, except for Mg deformed at TT compression, as the model shows a higher work hardening rate with respect to the experiments at strains above 0.04. This discrepancy can be due to a late activity from additional slip modes that are were not considered in the model and that may alter the θ_{or} values.

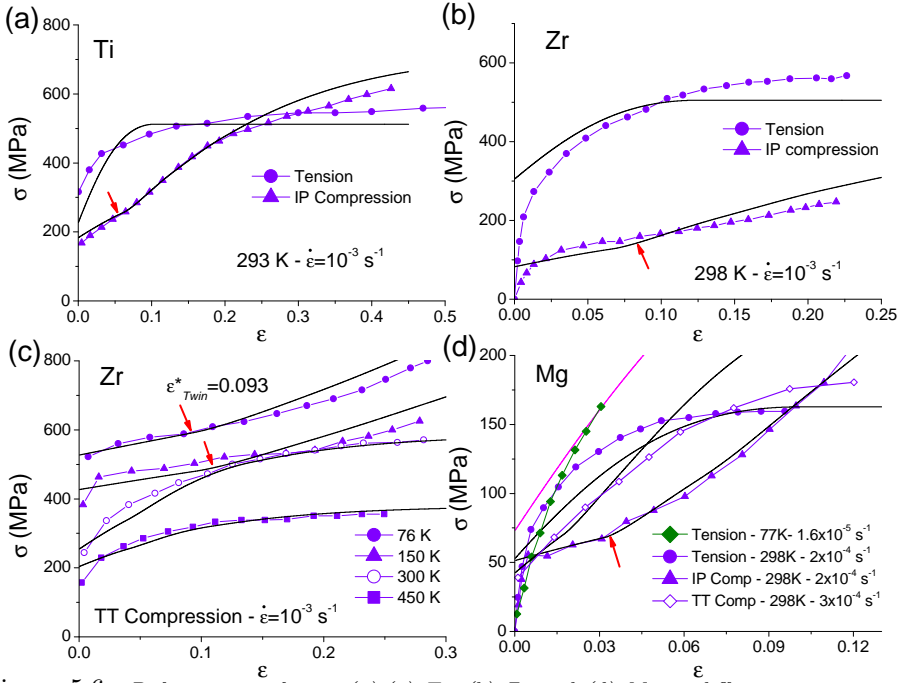


Figure 5.6: Deformation of pure (a),(c) Ti, (b) Zr and (d) Mg at different orientations. The arrows show the strain where twinning begins. Items (A), (B) and (E) are present in the Kocks–Mecking equation.

Figure 5.7(a) shows the volume fraction evolution f_v with strain for IP compression in previously rolled Mg, with its respective flow stress curve, and their comparison with experimental data obtained from [22]. The error bars display the limits between the estimated upper- and lower- volume fraction from neutron diffraction measurements. The model shows agreement in the evolution rate with respect to the experimental data, however it displays lower values than the measured ranges. It is worth noting that as the model accounts for deformation twinning that becomes macroscopically observable, below the critical strain for twin nucleation ε_{Twin}^* , the twin volume fraction is null. Figure 5.7(b) shows the compressive twins volume fraction evolution for pure (rolled) Zr being deformed at 76 K and 10^{-3} s^{-1} in IP and TT compression, and their comparison with experimental measurements; their corresponding flow stress curves are also shown; the experimental data was obtained from [211]. The model shows good agreement for both orientation conditions.

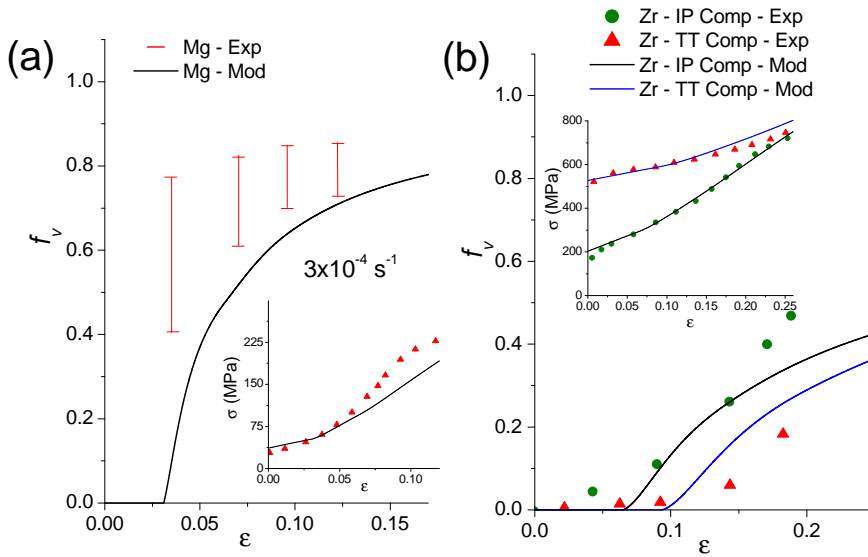


Figure 5.7: Twin volume fraction evolution with its respective flow stress curve for (a) Mg and (c) Zr at IP and TT compression at 76 K and at 10^{-3} s^{-1} .

5.4 Discussion

A new approach describing deformation twinning in HCP metals has been presented. Dislocation slip behaviour and accompanying interactions with growing twins are studied with a single parameter equation. A thermodynamic description of the favourable conditions for twin nucleation and growth have been presented. The balance between the strain energy induced by local stress concentrations in the material, and the dissipation effect from moving dislocations prior twin formation has been postulated to obtain the critical strain energy to form a twin embryo. The relatively good ductility of Ti and Zr with respect to Mg can be explained in terms of the critical strain for twin nucleation γ_{Twin}^* , showing lower values in Mg, where the critical strain energy from local stress concentrations is reached before than in Ti and Zr (Figure 5.3). Solid solution effects have also been incorporated in this approach; these results can be found in [193].

Further stress concentration from dislocation storage drives twin growth; such depends on the competition between dislocations storing at twin boundaries and their dissipation effect from slip. The previous expressions incorporate crystallographic features of twins to account for their dissimilarities with respect to the matrix. From this balance, tensile and compressive twin growth rates are compared to obtain the temperature regimes where each twin mode predominates. The dominant mode displays the higher the growth rate. Additional twin modes can be incorporated into the analysis.

An additional dislocation generation term in the dislocation evolution equation is introduced; this term equals the inverse average twin spacing of the predominant mode Λ_{Twin}^{-1} . It contains a strain delay γ_{Twin}^* due to the prior strain energy required for twin nucleation. Both parameters are obtained from the thermodynamic balance (equations 5.2 and 5.11).

The dislocation evolution equation when only slip occurs has been derived in Chapter 3 for FCC metals, and it is applied to HCP metals without additional alterations. The dislocation generation and dynamic recovery rates are expressed in terms of physical parameters and remain valid for different materials. For strains below $\varepsilon_{Twin}^* = \gamma_{Twin}^*/M$, where deformation by slip dominates, the model showed good agreement with the experimental observations.

An essential consideration of this theory is the introduction of a statistical entropy term that estimates the energy dissipation due to different dislocation migration paths. This term incorporates the temperature and strain rate effects on dislocation kinematic behaviour. It strongly features in the analysis, as it is related to the energy loss by dislocation slip prior to twin nucleation (equation 5.2) and for twin growth (equation 5.11). It also allows to determine the transition temperatures in which cross-slip and dislocation climb control dislocation annihilation (Table 5.5). These limits were validated for Ti and Mg.

The thermodynamic equations for twin nucleation and growth are equivalent to introduce a number of constitutive relations for the critical stress for twin nucleation and growth, and their evolution with strain. For instance, Oppedal *et al.* [22] have obtained the critical stress to nucleate or initiate twinning activity in their Visco-Plastic Self-Consistent (VPSC) model to equal 15 MPa in Mg, whereas the present model predicts that twinning commences ($\gamma = \gamma_{Twin}^*$) at ~ 18 MPa above the friction stress. Moreover, the transition temperatures for the dominant twin modes are a direct consequence of the present analysis, showing good agreement with respect to experimental observations. The model couples slip and twinning contributions to the material's mechanical response; this allows to simplify the thermodynamic analysis, as only one parameter is considered. Moreover, as only average energy values are employed, no specific twin nucleation and growth mechanisms need to be identified, as only thermodynamic variables are required, such as the strain energy from local stress concentrations and the entropy dissipation from dislocation slip.

5.4.1 Orientation effects and twin volume fraction

Different deformation orientations induce specific texture distributions, producing different macroscopic behaviours. An orientation function θ_{or} has been proposed to reproduce specific orientation and texture configurations described by the Taylor factor. M is an average orientation factor which accounts for the material's texture and crystallographic nature of the slip systems [201]. Cáceres and LuKác [197] have delineated a methodology to describe the Taylor factor as a function of the work hardening behaviour. Schmid factor estimations for different slip and twin systems aid in describing θ_{or} for other orientation conditions [196]. θ_{or} has been identified for specific orientation conditions (IP and TT compression, and tension); however, further analysis is required to characterise this parameter with specific texture evolution. Other modelling approaches can be employed to determine these values. Additional texture variations are reflected also in the yield stress behaviour; however, the current approach focuses on work hardening only.

The assumption that one predominant slip and twin mode occurs is well supported by experimental evidence for IP compression (Table 5.1); this is also in agreement with theoretical findings by other modelling approaches [21, 22, 178]. For instance, Zhang and Joshi [74] have pointed out that non-basal slip modes and compressive twins in pure Mg show negligible presence in the initial stages and become discernible only at the later stages of the deformation (without major contributions). However, this consideration has to be further validated for other orientation conditions.

The twin volume fraction is obtained by comparing the stress contributions from

pure slip and when slip and twinning are coupled. To illustrate this, Figure 5.8 shows the stress contributions in pure Mg deformed at (a) IP ($\theta_{or} = 1$) and (b) TT ($\theta_{or} = 0.7$) compression obtained with the model results. The former shows that before the critical strain for twin nucleation takes place ($\varepsilon \sim 0.035$), pure basal slip occurs, whereas above this value, twins contribute to work hardening; at a volume fraction (red line) of ~ 0.5 , tensile twinning contribution (dotted green line) overtakes slip contribution (dashed and dotted purple line) and continues increasing at a higher rate. For TT compression, a higher slip activity takes place, being caused by the activation of additional slip modes (prismatic); twinning activity becomes active at earlier stages, however its stress contribution decreases with respect to IP compression, due to a combined activity from compressive and tensile modes. This behaviour is in good agreement with previous experimental observations [170, 171].

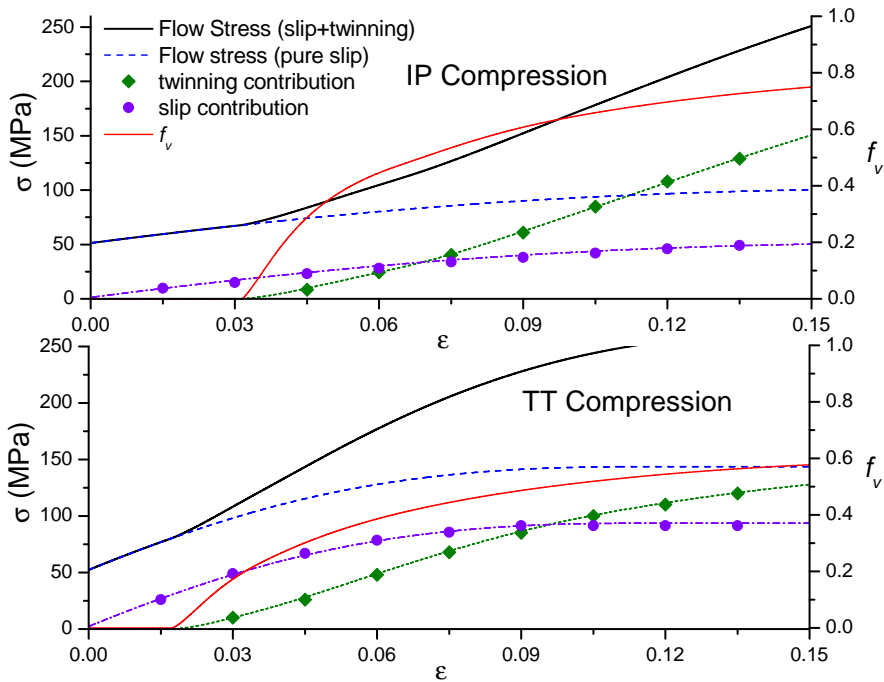


Figure 5.8: Stress contribution for different deformation mechanisms in pure Mg deformed at room temperature and at 10^{-3} s^{-1} for (a) IP and (b) TT compression, respectively.

5.4.2 Summary of the current approach

In summary, the present work proposes a different perspective for describing deformation twinning in hexagonal materials. It aids to reduce the number of constitutive relations and parameters to be identified for each material, by thermodynamic-based descriptions. This is inspired by the fact that it is usually difficult to describe the initial stress and strain states when twins feature (with their respective temperature and strain rate variations); in addition, dislocation evolution laws are not fully characterised for various processing and microstructure variations. Moreover, concomitant dislocation and twin interactions represent a challenge for describing their isolated contributions. This approach has been shown to be a good alternative to describe both dislocation and twin evolution, as it was applied to three metals without further modifications.

The model was tested against experimental stress–strain curves (where pure slip and twinning occur) and twin volume fraction evolution for different temperature, strain rate and orientation conditions in pure Ti, Mg and Zr. Only physical parameters and crystallographic features are employed as input.

This approach can be complemented by other modelling techniques. For instance, crystal plasticity can describe texture evolution; the evolution equation 5.20 can be divided to account for contributions from each slip and twinning mechanism. This methodology would also allow to identify the orientation parameter θ_{or} , or for introducing texture features in the model more explicitly. Moreover, the combination of these approaches would allow to define the critical conditions for slip and twinning in terms of microstructure (dislocation density) evolution. Further crystallographic considerations in the thermodynamic analysis can be introduced to include additional twin modes.

Shortcomings to the model include the description for coarse-grained metals only and no grain size effect is included in twinning behaviour (although for grain sizes $\geq 15 \mu\text{m}$ the main hardening contribution lies on the yield strength). The presence of additional microstructural defects, such as precipitates may significantly alter twinning behaviour; a similar case occurs for impurities and interstitial solute atoms; such effects were not included in the model. Their consideration may require the introduction of additional energy terms in the conditions for twin nucleation and growth.

5.5 Conclusions

A new approach for describing deformation twinning in HCP metals has been presented. This theory is able to describe:

1. Dislocation slip behaviour before twinning takes place.

2. Deformation twinning for different temperature and strain rate conditions.
3. The temperature ranges where different twin modes predominate, and the temperature at which transitions between them occur.
4. Twin volume fraction evolution with strain
5. Orientation behaviour for in-plane and through-thickness compression, and tension by varying the macroscopic Taylor factor (via an orientation factor θ_{or}).

The model describes the flow stress behaviour of pure Ti, Zr and Mg by employing only physical and crystallographic parameters as input. This allows to describe plastic deformation in HCP metals with a single-parameter formulation, incorporating temperature, strain rate and orientation effects. Further extensions, such as the inclusion of grain size and precipitation hardening effects can be incorporated in future work. The current approach can be input to other modelling techniques such as crystal plasticity or discrete dissociation dynamics, to describe detailed texture distributions.

Chapter 6

Hot deformation in metals: Dynamic recrystallisation

Extension of the theory to describe dislocation evolution in FCC metals undergoing dynamic recrystallisation is presented. Similar to the previous chapter, the overall recrystallisation behaviour is described in terms of an average dislocation density. An additional softening effect in the Kocks–Mecking equation is incorporated, which becomes active once a critical strain for grain nucleation is achieved. With this approximation, the use of the grain boundary mobility concept can be circumvented, and mobility fitting parameters are not required. The theory reproduces the stress oscillations with strain and its values as the steady state is approached; and captures well the temperature–strain rate dependency of dynamic recrystallisation. This allows to map the conditions under which dynamic recrystallisation occurs. The model results are successfully validated with data for Cu and Ni.

6.1 Introduction

Predicting the conditions for the occurrence of dynamic recrystallisation (DRX) during hot deformation of metals remains a problem of great technological importance as alloy mechanical properties become severely affected by this phenomenon. At high temperatures and/or low strain rates, dislocation-free grains nucleate and grow from high-angle subgrain boundaries (originated by significant dislocation accumulation at their boundaries), decreasing the total dislocation density [3]. This process occurs once a critical strain is reached.

Many efforts have been proposed to describe DRX. Won Lee and Im [212] combined a cellular automata model to predict grain coarsening and refinement with

the Kocks–Mecking equation describing the dislocation evolution in pure copper. Okuda and Rollett [213] have employed the Monte Carlo simulation method to investigate the growth behaviour (misorientation and mobility) of a grain nucleus when particle pinning takes place in steels. Takaki *et al.* [214, 215] have modelled dynamic recrystallisation with a multi phase field modelling approach, defining each growing grain as a phase field; the dislocation evolution is obtained by employing the Kocks–Mecking equation and it is combined with the phase-field simulation to estimate the recrystallisation effect. Brown and Bammann [92] combined a strain gradient method with thermodynamics to describe the evolution of static and dynamic recrystallisation in oxygen-free high conductivity (OFHC) copper; once again, a Kocks–Mecking–type equation is introduced to describe the dislocation evolution in the material, and an empirical function of the recrystallisation volume fraction and the interfacial area between recrystallised and unrecrystallised grains is introduced; this relation is combined with an expression for grain boundary mobility to obtain the recrystallisation fraction evolution; these equations are solved together to obtain the flow stress response. Fan and Yang [93] have proposed an internal-state-variable model to describe dynamic recrystallisation in a two-phase titanium alloy; the description of the dislocation density is given by the Kocks–Mecking equation, where the annihilation coefficient is expressed in the form of an Arrhenius equation. An additional term is introduced to the equation to account for dynamic recrystallisation softening; this term is null until a critical (incubation) strain is reached, and is function of the grain boundary velocity and the grain boundary area per unit volume; an evolution equation is proposed for the latter including the contributions of grain nucleation, growth and impingement. Additional secondary phase effects are also considered in the constitutive equations. On the other hand, Cram *et al.* [216, 217] have postulated a polycrystal mean-field model where the evolution of each grain is described and embedded into an average medium, a Rayleigh probability distribution describes the subgrain size patterning, where a critical size for grain nucleation is taken as the condition for grain nucleation. Grain growth evolution is postulated to be proportional to the grain boundary mobility and the difference between the total dislocation density and the dislocation density of the growing grain. The total dislocation density equals the surface-area-weighted dislocation average over all grains. The macroscopic stress is equated to the volume average of the stress over all grains.

Although these methods provide a description of DRX, phenomenological or empirical relations between the internal microstructure evolution and deformation conditions are introduced, and a number of parameters are fitted for each material, impeding their extension to more complex systems.

This chapter extends the approach presented in Chapter 3 to describing the conditions for dynamic recrystallisation and its evolution in pure FCC metals. Dy-

dynamic recrystallisation introduces an additional annihilation term in the Kocks-Mecking equation containing a delay (incubation), which increases as deformation continues. The dynamic recrystallisation coefficient f_{DRX} and critical strain for grain nucleation γ_{DRX}^* are obtained by applying the thermodynamic principles derived Chapter 3 for obtaining the activation energy for grain growth and the favourable energy conditions for grain nucleation. The model is tested for pure copper and nickel, describing well their characteristic stress-strain curves, as well as their steady state flow stress after recrystallisation takes place. The transitions for the occurrence of dynamic recrystallisation as a function of temperature and strain rate for a number of systems are precisely predicted.

6.2 Theory

At high temperatures and/or low strain rates, DRX decreases the dislocation density as dislocation-free grains nucleate and grow from highly dislocated subgrains (cells). This effect induces an additional annihilation term (F) in equation 2.30. An incubation strain γ_{DRX}^* is required for the formation and migration of high-angle grain boundaries (HAGBs) igniting grain nucleation and growth. Figure 6.1 shows a schematic representation of the dynamic recrystallisation process during deformation: (a) The initial state ($\gamma = 0$) has a low dislocation density (ρ_0); (b) plastic deformation takes place under the critical strain at which DRX occurs ($\gamma < \gamma_{DRX}^*$), and subgrains are formed (blue polygons) with dislocations in their interiors; (c) high-angle (sub)grain boundaries are formed in certain sites at $\gamma = \gamma_{DRX}^*$, leading to grain nucleation and growth (red polygons); the new grains contain a very low dislocation density (ρ_{DRX}); it can be assumed that $\rho_{DRX} \sim \rho_0$; (d) as plastic deformation continues ($\gamma > \gamma_{DRX}^*$), the dislocation density inside the grains ρ_{DRX} increases and grain growth continues on heavily deformed regions; ρ_{DRX} replaces ρ at those areas. The Kocks-Mecking equation accounts for the average dislocation density only, and does not distinguish between recrystallised and unrecrystallised regions. To preserve the dependence on a homogeneous dislocation density, the density inside the recrystallised region ρ_{DRX} is postulated to evolve at the same rate than when the material was initially deformed, *i.e.* $\rho_{DRX}[\gamma] = \rho[\gamma - \gamma_{DRX}^*]^1$ [95]. The capacity for dislocation-free grains to occupy the highly deformed matrix is proportional to ρ_{DRX} . Thus, the dislocation annihilation rate due to DRX ($\frac{d\rho_{DRX}}{d\gamma}$) is proportional to ρ_{DRX} , with the proportionality constant f_{DRX} being equal to the capability for recrystallised grains to grow and occupy the deformed regions. Although grain nucleation occurs from local strain concentrations, it is considered that at a macroscopic level, recrystallisation takes place when the overall stored energy reaches a critical

¹[] denotes functional dependence in γ .

value.

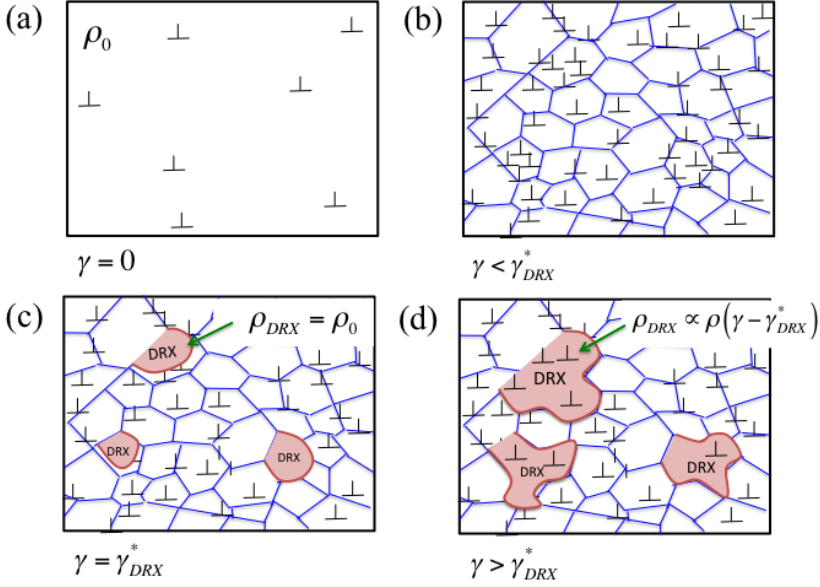


Figure 6.1: Schematic representation of dynamic recrystallisation process: (a) $\gamma = 0$: the material has a low dislocation density (ρ_0); (b) $\gamma < \gamma_{DRX}^*$: subgrains are formed (blue polygons); (c) $\gamma = \gamma_{DRX}^*$: grains nucleate at high-angle (sub)grain boundaries, the dislocation density inside these grains (ρ_{DRX}) is low ($\sim \rho_0$); (d) $\gamma > \gamma_{DRX}^*$: the dislocation density inside these grains (ρ_{DRX}) increases ($\propto \rho[\gamma - \gamma_{DRX}^*]$).

A uniform dislocation density is prescribed by the Kocks–Mecking equation; the development of dislocation density in the recrystallised grains (ρ_{DRX}) is equal to the development of ρ at $\gamma - \gamma_{DRX}^*$. Finally, term (F) in equation 2.30 becomes [95]

$$f_{DRX}\rho_{DRX} = f_{DRX}\rho[\gamma - \gamma_{DRX}^*]. \quad (6.1)$$

Note that this term is active only when $\gamma \geq \gamma_{DRX}^*$.

6.2.1 Dynamic recrystallisation coefficient

The dynamic recrystallisation coefficient measures the capability for recrystallised grains to grow and occupy the deformed regions. Such efficiency can be approximated by the ratio between the potential sites for growth and the number of growing grains N_{growth} (blue polygons in Figure 6.1b). The former is given by

the difference between the total number of subgrains N_{total} from which grain growth could occur, and the number of growing grains N_{growth} (red polygons in Figure 6.1c):

$$f_{DRX} = \frac{N_{total} - N_{growth}}{N_{growth}} = \frac{N_{total}}{N_{growth}} - 1. \quad (6.2)$$

Grain growth is a thermally activated process. N_{growth} can be expressed as [3]:

$$N_{growth} = N_{total} \exp\left(-\frac{Q_{DRX}}{k_B T}\right), \quad (6.3)$$

where Q_{DRX} is the energy barrier and is composed by:

1. The driving force to induce grain boundary motion (E_{disp}); and
2. the strain energy at the boundaries once high-angle grain boundaries form (E_{HAGB}).

The latter reduces the energy barrier to be overcome, as it features as a driving force for grain growth. Q_{DRX} is proportional to the available sites S_{sub} for grain nucleation on preexisting subgrains [77, 203], thus Q_{DRX} becomes:

$$Q_{DRX} = S_{sub}(E_{disp} - E_{HAGB}). \quad (6.4)$$

For coarse-grained materials, it can be assumed that subgrain boundaries are approximated by dislocation cells. Thus, E_{disp} is approximated by the energy induced by moving dislocations on the boundaries (equation 6.5):

$$E_{disp} = n_{GB} \frac{\bar{l}}{b} T \Delta S, \quad (6.5)$$

where n_{GB} is the number of dislocations comprising the boundaries.

The strain energy to drive grain growth is reduced by dynamic recovery, hence E_{HAGB} is proposed to be a fraction λ of the total strain energy stored in the boundaries [3, 116, 216]:

$$E_{HAGB} = n_{GB} \frac{\lambda}{2} \mu b^2 \bar{l}. \quad (6.6)$$

Assuming subgrains of cylindrical shape with diameter and depth equal to d_c , and employing equation 3.45, S_{sub} is equal to the subgrain boundary surface per unit volume per dislocation [77]

$$S_{sub} = \frac{A_{sub}}{V_{sub}} \frac{b}{n_{GB}} = \frac{\pi d_c^2 + 2\pi d_c^2/4}{\pi d_c^3/4} \frac{b}{n_{GB}} = \frac{6}{d_c} \frac{b}{n_{GB}} = \frac{6b}{n_{GB} \kappa_c \bar{l}}, \quad (6.7)$$

where A_{sub} and V_{sub} are the area and volume of a subgrain, respectively.

Combining equations 6.4, 6.5, 6.6 and 6.7, Q_{DRX} is expressed as:

$$Q_{DRX} = S_{sub}(E_{disp} - E_{HAGB}) = \frac{6}{\kappa_c} \left(T\Delta S - \frac{\lambda}{2} \mu b^3 \right). \quad (6.8)$$

Finally, by combining equations 6.2, 6.3 and 6.8, the dynamic recrystallisation coefficient becomes:

$$f_{DRX} = \frac{N_{total}}{N_{growth}} - 1 = \exp \left(\frac{6}{\kappa_c k_B T} \left(T\Delta S - \frac{\lambda}{2} \mu b^3 \right) \right) - 1. \quad (6.9)$$

When $f_{DRX} \leq 0$, no dynamic recrystallisation is present and f_{DRX} is set to zero. Such values are reached at low temperatures and/or high strain rates; the transition ranges are discussed in the following sections.

6.2.2 Critical shear strain for grain nucleation

The onset for dynamic recrystallisation occurs when high-angle grain boundaries (HAGBs) form via the accumulation of dislocations in the boundaries leading to grain nucleation [3]. In analogy to the analysis for cell formation, recrystallisation is considered to start when the stored energy at the boundaries ($E_{sub} = n_{GB} \frac{1}{2} \mu b^2 \bar{l}$) equals the addition of three contributions: (i) the strain energy to nucleate dislocation-free grains (E_{grain}); (ii) the displacement energy for boundary-dislocations to onset grain growth E_{disp} ; and (iii) the equivalent energy of dislocations migrating from the grain interior to the boundaries (E_{int}) [3]:

$$E_{sub} = E_{grain} + E_{disp} + E_{int}. \quad (6.10)$$

If tilt boundaries are initially formed, E_{grain} is approximated by the tilt boundary energy per unit area (equation 2.13) [3] around the area delimited by the boundaries of new grains A_{mig} :

$$E_{grain} = E_{tilt} A_{mig} = \frac{n_{GB} \mu b^2}{2\bar{l}} (b\bar{x}_{grain}), \quad (6.11)$$

where \bar{x}_{grain} represents the boundary length of the cross section of an incipient grain. Note that the average dislocation spacing in the forest (\bar{l}) is considered instead of the average spacing at the boundaries (\bar{l}_w), as the new grains contain a very low density.

E_{int} equals the displacement energy of n_{int} dislocations in the subgrain interiors migrating towards the boundaries [95]:

$$E_{int} = n_{int} \frac{\bar{l}}{b} T\Delta S \quad (6.12)$$

The ratio between n_{int} and n_{GB} can be approximated by taking the ratio between the average dislocation spacing on a dislocation forest (subgrain interiors) and the average cell size (subgrain boundaries):

$$\frac{n_{int}}{n_{GB}} = \frac{\bar{l}}{d_c} = \frac{1}{\kappa_c}. \quad (6.13)$$

Combining the previous expressions, equation 6.10 becomes:

$$\frac{n_{GB}}{2} \mu b^2 \bar{l} = \frac{\bar{x}_{grain} n_{GB} \mu b^3}{2\bar{l}} + n_{GB} \frac{\bar{l}}{b} T \Delta S + n_{int} \frac{\bar{l}}{b} T \Delta S. \quad (6.14)$$

Rearranging the previous expression, the equivalent critical shear strain to initiate DRX is obtained:

$$\gamma_{DRX}^* = \frac{b}{\bar{l}} \bar{x}_{grain} = b \rho \bar{x}_{grain} = 1 - 2 \left(1 + \frac{1}{\kappa_c} \right) \frac{T \Delta S}{\mu b^3}. \quad (6.15)$$

If $\gamma_{DRX}^* \leq 0$, then $\gamma_{DRX}^* = 0$. Once γ_{DRX}^* is reached, the dynamic recrystallisation term $f_{DRX} \rho [\gamma - \gamma_{DRX}^*]$ in equation 2.30 is active for the rest of the deformation process.

6.2.3 Results

The model for recrystallisation is compared with experimental axial stress results obtained from the literature for pure copper and nickel. Terms (A), (E) and (F) are present in equation 2.30. The physical parameters employed in the model have the same values from previous sections and can be found in Appendix A.

The value of λ is assumed to equal 0.6 for all tested materials, indicating that only 60% of the stored energy is required to drive grain growth as dynamic recovery is contributing to the dislocation annihilation process. A justification of this assumption for FCC metals is presented in Section 6.2.6.

Figure 6.2 shows the model results for the stress-strain curves for pure polycrystalline coarse-grain (300 μm) 7N copper deformed at different temperature and strain rate conditions, and their comparison with the experimental results obtained from [218]. The values of $\varepsilon_{DRX}^* = \gamma_{DRX}^*/M$ are shown for each curve. The model results show good agreement in the dynamic recrystallisation onset range and the stress when approaching steady state for strain rates below $2.7 \times 10^{-1} \text{ s}^{-1}$. Above this value, the recrystallisation onset is well predicted, however the experimental measurements show a stronger softening effect. This effect can be due to the presence of impurities, as they affect dramatically the kinetics of dynamic recrystallisation as pointed out by Gao *et al.* [218]. For instance, they found that the difference between the maximum stress for 4N Cu and 7N Cu can be up to

40 MPa when it is deformed at 773 K and at 0.2 s^{-1} and the oscillation behaviour is reduced as the impurity concentration increases. However, the temperature and strain rate dependence of steady state flow stresses during hot deformation for different purities is nearly the same. The incubation strain takes place before reaching the first peak stress as the dislocation density inside the growing grains increases until it equilibrates with the total dislocation density. Moreover, Yamagata *et al.* [219] found that the stress oscillation behaviour also changes as a function of the impurity concentration in pure aluminium. The incorporation of dilute solution concentrations and interstitial atoms into the analysis can also explain dissimilarities between the model results and experiments.

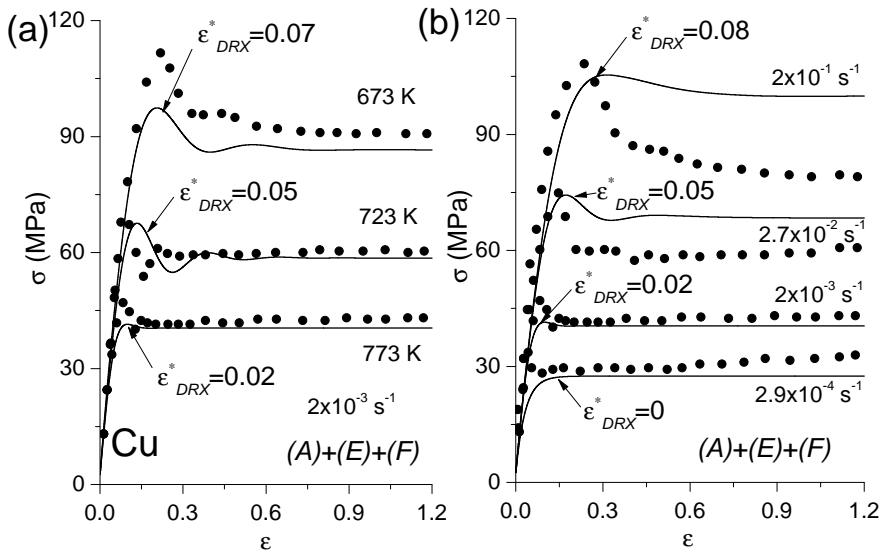


Figure 6.2: Stress-strain curves for 7N Cu deformed at (a) $2 \times 10^{-3} \text{ s}^{-1}$ for different temperatures, and (b) 773 K for different strain rates. Terms (A), (E) and (F) are present in equation 2.30.

Figure 6.3(a) shows the model's steady state stress for Cu of the same purity (7N) and initial grain size, at strain rates spanning four orders of magnitude and at different temperatures. The model results also show good agreement in the saturation stress for different temperatures and strain rates below $2.7 \times 10^{-1} \text{ s}^{-1}$. Above those values the model shows a weaker softening behaviour with respect to the experimental measurements. It is worth noting that no recrystallisation

takes place at stresses above ~ 200 MPa for these deformation conditions (next subsection). Figure 6.3(b) shows the model predictions and their comparison with experimental results for pure polycrystalline nickel with 99.9% of purity and an initial grain size $78 \mu\text{m}$ [220], showing good agreement with experiments.

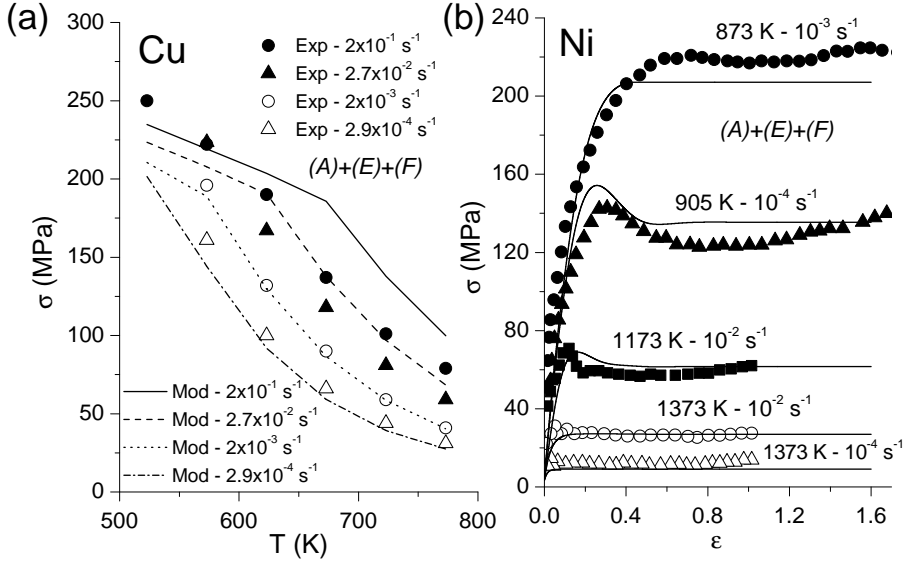


Figure 6.3: (a) Steady state stress for 7N Cu deformed at different temperatures and strain rates. (b) Dynamic recrystallisation evolution in pure nickel. Terms (A), (E) and (F) are present in equation 2.30.

When $\varepsilon_{DRX}^* \sim 0$, the flow stress oscillations disappear. This occurs at higher temperatures and/or lower strain rates (equation 6.15). A physical interpretation of this transition is that the energy required to nucleate dislocation-free grains is very low (equation 6.11) as the grain boundary displacement energy (E_{disp}) increases, provoking grain boundary migration to occur rapidly.

6.2.4 Discussion

The delay term in the Kocks–Mecking equation can induce oscillatory solutions as the eigenvalues of the characteristic equation display complex roots [221]; this depends on the values of γ_{DRX}^* and f_{DRX} . The concept to describe dynamic recrystallisation by using a delay differential equation was first proposed by J. K.

Lee [222]; however, the parameters of the Kocks-Mecking equation (f_{DRX} , f_{DRV} and γ_{DRX}^*) were obtained empirically, and no further physical explanation was supplied. Also, other authors such as Fan and Yang [93] have employed similar delay relations in KM equation.

To illustrate the softening contribution of dynamic recrystallisation in the flow stress response, Figure 6.4 shows a comparison of the model for pure copper including dynamic recovery and recrystallisation (solid lines), and when only dynamic recovery (without stage IV) is considered (dotted lines). At 573 K, the recrystallisation contribution to dislocation annihilation is low ($f_{DRX} = 0.11$) with respect to dynamic recovery ($f_{DRV} = 3.7$). At 673 K, the dynamic recrystallisation contribution increases ($f_{DRX} = 3.47$) and is almost equal than dynamic recovery ($f_{DRV} = 3.9$); the stress reduction due to recrystallisation at the steady state is ~ 75 MPa. At 773 K, dynamic recrystallisation is the dominant softening mechanism ($f_{DRX} = 9.65$) over dynamic recovery ($f_{DRV} = 4.33$); the stress reduction due to recrystallisation at the steady state is ~ 90 MPa.

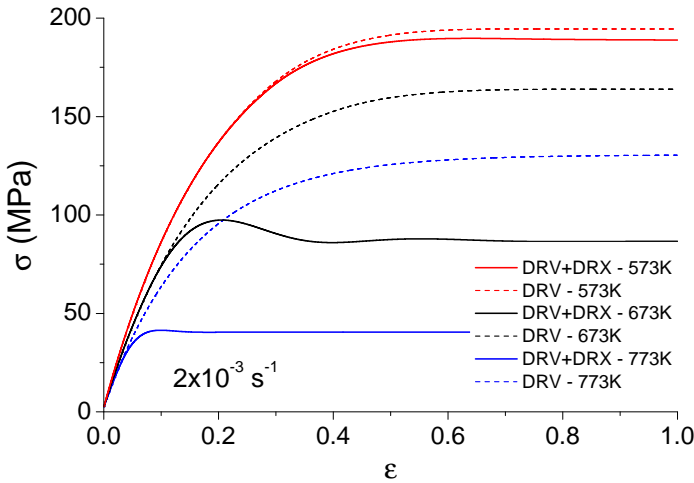


Figure 6.4: Comparison of the DRX and DRV softening effect for various deformation temperatures in copper.

The recrystallisation model describes the evolution of the average dislocation density. However, it cannot reproduce the spatial distribution of the alloy's microstructure in its actual form, such as grain distribution; and no texture evolution can be described. Nevertheless it can be input to other modelling techniques that are able to describe texture variation such as crystal plasticity, as it is able

to describe dislocation evolution for various temperatures, strain rates. Another shortcoming of the model is that the effect of the initial grain size on the critical strain for grain nucleation is not included; only the coarse-grain/single crystal case is described, however grain size refinement increases the grain nucleation rate [3]. This effect can explain discrepancies in the model for pure Cu at higher strain rates, as an additional effect of dislocations being stored at grain boundaries should be incorporated into the entropic term, accounting for the decrease on the dislocation's expected velocity. Additional softening effects may have been ignored. For instance, dislocation mobility is increased when grain growth occurs. These phenomenon induces additional number of microstates in the entropy as well, leading to an increase in the dislocation annihilation rate.

6.2.5 Condition for the occurrence of dynamic recrystallisation

The critical condition for the occurrence of dynamic recrystallisation is $f_{DRX} = 0$ (equation 6.9), which is it satisfied when the temperature, strain rate and solute composition follow the relation (equations 3.12 and 6.8):

$$\dot{\epsilon} = (\dot{\epsilon}_0 + \vartheta) \exp\left(-\frac{\lambda\mu b^3}{2k_B T}\right). \quad (6.16)$$

Figure 6.5 shows the dynamic recrystallisation transition maps for pure (a) copper and (b) nickel, and their comparison with experimental data obtained from the literature. The boundaries are obtained from equation 6.16. The shaded regions represent deformation conditions for the occurrence of DRX and the white regions span the conditions where no recrystallisation takes place. The experimental points were directly measured from the stress-strain curves where the curves fluctuated and/or eventually decreased confirming the occurrence of dynamic recrystallisation [3]. The black dots represent the experiments where dynamic recrystallisation takes place and the white dots represent the experiments where only dynamic recovery occurs. The data for coarse-grained materials were obtained from [123, 223] for polycrystalline copper, from [224] for 6N copper, and from [218] for 7N copper. For pure nickel the data were obtained from [129] for $\langle 111 \rangle$ single crystals, from [225] for polycrystalline nickel with an initial average grain size of 60 μm , from [220, 226] for nickel with 99.9% degree of purity with an initial average grain size of 78 μm . The results show good agreement in the transition regimes for both metals at different deformation conditions.

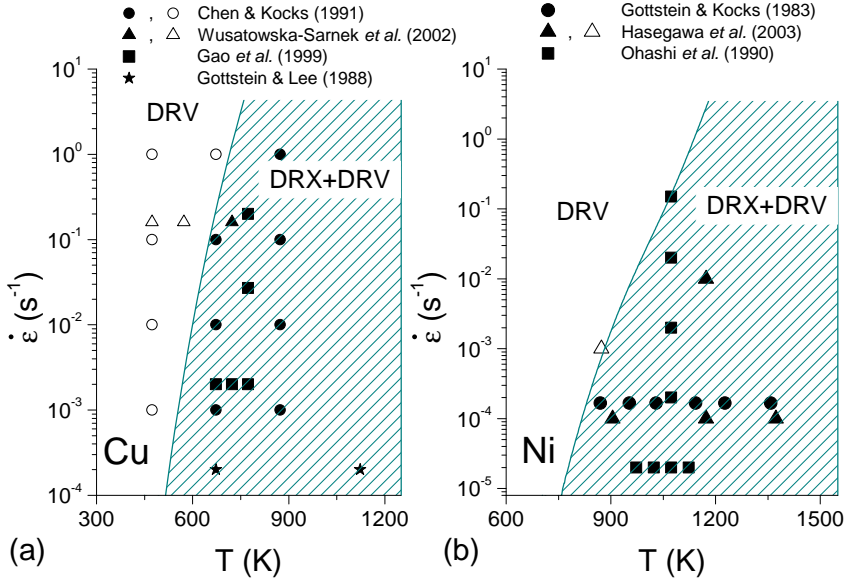


Figure 6.5: Transition map for the occurrence of dynamic recrystallisation and their comparison with experimental results for (a) Cu, and (b) Ni. The experimental data were obtained from [123, 223, 218, 224] and [129, 225, 220, 226] for Cu and Ni, respectively.

6.2.6 Grain boundary mobility

In order to obtain information on the value $\lambda = 0.6$ employed in the model, the strain energy at grain boundaries E_{HAGB} is related to the grain boundary self diffusion energy in this section.

In the classical literature, grain boundary velocity v_{GB} is determined by the grain boundary mobility M_{GB} and the driving force for recrystallisation F via the relation $v_{GB} = M_{GB}F$ [3]. Experimental evidence confirms that grain boundary diffusion and mobility are closely related [31]. Moreover, theoretical descriptions for dynamic recrystallisation include a grain boundary diffusion term to incorporate mobility [216, 93, 77, 203]: $M_{GB} = \alpha_{GB} \frac{\delta D_{GB} V_m}{b^2 RT}$, where α_{GB} is a constant, δ is the grain boundary thickness, V_m is the molar volume, and $D_{GB} = D_{GB}^0 \exp\left(-\frac{Q_D}{RT}\right)$ is the grain boundary diffusivity, where D_{GB}^0 is a pre-exponential factor and Q_D is the boundary self diffusion activation energy. Figure 6.6 shows a comparison between Q_D and the values of the stored energy at grain boundaries \tilde{E}_{HAGB} per

boundary and dislocation (equation 6.6):

$$\tilde{E}_{HAGB} = E_{HAGB} \frac{b}{n_{GB}l} = \frac{\lambda}{2} \mu b^3, \quad (6.17)$$

with $\lambda = 0.6$, for pure (a) Ni and Au, and (b) Cu and Al, for temperature ranges between $0.5T_m$ and T_m . Physical parameters of these materials are shown in Appendix A. For the case of gold, the Burgers vector was obtained from [227] and equals $b_{Au} = 0.288$ nm; the experimental values of shear modulus were obtained from [228] and were adjusted to the formula $\mu_{Au} = (29.57 - 1.3 \times 10^{-3}T - 6.5 \times 10^{-6}T^2)$ GPa. The results are expressed in terms of the homologous temperature $T_h = T/T_m$. The solid lines represent the model calculations and the dotted lines represent the values of Q_D that were obtained from [3, 229, 230, 231]; for the case of Ni, different values for Q_D were found and a region where these values lie is plotted instead in Figure 6.6a. Table 6.1 shows the average values of the energy to drive grain growth per dislocation E_{HAGB}^{av} between $0.5T_m$ and T_m , and the experimental values of Q_D . For high temperature ranges (where dynamic recrystallisation is likely to occur), the model results for the four materials are therefore very close to those values fitted for the grain boundary self diffusion when $\lambda = 0.6$, justifying the use of this parameter.

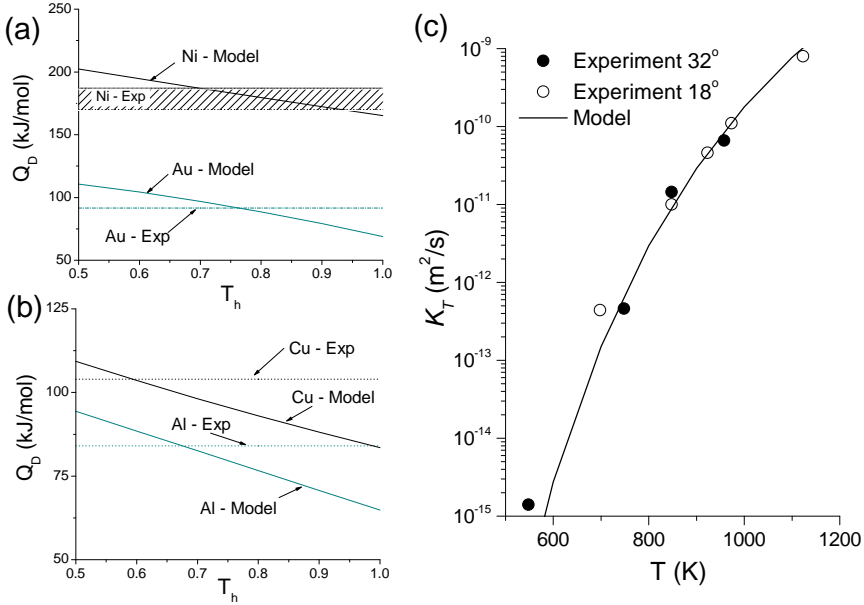


Figure 6.6: Grain boundary self diffusion energy and \bar{E}_{HAGB} with $\lambda = 0.6$ as a function of the homologous temperature ($T_h = T/T_m$) for (a) nickel, gold, (b) copper and aluminium. (c) Boundary displacement constant variation with temperature for misorientations of 18° and 32° for Cu [232].

Table 6.1: Grain boundary self diffusion energy comparison.

Metal	Q_D (kJ/mol)	Ref.	\bar{E}_{HAGB}^{av} (kJ/mol)
Cu	104	[3]	96
Al	84	[3]	79
Ni	170-187	[229, 230]	183
Au	91	[231]	94

On the other hand, Viswanathan and Bauer [232] used a bicrystal technique to measure the mobility of high angle boundaries in 5N copper inducing high misorientation angles of 18° and 32° about a [001] tilt boundary. They found that the grain boundary displacement (a) follows a parabolic relation $a^2 = K_T f(\theta_{GB}) t$, where K_T is a boundary displacement constant that depends on temperature only, $f(\theta_{GB})$ is a magnification function that depends on the misorientation an-

gle θ_{GB} , and t is time. K_T is related to the grain boundary mobility via the relation $K_T = 2M\xi$, where ξ is the surface boundary tension [3, 232]. They found that K_T follows an Arrhenius equation. Thus, K_T is proposed to be:

$$K_T = A \exp\left(-\frac{\tilde{E}_{HAGB}}{RT}\right), \quad (6.18)$$

where A is a material dependent constant that was fitted to 2×10^{-5} m²/s. Figure 6.6c shows the measured values of K_T and their comparison with the model when $\lambda = 0.6$ for different temperatures and misorientation angles. The model shows good agreement with respect to the experimental measurements.

A justification of the value of $\lambda = 0.6$ has been presented, showing that the energy to drive grain growth \tilde{E}_{HAGB} is closely related to grain boundary migration and self diffusion rates, and their respective activation energies [3, 36]. The value of λ remains valid for all the modelled FCC metals; however, it may differ for other crystalline structures.

6.3 Conclusions

An extension of a previous theory describing dynamic recrystallisation in pure FCC metals has been presented. The theory is successful in describing a number of metallurgical parameters essential for dynamic recrystallisation, these include:

1. The incubation strain to initiate dynamic recrystallisation.
2. The grain size of coarse-grain metals at the steady state, which is shown to be dependent on the initial grain size prior to deformation.
3. The oscillations in stress-strain space which appear prior to reaching the steady state.
4. The steady state stress when dislocation generation and annihilation reach equilibrium.
5. The temperature and strain rate dependence of all the above, which allows to create maps for the occurrence of dynamic recrystallisation in strain rate-temperature space.

The statistical entropy accounts for the driving energy for grain boundary migration during grain growth. It was also shown that the stored energy at grain boundaries E_{HAGB} is related to the grain boundary self diffusion energy. Thus, no grain boundary mobility fitting parameters are required. The same set of experimentally determined physical parameters used in previous chapters have been successfully employed in the model validation.

Chapter 7

Application of the theory to multicomponent metals

Multicomponent effects are incorporated to the theory to account for solid solution strengthening, dislocation annihilation, and twinning-induced-plasticity effects. Dislocation pinning around solute atoms offer equivalent dislocation generation terms, and extra slip configurations for the entropy, due to their average velocity reduction. They alter the activation energy barrier for dislocation recovery, grain nucleation and growth; and feature in the interactions with twins. Concentrated solution effects are initially considered in the hot deformation of Ni30Fe, Ni21Cr, Fe30Ni, Fe18Cr8Ni, Fe25Cr20Ni and Ni21Cr8Mo3Nb. The model is extended to describe effects of dilute concentrations of substitutional and interstitial atoms; hot deformation of 15 low alloy steels is described for wide ranges in composition, temperature and strain rate. Maps for dynamic recrystallisation occurrence are defined in terms of loading conditions and composition. An application to describe work hardening of twinning-induced-plasticity steels for different C and Mn concentrations at room temperature is additionally made by combining twinning and solid solution contributions in dislocation generation. Input to the model are only physical parameters and thermodynamic information from well accepted databases.

7.1 Introduction

Extensive experimental and theoretical work has been made to characterise hot deformation and recrystallisation kinetics in steels with different alloying elements [233, 234, 235, 236, 237, 238]. However, microstructural interactions during processing have not been fully understood yet. For instance, carbon-dislocation

interactions in α -iron have been widely explored at various scales. Clouet *et al.* [239] studied carbon atom interactions with screw and edge dislocations by employing the embedded atom method, as well as molecular statics¹ to obtain the binding energy of a carbon atom and a dislocation. They also obtained similar results by employing an elasticity theory model, simplifying the calculations. Kremaszky *et al.* [240] have used the interaction energy between a carbon atom and a dislocation to calculate the diffusion process of carbon atoms to both edge and screw dislocations. They found that the elastic energy of a crystal is reduced by the interaction of carbon atoms with dislocations, which is the driving force for the diffusion of carbon atoms towards dislocations, and the reason for pinning of dislocations by many carbon atoms. Queyreau *et al.* [241] have employed dislocation dynamics simulations for describing dislocation–dislocation interactions in α -iron with small carbon additions. Carbon effects in solid solution are incorporated in a friction stress τ_F , required to trigger dislocation slip. τ_F was fitted for different carbon concentrations. In spite of these findings, limited information is available for carbon and dislocation interactions in γ -iron. On the other hand, modelling techniques to describe low alloy steel’s mechanical response at a macroscopic scale are usually based on semiempirical equations that require constitutive relations, such as the Zener equation, to account for temperature, strain rate and composition effects [234, 235, 242, 243]. Zurob *et al.* [203] have coupled existing models for precipitation, recovery and recrystallisation, with their respective interdependencies, to describe the microstructural evolution for static conditions. All these approaches introduce fitting parameters for each specific steel grade, remaining valid for limited processing and compositional ranges. This impedes their extension to predict new scenarios. This impedes their extension to predict new compositional and heat treatment scenarios.

Another challenge for plasticity theory are high manganese twinning–induced–plasticity (TWIP) steels; these alloys have become one of the most attractive materials for structural applications in automotive industry due to their unique mechanical properties [12]. High manganese steels have low stacking fault energies inducing a high dislocation dissociation rate; as deformation continues, the glide of partial dislocations leads to the formation of twin boundaries, inducing an exceptional work hardening response due to the interaction of dislocations with these barriers. The response of TWIP steels depends on chemical composition, and their behaviour is most interesting for medium and low temperatures, as their processing takes place in these conditions.

This chapter extends the theory previously presented to deformation of single–phase multicomponent FCC alloys by incorporating solid solution effects on dislocation storage and annihilation in Sections 7.2 and 7.3, respectively; the model

¹Molecular statics employs analogous atom interactions than Molecular Dynamics (Section 2.4.1), however only steady state (no time dependency) configurations are analysed.

is validated for several face-centred multicomponent cubic systems with concentrated solutions (3 Fe- and 3 Ni-based alloys) in Section 7.4. The model is then extended to characterise dilute solution effects in work hardening evolution and dynamic recrystallisation kinetics of 15 low-alloy steels in Section 7.5. Results include the variation in composition of five substitutional (Mn, Nb, Si, Cr and Ti) and two interstitial (C and B) solute elements. Finally, combined effects of deformation twinning and solid (dilute and concentrated) solution strengthening are employed in Section 7.6 for describing work hardening behaviour of TWIP steels at room temperature.

7.2 Dislocation generation: $d\rho^+/d\gamma$

For a coarse-grain multicomponent system, the dislocation storage coefficient equals the inverse dislocation mean free path in a pure metal $\Lambda_{dis}^{-1} = k_1\sqrt{\rho}$ (term (A) in equation 2.30), accounting for dislocation-dislocation interactions, as well as for the inverse dislocation mean free path in the presence of solute strengtheners Λ_{SS}^{-1} (term (C) in equation 2.30) [95]:

$$\frac{d\rho^+}{d\gamma} = \frac{1}{b} \left(\underbrace{k_1\sqrt{\rho}}_{(A)} + \underbrace{\frac{1}{\Lambda_{SS}}}_{(C)} \right). \quad (7.1)$$

where the value of k_1 is depicted in equation 2.27.

Substitutional and interstitial atoms induce different dislocation generation rates. Substitutional atoms usually take positions occupied by a solvent atom, whereas interstitials locate in the interspaces of the solvent and/or substitutional lattices, allowing them to move more freely in the crystal lattice. Moreover, in order to reduce the lattice misfit energy, interstitials migrate towards dislocation lines with a higher rate than substitutionals; this is reflected by displaying much higher diffusion rates than substitutional atoms [244]. Thus, a stronger effect from dislocation-interstitial interactions can be expected [244, 245]. Λ_{SS}^{-1} can be divided to include contributions of dislocation pinning around substitutional Λ_{subs}^{-1} and interstitial Λ_{inter}^{-1} atoms [95, 246]:

$$\frac{1}{\Lambda_{SS}} = \underbrace{\frac{1}{\Lambda_{subs}}}_{(C_1)} + \underbrace{\frac{1}{\Lambda_{inter}}}_{(C_2)}. \quad (7.2)$$

7.2.1 Substitutional atoms

A dislocation in a randomly arranged solute configuration is subjected to isotropic interaction forces from its neighbouring atoms [96]. This effect depends on the

solvent–solute mixture arrangement (atomic landscape) in the alloy. By considering dislocation–solute atom interactions to be thermally activated [96], the respective magnitude of the energy barrier for a dislocation to pin around a substitutional is proposed to equal the Gibbs free energy of the alloy (mixture) ΔG_{sys} , accounting for the possible atomic arrangements in the lattice [247]. Λ_{subs} is postulated to be [6, 95]:

$$\Lambda_{subs} = \frac{\lambda_{SS}}{\Phi_{SS}b^3} \exp\left(\frac{\Delta G_{sys}}{RT}\right) \frac{1}{\sqrt{\rho}}, \quad (7.3)$$

where λ_{SS} is a constant, the sign in the exponential formula accounts for the negative values of ΔG_{sys} [247], and

$$\Phi_{SS} = \sum_i x_i/b^3 \quad (7.4)$$

is the solute atom concentration per unit volume, $0 \leq x_i < 0.5$ is the atom fraction of the i solute element; the $1/(\Phi_{SS}b^3)$ factor in equation 7.3 accounts for the solute spacing per unit volume [25]. It follows that $\sum_i x_i + x_{solvent} = 1$, where $x_{solvent}$ is the solvent's concentration. $-\Delta G_{sys}$ represents the free energy barrier for dislocations to interact with solute and solvent atoms, which effect is reduced to solute–dislocation interaction by incorporating the factor $1/(\Phi_{SS}b^3)$ [95]. The previous equation is defined for concentrated solutions, where no special distinction in the spatial arrangement for dislocation–solute interaction is needed. $\Phi_{SS}b^3$ is employed in the following sections (instead of simplifying its value to $\sum_i x_i$), as this parameter is replaced for dilute systems (Section 7.5).

7.2.2 Interstitial atoms

Due to their reduced size, interstitial atoms are located in interstices in the face-centred cubic crystal structures. In the case of C in Fe these are octahedral sites. They tend to diffuse (at a higher rate than substitutionals) into lattice defects offering energetically more favourable sites than those in the undisturbed lattice [97, 245]. In FCC crystal structures, they have a substitutional–like interaction with dislocations, as isotropic (hydrostatic) strains are induced around them [244]. The strain fields around misfitting interstitial atoms interfere with the motion of dislocations; the interaction incidence depends directly on the encountering frequency [96, 245]. Thus, it is proposed that Λ_{inter}^{-1} equals the probability P_{inter} of encountering interstitial atoms (located in interstitial sites) along a given slip direction, multiplied by the inverse dislocation mean free path (in the pure material) to account for the total dislocation encounter frequency [94]. If only carbon is considered, $P_{inter} = x_C^{1/3}$, where x_C is the carbon atom concentration,

and $x_C^{1/3}$ accounts for the interstitial concentration per unit length [25]. Λ_{inter}^{-1} then becomes:

$$\frac{1}{\Lambda_{inter}} = P_{inter} \frac{1}{\Lambda_{dis}} = \frac{x_C^{1/3}}{\Lambda_{pure}}. \quad (7.5)$$

The analysis in the following sections considers carbon effects only. However, other elements can be analysed by adding up their respective concentrations; for instance, if boron is also added, then $P_{inter} = (x_C + x_B)^{1/3}$.

7.3 Dislocation annihilation: $d\rho^-/d\gamma$

This section incorporates multicomponent effects in f_{DRV} , f_{DRX} and γ_{DRX}^* via the number of microstates for dislocation motion (slip+climb), and the solute energy contribution to dislocation annihilation.

Multicomponent statistical entropy

Dislocation slip is altered under the presence of (substitutional and interstitial) solute atoms reducing its expected velocity and increasing the number of microstates (Section 3.2). If independent events are considered, this effect can be incorporated in the total number of microstates Ω (equation 3.11) by a factor $\Omega_{SS} = \Omega_{subs} \cdot \Omega_{inter}$, stemming from the presence of solute atoms [95]. Ω then becomes:

$$\Omega = \Omega_{pure} \cdot \Omega_{SS} = \Omega_{pure} \cdot \Omega_{subs} \cdot \Omega_{inter}. \quad (7.6)$$

Ω_{pure} measures the degrees of freedom due to the possible dislocation paths during deformation in the absence of solute atoms, defining a characteristic number of atoms between a dislocation-slip initial point and N (maximum atomic displacement of a dislocation) [104, 95]. Within this range there will be an average of $n_x = \Phi_{SS} b^3 N = \sum_i x_i N$ substitutional atoms and affecting the slip behaviour in every microstate with respect to pure material case. The number of possible substitutional arrangements amounts to $(\Omega_{pure})^{n_x}$, the total expected substitutional–dislocation interactions of n_x solute atoms within a set of N atoms. This number is normalised by N to account for the effect of n_x per atom, giving the additional degrees of freedom due to substitutional–dislocation interaction Ω_{subs} [95]:

$$\Omega_{subs} = \Omega_{pure}^{\frac{n_x}{N}} = \Omega_{pure}^{N_{subs}} = \Omega_{pure}^{\Phi_{SS} b^3} = \left(\frac{\dot{\epsilon}_0 + \vartheta}{\dot{\epsilon}} \right)^{N_{subs}}, \quad (7.7)$$

where

$$N_{subs} = n_x/N = \Phi_{SS} b^3. \quad (7.8)$$

Dislocation kinetics is severely altered by encountering interstitial barriers in the lattice with respect to the substitutional case. At high temperatures, the high diffusion rate of interstitial atoms allows them to continuously interact with moving dislocations, whereas at lower temperatures, a higher dislocation population can induce interstitial migration towards the dislocation core lines, in spite of the diffusion rate being lower [244]. The probability of a dislocation to encounter one or more interstitials within N atoms (maximum atomic displacement of a dislocation) at a given time and slip direction is $x_C^{1/3} N$. If the N arrangement contains substitutional atoms, they will tend to interact with interstitials, either by attracting or repelling them [248, 249]; carbon atoms migrate towards energetically favourable sites, and additional dislocation–interstitial interactions may occur. Such is obtained by estimating the probability of interstitial and substitutional atoms encountering each other within the N arrangement: $x_C^{1/3} n_x$. Thus, the total expected interstitial–dislocation interactions within a set of N atoms scales with $(\Omega_{pure})^{(x_C^{1/3} N + x_C^{1/3} n_x)}$, where $x_C^{1/3} N$ and $x_C^{1/3} n_x$ account for pure dislocation and substitutional interactions, respectively. Similar to the substitutional case, the previous encounters are normalised by N to account for the configurational effects per atom. Ω_{inter} becomes [246]:

$$\begin{aligned}\Omega_{inter} &= (\Omega_{pure})^{(x_C^{1/3} N + x_C^{1/3} n_x)/N} \\ &= (\Omega_{pure})^{x_C^{1/3} (1 + N_{subs})} = \left(\frac{\dot{\epsilon}_0 + \vartheta}{\dot{\epsilon}} \right)^{x_C^{1/3} (1 + N_{subs})}.\end{aligned}\quad (7.9)$$

Ω_{inter} induces a stronger effect with respect to Ω_{subs} , as Ω_{subs} accounts for the possible atomic arrangements in the lattice affecting dislocation motion, nevertheless remaining *immobile*, whereas Ω_{inter} accounts for the possible dislocation encounters with a number of *moving* interstitials. It is worth noting that this analysis accounts for the possible interactions from a configurational viewpoint, and a further analysis is needed to incorporate solute atom diffusivities.

Combining equations 7.6, 7.7 and 7.9, the statistical entropy under the presence of solute atoms ΔS^{sol} becomes:

$$\Delta S^{sol} = k_B \ln \Omega = k_B \ln \Omega_{pure}^{(1 + x_C^{1/3})(1 + N_{subs})} = k_B \ln \left(\frac{\dot{\epsilon}_0 + \vartheta}{\dot{\epsilon}} \right)^{(1 + x_C^{1/3})(1 + N_{subs})}.\quad (7.10)$$

The statistical entropy for dynamic recovery that incorporates impingement effect becomes (equation 3.26):

$$\Delta S_{DRV}^{sol} = k_B \ln \Omega^N = k_B \ln \left(\frac{\dot{\epsilon}_0 + \vartheta}{\dot{\epsilon}} \right)^{(1 + x_C^{1/3})(1 + N_{subs})N}.\quad (7.11)$$

7.3.1 Multicomponent dynamic recovery

Dislocation mobility is affected by the presence of substitutional atoms, which modify the energy barrier for dislocation annihilation $\langle \Delta G \rangle$, by adding U_{SS} in $\langle \Delta G \rangle$ (equation 3.16) to account for solute-dislocation interactions in the annihilation process [95, 246]. The energy barrier $\langle \Delta G^{sol} \rangle$ then becomes:

$$\langle \Delta G^{sol} \rangle = \frac{b}{l} (U_{form} + U_{mig} + U_{vac} + U_{SS} - T \Delta S_{DRV}^{sol}). \quad (7.12)$$

The energy of a solid solution mixture per unit volume \tilde{U}_{SS} is approximated by the chemical work of solute atoms around a dislocation segment per unit volume [25, 95]:

$$\tilde{U}_{SS} = \frac{1}{b^3} \sum_i x_i \Delta G_{sys}. \quad (7.13)$$

The solute energy contribution around a dislocation segment undergoing annihilation (with volume V_{sys} , equation 3.15) becomes

$$U_{SS} = V_{sys} \tilde{U}_{SS} = l^* l b \sum_i x_i \Delta G_{sys}. \quad (7.14)$$

The velocity of a dislocation is reduced by its possible encounters with moving interstitials. Similar to the effect produced by the number of microstates Ω_{inter} , the velocity for annihilation $\langle v \rangle$ (equation 3.27) is modified to account for its reduction by moving interstitials, which is reflected by $(1 + P_{inter})$ [104, 246]:

$$\left(\frac{\langle v \rangle}{c + c_{int}} \right)^{(1+P_{inter})\mathcal{N}} = \left(\frac{\dot{\epsilon}}{\dot{\epsilon}_0 + \dot{\vartheta}} \right)^{(1+P_{inter})\mathcal{N}} = \exp \left(- \frac{\langle \Delta G^{sol} \rangle}{k_B T} \right). \quad (7.15)$$

The scaling effect in the previous equation is included for interstitials only, as they remain mobile; substitutional interactions with dislocations are accounted in the energy barrier for annihilation (equation 7.12).

Following the same process delineated in Chapter 3, and combining equations 7.12 and 7.15, the dynamic recovery coefficient for multicomponent systems equals²:

$$f_{DRV}^{sol} = \frac{N_A \rho_a b^2 l^* (w_a^{-1}) T \Delta S_{DRV}^{sol}}{\frac{1}{2} \mu b^3 + \sigma_Y A_{act} b^3 + \frac{l^*}{b} \delta (E_f + k_B T \ln c_m) + l^* b^2 \sum_i x_i \Delta G_{sys} - k_B T \ln \left(\frac{\dot{\epsilon}_0 + \dot{\vartheta}}{\dot{\epsilon}} \right)^{\left(1 + \frac{1}{c}\right)\mathcal{N}}} \quad (7.16)$$

²The values of μ , b , c , w_a and ρ_a are weighted with respect to composition. Details of these calculations are presented in the results section.

This equation describes the dynamic recovery rate during deformation in terms of composition, temperature and strain rate. It is expressed in terms of physical parameters that can be directly measured from experiments. Specific formulae of f_{DRV}^{sol} for different cases (concentrated and dilute substitutional, and interstitial solutions) are shown in the following sections.

7.3.2 Multicomponent dynamic recrystallisation

At high temperatures and/or low strain rates, DRX decreases the dislocation density as dislocation-free grains nucleate and grow from highly dislocated subgrains (cells). This effect induces an additional annihilation term in the Kocks–Mecking equation (item F in equation 2.30) equal to $f_{DRX}\rho[\gamma - \gamma_{DRX}^*]$, where f_{DRX} is the dynamic recrystallisation coefficient, and γ_{DRX}^* represents an incubation strain to form high-angle grain boundaries (HAGBs) igniting grain nucleation and growth (Section 6.2). The dynamic recrystallisation coefficient measures the capability for recrystallised grains to grow and occupy the deformed regions (Section 6.2.1). Such efficiency is estimated by the ratio between the potential sites for growth and the number of growing grains. f_{DRX} equals:

$$f_{DRX} = \exp\left(\frac{Q_{DRX}}{k_B T}\right) - 1, \quad (7.17)$$

where Q_{DRX} is the energy barrier for grain growth. It is worth noting that Q_{DRX} also varies with temperature, and the inverse temperature variation for f_{DRX} does not mean that it will be lower at higher temperatures, as Q_{DRX} usually displays stronger temperature variations (See 6.2.4).

For pure materials Q_{DRX} is composed by *i*) the driving force to induce grain boundary motion E_{disp} (proportional to $T\Delta S^{sol}$), and *ii*) the strain energy at the boundaries once high-angle grain boundaries form E_{HAGB} . Multicomponent systems require additional solute-drag energy to be overcome due to the segregation of substitutional (E_{sol}) and interstitial (E_{inter}) atoms into the boundaries [3, 95]. Thus, the energy barrier Q_{DRX}^{sol} becomes:

$$Q_{DRX}^{sol} = S_{sub}(E_{disp} - E_{HAGB} - E_{sol} - E_{inter}), \quad (7.18)$$

where S_{sub} is the subgrain area fraction per unit volume that accounts for the possible sites for grains to grow (equation 6.7).

By defining the volume for boundary–dislocation interaction to be

$$V_{SS} = l^* \bar{l} b, \quad (7.19)$$

where l^* is the dislocation's distortion length ($l^* = 12.5b$), the substitutional-drag energy is equal to the energy of the solution mixture per unit volume (equation 7.13) multiplied by V_{SS} for n_{GB} dislocations at the subgrain boundaries [95]:

$$E_{sol} = -n_{GB} \frac{2\bar{l}}{d_c} V_{SS} \tilde{U}_{SS} = -\frac{2n_{GB} l^* \bar{l} b}{\kappa_c} \tilde{U}_{SS} = -\frac{2n_{GB}}{\kappa_c} l^* \bar{l} b \Phi_{SS} \Delta G_{sys}, \quad (7.20)$$

where the factor \bar{l}/d_c accounts for the fraction of solute atoms arranged in the boundaries, the 2 factor incorporates the drag-effect from adjacent subgrains, and the negative sign accounts for the negative values of ΔG_{sys} .

Interstitial segregation at the boundaries impedes grain boundary migration during dynamic recrystallisation, therefore increasing the energy barrier for grain growth. E_{inter} is given by the grain boundary energy χ_{GB} (to be overcome) on the potential sites for carbon segregation at the boundaries. The latter can be estimated by the probability of dislocations at the boundaries³ encountering an interstitial atom: $2P_{inter}\pi n_{GB}\bar{l}b$, where $\pi n_{GB}\bar{l}$ accounts for the perimeter of a grain (assuming circular shape) and the 2 factor is to account for carbon segregation in both sides of a boundary. E_{inter} then equals [246]:

$$E_{inter} = \chi_{GB} \left(2P_{inter}\pi n_{GB}\bar{l}b \right) = 2\pi n_{GB} x_C^{1/3} \chi_{GB} \bar{l} b. \quad (7.21)$$

Combining equations 6.5, 6.6, 6.7, 7.20, and 7.21, Q_{DRX}^{sol} becomes:

$$\begin{aligned} Q_{DRX}^{sol} &= S_{sub} \left([(1 + N_{subs})(1 + x_C^{1/3})]^{-1} E_{disp} - E_{HAGB} - E_{sol} - E_{inter} \right) \\ &= \frac{6}{\kappa_c} \left([(1 + N_{subs})(1 + x_C^{1/3})]^{-1} T \Delta S^{sol} - \frac{\lambda}{2} \mu b^3 + \frac{2}{\kappa_c} l^* b^2 \Phi_{SS} \Delta G_{sys} - 2\pi x_C^{1/3} \chi_{GB} b^2 \right) \\ &= \frac{6}{\kappa_c} \left(k_B T \ln \left(\frac{\dot{\epsilon}_0 + \vartheta}{\dot{\epsilon}} \right) - \frac{\lambda}{2} \mu b^3 + \frac{2}{\kappa_c} l^* b^2 \Phi_{SS} \Delta G_{sys} - 2\pi x_C^{1/3} \chi_{GB} b^2 \right). \end{aligned} \quad (7.22)$$

where the factor $[(1 + N_{subs})(1 + x_C^{1/3})]^{-1}$ is to neglect dislocation self-interactions, as the boundaries become the main dislocation attractors [95, 246].

Finally, by combining equations 7.17 and 7.22, the dynamic recrystallisation coefficient for multicomponent systems f_{DRX}^{sol} becomes:

$$f_{DRX}^{sol} = \exp \left(\frac{6}{\kappa_c k_B T} \left(k_B T \ln \left(\frac{\dot{\epsilon}_0 + \vartheta}{\dot{\epsilon}} \right) - \frac{\lambda}{2} \mu b^3 + \frac{2}{\kappa_c} l^* b^2 \Phi_{SS} \Delta G_{sys} - 2\pi x_C^{1/3} \chi_{GB} b^2 \right) \right) - 1. \quad (7.23)$$

When $f_{DRX}^{sol} \leq 0$, no dynamic recrystallisation is present and f_{DRX}^{sol} is set to zero. Once again, this equation describes the annihilation rate due to dynamic recrystallisation in terms of alloy's composition, temperature and strain rate. Besides λ , no fitting parameters are required. A justification of $\lambda = 0.6$ for pure FCC metas was shown in Section 6.2.5.

³Grain boundaries are considered to be formed by dislocation arrangement.

7.3.3 Multicomponent critical strain for grain nucleation

The onset for dynamic recrystallisation occurs when high-angle grain boundaries (HAGBs) form via dislocation storage [3]. Recrystallisation, via grain nucleation, is considered to start when the stored energy at the boundaries E_{sub} equals the addition of [95]: (i) the strain energy to nucleate dislocation-free grains E_{grain} (equation 6.11); (ii) the displacement energy for boundary-dislocations to onset grain growth E_{disp} (equation 6.5); and (iii) the equivalent slip energy of dislocations migrating from the grain interior to the boundaries E_{int} for HAGB formation, where n_{int} is the number of dislocations in the subgrain interiors [116]). The presence of solute atoms induces additional solute-drag energy terms that contribute to E_{sub} . When a grain boundary tries to migrate away from the particles, the local energy increases and drag is forced on the boundary [244]. For substitutional atoms, this term equals E_{sol} (equation 7.20) [95]. On the other hand, Ushioda *et al.* [250] have found that the nucleation rate of recrystallisation increases with carbon concentration, and an additional interstitial-drag energy E_{inter} is also required. Thus, the energy balance becomes [95, 246]:

$$E_{sub} + 9E_{inter} + E_{sol} = E_{grain} + E_{disp} + E_{int}, \quad (7.24)$$

where 9 in E_{inter} represents the number of directions for interstitial atoms to interact with subgrain boundaries⁴.

Rearranging the previous expressions and following the same process delineated in Chapter 6, the critical strain for grain nucleation becomes [246]:

$$\gamma_{DRX}^* = b\rho\bar{x}_{grain} = 1 - \frac{4\bar{l}\Phi_{SS}V_{SS}\Delta G_{sys}}{d_c\mu b^3} + \frac{36\pi x_C^{1/3}\chi_{GB}}{\mu b} - 2\left(1 + \frac{1}{\kappa_c}\right)\frac{T\Delta S^{sol}}{\mu b^3}. \quad (7.25)$$

If $\gamma_{DRX}^* \leq 0$, then $\gamma_{DRX}^* = 0$.

7.3.4 Condition for the occurrence of dynamic recrystallisation

The critical condition for the occurrence of dynamic recrystallisation is $f_{DRX}^{sol} = 0$ (equation 7.23), which is satisfied when the temperature, strain rate and solute composition follow the relation (equation 7.22):

$$\dot{\epsilon} = (\dot{\epsilon}_0 + \vartheta) \exp\left(-\frac{\frac{\lambda}{2}\mu b^3 - \frac{2}{\kappa_c}l^*b^2\Phi_{SS}\Delta G_{sys} + 2\pi x_C^{1/3}\chi_{GB}b^2}{k_B T}\right). \quad (7.26)$$

⁴If a FCC unit cell is considered, there are 3 adjacent directions in a slip line where interstitials can be allocated. There are 3 possible forms to orient these directions. Thus, there are 9 possible adjacent directions for interstitials to interact with a dislocation on a given slip direction.

7.3.5 Physical parameters estimation

In order to obtain the physical input parameters of each alloy, a mixture rule is used for b , c , ρ_a , w_a and μ [61, 109]:

$$P = (1 - \sum_i x_i)P_{(1-\sum_i x_i)} + \sum_i x_i P_{x_i}, \quad (7.27)$$

where P_{x_i} and x_i represent the physical parameter and composition values of the i -th element⁵, respectively. Appendix A shows the values of the physical parameters of pure materials. It is worth noting that if $\sum_i x_i = 0$, the original expressions for pure metals are recovered [104, 109].

The model is tested against experimental data obtained from the literature in the form of the stress-strain curves for 6 different alloys, deformed at intermediate ($T_0 < T < T_f$) and high ($T > T_f$) temperatures. Table 7.1 shows the chemical composition of each alloy and their designations. For numerical modelling effects, elemental contents lower than 3 wt% are ignored, leading to 3 binary, 2 ternary and 1 quaternary alloy systems presented in this chapter. Carbon effects are not included in this analysis as values for the grain boundary energy were not found for these alloys. Dilute solutions and interstitial effects are considered in following sections.

Table 7.1: Alloy composition in weight percent.

Alloy name	Composition (wt%)	Reference
Ni30Fe	Ni-30Fe	[251]
Ni21Cr	Ni-21Cr-1.1Si-0.75Fe-0.31Al-0.08Ti-0.35Cr-0.05C	[252]
		[253]
Fe30Ni	Fe-30.3Ni-1.67Mn-1.51Mo-0.19Si-0.092C-0.009P-0.003S	[254]
Fe18Cr8Ni	Fe-18.09Cr-8.35Ni-0.15Cu-0.13Mo-0.95Mn-0.7Si-0.058C	[255]
Fe25Cr20Ni	Fe-25Cr20Ni-2.05Si-0.1Mn-0.17Al-0.12C-0.014P-0.014S	[256]
Ni21Cr8Mo3Nb	Ni-21.32Cr-8.58Mo-3.73Nb-	[257]
	0.11Fe-0.01Mg-0.18Al-0.16Ti-0.04Mn-0.09Si-0.053C	

The free energy values were obtained from Thermocalc software and were adjusted to polynomial expressions to simplify calculations. The corresponding correlation coefficient R^2 was in all cases greater or equal than 0.98. Table 7.2 shows the Gibbs free energy expressions as well as the temperature range (T_{range}) where the values were taken from.

⁵weighted contributions are computed expressing x_i in atom fraction

Table 7.2: Free energy expressions.

Alloy	ΔG_{sys} (kJ/mol)	T_{range} (K)
Ni70Fe	$-(5.17 + 0.023T + 2.34 \times 10^{-5}T^2)$	773-1373
Ni21Cr	$-(2.08 + 0.031T + 1.9 \times 10^{-5}T^2)$	500-1173
Fe70Ni	$-(9.61 + 0.043T + 1.5 \times 10^{-5}T^2)$	973-1323
Fe18Cr8Ni	$-(1.69 + 0.013T + 3.1 \times 10^{-5}T^2)$	573-1223
Fe25Cr20Ni	$(4.73 - 0.034T - 2 \times 10^{-5}T^2)$	1073-1573
Ni21Cr8Mo3Nb	$-(4.255 + 0.024T + 2.2 \times 10^{-5}T^2)$	1173-1473

Table 7.3 shows the additional physical parameters employed in the model. The yield stress was measured directly from the experimental flow stress-curves and expressed analytically to simplify calculations and to estimate the values of T_f [109]; the stacking fault energy was obtained from the literature; the vacancy formation and migration energies were adjusted as no values were found in the literature, except for the Ni30Fe alloy. The melting point was obtained from Thermocalc.

Table 7.3: Alloy physical parameters.

Alloy	χ (mJ/m ²)	Ref	E_f (kJ/mol)	E_m (kJ/mol)	Ref
Ni30Fe	63	[258]	154.35	106.05	[259]
Ni21Cr	55	[260]	154.35	74.2	-
Fe30Ni	23	[258]	165	125.7	-
Fe18Cr8Ni	21	[260]	154.4	96.5	-
Fe25Cr20Ni	38	[260]	168.8	93.9	-
Ni21Cr8Mo3Nb	35	[261]	144.7	101.3	-

Alloy	T_m (K)	T_f (K)	σ_Y (MPa)
Ni30Fe	1731	1074	$0.46T - 2.5 \times 10^{-4}T^2 - 112$
Ni21Cr	1693	854	$397 - 0.19T$
Fe30Ni	1716	1270	$301 - 0.175T$
Fe18Cr8Ni	1730	1055	$-282.9 + 1.185T - 7.4 \times 10^{-4}T^2$
Fe25Cr20Ni	1690	995	$112 - 0.05T$
Ni21Cr8Mo3Nb	1560	1105	$1948 - 2.316T + 6.9 \times 10^{-4}T^2$

The value of λ_{SS} was fixed to 1.6×10^4 for all materials in the following sections [95]. The vacancy concentration at the melting point is estimated from the formula $c_m = \exp(\Delta S_{form}/R) \exp(-E_f/RT_m)$ [156], where ΔS_{form} is the vacancy formation entropy and $\Delta S_{form}/R \simeq 1.5$ [156].

7.4 Results

The same procedure outlined in previous chapters is followed: the average dislocation density is estimated with the multicomponent Kocks–Mecking equation when concentrated substitutional concentrations are being considered:

$$\frac{d\rho[\gamma]}{d\gamma} = \frac{1}{b}(k_1 + k_{SS})\sqrt{\rho[\gamma]} - f_{DRV}^{sol}\rho[\gamma] - f_{DRX}^{sol}\rho[\gamma - \gamma_{DRX}^*], \quad (7.28)$$

where the values of k_{SS} , f_{DRV}^{sol} , f_{DRX}^{sol} and γ_{DRX}^* become [95]:

$$\begin{aligned} k_{SS} &= \frac{\sum_i x_i}{16,000} \exp\left(-\frac{\Delta G_{sys}}{RT}\right), \\ f_{DRV}^{sol} &= \frac{N_A \rho_a b^2 l^* (w_a^{-1})(1 + \sum_i x_i) \mathcal{N} k_B T \ln\left(\frac{\dot{\epsilon}_0 + \vartheta}{\dot{\epsilon}}\right)}{\frac{1}{2} \mu b^3 + \sigma_Y A_{act} b^3 + \frac{l^*}{b} \delta (E_f + k_B T \ln c_m) + \frac{l^*}{b} \sum_i x_i \Delta G_{sys} - k_B T \ln\left(\frac{\dot{\epsilon}_0 + \vartheta}{\dot{\epsilon}}\right)^{\mathcal{N}}}, \\ f_{DRX}^{sol} &= \exp\left(\frac{6}{\kappa_c k_B T} \left(k_B T \ln\left(\frac{\dot{\epsilon}_0 + \vartheta}{\dot{\epsilon}}\right) - 0.3 \mu b^3 + \frac{2l^*}{\kappa_c} \sum_i x_i \Delta G_{sys}\right)\right) - 1, \\ \gamma_{DRX}^* &= 1 - \frac{4l^*}{\kappa_c \mu b^3} \sum_i x_i \Delta G_{sys} - 2 \left(1 + \frac{1}{\kappa_c}\right) \left(1 + \sum_i x_i\right) \frac{k_B T \ln\left(\frac{\dot{\epsilon}_0 + \vartheta}{\dot{\epsilon}}\right)}{\mu b^3}. \end{aligned} \quad (7.29)$$

At large deformations stage IV takes place and the dislocation density is obtained with equation 3.71 (Section 3.3.4). If DRX takes place, stage IV is not considered. The flow stress response equals [76]: $\sigma = \sigma_Y + \alpha M b \mu \sqrt{\rho}$, where σ_Y accounts for the onset of plastic deformation (friction stress present due to solid solution strengthening).

Figures 7.1(a) and (c) show the model results and their comparison with the experimental values for coarse grained (200 μm) Ni30Fe alloy deformed at different temperatures and strain rates. Stage IV takes place after $\epsilon \simeq 0.3$ when the material is deformed at 973 and 1073 K and at 0.7 s^{-1} ; dynamic recrystallisation occurs for temperatures above 1073 K, except when it is deformed at 70 s^{-1} . The model shows good agreement with experimental results, except for $\dot{\epsilon} = 70 \text{ s}^{-1}$. Suh *et al.* [262] have reported the average cell size for this alloy with an initial grain size of 140 μm and $\epsilon = 2.3$, $T = 1073 \text{ K}$ at $\dot{\epsilon} = 0.1$ and $\dot{\epsilon} = 10 \text{ s}^{-1}$ to equal to 0.9 and 0.6 μm , respectively, whereas the model predicts an average cell size of 1.2 and 0.6 μm for the same deformation conditions, being in good agreement with the reported measurements. Figures 7.1(b), (d), and (f) show the model results and a comparison to experiments for polycrystalline Fe30Ni with an average grain size of 120 μm deformed at different temperatures and strain rates. Stage IV occurs when the material is deformed at 1123 K and 10 s^{-1} , whereas recrystallisation

occurs above this temperature and below this strain rate. The model is in good agreement with experimental values, except for temperatures above 1223 K at 0.1 s^{-1} , where the experiments show a stronger softening effect. Figure 7.1(e) shows the model results and a comparison with experiments for polycrystalline Fe18Cr8Ni (304 Austenitic stainless steel) with an average grain size of $25 \mu\text{m}$ for different temperatures, deformed at $\dot{\epsilon} = 8 \times 10^{-4} \text{ s}^{-1}$. The model shows good agreement with respect to experimental data. Belyakov *et al.* [255] conclude that when the alloy is deformed at 1023 K, dynamic recrystallisation is already present, whereas the model predicts the occurrence of dynamic recrystallisation after 973 K. This minute difference can be due to the grain size effect has been ignored in the present model.

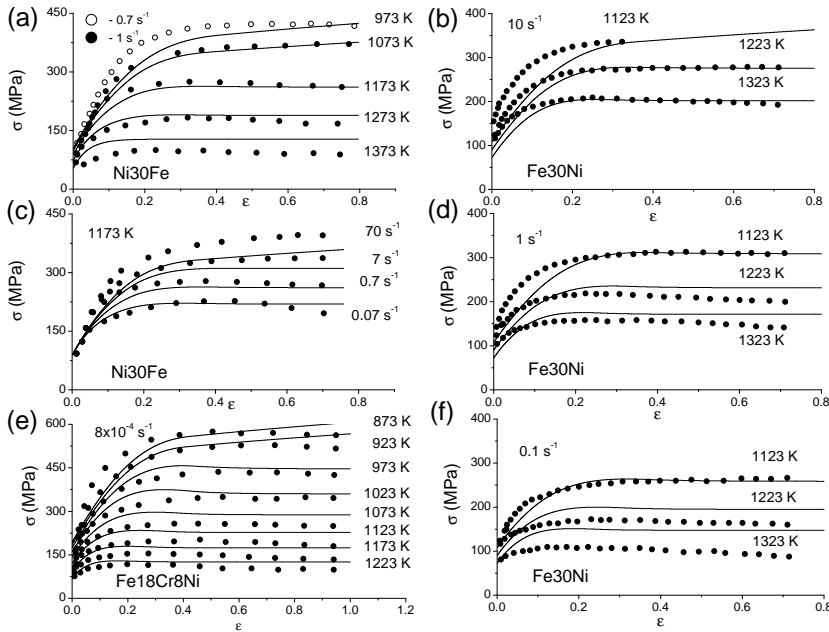


Figure 7.1: Stress-strain curves for Ni30Fe (a) and (c); Fe30Ni (b), (d) and (f); and (e) Fe18Cr8Ni. The solid lines represent the model results and the dots represent the experimental data.

Figures 7.2(a) and (c) show the model results and their comparison with experimental curves for polycrystalline Fe25Cr20Ni deformed at different temperatures and strain rates. Dynamic recrystallisation is already present for all deformation conditions. At higher temperatures, the model shows a discrepancy of $\sim 50 \text{ MPa}$; this difference can be due to the value of the yield stress formula employed in the

model being higher than experimental measurements. Figure 7.2(b) shows the model and experimental results for a Ni21Cr alloy with an average grain size of $80\ \mu\text{m}$ deformed at different temperatures and at $\dot{\epsilon} = 7 \times 10^{-4}\ \text{s}^{-1}$. The model shows good agreement with the experimental stress-strain curves. Moreover, Dudova *et al.* [252] report the occurrence of dynamic recrystallisation of this alloy to be between 873 and 973 K, and the model predicts the occurrence of dynamic recrystallisation between 873 and 923 K, in precise agreement with the experimental ranges. Figure 7.2(d) shows the model results and their comparison with the experimental data for a Ni21Cr8Mo3Nb alloy (Inconel 625) with an average grain size of $81\ \mu\text{m}$ deformed at different temperatures and at $\dot{\epsilon} = 0.1\ \text{s}^{-1}$. The model shows good agreement for strains below 0.3 and temperatures above 1273 K; beyond this strain, the experimental data show additional softening kinetics. At lower temperatures the experiments show a higher work-hardening rate. These discrepancies can be due to the presence of carbides and precipitates as well as the grain size effect, as pointed out by Guo *et al.* [257]; those effects are not included in the present calculations. Nevertheless, they concluded that dynamic recrystallisation occurs at 1223 K (when deformed at $\dot{\epsilon} = 0.1\ \text{s}^{-1}$), whereas the model results show that dynamic recrystallisation is already present at the same temperature for such strain rate. Experimental conclusions on the dynamic recrystallisation occurrence from the previous results were usually depicted by direct microstructural observations on the deformed samples.

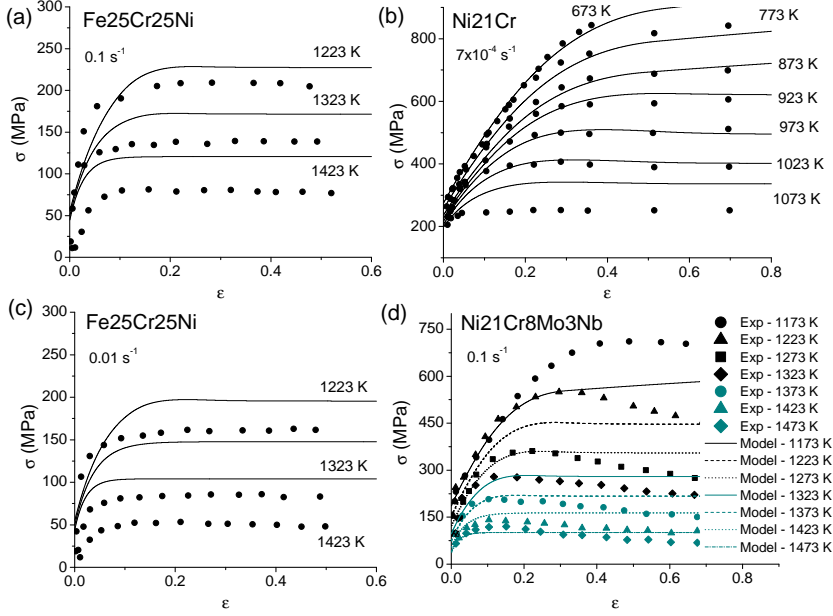


Figure 7.2: Stress-strain curves for the (a), (c) Fe25Cr25Ni, (b) Ni21Cr, and (d) Ni21Cr8Mo3Nb alloys deformed at different temperatures. The solid lines represent the model results and the dots represent the experimental data.

7.4.1 Design for dynamic recrystallisation

Figure 7.3 shows the transition maps for the occurrence of DRX for (a) Ni21Cr and (b) Ni21Cr8Mo3Nb, and their comparison with experimental results in terms of temperature and strain rate, showing the regions where recrystallisation takes place and when only dynamic recovery is present. For concentrated effects, the limits where DRX occurs are depicted by the equation:

$$\dot{\epsilon} = (\dot{\epsilon}_0 + \vartheta) \exp \left(- \frac{0.3\mu b^3 - \frac{2l^*}{\kappa_c} \sum_i x_i \Delta G_{sys}}{k_B T} \right). \quad (7.30)$$

Good agreement is shown for both alloys.

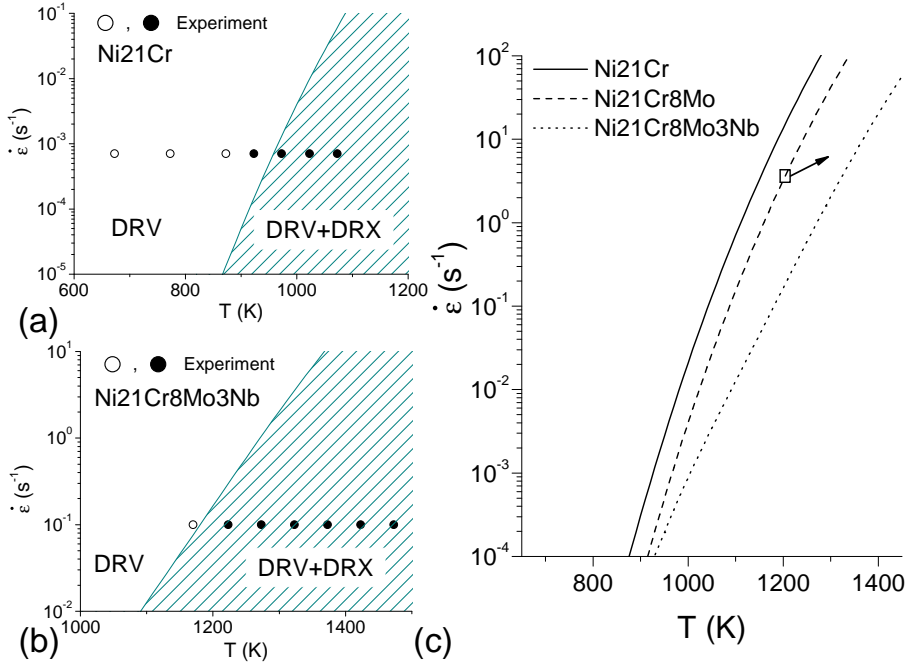


Figure 7.3: Transition map for the occurrence of dynamic recrystallisation and their comparison with experimental results for (a) Ni21Cr, (b) Ni21Cr8Mo3Nb alloys; and (c) a comparison of three Ni-based alloys.

To illustrate the use of this theory to design new alloys, the problem of increasing the temperature for the occurrence of DRX is considered in Figure 7.3c. This shows the transition limits (equation 7.30) for the previous alloys plus the addition of a hypothetical grade with composition Ni21Cr8Mo (wt%). The values of b , μ and c were obtained using equation 7.27; the values for E_m and σ_Y for this alloy were taken from Ni21Cr, as no experimental data were found in the literature, and the values of ΔG_{sys} and $T_m = 1660$ K were obtained from ThermoCalc and adjusted to the analytical expression ($R^2 = 0.99$): $\Delta G_{sys}^{Ni21Cr8Mo} = -(0.76 + 0.027T + 2.1 \times 10^{-5}T^2)$ kJ/mol. As κ_c depends on strain rate, in order to simplify the calculations in this case, it is fixed to be 20 for the three alloys [116]. For strain rates above 10^{-3} s^{-1} , the model shows an increase in the recrystallisation onset temperature of ~ 55 K when 8 wt% of molybdenum is incorporated to the Ni21Cr alloy, and a further increase of ~ 110 K if 3.7 wt% of niobium is additionally incorporated. The onset of recrystallisation of Ni21Cr alloy is increased by ~ 165

K if both 8Mo and 3.7Nb (wt%) are added.

7.5 Dilute concentrations: Application to low alloy steels

For moderate concentrations, a dislocation in a randomly dispersed substitutional solute atom field is subjected to interaction forces from the nearest effective solute atoms, experiencing repulsive or attractive forces. This effect depends on the solvent-solute mixture arrangement (atomic landscape) in the alloy, and no special distinction was considered. However, at low concentrations, a dislocation encounters only discrete and spread opposing obstacles (solute atoms), and their interaction becomes similar to the non-deformable particles case (*e.g.* precipitates acting as dislocation pins)[96, 27]. This strengthening effect is related to the ability of dislocations to bow around the particles, depending on the average particle spacing only, instead of spatial distributions [96]. A similar case occurs for grain boundaries [3]. Thus, it is proposed that linear encounters between substitutional atoms and dislocations are responsible for the strengthening and annihilation process, other than describing volumetric interactions in the inverse dislocation mean free path (Λ_{subs}), dislocation motion (N_{subs}), and effective volume for solute-drag grain boundary interaction (V_{SS}): Φ_{SS} (solute concentration per unit volume) is replaced by the solute concentration per unit length [25]

$$\psi_{SS} = \sum x_i^{1/3}/b, \quad (7.31)$$

with their respective volume/length modifications in Λ_{subs} and N_{subs} . This intensifies solute contributions when a discrete number of pinning obstacles are available. Table 7.4 shows the terms that are modified for concentrated and dilute solutions. On the other hand, for a given concentration x_j of substitutional j , the volume V_{SS}^j spanning the possible encounters of x_j atoms with subgrain boundaries equals the mean solute spacing in two dimensions $(b/x_j^{1/3})^2$ (accounting for the surface extension of substitutional atoms), multiplied by half the subgrain size $d_c/2$, where the 2 factor accounts for shared interactions in adjacent boundaries. The drag effect of element j in E_{sol} is reflected by the term $\tilde{U}_{SS}^j = -\frac{x_j}{b^3}\Delta G_{sys}$ (equation 7.13); then E_{sol} equals the contribution of all substitutional atoms:

$$E_{sol} = -\frac{2\bar{l}}{d_c} \sum_i V_{SS}^i E_{sol}^i = -\frac{\bar{l}}{b} \sum_i x_i^{1/3} \Delta G_{sys}. \quad (7.32)$$

Table 7.4: Concentrated *vs.* dilute solution effects.

Eq.	Param.	Concetrated	Dilute	Description
7.3	k_{SS}	$\frac{\Phi_{SS} b^3}{16000} \exp\left(-\frac{\Delta G_{sys}}{RT}\right)$	$\frac{\psi_{SS} b}{16000} \exp\left(-\frac{\Delta G_{sys}}{RT}\right)$	Dislocation mean free path in the presence of substitutional atoms
7.8	N_{subs}	$\Phi_{SS} b^3$	$\psi_{SS} b$	Additional number of microstates (interactions) for dislocation motion
7.19	V_{SS}	$l^* \bar{l} b$	$V_{SS}^j = \frac{d_c b^2}{2x_j^{2/3}}$	Solute-drag volume around subgrain boundaries
7.32	E_{sol}	$-n_{GB} \frac{2l^* \bar{l}}{d_c b} \sum_i x_i \Delta G_{sys}$	$-n_{GB} \frac{\bar{l}}{b} \sum_i x_i^{1/3} \Delta G_{sys}$	Solute-drag boundary energy

The previous modifications follow the assumption that particle spacing is more relevant than spatial distributions for low solute concentrations [96]. These are simple representations, as a detailed analysis in dislocation–solute atom behaviour is complex, and quantitative information (from physics–based descriptions) in their effect on work hardening and dynamic recrystallisation is not available yet.

7.5.1 Experimental procedure

Four different steels (Steels A–D) were subjected to uniaxial compression tests for temperatures and strain rates in the range of 850–950 °C and 0.01–1 s^{−1}, respectively. Table 7.5 shows the chemical composition of each alloy and its designation. The materials were provided by ArcelorMittal Maizières. The samples were austenitized at 1423 K for 120 s. Following this, they were cooled at rates of 20 K/s to the deformation temperature, and held for 30–45 s. Finally, the samples were subjected to uniaxial compression of up to a true strain of 0.7. This process was performed in a Gleeble 1500 thermomechanical simulator. The dimensions of the samples were of diameter and length 10 mm and 12 mm, respectively.

Experimental information on the stress–strain curves for 9 low–alloyed steels (Steels E–N) were additionally provided by ArcelorMittal Maizières to analyse the effect of six elements (C, Mn, Nb, Si, Cr, Ti). Their chemical composition and commercial designation is given in Table 7.5. The range of deformation temperatures and strain rates was 850–1050 °C, and 0.1–100 s^{−1}, respectively. In addition to these data, experimental information for two low–alloyed steels was obtained from the literature to observe boron effects on dynamic recrystallisation [263]. Table 7.5 shows the chemical composition of these alloys referred to as Steel N and O, respectively.

Table 7.5: Tested alloys. Chemical compositions are shown in weight percent.

No.	Steel	C	Mn	Nb	Si	Cr	Ti	B
1	A	0.1	2	0	0	0	0	0
2	B	0.1	2	0.03	0	0	0	0
3	C	0.1	2	0.07	0	0	0	0
4	D	0.1	1	0.07	0	0	0	0
5	E	0.002	0.208	0	0.004	0.017	0	0
6	F	0.002	0.123	0.016	0.005	0.019	0.015	0
7	G	0.004	0.195	0	0.124	0.025	0.002	0
8	H	0.054	1.18	0	0.125	0.465	0	0
9	I	0.055	0.362	0.055	0.013	0.025	0.001	0
10	J	0.080	1.48	0.063	0.029	0.020	0.002	0
11	K	0.185	1.66	0.001	1.605	0.033	0.003	0
12	L	0.210	1.44	0.002	0.22	0.018	0.001	0
13	M	0.385	0.673	0	0.203	0.269	0.001	0
14	N	0.04	1.46	0	0.354	0	0	0.003
15	O	0.04	1.46	0	0.354	0	0	0.010

7.5.2 Results

For this case, dilute substitutional and interstitials concentrations are considered; the evolution equation becomes [246]:

$$\frac{d\rho[\gamma]}{d\gamma} = \frac{1}{b}((1+x_C^{1/3})k_1 + k_{SS})\sqrt{\rho[\gamma]} - f_{DRV}^{sol}\rho[\gamma] - f_{DRX}^{sol}\rho[\gamma - \gamma_{DRX}^*], \quad (7.33)$$

with:

$$\begin{aligned} k_{SS} &= \frac{\sum_i x_i^{1/3}}{16,000} \exp\left(-\frac{\Delta G_{sys}}{RT}\right), \\ f_{DRV}^{sol} &= \frac{N_A \rho_a b^2 l^* (w_a^{-1})(1+x_C^{1/3})(1+\sum_i x_i^{1/3}) \mathcal{N} k_B T \ln\left(\frac{\dot{\epsilon}_0 + \dot{\theta}}{\dot{\epsilon}}\right)}{\frac{1}{2}\mu b^3 + \sigma_Y A_{act} b^3 + \frac{l^*}{b} \delta (E_f + k_B T \ln c_m) + \sum_i x_i \Delta G_{sys} - k_B T \ln\left(\frac{\dot{\epsilon}_0 + \dot{\theta}}{\dot{\epsilon}}\right) (1+x_C^{1/3})^{\mathcal{N}}}, \\ f_{DRX}^{sol} &= \exp\left(\frac{6}{\kappa_c k_B T} \left(k_B T \ln\left(\frac{\dot{\epsilon}_0 + \dot{\theta}}{\dot{\epsilon}}\right) - 0.3\mu b^3 + \sum_i x_i^{1/3} \Delta G_{sys} + 2\pi x_C^{1/3} \chi_{GB} b^2\right)\right) - 1, \\ \gamma_{DRX}^* &= 1 - \frac{2}{\mu b^3} \sum_i x_i^{1/3} \Delta G_{sys} + 36\pi x_C^{1/3} \frac{\chi_{GB} b^2}{\mu b^3} - \left(1 + \frac{1}{\kappa_c}\right) \frac{2k_B T}{\mu b^3} \ln\left(\frac{\dot{\epsilon}_0 + \dot{\theta}}{\dot{\epsilon}}\right) (1+x_C^{1/3})(1+\sum_i x_i^{1/3}), \end{aligned} \quad (7.34)$$

where $\sum_i x_i^{1/3}$ represents the sum of the atom concentrations of Mn, Nb, Si, Cr and Ti, respectively. An initial dislocation density of 10^{11} m^{-2} was considered for

all cases. The flow stress response is described by employing the Taylor equation: $\sigma = \sigma_Y + 0.3M\mu b\sqrt{\rho}$. At large deformations stage IV of deformation is present. If DRX takes place, stage IV is not considered.

The physical parameters employed in the present model are shown in Appendix A, they were all obtained from the literature, except for the vacancy formation and migration energies for γ -iron, whose values were fitted to $E_m = 1.28$ eV and $E_f = 1.6$ eV, as no information was found in the literature. The vacancy concentration at the melting point is estimated from the formula [156]: $c_m = \exp(1.5) \exp(-E_f/RT_m)$. It is considered that dislocation climb dominates at the tested temperature range. This implies that the vacancy energy contribution to dislocation annihilation is fully present and $\delta = 1$ in equation 7.16. $\chi_{GB} = 0.34$ J/m² was obtained from [3]. It is worth noting that the physical parameters are not considered to depend on the chemical composition for dilute concentrations. ΔG_{sys} values were obtained from ThermoCalc and fitted to a formula (with correlation factor of $R^2 = 0.99$) to describe the temperature variation $\Delta G_{sys} = 16 - 0.045T - 1.4 \times 10^{-5}$ kJ/mol; for the tested composition ranges, as ΔG_{sys} did not vary significantly with composition (less than -2 kJ/mol), the same formula was employed for all cases.

Figure 7.4(a) shows the yield stress experimental values, they were directly determined from experimental stress-strain curves. Figures 7.4(b-d) show the model results and their comparison with the experimental data obtained in this work for Steel A for different temperatures and strain rates. The model shows excellent agreement on the work hardening rate and on recrystallisation onset and softening kinetics for the tested temperatures.

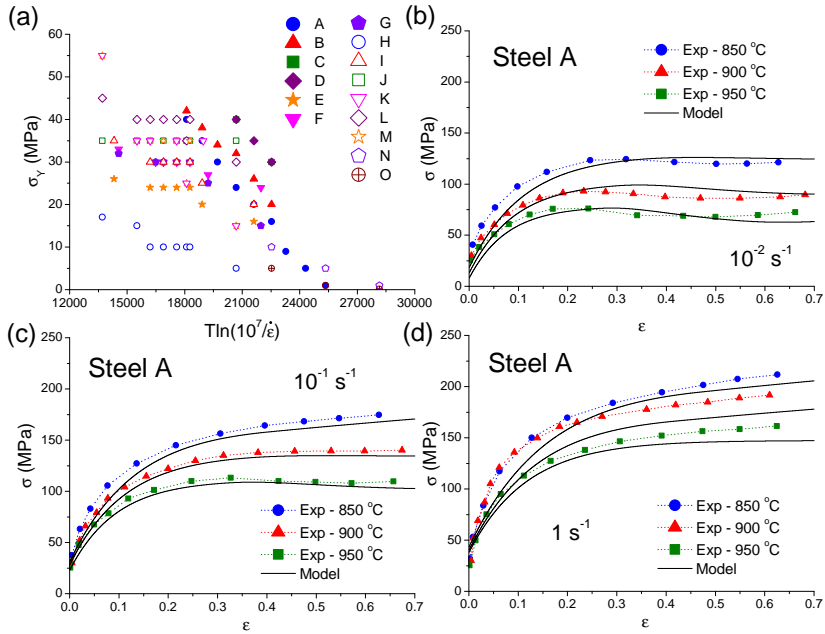


Figure 7.4: (a) Yield stress for the tested steels. Model stress–strain curves and their comparison with the experiments for steel A at different temperatures and at (b) 10^{-2} s^{-1} , (c) 10^{-1} s^{-1} and (d) 1 s^{-1} .

Figure 7.5 shows the model results and its comparison with the experimental data for Steels B, C and D for different temperatures and strain rates. The model shows good agreement in the absence of dynamic recrystallisation, however it predicts recrystallisation to take place before the experimental evidence. An explanation of this behaviour is that these steels contain high Nb concentration (0.03-0.07 wt%) that may cause NbC formation; this structure tends to segregate at grain boundaries, preventing recrystallisation and grain growth to occur prematurely [3]. Further extensions to the model to include this effect can be explored in future work.

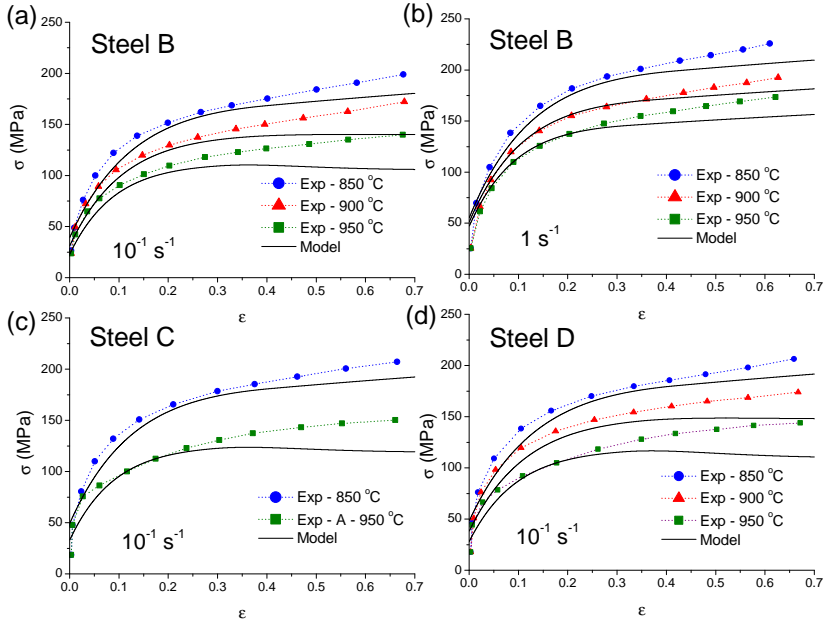


Figure 7.5: Model stress–strain curves and their comparison with the experiments for steel B, C and D at different temperatures and strain rates.

Substitutional and interstitial atoms effects on work hardening and recrystallisation kinetics are tested in Figures 7.6, 7.7, 7.8, 7.9 and 7.10. The model results are compared with experimental stress–strain curves for 11 steels at different temperatures and strain rates. The comparison shows a remarkable agreement for such wide composition, temperature and strain rate ranges. However, the model’s initial work hardening rates in steels with higher carbon concentrations (Figures 7.11(c),(d) and 7.10(a),(b)) is lower than the ones displayed in experiments. This discrepancy can be due to an increase in the friction stress, as carbon segregates at the boundaries and a dynamic Hall–Petch effect is present at low strains only [264]. Figures 7.10(c) and (d) show the effect of boron in Steels N and O, the experiments show a small decrease in the friction (onset) stress when boron concentration is increased, however similar work hardening behaviour is displayed in both alloys; the model shows almost no variation in the flow stress. This can be due to the reduced boron concentration in the steels.

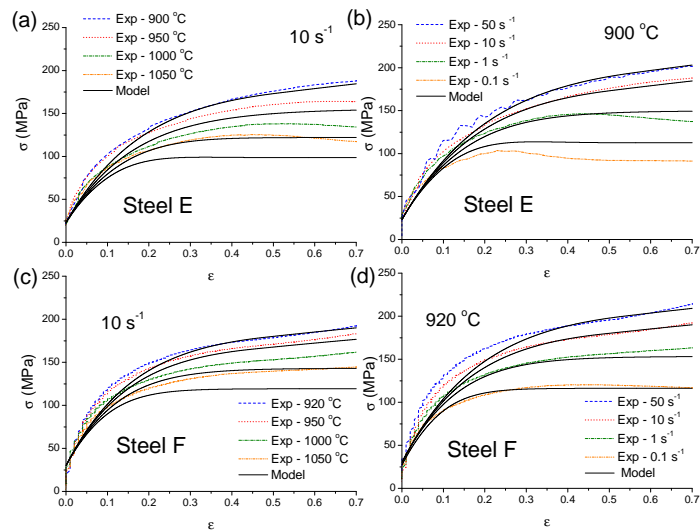


Figure 7.6: Model stress–strain curves and their comparison with the experiments for steel E and F at different temperatures and strain rates.

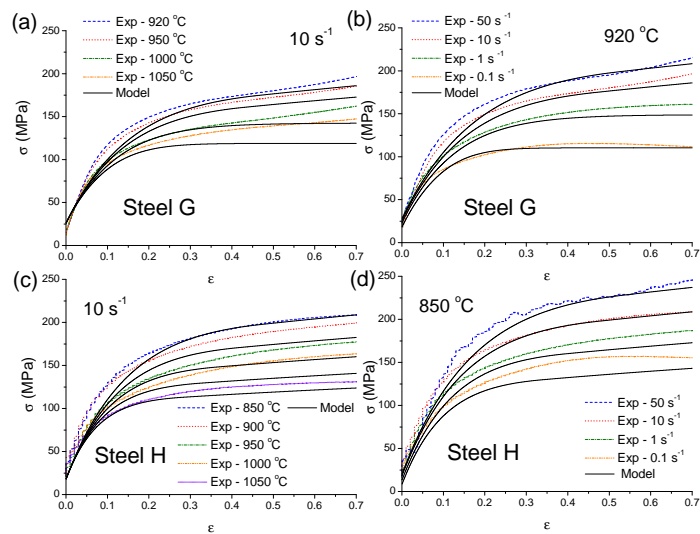


Figure 7.7: Model stress–strain curves and their comparison with the experiments for steel G and H at different temperatures and strain rates.

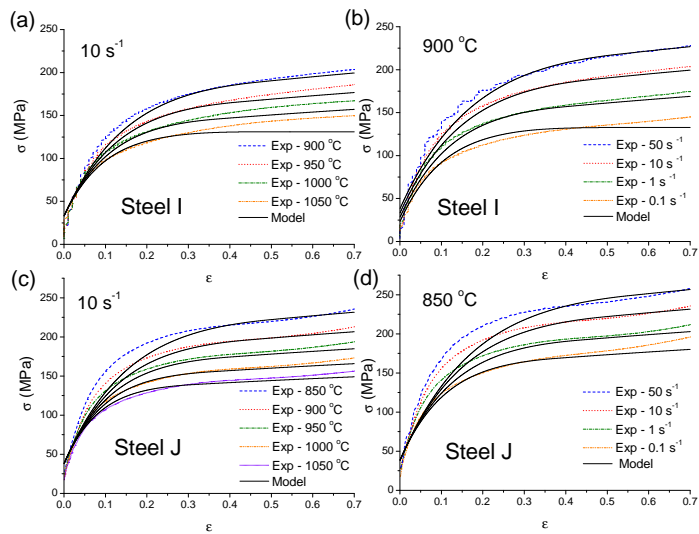


Figure 7.8: Model stress–strain curves and their comparison with the experiments for steel I and J at different temperatures and strain rates.

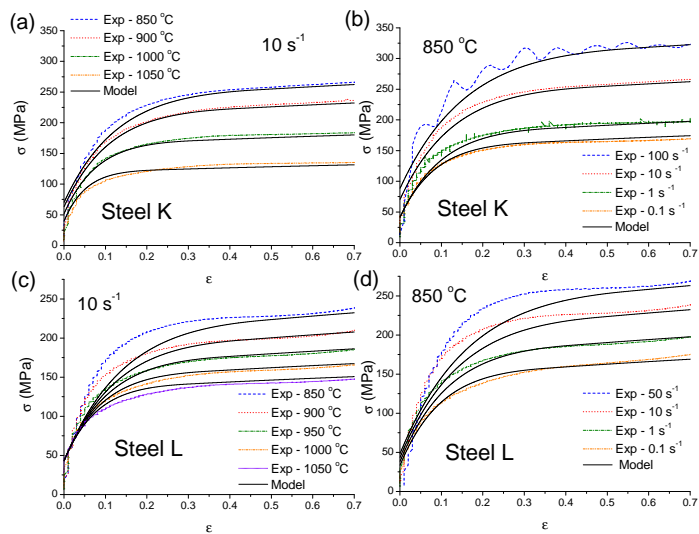


Figure 7.9: Model stress–strain curves and their comparison with the experiments for steel K and L at different temperatures and strain rates.

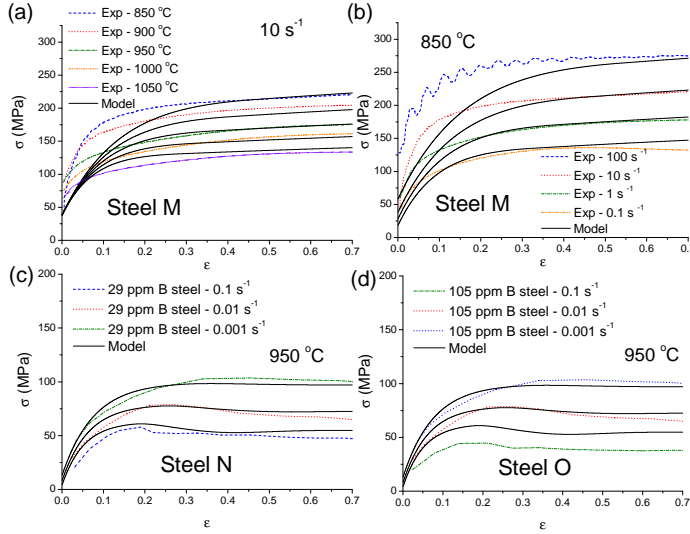


Figure 7.10: Model stress–strain curves and their comparison with the experiments for steel *M*, *N* and *O* at different temperatures and strain rates.

Critical conditions for dynamic recrystallisation to occur can be obtained from equation 7.26. For dilute substitutional and interstitial effects, this equation becomes:

$$\dot{\epsilon} = (\dot{\epsilon}_0 + \vartheta) \exp \left(- \frac{0.3\mu b^3 - \sum_i x_i^{1/3} \Delta G_{sys} + 2\pi x_C^{1/3} \chi_{GB} b^2}{k_B T} \right). \quad (7.35)$$

Figures 7.11(a) and (b) show the dynamic recrystallisation transition maps for two steels with different compositions and their comparison with the experimental data obtained from the literature. The boundaries are obtained from solving equation 7.35 for T ; the shadowed and white regions represent deformation conditions for DRX occurrence and where no recrystallisation is favourable, respectively. The experimental measurements were directly measured from the stress–strain curves where softening eventually occurs. These conclusions were confirmed by direct microstructural observation. The filled dots represent the experiments where recrystallisation takes place, and the white dots represent the experiments where only dynamic recovery occurs. The data for these steels were obtained from [265, 266] with grain sizes in the range of 18–60 μm . For Figure 7.11(a), Cu, Al and Ni effects (as substitutionals) were also added. The model shows good results with respect to the experimental data in Fig 7.11(a), except at 1223 K and 10^{-1} , where it predicts DRX occurrence, whereas experiment shows

only DRV at these conditions. This discrepancy can be due to the presence NbC in the specimen, effect not incorporated in the model. For the steel with no Nb (Fig. 7.11(b)), the model shows good results with respect to the experimental measurements.

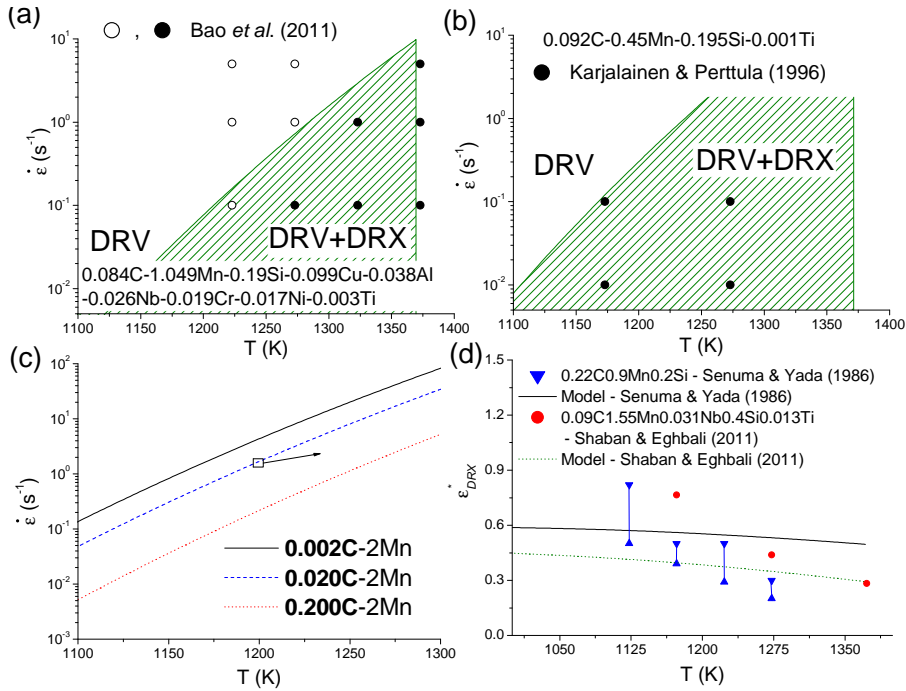


Figure 7.11: Dynamic recrystallisation maps for low alloy steels with compositions (a) $0.084\text{C}-1.049\text{Mn}-0.026\text{Nb}-0.19\text{Si}-0.019\text{Cr}-0.003\text{Ti}$ (wt%) and (b) $0.092\text{C}-0.45\text{Mn}-0\text{Nb}-0.19\text{Si}-0\text{Cr}-0.001\text{Ti}$ (wt%); the experimental data were obtained from [265] and [266], respectively. (c) Transition map for the occurrence of dynamic recrystallisation for different carbon concentrations. (d) Dynamic recrystallisation incubation strain ϵ_{DRV}^* predictions at different temperatures and strain rates and their comparison with experimental results obtained from [267, 268, 269].

This theory can be used to predict and design for austenite recrystallisation by varying composition. To illustrate this, Figure 7.11(c) shows the DRX transition maps for three hypothetical grades with compositions $0.002\text{C}-2\text{Mn}$, $0.020\text{C}-2\text{Mn}$ and $0.200\text{C}-2\text{Mn}$ to observe the carbon effect on recrystallisation kinetics. A stronger effect of carbon variation can be observed (with respect to substitutional atoms), as there is an increase in the recrystallisation temperature of $\sim 30^\circ\text{C}$ if

0.018wt % of carbon is increased (with respect to 0.002C-2Mn) and a further ~ 75 °C if 0.18 wt% of carbon is included in the steel. Figure 7.11(d) shows the critical strain for grain nucleation (ε_{DRX}^*) predictions at different temperatures and strain rates, and their comparison with experimental data for two steels, obtained from [267, 268]. The model shows good agreement at temperatures between 1150 and 1275 K, however temperature variation shows a lower rate with respect to the experimental measurements. It is worth noting that the model predicts the strain where grain nucleation occurs, however grain embryos can be small to be directly observed.

7.6 Combined effects: Twinning induced plasticity of high Mn steels

7.6.1 Model

High manganese steels with low stacking fault energies present a high dislocation dissociation rate. Similar to hexagonal metals (Chapter 5), the pile-up of dislocations leads twin formation (by dislocation dissociation) as deformation evolves, increasing the work hardening rate via additional dislocation generation. This term contains a delay due to a strain required for twin nucleation γ_T^* .

TWIP steels present a combined effect of solid solution and twinning induced plasticity in the dislocation generation term. Items (A), (B) (C) for dislocation generation are present in the Kocks–Mecking equation (equation 2.30)[79]:

$$\frac{d\rho^+[\gamma]}{d\gamma} = \frac{1}{b} \left(\frac{1}{\Lambda_{dis}} + \frac{1}{\Lambda_T} + \frac{1}{\Lambda_{SS}} \right). \quad (7.36)$$

The formation and distribution of twins depends on piling-up enough dislocations to reach a critical strain for dissociation [270, 12]. Similar to HCP metals, Λ_T is considered to be proportional to the average dislocation spacing once the critical strain for twin nucleation occurs (equation 5.18) [79]. Then Λ_T^{-1} becomes:

$$\frac{1}{\Lambda_T} = \frac{k_T}{\bar{l}} = k_T \sqrt{\rho[\gamma - \gamma_T^*]}, \quad (7.37)$$

where k_T and γ_T^* are constants related to the material, stacking fault energy and deformation conditions. The previous term is present when $\gamma \geq \gamma_T^*$.

On the other hand, $\Lambda_{SS}^{-1} = \Lambda_{subs}^{-1} + \Lambda_{inter}^{-1}$ accounts the hardening effect of substitutional (Mn) and interstitial (C) atoms. The former is depicted in equation 7.3 with $\Phi_{SS}b^3 = x_{Mn}$, where x_{Mn} is the atomic concentration of manganese. On the other hand, as twins are considered to be a dislocation arrangement, interstitials also affect Λ_T . Thus, following Section 7.2.2, Λ_{inter}^{-1} is equal to the probability of

encountering a carbon atom P_{inter} on a slip direction, multiplied by the inverse dislocation mean free path in the pure material and the average twin thickness (equation 7.5):

$$\Lambda_{inter}^{-1} = P_{inter}(\Lambda_{dis}^{-1} + \Lambda_T^{-1}) = x_C^{1/3} \left(k_1 \sqrt{\rho[\gamma]} + k_T \sqrt{\rho[\gamma - \gamma_T^*]} \right). \quad (7.38)$$

Combining the previous expressions, the evolution equation for TWIP steels becomes:

$$\begin{aligned} \frac{d\rho[\gamma]}{d\gamma} &= \frac{1}{b} \left(\frac{1}{\Lambda_{dis}} + \frac{1}{\Lambda_{subs}} + \frac{1}{\Lambda_{inter}} + \frac{1}{\Lambda_T} \right) - f_{DRV}^{sol} \rho[\gamma] \\ &= \frac{1}{b} \left((1 + x_C^{1/3}) k_1 + k_{SS} \right) \sqrt{\rho[\gamma]} + \frac{x_C^{1/3} k_T}{b} \sqrt{\rho[\gamma - \gamma_T^*]} - f_{DRV}^{sol} \rho[\gamma], \end{aligned} \quad (7.39)$$

with

$$\begin{aligned} k_{SS} &= \frac{x_{Mn}}{16,000} \exp \left(- \frac{\Delta G_{sys}}{RT} \right), \\ f_{DRV}^{sol} &= \frac{N_A \rho_a b^2 l^* (w_a^{-1}) (1 + x_C^{1/3}) (1 + x_{Mn}) \mathcal{N} k_B T \ln \left(\frac{\dot{\epsilon}_0 + \vartheta}{\dot{\epsilon}} \right)}{\frac{1}{2} \mu b^3 + \sigma_Y A_{act} b^3 + \frac{l^*}{b} x_{Mn} \Delta G_{sys} - k_B T \ln \left(\frac{\dot{\epsilon}_0 + \vartheta}{\dot{\epsilon}} \right) (1 + x_C^{1/3}) \mathcal{N}}, \end{aligned} \quad (7.40)$$

where a vacancy migration energy E_m was assumed equal to 1.2 eV. In order to avoid vacancy annihilation contributions, $\delta = 0$ is set in equation 7.16. k_T and γ_T^* can be obtained by performing a similar analysis shown in Chapter 5, for twin nucleation and growth at different temperatures and strain rates. However, the aim of this section is to show that the theory can combine twinning and solute atom effects in the same formulation at room temperature. Linear relationships are found for (low) carbon and (high) manganese effects in Section 7.6.2.

7.6.2 Results

The model is employed to describe the flow stress response in TWIP steels for different carbon and manganese concentration, by obtaining the dislocation density from equation 7.39 and employing the Taylor equation: $\sigma = \sigma_Y + \alpha M \mu b \sqrt{\rho}$. The physical parameters employed in the model were obtained from the literature; $\mu = 65$ GPa was obtained from [12]; ρ_a , w_a , c were taken equal to those for pure iron [227]. $\Delta G_{sys} = -8.4$ kJ/mol was obtained from Thermocalc; due to its low value, it was considered constant for different chemical compositions. Table 7.6

shows the carbon and manganese concentration for the tested steels, and their respective stacking fault energy and σ_Y values; they were obtained from [271].

Table 7.6: Stacking fault energy and σ_Y for different chemical composition. Values obtained from [271].

C (wt%)	Mn (wt%)	χ (mJ/m ²)	σ_Y (MPa)
0	30	34	150
0.5	30	42	275
1	30	49	325
0.6	22	37	250
1.2	22	49	370
0.95	17	42	420
1.2	12	47	450

Table 7.7 shows the fitted values of k_T and γ_T for different carbon and manganese composition. These parameters show linear dependence in the carbon and manganese concentration per unit length ($x_C^{1/3}$) and volume (x_{Mn}), respectively; no additional functional relations are required.

Table 7.7: Model parameters

Parameter	Fitted formula
k_T	$0.08(x_C^{1/3} + x_{Mn} - 0.35)$
γ_T^*	$1.75(x_{Mn} - 0.044)$

Figure 7.12 shows the model results for different concentrations and their comparison with the experimental curves obtained from the literature [272, 271, 12]; tensile tests were performed at room temperature and an average strain rate of $\dot{\epsilon} = 10^{-3} \text{ s}^{-1}$. The model results show good agreement in the work hardening rate for different chemical compositions. Moreover, for the Fe30Mn steel, no deformation twinning is observed [271], and cellular structures are formed, whereas the value of $k_T \approx 0$. For the case of the Fe17Mn0.95C and Fe12Mn1.2C steels, the model shows a lower work hardening rate with respect to the experiments; this effect can be due to the transition to stage IV, which has been neglected.

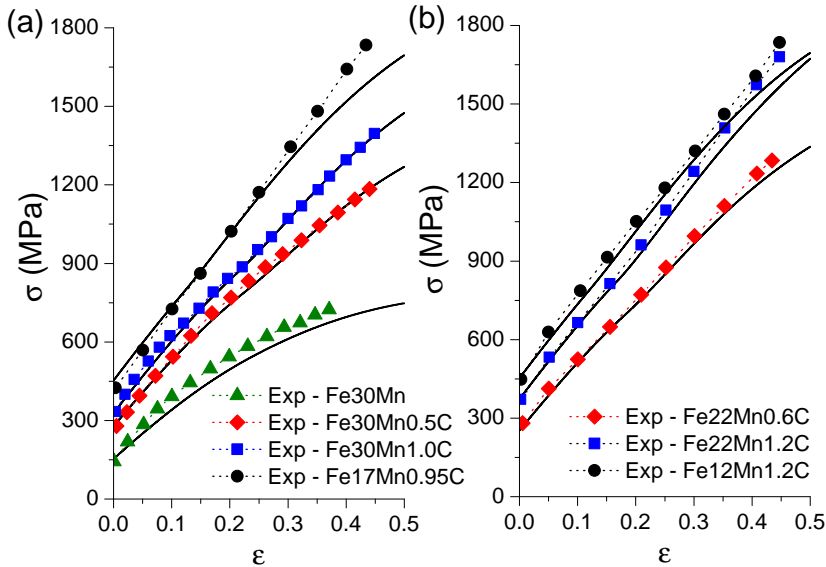


Figure 7.12: *Stress-strain response in TWIP steels for different carbon and manganese composition at room temperature.*

7.7 Discussion

This chapter incorporates effects of substitutional and interstitial atoms on dislocation evolution and kinetics. Substitutional atoms induce isotropic distortion in the lattice, which interactions with dislocations depend on their spatial arrangement. The free energy of the mixture is taken to account for the interaction induced by the possible solute atom arrangements in the alloy. This is included in the activation energy for dislocation annihilation (equation 7.12), and for grain growth during recrystallisation (equation 7.18), as well as in the energy balance for grain nucleation (equation 7.24). Additional number of microstates are also considered to account for the velocity reduction when dislocations encounter substitutional atoms, increasing the number of possible dislocation glide configurations; this is obtained by scaling the number of microstates in the pure material by the possible solute arrangements in the lattice. On the other hand, interstitial atoms induce an additional dislocation generation term to account for dislocation pinning around interstitials; it equals the fraction of dislocations pinning interstitials and it is proportional to the inverse dislocation mean free path. Pinning also

affects dislocation kinetics through the dislocation entropy ΔS^{sol} (depicted in the increase of the number of miscrotates). The additional energy barriers for grain nucleation and growth are estimated from the grain boundary energy in relation to segregated carbon atoms. All these terms are found to be proportional to $x_C^{1/3}$ for the range of the tested alloys. However, saturation from carbon segregation at grain boundaries may take place at higher concentrations [273].

The effect of dilute concentrations is introduced for both generation and annihilation. Same energy contributions are present for concentrated and dilute substitutional solutions. However, linear interactions are considered instead of volumetric effects (Table 7.4); for low concentrations, a dislocation encounters only discrete and spread solute atoms, representing a stronger interaction effect than for concentrated solutions; the interaction effect concentrated solutions is dispersed by the atomic distribution in the alloy. However, transition limits from dilute to concentrated solutions need to be defined.

Substitutional atoms add-up effects on dislocation behaviour from the pure material, whereas interstitials multiply such effects. For instance, substitutional atoms linearly add hardening effects in dislocation generation (equation 7.2) by $k_{SS}\sqrt{\rho}$, whereas interstitial effects multiply the dislocation generation term in the pure material by $(1 + x_C^{1/3})k_1\sqrt{\rho}$. A similar case occurs in the number of dislocation migration paths, as the presence of substitutionals scale the number of slip configurations in the pure material Ω_{pure} by $(1 + \sum_i x_i^{1/3})$ (equation 7.7), whereas carbon atoms scale Ω_{pure} by $(1 + \sum_i x_i^{1/3})(1 + x_C^{1/3})$ (equation 7.9). These results are in good agreement with the well established relationship that interstitial atoms interactions with dislocations have a stronger effect than substitutional solutions [244].

The model for hot deformation was tested against experimental stress-strain curves for 6 alloys with concentrated substitutional solutions (3 Fe- and 3 Ni-based); and for 15 steels containing different carbon concentrations and five elements acting as substitutional atoms (Mn, Nb, Si, Cr and Ti) in dilute concentrations. They were compared for very wide temperature and strain rate ranges. Boron effects on DRX were also examined. Additional elements in the form of solid solution can be readily included in the model.

Different elemental additions induce specific mechanical response, as they modify the alloy's Gibbs free energy of the mixture (ΔG_{sys}), its physical parameters (*e.g.* μ , b , E_f and E_m), and the solute atom concentration available for dislocation interaction. For instance, Mo displays a higher shear modulus than Cr at high temperatures (Appendix A), then an alloy containing Mo will offer a higher shear modulus than if it would contain the same Cr concentration [274]. However, local lattice distortion induced by each element is neglected for dislocation pinning effects. This analysis can be extended in future work.

Maps can be drawn to observe temperature, strain rate and chemical composition effects on the favourable conditions for dynamic recrystallisation when $Q_{DRX} = 0$. The model results were compared against experimental observations with good agreement for various alloys.

A combined model containing solid solution and deformation twinning effects for TWIP steels has also been presented. The most prominent feature in the TWIP treatment is the inclusion of a delay effect in the evolution equation, that accounts for twin formation. Twins will form once a critical strain is achieved. The twin growth coefficient k_T and the critical strain for twin nucleation γ_T^* were fitted to observe their variation with composition. Linear relationships between $x_C^{1/3}$ and x_{Mn} were obtained. However, a more fundamental analysis is required to justify these parameters, and to incorporate temperature and strain rate variations.

Coefficient values in the dislocation evolution equation are expressed in terms of temperature, strain rate and composition for each studied case: concentrated solutions, low alloy and TWIP steels are shown in equations 7.29, 7.34 and 7.40, respectively.

Shortcomings of the theory include the description for coarse-grained microstructures only, and no grain size effect is included in recrystallisation kinetics, and the recrystallised grain size evolution. Also the presence of additional microstructural features such as Nb and Ti carbides that significantly alter recrystallisation kinetics is not described. This may require the introduction of an additional energy term in the activation energy for grain growth (equation 7.18) to account for this effect. Additional modifications on interstitial atom effects for body-centered cubic alloys may be included, as their interactions with dislocations are no longer isotropic and their solubility is severely reduced; a stronger interaction takes place in the dominant direction of a dislocation strain field [244]. For concentrated solutions, the vacancy formation and migration energies were fitted, however these may differ from the real values, as additional dilute elements were neglected.

Although two parameters are fitted in the model, $\lambda = 0.6$ and $\lambda_{SS} = 16000$, they remain constant for all tested alloys. For the former, a justification of this value was presented in the previous chapter.

7.8 Conclusions

Multicomponent effects in deformation of FCC metals are introduced via several contributions:

1. The dislocation mean free path (equations 7.2 and 7.36), which otherwise would only be altered by the presence of the dislocation forest and the formation of subgrains, grains or twins.

2. The number of microstates for dislocation slip (equation 7.6), as solute atoms in the crystal structure increase the number of thermally activated paths available to dislocation segments.
3. The energy barrier for dislocation annihilation (equation 7.12). The presence of solute alters the work required for the dislocation line to migrate towards an annihilation event.
4. The energy barrier to drive grain growth (equation 7.18). This is increased by solute-drag effect on the subgrain boundaries, retarding dynamic recrystallisation occurrence.
5. The strain required to initiate dynamic recrystallisation (equation 7.25), as solute-drag effects alter the mobility of the recrystallisation front.
6. Physical parameters governing plasticity (equation 7.27), such as the magnitude of the Burgers vector, the speed of sound in the material, its density and shear modulus among others.

The present unified approach describes stages II, III and IV of deformation. The latter can be substituted by dynamic recrystallisation when it becomes energetically favourable at high temperatures. The average dislocation cell size is also recovered. Work hardening in TWIP steels is predicted various compositions. Notwithstanding its relatively simple analytical form, this theory successfully describes the hot deformation of Ni₃₀Fe, Ni₂₁Cr, Fe₃₀Ni, Fe₁₈Cr₈Ni, Fe₂₅Cr₂₀Ni, Ni₂₁Cr₈Mo₃Nb, and 15 low alloy steels with composition variations in 7 different elements in solid solution (C, Mn, Nb, Si, Cr, Ti and B). It has been demonstrated that the design of alloys for tailored dynamic recrystallisation behaviour is possible under such formulation. The only fitting parameters are $\lambda = 0.6$ (equation 6.6) and $\lambda_{SS} = 16000$ (equation 7.3). These parameters are employed in all calculations, for both unary and multicomponent systems and for all systems considered in this thesis. The rest are physical parameters that can be directly measured from experiments, such as shear modulus, melting point and yield stress; the vacancy formation and migration energy, and the stacking fault energy can be obtained from atomistic or first principles approaches.

Summary

Dislocation evolution and interaction with other crystal defects during plastic deformation is central to determine mechanical properties for metallic alloys. Engineering alloys often display an elaborate composition and/or thermal processing schedules. Their ability to withstand loads stems from the interactions between crystal defects with the microstructure. Determining dislocation population and kinematic behaviour along with interactions with other crystal defects is central to this problem. Developing theoretical tools for describing such interactions in terms of composition and loading conditions can be crucial for designing alloys. The objective of this thesis has been to present a theory for dislocation evolution based on statistical thermodynamics. The dislocation entropy ΔS is proposed to incorporate the possible velocities for dislocation motion. Plastic deformation is a highly dissipative process; over 90% of the energy needed to impose plastic deformation is dissipated in the form of heat [31]. This study is focused on providing succinct expressions for the average dislocation density evolution in terms of physical parameters and loading conditions. Plastic deformation and flow stress evolution in FCC, BCC and HCP metals are described along with their concomitant deformation mechanisms.

Chapter 1 introduces the main deformation mechanisms in metals being covered in this work; dislocations are shown to have specific contributions for each case: 1) deformation by slip is caused by accumulation and slip of dislocations to accommodate strain. 2) Deformation twinning occurs when dislocations encounter each other, creating self-barriers for the continuation of gliding; stress accumulation arise around them, inducing dislocation dissociation and twin boundary nucleation, reducing the strain energy around them; twins grow as strain evolves, inducing additional dislocation generation. 3) Grain boundary sliding occurs in ultra-fine-grain materials where adjacent grains displace with respect to each other to continuously accommodate strain. Intragranular movement of dislocations facilitates grain boundary displacement. This process allows materials to reach high tensile elongations, ranging from 200 up to a few thousand percent before failure.

In **Chapter 2**, basic dislocation concepts are introduced; the dislocation arrangements that are relevant for this work are presented, such as dislocation cells, tilt boundaries and nanotwins. The formation entropy of a dislocation and thermodynamic principles of dislocations are discussed; preliminary motivation for employing statistical thermodynamics to describe dislocation mobility is depicted. This section is followed by presenting some of the most common modelling techniques for describing plastic deformation and dislocation behaviour at various scales. A special emphasis is made on the Kocks–Mecking equation; this formulation characterises the dislocation population evolution with strain; it is demonstrated in this thesis that this equation can be applied to describe multiscale plasticity under various scenarios, by employing the average dislocation density evolution. However, an additional ingredient is required to predict dislocation population: to describe dislocation kinetics in terms of composition and loading conditions.

Quantitative understanding of dislocation motion is essential to describe plasticity in crystalline materials. Dislocation mobility controls the materials ability to accommodate strain and modify its microstructure. In **Chapter 3** a thermo-statistical framework is derived for describing dislocation kinetics and estimating the energy loss due to different velocity distributions of a dislocation, instead of describing its instantaneous velocity at every moment. In this chapter, the theory is initially defined for pure FCC metals.

The statistical entropy ΔS associated to the energetically favourable dislocation paths during deformation is introduced. A microstate (specific dislocation configuration) is defined as the specific velocity a dislocation will have during a time interval⁶. A total number of microstates Ω_{dis} for the total number of dislocation velocity configurations is obtained. At high temperatures, the vacancy–dislocation interaction becomes dominant, increasing the possibilities for dislocation migration paths via vacancy–assisted dislocation climb, and consequently additional number of microstates are incorporated (Ω_{v-d}). This gives a total number of possible configurations for slip and climb to be equal to $\Omega = \Omega_{dis} + \Omega_{v-d}$. Statistical thermodynamics can be applied to describe plasticity, as only average atomic displacements (expressed in terms of a dislocation’s average velocity) are considered. Moreover, the speed of sound c limits the number of possible dislocation configurations [29, 5].

The transition between low to intermediate (T_0), and intermediate to high temperature (T_f) dislocation annihilation regimes are delimited by transitions in the number of microstates. This is obtained by comparing Ω_{dis} and Ω_{v-d} ; at low temperatures dislocation slip/cross-slip dominates dislocation annihilation, and Ω_{dis} displays the highest values; at high temperatures, vacancy–assisted disloca-

⁶To be consistent with classical statistical thermodynamics concepts, the analysis is defined in terms of atom displacements. They are directly related to the dislocation velocity.

tion climb prevails, and Ω_{v-d} dominates; at medium temperatures, a mixture of slip/cross-slip and climb is present, as Ω_{dis} and Ω_{v-d} have the same order of magnitude. The transition limits T_0 and T_f are initially validated for FCC metals, and later confirmed for BCC and HCP metals in Chapter 4 and 5, respectively. This thermostatistical framework is applied to obtain an expression for the dynamic recovery term in the Kocks–Mecking equation. A thermodynamic analysis on an annihilating dislocation segment is performed to determine the energy barrier for dislocation annihilation $\langle \Delta G \rangle$. It is composed by (1) a dislocation formation energy term, approximated by the strain energy around the annihilating segment; (2) a migration energy term, which is proportional to the critical resolved shear stress to initiate slip; (3) a vacancy energy contribution to dislocation annihilation at higher temperatures (via dislocation climb), induced by the vacancy chemical work around the segment; and (4) a statistical entropy contribution $T\Delta S$. Beyond a certain strain, dislocations start to interact as their strain fields screen each other, inducing additional number of configurations Ω_{imp} in ΔS .

The average dislocation cell size is obtained by performing an energy balance between the dislocation forest and the cellular structure formation, expressing the slip energy required for cell formation in terms of $T\Delta S$. The Young–Laplace equation is applied to obtain the cell misorientation angle at stages III and IV of deformation. This equation is also applied to obtain an expression for the dislocation density evolution at stage IV. The model reproduces experimental saturation stress, stress–strain relationships, and average cell size and misorientation evolution at wide temperature ranges for pure FCC metals at a variety of strain rates. The same set of input physical parameters are employed for all cases.

Chapter 4 extends the theory for describing plastic deformation to BCC metals. The distinctions between FCC and BCC stem primarily from the possible directions and planes for dislocation slip and cross-slip, as well as from the occurrence of the kink–pair mechanism for dislocation migration in BCC, which are incorporated to the mathematical formulation of the model. The motion of a dislocation in a BCC metal is composed of the migration of two thermally activated kinks; this behaviour induces a double kinetic effect for a dislocation to slip, *i.e.* the total number of microstates Ω is squared. The model describes the stress–strain response for pure iron, molybdenum, tantalum, vanadium and tungsten, employing physical parameters as input; the description is made for wide ranges of temperature and strain rate. Additionally, succinct equations to predict dislocation cell size variation with strain, strain rate and temperature are provided and validated for pure iron.

Deformation twinning in HCP metals is described in **Chapter 5**. A dislocation generation term Λ_T^{-1} accounting for twin propagation is added to the Kocks–

Mecking equation, where Λ_T^{-1} is the inverse average twin spacing. This term becomes active once a critical strain γ_T^* for twin nucleation is reached. γ_T^* is obtained by performing a balance between the dislocation forest, and the twin formation and propagation energies; these terms are reduced by the dissipation effects from dislocation slip. Additional dislocation storage drives further twin growth; the corresponding driving force accounts for the additional number of stored dislocations at twin boundaries increasing local stress concentrations; Λ_T^{-1} is obtained from this balance. The energy dissipated during twin formation and growth is quantified as $T\Delta S$. Deformation by dislocation slip, at strains below twin nucleation occurs, is described by the theory for FCC metals previously derived in Chapter 3. The model describes work hardening and twin volume fraction behaviour of Ti, Zr and Mg for various temperature and orientation conditions. The transition temperatures where tensile or compressive twin modes are dominant are also prescribed.

Extension of the theory to describe dislocation evolution in FCC metals undergoing dynamic recrystallisation is presented in **Chapter 6**. An additional softening effect $f_{DRX}\rho_{DRX}$ in the Kocks–Mecking equation is incorporated, where f_{DRX} is the dynamic recrystallisation coefficient, and ρ_{DRX} is the dislocation density inside the growing grains; this term becomes active once a critical strain for grain nucleation is achieved. f_{DRX} is directly related to the energy barrier Q_{DRX} for grain growth. Q_{DRX} is composed by the competition between the boundary displacement energy, acting as driving force for grain boundary motion, and the strain energy (at grain boundaries) once high-angle grain boundaries form. The boundary displacement energy is shown to be proportional to $T\Delta S$. With this approximation, the use of the grain boundary mobility concept can be circumvented, and mobility fitting parameters are not required. The theory reproduces the stress oscillations with strain and its values when steady state is approached; and captures well the temperature–strain rate dependency of dynamic recrystallisation. This allows to map the conditions under which dynamic recrystallisation occurs. The model results are successfully validated with data for Cu and Ni. The same set of experimentally determined physical parameters used in Chapter 3 is successfully employed in the recrystallisation model validation.

In **Chapter 7**, multicomponent effects are incorporated to the theory to account for solid solution strengthening, recrystallisation, and twinning induced plasticity effects. Dislocation pinning around solute atoms induces equivalent dislocation generation terms in the Kocks–Mecking equation (Λ_{SS}^{-1}) to account for this effect. Moreover, the dislocation average velocity is also reduced by pinning around solute atoms, and additional dislocation configurations are incorporated into Ω to account for the presence of substitutional (Ω_{subs}) and interstitial (Ω_{inter}) atoms. Finally, additional energy barriers are incorporated into $\langle\Delta G\rangle$ and Q_{DRX} .

Concentrated–solution effects are initially considered in the hot deformation of

Ni30Fe, Ni21Cr, Fe30Ni, Fe18Cr8Ni, Fe25Cr20Ni and Ni21Cr8Mo3Nb. The model is later extended to describe dilute concentrations of substitutional and interstitial atoms; hot deformation of 15 low alloy steels is described for wide ranges in composition, temperature and strain rates. Maps for dynamic recrystallisation occurrence are defined in terms of temperature, strain rate and composition. Input to the model are only physical parameters and thermodynamic information from well accepted databases.

The description of work hardening of twinning–induced–plasticity steels for different C and Mn concentrations at room temperature is also made by combining twinning (Λ_T^{-1}) and solid solution contributions (Λ_S^{-1}) in dislocation generation. The dislocation entropy allows to define a “modular” approach for describing dislocation evolution under various scenarios as 1) the number of possible dislocation paths; 2) the barriers for the activation energies for dislocation annihilation $\langle \Delta G \rangle$ and for grain growth Q_{DRX} ; and 3) dislocation generation sources are modified when various crystal defects are present. The latter has been schematically introduced in the Kocks–Mecking equation previously [94]. However, specific expressions for each case are described in this thesis.

By employing the notation \perp for dislocations, \emptyset for vacancies, \oplus for substitutional atoms and \odot for interstitial atoms, and by employing the notation $\perp \cdot i$ to denote the interaction of a dislocation with an i –defect, where $i = \emptyset, \oplus, \odot$, Table S.1 schematically shows the contribution of other crystal defects to dislocation population and kinetics for several systems. It is worth noting that $\Omega_{\perp \cdot \perp}$, $\Omega_{\perp \cdot \emptyset}$ and $\Omega_{\perp \cdot \perp} \cdot \Omega_{\perp \cdot \emptyset}$, schematically represent Ω_{dis} , Ω_{v-d} and $\Omega_{dis} + \Omega_{v-d}$ respectively; in $\langle \Delta G \rangle$, the dislocation formation and migration energies are schematically represented by $U_{\perp \cdot \perp} = U_{form} + U_{mig}$, whereas the energy terms for Q_{DRX} are displayed with inverse signs (to preserve symmetry, see equation 7.18), and E_{HAGB} is schematically represented by $U_{\perp \cdot \perp} = E_{HAGB}$. Case 1 shows that when (single crystal) pure metals are deformed at low temperatures ($T < T_0$), the number of microstates and energy barrier contributions are given by dislocation behaviour only, also $Q_{DRX} = 0$; a Ni30Fe alloy being deformed at higher temperatures ($T > T_0$) is shown in Case 2, where dislocation interactions with vacancies and substitutional atoms take place (no vacancy contribution to dislocation generation is considered); Case 3 presents a low alloy steel deformed at high temperatures ($T > T_f$), where vacancies, substitutional and interstitial atoms modify dislocation behaviour. This modular approach is validated by describing plastic deformation and dislocation evolution in several materials, including pure metals and alloys.

Table S.1: Schematic representation of the modular effects in the number of dislocation migration paths and energy barriers for various materials deformed at different temperatures.

Case	Material	Def. Temp.	Microstates
1	Pure metal	$T < T_0$	$\Omega_{\perp.\perp}$
2	Ni30Fe	$T > T_0$	$\Omega_{\perp.\perp} \cdot \Omega_{\perp.\emptyset} \cdot \Omega_{\perp.\oplus}$
3	Low alloy steel	$T > T_f$	$\Omega_{\perp.\perp} \cdot \Omega_{\perp.\emptyset} \cdot \Omega_{\perp.\oplus} \cdot \Omega_{\perp.\odot}$
4	Ni superalloy	$T > T_f$	$\Omega_{\perp.\perp} \cdot \Omega_{\perp.\emptyset} \cdot \Omega_{\perp.\oplus} \cdot \Omega_{\perp.\odot} \cdot \Omega_{\perp.\square}$
Case	Material	Def. Temp.	Barriers in $\langle \Delta G \rangle$ and Q_{DRX}
1	Pure metal	$T < T_0$	$U_{\perp.\perp} - T\Delta S$
2	Ni30Fe	$T > T_0$	$U_{\perp.\perp} + U_{\perp.\emptyset} + U_{\perp.\oplus} - T\Delta S$
3	Low alloy steel	$T > T_f$	$U_{\perp.\perp} + U_{\perp.\emptyset} + U_{\perp.\oplus} + U_{\perp.\odot} - T\Delta S$
4	Ni superalloy	$T > T_f$	$U_{\perp.\perp} + U_{\perp.\emptyset} + U_{\perp.\oplus} + U_{\perp.\odot} + U_{\perp.\square} - T\Delta S$
Case	Material	Def. Temp.	Dislocation generation
1	Pure metal	$T < T_0$	$\Lambda_{\perp.\perp}^{-1}$
2	Ni30Fe	$T > T_0$	$\Lambda_{\perp.\perp}^{-1} + \Lambda_{\perp.\oplus}^{-1}$
3	Low alloy steel	$T > T_f$	$\Lambda_{\perp.\perp}^{-1} + \Lambda_{\perp.\emptyset}^{-1} + \Lambda_{\perp.\oplus}^{-1} + \Lambda_{\perp.\odot}^{-1}$
4	Ni superalloy	$T > T_f$	$\Lambda_{\perp.\perp}^{-1} + \Lambda_{\perp.\emptyset}^{-1} + \Lambda_{\perp.\oplus}^{-1} + \Lambda_{\perp.\odot}^{-1} + \Lambda_{\perp.\square}^{-1}$

This table illustrates where different microstructural features alter dislocation behaviour. Furthermore, it schematically shows how additional features, such as precipitates, compounds and grain boundaries, can be introduced in the theory in future work. For instance, by employing the notation \square , Case 4 in Table S.1 hypothetically shows that additional configurational effects ($\Omega_{\perp.\square}$) and barriers on $\langle \Delta G \rangle$ and Q_{DRX} ($U_{\perp.\square}$) can be introduced in the model for a (coarse-grained) Ni-based superalloy deformed at high temperatures ($T > T_f$), where intermetallic precipitates induce dislocation-pinning around them, along with vacancy-assisted climb and substitutional atom interactions; $\Lambda_{\perp.\square}$ and $\Omega_{\perp.\square}$ may have a dominant contribution to the alloy's strength with respect to other terms [27]. However, this case has yet to be validated and the previous terms need to be identified. A case for grain boundary strengthening in Fe has been developed in previous work [274].

Configurational entropy effects for dislocation *nucleation* were initially derived by Cottrell [29]; this was done by accounting for the possible locations of a dislocation in the crystal lattice when it is nucleated (equation 2.10). This work has gone one step further, as the possible configurations for dislocations slip during strain are obtained. This theory not only allows to describe dislocation spatial arrangements, *e.g.* forest density, cells and twins; but (via the strain rate) it also incorporates their evolution during time.

Possible directions in future work are: 1) to incorporate additional microstructural features at high temperatures. For instance, Nb and Ti carbides in Low alloy steels delay dynamic recrystallization occurrence, inducing additional barriers for grain nucleation and growth. Intermetallic precipitates in polycrystalline Ni-based alloys increase their strength at high temperatures, inducing an additional generation term and barriers in dislocation annihilation and grain growth. 2) To describe the average grain size evolution when dynamic recrystallisation occurs and the recrystallised volume fraction, as these are important variables when designing new alloys; to modify the theory for intermediate and high carbon concentration effects in low alloy steels, where segregation saturation occurs at grain boundaries. 3) To combine this framework with other modelling techniques, such as crystal plasticity and finite element method, to describe microstructure spatial arrangements, and characterise orientation and texture distributions for different composition and processing conditions. 4) To extend the theory for static recovery and recrystallisation (strain is fixed); the theory has to be modified, as time (instead of strain) is the variable modifying the dislocation population and kinematic behaviour; the Kocks–Mecking equation is no longer valid and a new equation is required. Moreover, a microstate is defined for a fixed time interval, the thermostatistical formalism then may be modified to account for time increment for a fixed strain.

Samenvatting

Inzicht in het dislocatieverloop en de interactie met andere kristaldefecten tijdens plastische deformatie is onontbeerlijk voor het bepalen van mechanische eigenschappen voor metallische legeringen. Technische legeringen hebben vaak een complexe samenstelling en ondergaan veelal een complexe warmtebehandeling. Hun vermogen om mechanische belasting te weerstaan wordt bepaald door de interacties tussen kristaldefecten en de microstructuur. Het bepalen van de dislocatiepopulatie en het kinematisch gedrag samen met de interacties met andere kristaldefecten is centraal voor dit probleem. Het ontwikkelen van theorie voor het beschrijven van zulke interacties in termen van samenstelling en mechanische belasting kan zeer belangrijk zijn voor het ontwerpen van legeringen. Het doel van dit proefschrift is om een theorie voor het verloop van de dislocaties, die gebaseerd is op statische thermodynamica, op te stellen. We stellen dat de dislocatieentropie ΔS de mogelijke snelheden voor dislocatiebeweging bevat. Plastische vervorming is een zeer dissipatief proces; meer dan 90 % van de energie nodig om plastische vervorming wordt gedissipeerd in warmte [31]. Deze studie richt zich op het verstrekken van beknopte uitdrukkingen voor de gemiddelde dislocatiedichtheid als functie van fysische parameters en belasting. De plastische vervorming en het vloeispanningsverloop in FCC, BCC en HCP metalen worden beschreven met hun gelijktijdige vervormingsmechanismen.

Hoofdstuk 1 voert de belangrijkste vervormingsmechanismen in voor de metalen die hier behandeld worden; we laten zien dat dislocaties bepaalde bijdragen hebben voor ieder geval: 1) glijvervorming wordt veroorzaakt door opéénhoping en het glijden van dislocaties om de rek tegemoet te komen. 2) Vervormingstwinning treedt op als dislocaties elkaar tegenkomen, waarbij ze zelf-barrières voor het vervolg van het glijden vormen; eromheen ontstaat spanningsophoping, waarbij ze aanleiding tot dislocatiedissociatie en tweelingsrandnucleatie geven, de rekenergie eromheen verlagen; tweelingen groeien als de rek zich ontwikkelt, waarbij ze extra dislocaties aanmaken. 3) Het glijden van korrelgrenzen vindt plaats in materialen met ultra-fijne korrels waar naburige korrels zich verplaatsen ten opzichte van elkaar om steeds de rek tegemoet te komen. Intragranulaire beweging van dislo-

caties vergemakkelijkt verplaatsing van korrelgrenzen. Dit proces laat materialen hoog rekbare verlenging te bereiken, met waarden van 200 tot een paar duizend procent voordat falen optreedt.

In hoofdstuk 2 worden basis dislocatie concepten ingevoerd; de dislocatierangschikkingen die belangrijk zijn voor dit werk, zoals dislocatiecellen, gekantelde randen en nanotwins, worden ingevoerd. De vervormingsentropie van een dislocatie en thermodynamische principes van dislocaties worden besproken; een voorlopige motivatie voor het gebruik van statische thermodynamica om dislocatiemobiliteit te beschrijven wordt geschetst. Deze sectie wordt gevolgd door het beschrijven van de meest gangbare modelleertechnieken om plastische deformatie en dislocatiegedrag te simuleren. De nadruk wordt gelegd op de Kocks–Mecking vergelijking; deze formulering karakteriseert de dislocatie populatiedynamica met de rek; er wordt in dit proefschrift aangetoond dat deze vergelijking gebruikt kan worden om plasticiteit onder verschillende omstandigheden op meerdere schalen te beschrijven door het gebruik van het verloop van de gemiddelde dislocatiedichtheid te gebruiken. Een extra ingrediënt is echter vereist om de dislocatie populatie te voorspellen: om dislocatiekinetiek in termen van samenstelling en mechanische belasting te beschrijven. Kwantitatief begrip van de beweging van dislocaties is van belang om plasticiteit in kristallijne materialen te beschrijven. De mobiliteit van dislocaties bepaalt het vermogen van het materiaal om rek te ondergaan en zijn microstructuur aan te passen. In hoofdstuk 3 wordt een thermodynamisch raamwerk afgeleid voor het beschrijven van de dislocatiekinetiek en het energieverlies ten gevolge van verschillende snelheidsverdelingen van een dislocatie te schatten, in plaats van de instantane snelheid op ieder tijdstip te beschrijven. In dit hoofdstuk, wordt de theorie eerst ingevoerd voor zuivere FCC metalen.

De statistische entropie ΔS , die bij de energetisch voordelige dislocatiepaden tijdens vervorming hoort, wordt ingevoerd. Een microstate (specifieke dislocatieconfiguratie) wordt gedefinieerd als de specifieke snelheid van een dislocatie in een tijdsinterval⁷. Een totaal aantal microstates Ω_{dis} voor het totale aantal dislocatie snelheidsconfiguraties wordt verkregen. Op hoge temperatuur wordt de vacature–dislocatie interactie belangrijk, wat het aantal mogelijkheden voor dislocatiemigratiepaden met dislocatieklim behulp van vacatures vermeerderd, en daarmee wordt een extra aantal microstates opgenomen (Ω_{v-d}). Dit geeft een totaal aantal mogelijke configuraties voor slip en klim dat gelijk is aan $\Omega = \Omega_{dis} + \Omega_{v-d}$. Statistische thermodynamica kan worden gebruikt om plasticiteit te beschrijven, als enkel gemiddelde atomaire verplaatsingen (uitgedrukt in de gemiddelde snelheid van een dislocatie) beschouwd worden. Bovendien

⁷Om consistent met het jargon van de klassieke statistische thermodynamische te zijn, wordt de analyse gedefinieerd in termen van atomaire verplaatsingen. Deze zijn direct gerelateerd aan de dislocatiesnelheid.

beperkt de geluidssnelheid c het aantal mogelijke dislocatieconfiguraties [29, 5]. In de overgang tussen laag tot middelhoge (T_0), en middelhoge tot hoge temperatuur (T_f), worden de dislocatievernietigingsregimes afgebakend door overgangen in het aantal microstates. Deze worden verkregen door het vergelijken van Ω_{dis} en Ω_{v-d} ; op lage temperatuur bepaalt dislocatie slip/cross-slip de vernietiging van dislocaties, en Ω_{dis} laat de hoogste waarden zien; op hoge temperatuur overheerst dislocatieklim middels vacatures en Ω_{v-d} domineert dan; op middelhoge temperaturen is een mengsel van slip/cross-slip aanwezig daar Ω_{dis} en Ω_{v-d} dezelfde grootte-orde hebben. De overgangslimieten T_0 en T_f worden eerst gevalideerd voor FCC metalen, en later achtereenvolgens bevestigd voor BCC en HCP metalen in hoofdstukken 4 en 5. Dit thermostatische raamwerk wordt gebruikt om een uitdrukking te krijgen voor de dynamische herstelterm in de Kocks-Mecking vergelijking. Een thermodynamische analyse aan een ternietdoend dislocatiesegment is uitgevoerd om de energiebarriere voor dislocatievernietiging $\langle \Delta G \rangle$ te bepalen. Deze bestaat uit (1) een dislocatie energieterm, die benaderd wordt door de rekenergie rond het tenietdoende segment; (2) een migratie energieterm, die evenredig is met de kritische afschuifspanning nodig om slip te bewerkstelligen; (3) een vacature energiebijdrage voor dislocatievernietiging op hogere temperatuur (via dislocatieklim), bewerkstelligd door de vacature chemische arbeid rond het segment; en (4) een statistische entropiebijdrage $T\Delta S$. Boven een bepaalde rek beginnen dislocaties op elkaar in te werken als hun rekvelden elkaar voelen, daarmee wordt een extra aantal configuraties Ω_{imp} in ΔS opgeleverd.

De gemiddelde celgrootte van dislocaties wordt verkregen door de energiebalans tussen de dislocaties en de formatie van de celstructuur op te stellen, en door de vereiste slipenergie voor celformatie uit te drukken in $T\Delta S$. De Young-Laplace vergelijking wordt gebruikt om de cel misorientatie-hoek op stadia III en IV van deformatie te verkrijgen. Deze vergelijking wordt ook gebruikt om een uitdrukking te krijgen voor het verloop van de dislocatiedichtheid in stadium IV. Het model reproduceert de experimentele verzadigingsspanning, spanning-rek relaties, gemiddelde celgrootte en het misorientatieverloop voor een groot temperatuurbereik voor zuivere FCC metalen in een wijd spectrum van reksnelheden. Dezelfde set invoerparameters wordt gebruikt in alle gevallen.

Hoofdstuk 4 breidt de theorie voor plastische vervorming uit naar BCC metalen. De verschillen tussen FCC en BCC stammen in de eerste plaats af van mogelijke richtingen en vlakken voor dislocatieslip en cross-slip, alsmede van de aanwezigheid van het kink-pair mechanisme voor dislocatiemigratie in BCC, die meegenomen zijn in het wiskundige model. De beweging van een dislocatie in een BCC metaal bestaat uit de migratie van twee thermisch geactiveerde kinks; dit gedrag levert een dubbel kinetisch effect voor een dislocatie aan de slip op, ofwel het kwadraat van het totale aantal microstates Ω . Het model beschrijft de spannings-rek gedrag voor zuiver ijzer, molybdenum, tantalum, vanadium

en wolfram, waarbij van natuurkundige parameters als invoer gebruikgemaakt wordt; de beschrijving is gemaakt voor een groot temperatuurbereik en een groot bereik van de reksnelheid. Verder worden er eenvoudige vergelijkingen om de dislocatie celgroottevariatie met de rek, reksnelheid en temperatuur gegeven en gevalideerd voor zuiver ijzer.

De vervormingstwinning in HCP metalen wordt beschreven in hoofdstuk 5. Een dislocatie-aanmaakterm Λ_T^{-1} voor twinpropagatie wordt toegevoegd aan de Kocks-Mecking vergelijking, waarin Λ_T^{-1} de reciproke gemiddelde twin-afstand is. Deze term speelt een rol als een kritische rek γ_T^* bereikt wordt. γ_T^* wordt verkregen door het opstellen van een balans tussen de verzameling dislocaties en de twin-formatie en propagatieenergieën; deze termen worden verminderd door de dissipatieeffecten van dislocatieslip. Verdere dislocatieopslag zorgt voor verdere twin-groei; de ermee gerelateerde drijvende kracht geeft het extra aantal opgeslagen dislocaties op twin-randen die de plaatselijke spanningsconcentraties doen toenemen; γ_T^* wordt uit deze balans verkregen. De gedissipeerde energie tijdens twin-formatie en groei wordt bepaald door $T\Delta S$. Vervorming door dislocatieslip voor rekken onder twin-nucleatie, wordt beschreven middels de eerder afgeleide theorie voor FCC metalen uit hoofdstuk 3. Het model beschrijft work hardening en het gedrag van de volumefractie van twins van Ti, Zr, en Mg voor verschillende temperaturen en orientatie. De transitietemperaturen, waarin rekbare of samengedrukte twin-modes overheersen, worden ook beschreven.

Uitbreiding van de theorie om het dislocatieverloop te beschrijven in FCC metalen die dynamische rekristallisatie ondergaan wordt gegeven in hoofdstuk 6. Een extra verzachttingseffect $f_{DRX}\rho_{DRX}$ wordt meegenomen in de Kocks-Mecking vergelijking, waarin f_{DRX} de dynamische rekristallisatie coefficient is, en ρ_{DRX} de dislocatiedichtheid in de groeiende korrels voorstelt; deze term speelt een rol als een kritische rek voor korrelnucleatie bereikt wordt. f_{DRX} is direct gerelateerd aan de energiebarriere Q_{DRX} voor korrelgroei. Q_{DRX} bestaat uit de competitie tussen de grensverplaatsingsenergie die een drijvende kracht voor korrelgrensverplaatsing is, en de rekenergie (op korrelgrenzen) als korrelgrenzen met grote hoeken ontstaan. We tonen aan dat de grensverplaatsingsenergie evenredig is met $T\Delta S$. Met deze benadering kan het gebruik van de korrelgrensmobiliteit vermeden worden, en mobiliteit fitting parameters zijn dan niet nodig. De theorie reproduceert de spanningsoscillaties met rek en zijn waarden wanneer de stationaire toestand benaderd wordt; en vangt de temperatuur-rek afhankelijkheid tijdens dynamische rekristallisatie goed. Dit laat het toe om de voorwaarden waaronder dynamische rekristallisatie optreedt in kaart te brengen. De modelresultaten worden met succes gevalideerd met gegevens voor Cu en Ni. Dezelfde set experimenteel bepaalde natuurkundige parameters die gebruikt zijn in hoofdstuk 3 wordt met vrucht gebruikt voor de validatie van het model voor rekristallisatie. In hoofdstuk 7 worden multi-component effecten toegevoegd aan de theorie om

rekening te houden met vaste-oplossing versterking, rekristallisatie, en twinning geïnduceerde plasticiteit. Dislocatie-pinning rond opgeloste atomen zorgen voor gelijkwaardige dislocatiegeneratie termen in de Kocks-Meching vergelijking (Λ_{SS}^{-1}). Bovendien vermindert de gemiddelde dislocatiesnelheid door pinning rond opgeloste atomen, en verdere dislocatieconfiguraties worden toegevoegd aan Ω om rekening te houden met de aanwezigheid van substitutionele (Ω_{subs}) en interstitionele (Ω_{inter}) atomen. Tenslotte worden verdere energiebarrières toegevoegd aan $\langle \Delta G \rangle$ en Q_{DRX} .

Geconcentreerde oplossingeffecten worden eerst beschouwd in de warmvervorming van Ni30Fe, Ni21Cr, Fe30Ni, Fe18Cr20Ni en Ni21Cr8Mo3Nb. Het model wordt later uitgebreid om lage concentraties van substitutionele en interstitionele atomen te beschrijven; warmvervorming van 15 laag gelegerde stalen wordt beschreven voor grote spreiding in samenstelling, temperatuur en reksnelheid. Kenmerken voor het plaatsvinden van dynamische rekristallisatie worden gedefinieerd in termen van temperatuur, reksnelheid en samenstelling. De invoer voor het model bestaat uit louter natuurkundige parameters en thermodynamische informatie van gevestigde databases.

De beschrijving van work-hardening van twinninggeïnduceerde plasticiteitsstalen voor verschillende C en Mn concentraties op kamertemperatuur wordt ook verwezigd door combinatie van twinning (Λ_T^{-1}) en vasteoplossing bijdragen (Λ_{SS}^{-1}) in de vorming van dislocaties. De dislocatieentropie laat een 'modulaire' benadering definiëren voor het beschrijven van het dislocatieverloop onder verschillende scenario's als 1) het aantal mogelijke dislocatiepaden; 2) de barrières voor de activeringsenergieën voor dislocatievernietiging $\langle \Delta G \rangle$ en voor korrelgroei Q_{DRX} ; en 3) dislocatievormings bronnen zijn aangepast als verscheidene kristaldefecten aanwezig zijn. Het laatste is eerder schematisch geïntroduceerd in de Kocks-Mecking vergelijking [94]. De specifieke uitdrukkingen voor ieder geval worden in dit proefchrift gegeven.

Door gebruik van de notatie \perp voor dislocaties, \emptyset voor dislocaties, \oplus voor substitutionele atomen en \odot voor interstitionele atomen, en door het gebruik van $\perp \cdot i$ om de interactie van een dislocatie met een i -defect, met $i \in \{\emptyset, \oplus, \odot\}$, laat Tabel S.1 schematisch de bijdrage van andere kristaldefecten op de dislocatiepopulatie en migratieenergie voor meerdere systemen zien. We merken op dat $\Omega_{\perp \cdot \perp}$, $\Omega_{\perp \cdot \emptyset}$ en $\Omega_{\perp \cdot \perp} \Omega_{\perp \cdot \emptyset}$ achtereenvolgens Ω_{dis} , Ω_{v-d} en $\Omega_{dis} + \Omega_{v-d}$ voorstellen; in $\langle \Delta G \rangle$ worden de dislocatievorming- en migratieenergieën schematisch voorgesteld door $U_{\perp \cdot \perp} = U_{form} + U_{mig}$, terwijl de energitermen voor Q_{DRX} weergegeven worden door tegengestelde tekens (om symmetrie te behouden, zie vergelijking 7.18), verder wordt E_{HAGB} schematisch voorgesteld door $U_{\perp \cdot \perp} = E_{HAGB}$. Geval 1 laat zien dat als (enkel kristal) zuivere metalen vervormd worden op lage temperatuur ($T < T_0$), het aantal microstates en energiebarrière bijdragen bepaald worden door enkel het dislocatiegedrag, verder geldt $Q_{DRX} = 0$; een Ni30Fe leg-

ering die vervormd wordt op hogere temperatuur ($T > T_0$), wordt getoond in geval 2, waarin dislocatiewisselwerking met vacatures en substitutionele atomen plaatsvindt (de bijdrage van vacatures aan aanmaak van dislocaties wordt niet meegenomen); Geval 3 laat een laag gelegeerde staal zien die vervormd wordt op hoge temperatuur ($T > T_f$), waarin de vacatures, substitutionele en interstitionele atomen het dislocatiegedrag beïnvloeden. Deze modulaire benadering wordt gevalideerd door het beschrijven van plastische vervorming en het verloop van de dislocaties in verscheidene metalen, waaronder zuivere metalen en legeringen.

Deze tabel illustreert waar verschillende microstructurele kenmerken het dislocatiegedrag veranderen. Verder laat het zien hoe extra kenmerken, zoals precipitaten, samenstelling en korrelgrenzen, ingebed kunnen worden in de theorie voor vervolgstudie. Bijvoorbeeld, door gebruik van de notatie \square , laat geval 4 in Tabel S.1 zien hoe extra configuratieeffecten ($\Omega_{\perp.\square}$) en barrières voor $\langle \Delta G \rangle$ en Q_{DRX} ($U_{\perp.\square}$) ingevoerd kunnen worden in het model voor de vervorming van een (grofkorrelig) Ni-superlegering op hoge temperatuur ($T > T_f$), waarbij intermetallische deeltjes voor dislocatiepinning eromheen zorgen, met vacaturegeassisteerde klim en substitutionele atomaire wisselwerking; $\Lambda_{\perp.\square}$ en $\Omega_{\perp.Box}$ kunnen een overheersende bijdrage hebben aan de sterkte van de legering ten opzichte van de andere termen [27]. Dit geval is echter nog niet gevalideerd en de vorige termen moeten worden gezien. Een geval van korrelgrensversterking in Fe is ontwikkeld in vroeger werk [274].

Configuratiele entropieeffecten voor dislocatienucleatie werden eerst afgeleid door Cottrell [29]; dit werd gedaan door rekening te houden met mogelijke locaties voor dislocaties in het kristalrooster waarin deze ontstaan (vergelijking 2.10). Het huidige werk gaat verder in de zin dat de mogelijke configuraties voor dislocatieslip tijdens rek verkregen zijn. Deze theorie laat niet alleen dislocatieplaatsordeningen beschrijven, bijv. dichtheid, cellen en twins; maar beschrijft ook hun verloop (via de reksnelheid) over de tijd.

Mogelijke richtingen voor toekomstig werk zijn: 1) het meenemen van extra microstructuurkenmerken op hoge temperatuur. Nb en Ti-carbiden in laaggelegeerd staal vertragen bijvoorbeeld dynamische rekristallisatie, waarin extra barrières voor korrelnucleatie en groei worden geïnduceerd. Intermetallische precipitaten in polykristallijne Ni-legeringen verhogen de sterkte op hoge temperatuur, waarbij een extra term en barrières in dislocatievernietiging en korrelgroei geïnduceerd worden. 2) Het beschrijven van het verloop van de gemiddelde korrelgrootte en de gerekristalliseerde volumefractie tijdens dynamische rekristallisatie. Dit zijn namelijk belangrijke grootheden voor het ontwerpen van nieuwe legeringen; Verder kan men de theorie aanpassen voor middelhoge en hoge concentraties koolstofconcentratie in laaggelegeerde stalen, waarin segregatieverzadiging op korrelgrenzen plaatsvindt. 3) Het combineren van dit raamwerk met andere mod-

elleertechnieken, zoals kristalplasticiteit en de eindige elementen methode om ruimtelijke rangschikkingen te beschrijven en de orientatie en textuurverdeling voor verschillende samenstellingen en procesomstandigheden te karakteriseren.

4) Uitbreiding van de theorie naar statisch herstel en rekristallisatie (rek is vast); hiervoor moet de theorie worden aangepast, omdat tijd (in plaats van rek) de grootte is die de dislocatiepopulatie en het kinematisch gedrag beïnvloedt; de Kocks–Mecking vergelijking wordt gedefinieerd voor een vast tijdsinterval, het thermostatische formalisme moet dan mogelijk worden aangepast voor het tijdsverloop voor een vaste rek.

Appendix A Physical parameters

Tables A.1, A.2, A.3 and A.4 show the physical parameter values of all metals employed in this work; unless noted otherwise, they were obtained from the literature and their sources are indicated respectively. The yield stress and shear modulus were fitted to analytical formulae to simplify the model calculations. It is worth noting that for BCC and HCP metals (Chapters 4 and 5), the yield stress formulae were employed to estimate the upper transition temperature where vacancy-assisted climb becomes the predominant dislocation annihilation mechanism (T_f) *only*. The experimental values employed for describing the stress-strain curves in these metals are shown in Figures 4.1 and 5.4.

$A_{act}b^2$ values for Cu and Al were obtained from experimental measurements [7]. In this case [104, 109], the relationship $A_{act}b^2 = \frac{1}{2}r_0l^*$ applies and r_0 accounts for the experimental distance between partials in the cross-slip plane (see Section 3.3.1), and is used to obtain the critical radius for impingement in FCC metals via equation 3.32. In BCC and FCC systems, measurements for $A_{act}b^2$ are not available. Employing the distance between partials at equilibrium [27] $r_0^{eq} = \frac{\mu b(2+\nu)}{24\pi(1-\nu)\chi}$, where χ is the stacking fault energy, it was found that the experimental values for $A_{act}b^2$ for FCC can be recovered by substituting $r_0 = 4r_0^{eq}$. This factor accounts for temperature variations above 0 K and the concomitant annihilation process taking place. We therefore employed the relationship [147]:

$$A_{act}b^2 = 4r_0^{eq}\frac{l^*}{2} = \frac{\mu_0bl^*(2+\nu)}{12\pi(1-\nu)\chi}. \quad (\text{A.1})$$

Although dislocation partials are not formed in BCC metals [5], a generalised stacking fault energy on the principal slip directions can define the activation area for cross-slip [147].

Table A.1: Physical parameters employed in the theory.

Material	$A_{act}b^2$ (m ²)	b (nm)	c (m/s)	E_f (kJ/mol)	E_m (kJ/mol)	ρ_a (kg/m ³)	T_m (K)	w_a (g/mol)
Ag	$613b^2$	0.289 [227]	2680 [227]	106 [97]	64 [97]	10490 [227]	1234 [227]	107.8 [227]
Al	$50b^2$ [7]	0.286 [227]	5000 [227]	67 [275]	60 [275]	2700 [227]	933 [227]	26.9 [227]
Cr		0.256 [227]	5940 [227]			7190 [227]		51.99 [227]
Cu	$300b^2$ [7]	0.256 [227]	3810 [227]	97 [275]	87 [275]	8940 [227]	1357 [227]	63.5 [227]
Fe (BCC)	$145b^2$	0.248 [108]	5120 [227]	205 [4]	73.3 [4]	7894 [227]	1811 [227]	55.845 [227]
Fe (FCC)		0.258 [276]						
Mg	$50b^2$	0.32 [25]	4940 [227]	202.6 [97]	57.5 [97]	1730 [227]	923 [227]	24.3 [227]
Mo	$68b^2$	0.272 [227]	5400 [227]	270 [97]	130.2 [97]	1028 [227]	2896 [227]	95.96 [227]

Table A.2: Physical parameters employed in the theory.

Material	$A_{act}b^2$ (m ²)	b (nm)	c (m/s)	E_f (kJ/mol)	E_m (kJ/mol)	ρ_a (kg/m ³)	T_m (K)	w_a (g/mol)
Nb		0.292	3480			8570		92.9
		[227]	[227]			[227]		[227]
Ni	$200b^2$	0.256	4900	135	135	8908	1728	58.7
		[227]	[227]	[97]	[97]	[227]	[227]	[227]
Ta	$60b^2$	0.286	3400	300	67.5	16690	3290	180.94
		[227]	[227]	[97]	[97]	[227]	[227]	[227]
Ti	$54b^2$	0.29	5090	202.6	125.4	45000	1941	47.87
		[227]	[227]	[277]	[277]	[227]	[227]	[227]
V	$115b^2$	0.263	4560	202	125.4	6000	2183	50.94
		[227]	[227]	[278]	[278]	[227]	[227]	[227]
W	$121b^2$	0.274	4620	318	183.3	19250	3695	183.84
		[227]	[227]	[97]	[97]	[227]	[227]	[227]
Zn		0.268	3850	38.5	48.2	7140	692.5	65.38
		[227]	[227]	[97]	[97]	[227]	[227]	[227]
Zr	$60b^2$	0.32	3800	144	57.8	6520	2128	91.22
		[227]	[227]	[97]	[97]	[227]	[227]	[227]

Table A.3: Physical parameters employed in the theory. For σ_Y and μ , T is expressed in K.

Material	χ (mJ/m ²)	μ (GPa)	μ_0 (GPa)	σ_Y (MPa)
Ag	16 [5]	$30 - 0.012T - 8 \times 10^{-8}T^2$ [120]	30	$63 - 0.05T$ [279]
Al	166 [5]	$29.4 - 0.015T$ [120]	29.4	$100 \exp(-6.67 \times 10^{-3}T)$ [280, 281, 136, 282]
Cr		$118 - 0.017T$ [283]	118	
Cu	47 [5]	$47.4 \exp(-3.97 \times 10^{-4}T)$ [120]	47.4	$73 + 3.5 \times 10^{-3}T - 1.33 \times 10^{-5}T^2$ [284]
Fe (BCC)	240 [157]	$121.9 - 0.02T$ [285]	121.9	$1354 \exp(-0.0097T)$ [160, 161, 162]
Fe (FCC)		$85.3 - 0.034T$ [276]	85.3	
Mg	125 [3]	$18.5 - 4.5 \times 10^{-3}T - 8.7 \times 10^{-6}T^2$ [286]	18.5	$85 \exp(-0.0023T)$ [183, 13, 207]
Mo	640 [158]	$139 - 0.02T$ [287]	139	$1423 \exp(-0.0024T)$ [165]

Table A.4: Physical parameters employed in the theory. For σ_Y and μ , T is expressed in K.

Material	χ (mJ/m ²)	μ (GPa)	μ_0 (GPa)	σ_Y (MPa)
Nb		38	38	
		[288]		
Ni	125	$87.4 - 0.032T - 7.9 \times 10^{-8}T^2$	87.4	$13.2 + 112/(1 + \exp(-(T - 321/79)))$
	[5]	[120]		[289]
Ta	480	$87.3 - 2080/(\exp(96/T) - 1)$	87	$554 \exp(-0.0037T)$
	[158]	[290]		[166]
Ti	320	$52.0.03T$	52	$335.8 \exp(-0.0037T)$
	[3]	[291]		[191]
V	150	$55.89 - 0.01T$	55.89	$947 \exp(-0.0037T)$
	<i>fitted</i>	[292]		[168]
W	500	$192 - 0.017T$	192	$2013 \exp(-0.0037T)$
	[159]	[293]		[167]
Zn	140	$47.3 \exp(-0.003(T - 273))$	45.9	
	[3]	[294]	[295]	
Zr	240	$40.7 - 0.031T$	40.7	$239 \exp(-0.0034T)$
	[3]	[291]		[21]

Bibliography

- [1] A.P. Sutton. *Electronic Structure of Materials*. Oxford University Press, 1993.
- [2] A.H. Cottrel. *Dislocations and Plastic Flow in Crystals*. Oxford University Press, 1953.
- [3] F.J. Humphreys and M. Hatherly. *Recrystallization and related annealing phenomena*. Elsevier, 2004.
- [4] R.E. Smallman and R.J. Bishop. *Modern Physical Metallurgy and Materials Engineering*. Butterworth-Heinemann, 1999.
- [5] J. Hirth and J. Lothe. *Theory of dislocations*. Wiley Interscience Publication, 1982.
- [6] U.F. Kocks and H. Mecking. Physics and phenomenology of strain hardening: the FCC case. *Prog. Mater. Sci.*, 48:171–273, 2003.
- [7] W. Puschl. Models for dislocation cross-slip in close-packed crystal structures: a critical review. *Prog. Mater. Sci.*, 47:415–461, 2002.
- [8] A.S. Argon and W.C. Moffatt. Climb of extended edge dislocations. *Acta Metall.*, 29:293–299, 1980.
- [9] M.H. Yoo. Slip, twinning, and fracture in hexagonal close-packed metals. *Metall. Trans. A*, 12A:409–418, 1981.
- [10] D.G. Westlake. Twinning in zirconium. *Acta Metall.*, 9:327–331, 1961.
- [11] L. Lu, Y. Shen, X. Chen, L. Qian, and K. Lu. Ultrahigh strength and high electrical conductivity in copper. *Science*, 302:422–426, 2004.
- [12] O. Bouaziz, S. Allain, C.P. Scott, P. Cugy, and D. Barbier. High manganese austenitic twinning induced plasticity steels: A review of the microstructure properties relationships. *Curr. Opin. Solid St. M.*, 15:141–168, 2011.

- [13] Y. Li and M. Enoki. Evaluation of the twinning behaviour of polycrystalline magnesium at room temperature by acoustic emission. *Mater. Trans.*, 48:1215–1220, 2007.
- [14] M.A. Meyers, A. Mishra, and D.J. Benson. Mechanical properties of nanocrystalline materials. *Prog. Mater. Sci.*, 51:427–556, 2006.
- [15] TG Nieh, J Wadsworth, and OD Sherby. *Superplasticity in metals and ceramics*. Cambridge University Press, 2005.
- [16] T.G. Langdon. Grain boundary sliding revisited: Developments in sliding over four decades. *J. Mater. Sci.*, 41:597–609, 2006.
- [17] H. Van Swygenhoven, M. Spaczer, and A. Caro. Microscopic description of plasticity in computer generated metallic nanophase samples: A comparison between Cu and Ni. *Acta Mater.*, 47:3117–3126, 1999.
- [18] H. Van Swygenhoven and P.M. Derlet. Grain–boundary sliding in nanocrystalline fcc metals. *Phys. Rev. B.*, page 224105, 2001.
- [19] E.I. Galindo-Nava, G. Torres-Villaseñor, and P.E.J. Rivera-Díaz-del-Castillo. Thermostatistical theory of superplasticity in alloys. Under review.
- [20] S. Yip. *Handbook of materials modelling A*. Springer. p. 565-611, 2005.
- [21] I.J. Beyerlein and C.N. Tomé. A dislocation-based constitutive law for pure Zr including temperature effects. *Int. J. Plas.*, 24:867–895, 2008.
- [22] A.L. Oppedal, H. El Kadiri, C. N. Tomé, G. C. Kaschner, S. C. Vogel, J. C. Baird, and M. F. Horstemeyer. Effect of dislocation transmutation on modeling hardening mechanisms by twinning in magnesium. *Int. J. Plas.*, 30-31:41–61, 2012.
- [23] V.V. Bulatov and W. Cai. *Computer Simulations of dislocations*. Oxford series on materials modelling, 2006.
- [24] V. Gerlod. *Structure of Solids Vol 1*. VCH, 1993.
- [25] D. Hull and D.J. Bacon. *Introduction to dislocations*. Butterworth-Heinemann, 1999.
- [26] D. Caillard and J.L. Martin. *Thermally activated mechanisms in crystal plasticity*. Pergamon, 2003.
- [27] R.C. Reed. *The superalloys: Fundamentals and applications*. Cambridge University Press, 2006.

- [28] R. Phillips. *Crystal, defects and microstructures, modelling across scales*. Cambridge University Press, 2004.
- [29] A.H. Cottrell. *Dislocations and plastic flow in crystals*. Clarendon Press, 1965.
- [30] W.T. Read. *Dislocations in crystals*. McGraw–Hill, 1953.
- [31] J.W. Martin, R.D. Doherty, and B. Cantor. *Stability of microstructure in Metallic systems*. Cambridge University Press, 1997.
- [32] W. Cai, V.V. Bulatov, and S. Yip. Kinetic monte carlo method for dislocation glide in silicon. *J. Comput. Aided Mater. Des.*, 6:175–183, 1999.
- [33] S. Ryu, K. Kang, and W. Cai. Entropic effect on the rate of dislocation nucleation. *Proc. Natl. Acad. Sci.*, 108:5174–5178, 2011.
- [34] J.S. Langer, E. Bouchbinder, and T. Lookman. Thermodynamic theory of dislocation–mediated plasticity. *Acta Mater.*, 58:3718–3732, 2010.
- [35] P.E.J. Rivera–Díaz–del–Castillo and M. Huang. Dislocation annihilation in plastic deformation: I. multiscale irreversible thermodynamics. *Acta Mater.*, 60:2606–2614, 2012.
- [36] G. Gottstein and L.S. Shvindlerman. *Grain boundary migration in metals*. CRC Press, 2010.
- [37] D. Kuhlmann-Wilsdorf. Dislocation cell formation and work hardening in the unidirectional glide of FCC metals. *Mater. Sci. Eng.*, 60:7–24, 1983.
- [38] E.F. Rauch. Effects of metal characteristics and experimental conditions on dislocation self–organization. *Rev. Metall.-CIT*, pages 1007–1019, 2004.
- [39] D. Kuhlmann-Wilsdorf and J.H. van der Merwe. Theory of dislocation cell sizes in deformed metals. *Mater. Sci. Eng.*, 55:79–83, 1982.
- [40] C.M. Kuo and C.S. Lin. Static recovery activation energy of pure copper at room temperature. *Scripta Mater.*, 57:667–670, 2007.
- [41] D. Holt. Dislocation cell formation in metals. *J. Appl. Phys.*, 41(8):3197, 1970.
- [42] M.R. Staker and D.L. Holt. The dislocation cell size and dislocation density in copper deformed at temperatures between 25 and 700°C. *Acta Metall.*, 20:569–579, 1972.

- [43] C.T. Young, T.J. Headley, and J.L. Lytton. Dislocation substructures formed during the flow stress recovery of high purity aluminium. *Mater. Sci. Eng.*, 81:391–407, 1986.
- [44] I. Barker, N. Hansen, and B. Ralph. The development of deformation substructures in face-centred cubic metals. *Mater. Sci. Eng. A*, 113:449–454, 1989.
- [45] E. Moin and L.E. Murr. Interactive effects of shock loading parameters on the substructure and mechanical properties of nickel and stainless steel. *Mater. Sci. Eng.*, 37:249–269, 1979.
- [46] D.A. Hughes. Microstructure evolution, slip patterns and flow stress. *Mater. Sci. Eng. A*, 319-321:46, 2001.
- [47] D.A. Hughes, Q. Liu, D.C. Chrzan, and N. Hansen. Scaling of microstructural parameters: Misorientations of deformation induced boundaries. *Acta Mater.*, 45(1):105–112, 1997.
- [48] W. Pantleon. On the distribution function of disorientations in dislocation cell structures. *Scripta Mater.*, 35(4):511–515, 1996.
- [49] Y.F. Shen, L. Lu, Q.H. Lu, Z.H. Jin, and K. Lu. Tensile properties of copper with nano-scale twins. *Acta Mater.*, 52:989–994, 2005.
- [50] L. Lu, R. Schwaiger, Z.W. Shan, M. Dao, K. Lu, and S. Suresh. Nano-sized twins induce high rate sensitivity of flow stress in pure copper. *Acta Mater.*, 53:2169–2179, 2005.
- [51] Z.S. You, L. Lu, and K. Lu. Temperature effect on rolling behaviour of nano-twinned copper. *Scripta Mater.*, 62:514–418, 2010.
- [52] A.J. Cao and Y.G. Wei. Molecular dynamics simulation of plastic deformation of nano twinned copper. *J. Appl. Phys.*, 102:083511, 2007.
- [53] A. Moncevicz, P.C. Clapp, and J.A. Rifkin. Dislocation mobilities in NiAl from molecular dynamics simulations. *MRS Proceedings*, 209:213–218, 1991.
- [54] W. Cai and V.V. Bulatov. Mobility laws in dislocation dynamics simulations. *Mater. Sci. Eng. A*, 387-389:277–281, 2001.
- [55] S. Queyreau, J. Marian, M.R. Gilbert, and B.D. Wirth. Edge dislocation mobilities in bcc Fe obtained by molecular dynamics. *Phys. Rev. B*, 84:064106, 2011.

- [56] D. Cereceda, J.M. Perlado, and J. Marian. Techniques to accelerate convergence of stress-controlled molecular dynamics simulations of dislocation motion. *Comp. Mater. Sci.*, 62:272–275, 2012.
- [57] D.H. Ruiz, L.M. Gribaudo, and A.M. Monti. Self-diffusion in the hexagonal structure of zirconium and hafnium. computer simulation studies. *Mater. Res.*, 8:431–434, 2005.
- [58] J.M. Zhang, X.L. Song, X.J. Zhang, and K.W. Xu. The properties and structures of the mono- and the di- vacancy in Cu crystal. *J. Phys. Chem. Sol.*, 67:714–719, 2006.
- [59] R. Meyer and L.J. Lewis. Stacking-fault energies for Ag, Cu and Ni from empirical tight-binding potentials. *Phys. Rev. B*, 66:052106, 2002.
- [60] D.L. Olmsted, E.A. Holm, and S.M. Foiles. Survey of computed grain boundary properties in face-centered cubic metals-II: Grain boundary mobility. *Acta Mater.*, 57:3704–3713, 2009.
- [61] I. Toda-Caraballo, P.D. Bristowe, and C. Capdevilla. A molecular dynamics study of grain boundary free energies, migration mechanisms and mobilities in a bcc Fe-20Cr alloy. *Acta Mater.*, 60:1116–1128, 2012.
- [62] L.P. Kubin and G. Canova. The modelling of dislocation patterns. *Scripta Metall.*, 27:957–962, 1992.
- [63] Y. Gao, Z. Zhuang, Z.L. Liu, Z.C. You, X.C. Zhao, and Z.H. Zhang. Investigations of pipe-diffusion-based dislocation climb by discrete dislocation dynamics. *Int. J. Plas.*, 27:1055–1071, 2011.
- [64] H.D. Espinosa, M. Panico, S. Berbenni, and K.W. Schwarz. Discrete dislocation dynamics simulations to interpret plasticity size and surface effects in freestanding in FCC thin films. *Int. J. Plas.*, 22:2091–2117, 2006.
- [65] M. Huang, L. Zhao, and J. Tong. Discrete dislocation dynamics modelling of mechanical deformation of nickel-based single crystal superalloys. *Int. J. Plas.*, 28:141–158, 2012.
- [66] B. Devincre, T. Hoc, and L. Kubin. Dislocation mean free paths and strain hardening of crystals. *Science*, 320:1745–1748, 2008.
- [67] Y. Huang, S. Qu, K.C. Hwang, M. Li, and H. Gao. A conventional theory of mechanism-based strain gradient plasticity. *Int. J. Plas.*, 20:753–782, 2004.

- [68] F. Roters, P. Eisenlohr, L. Hantcherli, D.D. Tjahjanto, T.R. Bieler, and D. Raabe. Overview of constitutive laws, kinematics, homogenisation and multi scale methods in crystal plasticity finite–element modelling: Theory, experiments, applications. *Acta Mater.*, 58:1152–1211, 2010.
- [69] J. Alcalá, O. Casals, and J. Ocenásek. Micromechanics of pyramidal indentation in fcc metals: Single crystal plasticity finite element analysis. *J. Mech. Phys. Sol.*, 56:3277–3303, 2008.
- [70] M.G. Lee, H. Lim, B.L. Adams, J.P. Hirth, and R.H. Wagoner. A dislocation density-based single crystal constitutive equation. *Int. J. Plas.*, 26:925–938, 2010.
- [71] C. Keller, E. Hug, A.M. Habraken, and L. Duchene. Finite element analysis of the free surface effects on the mechanical behavior of thin nickel polycrystals. *Int. J. Plas.*, 29:155–172, 2012.
- [72] S.M.A. Khan, H.M. Zbib, and D.A. Hughes. Modeling planar dislocation boundaries using multi–scale dislocation dynamics plasticity. *Int. J. Plas.*, 20:1059–1092, 2004.
- [73] M. Wallin, W.A. Curtin, M. Ristinmaa, and A. Needleman. Multi–scale plasticity modelling: Coupled discrete dislocation and continuum crystal plasticity. *J. Mech. Phys. Sol.*, 56:3167–3180, 2008.
- [74] J. Zhang and S.P. Joshi. Phenomenological crystal plasticity modeling and detailed micromechanical investigations of pure magnesium. *Int. J. Plas.*, 27:1721–1738, 2012.
- [75] T. Hama and H. Takuda. Crystal-plasticity finite-element analysis of inelastic behaviour during unloading in a magnesium alloy sheet. *Int. J. Plas.*, 27:1072–1092, 2011.
- [76] G.E. Dieter. *Mechanical Metallurgy*. McGraw Hill, 1988.
- [77] M. Huang, P.E.J. Rivera-Díaz-del-Castillo, O. Bouaziz, and S. van der Zwaag. Modelling the steady state deformation stress under various deformation conditions using a single irreversible thermodynamics based formulation. *Acta Mater.*, 57:3431–3438, 2009.
- [78] I. Prigogine. *Introduction to Thermodynamics of Irreversible Process*. John Wiley and Sons, New York, 1961.
- [79] P.E.J. Rivera-Díaz-del-Castillo, K. Hayashi, and E.I. Galindo-Nava. Design and modelling of nanostructured steels. *Mater. Sci. Tech.*, In press, 2012.

- [80] P. Zhu, Y. Hu, F. Fang, and H. Wang. Multiscale simulations of nano indentation and nanoscratch of single crystal copper. *App. Surf. Sci.*, 258:4624–4631, 2012.
- [81] S. Groh and H.M. Zbib. Advances in discrete dislocations dynamics and multiscale modeling. *J. Eng. Mater. Technol.*, 131:041209, 2009.
- [82] M. Zbib and T. Diaz-de-la-Rubia. A multiscale model of plasticity. *Int. J. Plas.*, 18:1133–1163, 2002.
- [83] Z.L. Liu, X.M. Liu, Z. Zhuang, and X.C. You. A multi-scale computational model of crystal plasticity at sub micron-to-nanometer scales. *Int. J. Plas.*, 25:1436–1455, 2009.
- [84] V. Sundararaghavan and M. Zabarar. On the synergy between texture classification and deformation process sequence selection for the control of texture-dependent properties. *Acta Mater.*, 53:1015–1027, 2005.
- [85] V. Sundararaghavan and M. Zabarar. Design of microstructure-sensitive properties in elasto-viscoplastic polycrystals using multi-scale homogenization. *Int. J. Plas.*, 22:1799–1824, 2006.
- [86] V. Sundararaghavan and A. Kumar. Probabilistic modeling of microstructure evolution using finite element representation of statistical correlation functions. *Int. J. Plas.*, 30-31:62–80, 2012.
- [87] D. McDowell. A perspective on trends in multiscale plasticity. *Int. J. Plas.*, 26:1280–1309, 2010.
- [88] S. Benkaseem, L. Capolungo, and M. Cherkaoui. Mechanical properties and multi-scale modelling of nanocrystalline materials. *Acta Mater.*, 55:3563–3572, 2007.
- [89] V. Favier and D. Barbier. Micromechanical modelling of twinning-induced plasticity steels. *Scripta Mater.*, 66:972–977, 2012.
- [90] Z.L. Liu, Z. Zhuang, X.M. Liu, X.C. Zhao, and Z.H. Zhang. A dislocation dynamics based higher-order crystal plasticity model and applications on confined thin-film plasticity. *Int. J. Plas.*, 27:201–216, 2011.
- [91] A.L. Oppedal, H. El Kadiri, C.N. Tomé, G.C. Kaschner, S.C. Vogel, J.C. Baird, and M.F. Horstemeyer. Effect of dislocation transmutation on modeling hardening mechanisms by twinning in magnesium. *Int. J. Plas.*, 30-31:41–61, 2012.

- [92] A. Brown and D. Bammann. Validation of a model for static and dynamic recrystallization in metals. *Int. J. Plas.*, 32-33:17–35, 2012.
- [93] X.G. Fan and H. Yang. Internal-state-of-the-art variable based self-consistent constitutive modeling for hot working of two-phase titanium alloys coupling microstructure evolution. *Int. J. Plas.*, 27:1833–1852, 2011.
- [94] Y. Estrin and H. Mecking. A unified phenomenological description of work hardening and creep based on one-parameter model. *Acta Metall.*, 32:57–70, 1984.
- [95] E.I. Galindo-Nava and P.E.J. Rivera-Díaz-del-Castillo. Thermostatistical modelling of hot deformation in FCC metals. *Int. J. Plas.*, In press: 10.1016/j.ijplas.2013.02.002, 2012.
- [96] A.S. Argon. *Strengthening mechanisms in crystal plasticity*. Oxford University Press, 2008.
- [97] R. Cahn and P. Haasen. *Physical Metallurgy*. North Holland, 1996.
- [98] H.H. Guberman. Stress dependence of dislocation velocity in single crystal niobium. *Acta Metall.*, 16:713–721, 1968.
- [99] R.C. Blish and T. Vreeland. Dislocation velocity on the $\{\bar{1}2\bar{1}2\}$ $\langle\bar{1}2\bar{1}3\rangle$ slip system of zinc. *J. Appl. Phys.*, 40:884–890, 1969.
- [100] R.J. Amodeo and N.M. Ghoniem. Dislocation dynamics. i. a proposed methodology for deformation micromechanics. *Phys. Rev. B*, 41:6958–6967, 1990.
- [101] U.F. Kocks. On the temperature and stress dependence of the dislocation velocity stress exponent. *Scripta Metall.*, 4:29–32, 1970.
- [102] T.M. Cover and J.A. Thomas. *Elements of information theory*. Wiley-Interscience, 2006.
- [103] R.M. Gray. *Entropy and Information theory*. Springer, 2011.
- [104] E.I. Galindo-Nava, J. Sietsma, and P.E.J. Rivera-Díaz-del-Castillo. Dislocation annihilation in plastic deformation: II Kocks-Mecking analysis. *Acta Mater.*, 60:2615–2624, 2012.
- [105] E.T. Jaynes. Information theory and statistical mechanics. *Phys. Rev.*, 106:620–630, 1957.
- [106] E.T. Jaynes. Information theory and statistical mechanics. II. *Phys. Rev.*, 108:171–190, 1957.

- [107] H.B. Callen. *Thermodynamics and an Introduction to Thermostatistics*. Wiley & Sons, 1985.
- [108] P.S. Follansbee. Analysis of deformation kinetics in seven body-centred-cubic pure metals using a two-obstacle model. *Metall. Mater. Trans. A*, 41:3080–3090, 2010.
- [109] E.I. Galindo-Nava and P.E.J. Rivera-Díaz-del-Castillo. A thermostatical theory of low and high temperature deformation in metals. *Mater. Sci. Eng. A*, 543:110–116, 2012.
- [110] O.D. Sherby, J.L. Lytton, and J.E. Dorn. Activation energies for creep of high-purity aluminium. *Acta Metall.*, 5:219–227, 1957.
- [111] P.N.B. Anongba, J. Bonneville, and J.L. Martin. Hardening stages of [112] copper single crystals at intermediate and high temperatures—I. mechanical behaviour. *Acta Metall.*, 41(10):2897–2906, 1993.
- [112] C.W. Zhao, Y.M. Xing, C.E. Zhou, and P.C. Bai. Experimental examination of displacement and strain fields. *Acta Mater.*, 56:2570–2575, 2008.
- [113] Y. Nohara, E. Tochigi, N. Shibata, T. Yamamoto, and Y. Ikuhara. Dislocation structures and strain fields in [111] low-angle tilt grain boundaries in zirconia bicrystals. *Journal of Electron Microscopy*, 59 (Supplement):s117–s121, 2010.
- [114] C.L. Johnson, M.J. Hytch, and P.R. Busek. Displacement and strain fields around a [100] dislocation in olivine measured to sub-angstrom accuracy. *American Mineralogist*, 89:1374 – 1379, 2004.
- [115] A. Howie and P.R. Swann. Direct measurements of stacking-fault energies from observations of dislocation nodes. *Prog. Mater. Sci.*, 70(6):1215–1226, 1961.
- [116] E.I. Galindo-Nava and P.E.J. Rivera-Díaz-del-Castillo. A thermodynamic theory for dislocation cell formation in FCC metals. *Acta Mater.*, 60:4370–4378, 2012.
- [117] L.C. Chang and H.K.D.H. Bhadeshia. Austenite films in bainitic microstructures. *Mater. Sci. Tech.*, 11:874–881, 1995.
- [118] D. Myers. *Surfaces, Interfaces, and Colloids*. John Wiley and Sons, 2004.
- [119] J.E. Marsden and A.J. Tromba. *Vector Calculus*. W.H. Freeman, 2003.

- [120] E. Nes. Modelling of work hardening and stress saturation in fcc metals. *Prog. Mater. Sci.*, 41:129–193, 1997.
- [121] W. Pantleon. Stage iv work-hardening related to disorientations in dislocation structures. *Mater. Sci. Eng. A*, 387-389:257–261, 2004.
- [122] H. Mecking, B. Nicklas, N. Zarubova, and U.F. Kocks. A universal temperature scale for plastic flow. *Acta Metall.*, 34:527–535, 1986.
- [123] S.R. Chen and U.F. Kocks. High-temperature plasticity in copper. *Am. Soc. Mech. Eng.*, 1:1–12, 1991.
- [124] G. Gottstein, T. Lee, and U. Schmidt. Deformation temperature and recrystallization. *Mater. Sci. Eng. A*, 114:21–28, 1989.
- [125] G. Gottstein, J. Bewerunge, H. Mecking, and H. Wollenberger. Stored energy of 78 k tensile deformed copper crystals. *Acta Metall.*, 23(5):641–652, 1974.
- [126] M. Zehetbauer and V. Seumer. Cold work hardening in stages IV and V of F.C.C. metals-I. experiments and interpretation. *Acta. Metall. Mater.*, 41(2):577–588, 1993.
- [127] A. Belyakov, T. Sakai, H. Miura, and K. Tsuzaki. Grain refinement in copper under large strain deformation. *Phil. Mag. A*, 81(11):2629–2643, 2001.
- [128] U.F. Kocks and S.R. Chen. On the two distinct effects of thermal activation on plasticity. *Phys Status Solidi (a)*, 131:403–413, 1992.
- [129] G. Gottstein and U.F. Kocks. Dynamic recrystallization and dynamic recovery in $\langle 111 \rangle$ single crystals of nickel and copper. *Acta Metall.*, 31:175–188, 1983.
- [130] P.S. Follansbee and G. T. Gray. The response of single crystal and polycrystal nickel to quasi static and shock deformation. *Int. J. Plas.*, 7:651–660, 1991.
- [131] D.A. Hughes and N. Hansen. Microstructural evolution in nickel during rolling from intermediate to large strains. *Metall. Mater. Trans. A*, 24(9):2022–2037, 1993.
- [132] D.A. Hughes and W.D. Nix. The absence of steady-state flow during large strain plastic deformation of some Fcc metals at low and intermediate temperatures. *Metall. Trans. A*, 19A:3013–3024, 1988.

- [133] Q.Z. Chen, N. Jones, and D.M. Knowles. The microstructures of base/modified RR2072 SX superalloys and their effects on creep properties at elevated temperatures. *Acta Mater.*, 50:1095–1112, 2002.
- [134] U.F. Kocks. Laws for work-hardening and low-temperature creep. *Am. Soc. Mech. Eng. H*, 98:76–85, 1976.
- [135] A.J. Beaudoin, A. Acharya, S.R. Chen, D.A. Korzekwa, and M.G. Stout. Consideration of grain-size effect and kinetics in the plastic deformation of metal polycrystals. *Acta Mater.*, 48:3409–3423, 2000.
- [136] W.F. Hosford, R.L. Fleischer, and W.A. Backofen. Tensile deformation of aluminium single crystals at low temperature. *Acta Metall.*, 8:187–199, 1960.
- [137] L. Lu, Z.S. You, and K. Lu. Work hardening of polycrystalline Cu with nanoscale twins. *Scripta Mater.*, 66:837–842, 1996.
- [138] O. Bouaziz, S. Allain, and C. Scott. Effect of grain and twin boundaries on the hardening mechanisms of twinning-induced plasticity steels. *Scripta Mater.*, 58:484–487, 2008.
- [139] E.I. Galindo-Nava and P.E.J. Rivera-Díaz-del-Castillo. Modelling multi-scale plasticity: A thermostatistical approach. *Scripta Mater.*, 67:915–918, 2012.
- [140] M. Huang, P.E.J. Rivera-Díaz-del-Castillo, O. Bouaziz, and S. van der Zwaag. Modelling strength and ductility of ultrafine grained BCC and FCC alloys using irreversible thermodynamics. *Mater. Sci. Tech.*, 25:833, 2008.
- [141] L. Lu, X. Chen, X. Huang, and K. Lu. Revealing the maximum strength in nanotwinned copper. *Science*, 323:607–610, 2009.
- [142] X.H. Chen, L. Lu, and K. Lu. Grain size dependence of tensile properties in ultrafine-grained Cu with nanoscale twins. *Scripta Mater.*, 64:311–314, 2011.
- [143] Y.F. Shen, L. Lu, Q.H. Lu, Z.H. Jin, and K. Lu. Tensile properties of copper with nano-scale twins. *Scripta Mater.*, 52:989–994, 2005.
- [144] M. Huang, P.E.J. Rivera-Díaz-del-Castillo, O. Bouaziz, and S. van der Zwaag. A constitutive model for high strain rate deformation in fcc metals based on irreversible thermodynamics. *Mech. Mater.*, 41:982–988, 2009.

- [145] A.A. Galkin, V.V. Tokii, and B.P. Filatov. Dislocation multiplication: II. The effect of the initial defect structure and deformation conditions on the dissociation multiplication. *Phys. Stat. Sol. (a)*, 45:327–332, 1978.
- [146] M. Kabir, T.T. Lau, D. Rodney, S. Yip, and K.J. Van Vliet. Predicting dislocation climb and creep from explicit atomistic details. *Phys. Rev. Lett.*, 105:095501, 2010.
- [147] E.I. Galindo-Nava and P.E.J. Rivera-Díaz-del-Castillo. Modelling plastic deformation in bcc metals: dynamic recovery and cell formation effects. *Mater. Sci. Eng. A*, 558:641–648, 2012.
- [148] D. Brunner and J. Diehl. Strain-rate and temperature dependence of the tensile flow stress of high-purity α -iron above 250 K (Regime I) studied by means of stress-relaxation tests. *Phys. Stat. Sol. A*, 124:155–170, 1991.
- [149] D.J. Quesnel, A. Sato, and M. Meshi. Solution softening and hardening in the iron-carbon system. *Mater. Sci. Eng.*, 18:199–208, 1975.
- [150] J. Richter. The influence of temperature on slip behaviour of molybdenum single crystals deformed in tension in the range from 203 to 573 K. *Phys Stat. Sol.*, 40:565–572, 1970.
- [151] R.T. Sato and A.K. Mukherjee. The asymmetric temperature dependence of yield stress in tantalum single crystals at low temperatures. *Mater. Sci. Eng.*, 8:74–82, 1971.
- [152] M. Bocek and H. Schneider. Internal stress measurements on vanadium at elevated temperatures. *Scripta Metall.*, 4:369–374, 1970.
- [153] D. Brunner. Peculiarities of work hardening of high-purity tungsten single crystals below 800 K. *Mater. Sci. Eng. A*, 387-389:167–170, 2004.
- [154] J.W. Christian. Some surprising features of the plastic deformation of body-centered cubic metals and alloys. *Metall. Trans. A*, 14:1237–1256, 1983.
- [155] R. Peierls. The size of a dislocation. *Proc. Phys. Soc.*, 53(1):34, 1940.
- [156] J.H. Crawford. *Point defects in solids*. Plenum Press, 1972.
- [157] R. Watanabe. Generalised stacking fault energy in body centred cubic iron. *Strength, Fracture and Complexity*, 5:13–25, 2007.
- [158] C. Segall, D.E. Li, and G. Xu. Corroboration of a multiscale approach with all atom calculations in analysis of dislocation nucleation from surface steps. *Phil. Mag.*, 86(32):5083–5101, 2006.

- [159] C.S. Hartley. On the dissociation of dislocations on $\{112\}$ planes of anisotropic b.c.c. metals. *Acta Metall.*, 14:1133–1136, 1966.
- [160] T.L. Altshuler and J.W. Christian. The mechanical properties of pure iron tested in compression over the temperature range 2 to 293 degrees k . *Phil. Trans. R. Soc. A*, 261:253–287, 1967.
- [161] D.J. Dingley and D. McLean. Components of the flow stress of iron. *Acta Metall.*, 15:885–901, 1967.
- [162] H. Conrad and S. Frederick. The effect of temperature and strain rate on the flow stress of iron. *Acta Metall.*, 10:1013–1020, 1962.
- [163] Y. Lan, H.J. Klaar, and W. Dahl. Evolution of dislocation structures and deformation behaviour of iron at different temperatures: Part I. Strain hardening curves and cellular structures. *Metall. Trans. A*, 23:537–544, 1992.
- [164] S. Ikeda. Dislocation distribution and work-hardening in iron on single crystals extended in the $[100]$ and the $[110]$ axes. *J. Phys. Soc. Jap.*, 27:1564–1578, 1969.
- [165] S. Nemat-Nasser, W. Guo, and M. Liu. Experimentally-based micromechanical modelling of dynamic response of molybdenum. *Scripta Mater.*, 40(7):859–872, 1999.
- [166] J.F. Maudlin, J.W. Bingert, P.J. House, and S.R. Chen. On the modeling of the Taylor cylinder impact test for orthotropic textured materials: experiments and simulations. *Int. J. Plas.*, 15:139–166, 1999.
- [167] H. Bechtold. Strain rate effects in tungsten. *J. Met.*, 8:142–146, 1956.
- [168] T.C. Lindley and R.E. Smallman. The plastic deformation of polycrystalline vanadium at low temperatures. *Acta Metall.*, 11:361–371, 1963.
- [169] K. Yasunaga, M. Iseki, and M. Kiritani. Dislocation structures introduced by high-speed deformation in bcc metals. *Mater. Sci. Eng. A*, 350:76–80, 2003.
- [170] S.R. Agnew, C.N. Tomé, D.W. Brown, T.M. Holden, and S.C. Vogel. Study of slip mechanisms in a magnesium alloy by neutron diffraction and modelling. *Scripta Mater.*, 48:1003–1008, 2003.
- [171] D.W. Brown, S.R. Agnew, M.A.M Bourke, T.M. Holden, S.C. Vogel, and C.N. Tomé. Internal strain and texture evolution during deformation twinning in magnesium. *Mater. Sci. Eng. A*, 399:1–12, 2005.

- [172] P.B. Hirsch and J.S. Lally. The deformation of magnesium single crystals. *Phil. Mag.*, 12:595–648, 1965.
- [173] L.B. Addessio, E.K. Cerreta, and G.T. Gray III. Mechanical behaviour of zirconium and hafnium in tension and compression. *Metall. Mater. Trans. A*, 36A:2893–2903, 2005.
- [174] Z. Zeng and S. and Roven H.J. Jonsson. The effects of deformation conditions on microstructure and texture of commercially pure Ti. *Acta Mater.*, 57:5822–5833, 2009.
- [175] R.J. McCabe, E.K. Cerreta, A. Misra, G.C. Kaschner, and C.N. Tomé. Effects of texture, temperature and strain on the deformation modes of zirconium. *Phil. Mag.*, 86:3595–3611, 2006.
- [176] S.G. Song and G.T. Gray III. Structural interpretation of the nucleation and growth of deformation twins in Zr and Ti-II tem study of twin morphology and defect reactions during twinning. *Acta Metall. Mater.*, 43:2339–2350, 1995.
- [177] J.R. Morris, Y.Y. Ye, K.M. Ho, C.T. Chan, and M.H. Yoo. Structures and energies of compression twin boundaries in hcp Ti and Zr. *Phil. Mag. A*, 72:751–763, 1995.
- [178] H. Wang, P.D. Wu, J. Wang, and C.N. Tomé. A crystal plasticity model for hexagonal close packed (HCP) crystals including twinning and de-twinning mechanisms. *Int. J. Plas.*, 2013. In press: 10.1016/j.ijplas.2013.02.016.
- [179] A. Khosravani, J. Scott, M.P. Miles, D. Fullwood, B.L. Adams, and R.K. Mishra. Twinning in magnesium alloy AZ31B under different strain paths at moderately elevated temperatures. *Int. J. Plas.*, 45:160–173, 2013.
- [180] B.C. Wonsiewicz and W.A. Backofen. Plasticity of magnesium crystals. *Trans. TMS-AIME*, 239:1422–1431, 1967.
- [181] P. Klimanek and A. Potzsch. Microstructure evolution under compressive plastic deformation of magnesia at different temperatures and strain rates. *Mater. Sci. Eng. A*, 324:145–150, 2002.
- [182] N. Ono, R. Nowak, and S. Miura. Effect of deformation temperature on hall-petch relationship registered for polycrystalline magnesium. *Mater. Lett.*, 58:39–43, 2003.
- [183] S. Ando and H. Tonda. Non-basal slip in magnesium-lithium alloy single crystals. *Mater. Trans. JIM*, 41:1188–1191, 2000.

- [184] H. Sasano and H. Kimura. The effect of deformation twinning on mechanical properties of α -titanium alloys at low temperatures. *J. Jpn. Inst. Met.*, 41:933–939, 1977.
- [185] A.A. Salem, S.R. Kalidindi, and R.D. Doherty. Strain hardening of titanium: role of deformation twinning. *Acta Mater.*, 51:4225–4237, 2003.
- [186] M. Battaini, E.V. Pereloma, and C.H.J. Davies. Orientation effect on mechanical properties of commercially pure titanium at room temperature. *Metall. Mater. Trans. A*, 38A:276–285, 2003.
- [187] E.D. Tabachnikova, A.V. Podolskiy, B. Bonarski, C. Mangler, V.Z. Bengus, S.N. Smirnov, A.N. Velikodny, M.A. Tikhonovsky, and M.J. Zehetbauer. Mechanical properties and microstructure evolution during deformation of ultra fine grained zirconium at low temperatures. *Rev. Adv. Mater. Sci.*, 25:168–175, 2010.
- [188] H. Abdolvand, M.R. Daymond, and C. Mareau. Incorporation of twinning into a crystal plasticity finite element model: evolution of lattice strains and texture in Zircaloy-2. *Int. J. Plas.*, 27:1721–1738, 2011.
- [189] T. Mayama, M. Noda, R. Chiba, and M. Kuroda. Crystal plasticity analysis of texture development in magnesium alloy during extrusion. *Int. J. Plas.*, 27:1916–1935, 2011.
- [190] A. Jain and S.R. Agnew. Modelling the temperature dependent effect of twinning on the behaviour of magnesium alloy AZ31B sheet. *Mater. Sci. Eng. A*, 462:29–36, 2007.
- [191] S. Nemat-Nasser, W.G. Guo, and J.Y. Cheng. Mechanical properties and deformation mechanisms of a commercially pure titanium. *Acta Mater.*, 47:3705–3720, 1999.
- [192] Z. Zeng, S. Jonsson, and Y. Zhang. Constitutive equations for pure titanium at elevated temperatures. *Mater. Sci. Eng. A*, 505:116–119, 2008.
- [193] E.I. Galindo-Nava and P.E.J. Rivera-Díaz-del-Castillo. Thermostistical modelling of deformation twinning in HCP metals. Under review.
- [194] C.K. Chyung and C.T. Wei. Nucleation of deformation twins in zinc bicrystals. *Phil. Mag.*, 15:161–175, 1967.
- [195] W.B. Hutchinson and M.R. Barnett. Effective values of critical resolved shear stress for slip in polycrystalline magnesium and other hcp metals. *Scripta Mater.*, 63:737–740, 2010.

- [196] X.L. Nan, H.Y. Wang, L. Zhang, J.B. Li, and Q.C. Jiang. Calculation of Schmid factors in magnesium: Analysis of deformation behaviours. *Scripta Mater.*, 67:443–446, 2012.
- [197] C.H. Cáceres and P. Lukác. Strain hardening behaviour and the Taylor factor of pure magnesium. *Phil. Mag. A*, 88:977–989, 2009.
- [198] M.R. Barnett, Z. Keshavarz, A.G. Beer, and D. Atwell. Influence of grain size on the compressive deformation of wrought Mg–3Al–1Zn. *Acta Mater.*, 52:5093–5103, 2004.
- [199] L. Capolungo, I.J. Beyerlein, and C.N. Tomé. Slip-assisted twin growth in hexagonal close-packed metals. *Scripta Mater.*, 60:32–35, 2009.
- [200] A. Akhtar. Prismatic slip in zirconium single crystals at elevated temperatures. *Metall. Trans. A*, 6A:1217–1222, 1973.
- [201] H. Mecking, U.F. Kocks, and Ch. Hartig. Taylor factors in materials with many deformation modes. *Scripta Mater.*, 35:465–471, 1996.
- [202] S. Ando, K. Nakamura, T. Kazuki, and H. Tonda. $\{11\bar{2}2\}$ $\langle\bar{1}123\rangle$ slip in magnesium single crystal. *JILM*, 42:765–771, 1992.
- [203] H.S. Zurob, C.R. Hutchinson, Y. Brechet, and G. Purdy. Modelling recrystallization of microalloyed austenite: effect of coupling recovery, precipitation and recrystallization. *Acta Mater.*, 50:3077–3094, 2002.
- [204] C. Yin, M. Doner, and H. Conrad. The internal stress in titanium deformed at low temperatures ($T < 0.33T_m$). *Metall. Trans. A*, 6:1901–1908, 1971.
- [205] A. Galiyev, O. Sitdikov, and R. Kaibyshev. Deformation behaviour and controlling mechanisms for plastic flow of magnesium and magnesium alloy. *Mater. Trans.*, 44:426–435, 2003.
- [206] Q.Y. sun and H.C. Gu. Tensile and low-cycle fatigue behaviour of commercially pure titanium and Ti-5Al-2.5Sn alloy at 293 and 77 k. *Mater. Sci. Eng. A*, 316:80–86, 2001.
- [207] R. Gehrman, M.M. Frommert, and G. Gottstein. Texture effects on plastic deformation of magnesium. *Mater. Sci. Eng. A*, 395:338–349, 2005.
- [208] Y. Li and M. Enoki. Deformation and an elastic recovery of pure magnesium and AZ31B alloy investigated by AE. *Mater. Trans.*, 48:2343–2348, 2007.
- [209] M.P. Biget and G. Saada. Low-temperature plasticity of high-purity (α -)titanium single crystals. *Phil. Mag. A*, 59:747–757, 1989.

- [210] S.G. Song and G.T. Gray III. Influence of temperature and strain rate on slip and twinning behaviour of Zr. *Metall. Mater. Trans. A*, 26:2665–2675, 1995.
- [211] R.J. McCabe, G. Proust, E.K. Cerreta, and A. Misra. Quantitative analysis of deformation twinning in zirconium. *Int. J. Plas.*, 25:454–472, 2009.
- [212] H. Won Lee and Y.T. Im. Cellular automata modeling of grain coarsening and refinement during the dynamic recrystallization of pure copper. *Mater. Trans.*, 51:1614–1620, 2010.
- [213] K. Okuda and A.D. Rollet. Monte carlo simulation of elongated recrystallized grains in steels. *Comp. Mater. Sci.*, 34:264–273, 2005.
- [214] T. Takaki, T. Hirouchi, Hisakuni, Y., A. Yamanaka, and Y. Tomita. Multi-phase-field to simulate microstructure evolution during dynamic recrystallization. *Mater. Trans.*, 11:2559–2565, 2008.
- [215] T. Takaki, T. Hirouchi, Hisakuni, Y., A. Yamanaka, and Y. Tomita. Multi-phase-field simulations for dynamic recrystallization. *Comp. Mater. Sci.*, 45(1):881–88, 2009.
- [216] D.G. Cram, H.S. Zurob, Y.J.M. Brechet, and C.R. Hutchinson. Modelling discontinuous dynamic recrystallization using a physically based model for nucleation. *Acta Mater.*, 57:5218–5228, 2009.
- [217] D.G. Cram, X.Y. Fange, H.S. Zurob, Y.J.M. Brechet, and C.R. Hutchinson. The effect of solute on discontinuous dynamic recrystallization. *Acta Mater.*, 60:6390–6404, 2012.
- [218] W. Gao, A. Belyakov, H. Miura, and T. Sakai. Dynamic recrystallization of copper polycrystals with different purities. *Mater. Sci. Eng. A*, 265:233–239, 1999.
- [219] H. Yamagata, Y. Ohuchida, N. Saito, and M. Otsuka. Nucleation of new grains during discontinuous dynamic recrystallization of 99.998 mass% aluminum at 453 K. *Scripta Mater.*, 45:1055–1061, 2001.
- [220] M. Hasegawa, M. Yamamoto, and H. Fukutomi. Formation mechanism of texture during dynamic recrystallization in γ -TiAl, nickel and copper examined by microstructure observation and grain boundary analysis based on local orientation measurements. *Acta Mater.*, 51:3939–3950, 2003.
- [221] T. Erneux. *Applied delay differential equations*. Springer, 2009.

- [222] J.K. Lee. Understanding dynamic recrystallization behaviour through a delay differential equation approach. *Mater. Sci. Forum*, 558-559:441–448, 2007.
- [223] G. Gottstein and T. Lee. Deformation temperature and recrystallization. *Mater. Sci. Eng. A*, 114:21–28, 1989.
- [224] A.M. Wusatowska-Sarnek, H. Miura, and T. Sakai. Nucleation and microtexture development under dynamic recrystallization of copper. *Mater. Sci. Eng. A*, 323:177–186, 2002.
- [225] M. Ohashi, T. Endo, and T. Sakai. Effect of initial grain size on dynamic recrystallization of pure nickel. *J. Japan Inst. Metals*, 54(4):435–441, 1991.
- [226] M. Hasegawa and H. Fukutomi. Microstructural study on dynamic recrystallization and texture formation in pure nickel. *Mater. Trans.*, 43(5):1183–1190, 2002.
- [227] D.R. Lide. *CRC Handbook of Chemistry and Physics*. CRC Press, 2008.
- [228] S.M. Collard and R.B. McLellan. High-temperature elastic constants of gold single-crystals. *Acta Metall. Mater.*, 39:3143–3151, 1991.
- [229] P. Neuhaus and C. Herzig. Temperature dependence of the grain boundary diffusion of tin in nickel. *Acta Metall.*, 35:881–886, 1987.
- [230] R.F. Canon and J.P. Stark. Grain boundary self diffusion in nickel. *J. Appl. Phys.*, 40:4366, 1969.
- [231] D. Gupta. On the direct measurement of diffusion at temperatures less than $0.5t_m$. *Thin solid films*, 25:231–244, 1975.
- [232] R. Viswanathan and C.L. Bauer. Kinetics of grain boundary migration in copper. *Acta Metall.*, 21:1099–1109, 1973.
- [233] H.L. Andrade, M.G. Akben, and J.J. Jonas. Effect of molybdenum, niobium, and vanadium on static recovery and recrystallization and on solute strengthening in microalloyed steels. *Metall. Trans. A*, 14:1967–1977, 1983.
- [234] J.H. Beynon and C.M. Sellars. Modelling microstructure and its effects during multi pass hot rolling. *ISIJ Int.*, 42:319–329, 2011.
- [235] H.J. McQueen, S. Yue, N.D. Ryan, and E. Fry. Hot working characteristics of steels in austenitic state. *J. Mater. Process. Tech.*, 53:293–310, 1995.

- [236] W.P. Sun and E.B. Hawbolt. Comparison between static and metadynamic recrystallization—an application to the hot rolling of steels. *ISIJ Int.*, 37:1000–1009, 1997.
- [237] R. Lagneborg, T. Siwecki, S. Zajac, and B. Hutchinson. The role of vanadium in microalloyed steels. *Scand. J. Metall.*, 28:186–241, 1999.
- [238] B. Mintz. The influence of composition on the hot ductility of steels and to the problem of transverse cracking. *ISIJ Int.*, 39:833–855, 1999.
- [239] E. Clouet, S. Garruchet, H. Nguyen, M. Perez, and C.S. Becquart. Dislocation interaction with C in α -Fe: A comparison between atomic simulations and elasticity theory. *Acta Mater.*, 56:3450–3460, 2008.
- [240] C. Kremaszky, U. Liedl, and E.A. Werner. A note on the diffusion of carbon atoms to dislocations. *Comp. Mater. Sci.*, 38:90–97, 2006.
- [241] S. Queyreau, G. Monnet, and B. Devincre. Slip systems interactions in α -iron determined by dislocation dynamics simulations. *Int. J. Plas.*, 25:361–377, 2009.
- [242] P.D. Hodgson and R.K. Gibbs. A mathematical model to predict the mechanical properties of hot rolled C–Mn and microalloyed steels. *ISIJ Int.*, 32:1329–1338, 1992.
- [243] A. Manohar, M. Ferry, and T. Chandra. Five decades of the zener equation. *ISIJ Int.*, 38:913–924, 1998.
- [244] H.K.D.H. Bhadeshia and R.W.K. Honeycombe. *Steels: Microstructure and properties*. Butterworth-Heinemann, 2006.
- [245] J.W. Christian. *The theory of transformations in metals and alloys. Part I*. Pergamon Press, 1975.
- [246] E.I. Galindo-Nava, A. Perlade, and P.E.J. Rivera-Díaz-del-Castillo. A thermostatical theory for solid solution effects in hot deformation of alloys: An application to low-alloy steels. *Under review*.
- [247] R.T. DeHoff. *Thermodynamics in Materials Science*. CRC/Taylor and Francis, 2006.
- [248] M.S. Blanter. Strain-induced interaction of dissolved atoms in γ -Fe. *J. Alloy. Comp.*, 291:167–174, 1999.

- [249] X.S. Guan, Y. Nishizawa, H. Okamura, K. Numakura, and M. Koiwa. Interaction between substitutional and interstitial solute atoms in α iron studied by isothermal mechanical spectroscopy. *Mater. Sci. Eng. A*, 370:73–77, 2004.
- [250] K. Ushioda, U. Schlippenbach, and W.B. Hutchinson. The effect of carbon content on recrystallization and texture development in steel. *Texture Microstruct.*, 7:11–28, 1987.
- [251] P.J. Hurley, P.D. Hodgson, and B.C. Muddle. A study of deformation substructures in austenite using a model Ni-30 wt% Fe alloy. *Scripta Metall.*, 45:25–32, 2001.
- [252] N. Dunova, A. Belyakov, T. Sakai, and R.O. Kaibyshev. Dynamic recrystallization mechanisms operating in a Ni-20%Cr alloy under hot-to-warm working. *Acta Mater.*, 58:3624–3632, 2010.
- [253] N.R. Dunova and R.O. Kaibyshev. Short-range ordering and mechanical properties of a Ni-20%Cr alloy. *J. Phys.*, 240:012081, 2010.
- [254] M.F. Abbod, C.M. Sellars, P. Cizek, D.A. Linkens, and M. Mahfouf. Modelling the flow behaviour, recrystallization, and crystallographic texture in hot deformed Fe-30 wt pct Ni austenite. *Metall. Mater. Trans. A*, 38A:2400–2409, 2007.
- [255] A. Belyakov, H. Miura, and T. Sakai. Dynamic recrystallization under warm deformation of a 304 type austenitic stainless steel. *Mater. Sci. Eng. A*, 255:139–147, 1998.
- [256] H.Y. Leng, K. Yang, and W.X. Han. Dynamic mechanical behaviours of as-cast stainless steel 1Cr25Ni20Si2 during hot deformation. *Acta Metall. Sin.*, 13:465–469, 2000.
- [257] Q. Guo, D. Li, S. Guo, H. Peng, and J. Hu. The effect of deformation temperature on the microstructure evolution of Inconel 625 superalloy. *J. Nucl. Mater.*, 414:440–450, 2011.
- [258] W. Charnock and J. Nutting. The effect of carbon and nickel upon the stacking-fault energy of iron. *Metal. Sci. J.*, 1:123–127, 1967.
- [259] W. Chambron and A. Caplain. Study of vacancies in very low concentration in an iron 70 at % nickel alloy by the magnetic anisotropy method. *Acta Metall.*, 22:357–366, 1974.
- [260] A.P. Miodownik. The calculation of stacking fault energies in Fe-Ni-Cr alloys. *Calphad*, 2:207–226, 1978.

- [261] L.E. Murr. *Interfacial Phenomena in Metals and Alloys*. Addison-Wesley Publishing, 1975.
- [262] D.W. Suh, S. Torizuka, A. Ohmori, T. Inoue, and K. Nagai. Dynamic restoration process of Ni-30Fe alloy during hot deformation. *ISIJ Int.*, 42:432–439, 2002.
- [263] I. Mejía, E. López-Chipres, C. Maldonado, A. Belloda-Jacuinde, and J.M. Cabrera. Modeling of the hot deformation behavior of boron microalloyed steels under uniaxial hot-compression conditions. *Int. J. Mat. Res.*, 99:1336–1345, 2008.
- [264] M. Huang, P.E.J. Rivera-Díaz-del-Castillo, O. Bouaziz, and S. van der Zwaag. Modelling strength and ductility of ultra fine grained BCC and FCC alloys using irreversible thermodynamics. *Mater. Sci. Tech.*, 25:833–839, 2009.
- [265] S. Bao, G. Zhao, C. Yu, Q. Chang, C. Ye, and X. Mao. Recrystallization behaviour of a Nb-microalloyed steel during hot compression. *Appl. Math. Model.*, 35:3268–3275, 2011.
- [266] L.P. Karjalainen and J. Perttula. Characteristics of static and metadynamic recrystallization and strain accumulation in hot-deformed austenite as revealed by the stress relaxation method. *ISIJ International*, 36:729–736, 1996.
- [267] T. Senuma and H. Yada. Microstructural evolution of plain carbon steels in multiple hot working. In *Annealing Processes - Recovery, Recrystallization and Grain Growth. Proceedings of the 7 Risø International Symposium on Metallurgy and Materials Science*, pages 547–552, 1986.
- [268] M. Shaban and B. Eghbali. Characterization of austenite dynamic recrystallization under different Z parameters in a microalloyed steel. *J. Mater. Sci. Technol.*, 27:359–363, 2011.
- [269] A.I. Fernández, P. Uranga, B. López, and J.M. Rodríguez-Ibabe. Dynamic recrystallization behaviour covering a wide austenite grain size range in Nb and Nb–Ti microalloyed steels. *Mater. Sci. Eng. A*, 361:367–376, 2003.
- [270] X. Liang, J.R. McDermind, O. Bouaziz, X. Wang, J.D. Embury, and H.S. Zurob. Microstructural evolution and strain hardening of Fe-24Mn and Fe-30Mn alloys during tensile deformation. *Acta Mater.*, 57:3978–3988, 2009.
- [271] O. Bouaziz, H. Zurob, B. Chehab, J.D. Embury, S. Allain, and M. Huang. Effect of chemical composition on work hardening of Fe-Mn-C twip steels. *Mater. Sci. Tech.*, 27:707–709, 2011.

- [272] X. Wang, H.S. Zurob, J.D. Embury, X. Ren, and I. Yakubtsov. Microstructural features controlling the deformation and recrystallization behaviour Fe-30%Mn and Fe-30%Mn-0.5%C. *Mater. Sci. Eng. A*, 527:3785–3791, 2010.
- [273] M. Yamaguchi. First-principles study on the grain boundary embrittlement of metals by solute segregation: Part I. Iron (Fe)-Solute (B, C, P, and S) systems. *Metall. Mater. Trans. A*, 42:319–329, 2011.
- [274] I. Toda-Caraballo, E.I. Galindo-Nava, and P.E.J. Rivera-Díaz-del-Castillo. Unravelling the materials genome: symmetry relationships in alloy properties. *J. Alloy Compd. In press: 10.1016/j.jallcom.2013.02.148.*, 2013.
- [275] P. Wynblatt. Calculation of the vacancy migration energy in cubic crystals. *J. Phys. Chem. of Solids*, 29:215–224, 1968.
- [276] M. Huang, P.E.J. Rivera-Díaz-del-Castillo, O. Bouaziz, and S. van der Zwaag. Modelling the strength of ultrafine-grained and nanocrystalline FCC metals. *Acta Metall.*, 61:1113–1116, 2009.
- [277] O. Le-Bacq and F. Willaime. Unrelaxed vacancy formation energies in group-IV elements calculated by the full-potential linear muffin-tin orbital method: Invariance with crystal structure. *Phys. Rev. B*, 59:8508–8515, 1999.
- [278] M. Maier, B. Peo, H.E. Saile, K. Schaefer, and A. Seeger. Hightemperature positron annihilation and vacancy formation in refractory metals. *Phil. Mag. A*, 40:701–728, 1979.
- [279] D.R. Smith and F.R. Fickett. Low-temperature properties of silver. *J. Res. Nat. Inst. Stand. Technol.*, 100:119–171, 1995.
- [280] A. Rosen and S.R. Bodner. The influence of strain rate and strain ageing on the flow stress of commercially-pure aluminium. *J. Mech. Phys. of Solids*, 15:47–62, 1967.
- [281] M.E. Kassner and X. Li. The effect of grain size on the elevated temperature yield strength of polycrystalline aluminum. *Scripta Metall. et Mater.*, 25:2833–2838, 1991.
- [282] R.H. Bush and R.A. Huggins. Yield points in aluminium at high temperatures. *Acta Metall.*, 12:697–704, 1964.
- [283] R. Street. Elasticity and anelasticity of chromium. *Phys. Rev. Lett.*, 10:210–211, 1963.

- [284] R.P. Carreker and W.R. Hibbard. Tensile deformation of high-purity copper as a function of temperature, strain rate, and grain size. *Scripta Metall.*, 1:654–663, 1953.
- [285] J.J. Adams, D.S. Agosta, R.G. Leisure, and H. Ledbetter. Elastic constants of monocrystals iron from 3 to 500 K. *J. Appl. Phys.*, 100:113530, 2006.
- [286] M. Delannoy-Coutris, N. Toupance, and J. Boustel de Belloy. Temperature dependence of elastic moduli for non-cubic solids: application to cadmium, magnesium and zinc. *J. Phys: Appl. Phys.*, 23:1695–1702, 1965.
- [287] J.M. Dickinson and P.E. Armstrong. Temperature dependence of the elastic constants of molybdenum. *J. Appl. Phys.*, 38:602–606, 1967.
- [288] R.J. Farraro and R.B. McLellan. High temperature elastic properties of polycrystalline niobium, tantalum, and vanadium. *Metall. Mater. Trans. A*, 10:1699–1702, 1979.
- [289] R.G. Davies and N.S. Stoloff. On the yield stress of aged Ni-Al alloys. *Trans. Metall. Soc. AIME*, 233:714–719, 1965.
- [290] R. Becker. Tantalum shear modulus from homogenization of single crystal data. *Lawrence Livermore National Laboratory*, pages UCRL-TR-234680, 2007.
- [291] Z. Trojanová, P.A. Maksimiyuk, and P. Lukác. Temperature dependence of Young's modulus of α -titanium polycrystals. *Phys. Stat. Sol. a*, 143:75–77, 1994.
- [292] O.N. Greiner, J.D. Carlson, and J.F. Smith. Single crystal elastic constants of vanadium and vanadium with oxygen. *J. Appl. Phys.*, 50:4394–4398, 1979.
- [293] V.A. Dreshpak. Elastic properties of tungsten and molybdenum single crystals. *Strength Mater. 1*, 6:669–670, 1969.
- [294] J.P. Andrews. The variation of Young's modulus at high temperatures. *Proc. Phys. Soc. London*, 37:169–177, 1924.
- [295] C.W. Garland and R. Dalven. Elastic constants of Zinc from 4.2° K to 77.6° K. *Phys. Rev.*, 111:1232–1234, 1958.

Acknowledgements

This work is the summary of the four-year research work carried out at three different groups: Microstructure Control in Metals (MCM), Delft University of Technology, Netherlands; Metallurgy Prospects and Manufacturing, ArcelorMittal Mazières Research, France; and the Department of Materials Science and Metallurgy, University of Cambridge, United Kingdom. This thesis would not have been possible without the support and help of many people, to whom I would like to express my sincere gratitude.

The first person I want to thank is my promoter Prof. ir. Jilt Sietsma, for accepting me in MCM. I appreciate his support and guidance, especially during the early stages of my research. He always provided me the appropriate feedback when I presented a new mathematical model.

Special mention goes to my copromoter, Dr. Pedro Rivera. He helped me to (initially) come to Delft, as well as to continue my research at Cambridge. I want to thank him for his enormous efforts and long hours spent on my project. During the early stages of my research, he helped me to define the seminal ideas contained this work. I appreciate all the scientific and non-scientific discussions we had during this time, either at the office or a pub. I am deeply indebted to him for always helping me to promote my career, and for allowing me to meet many people in the local and international scientific community. Thank you Pedro!

I would like to thank the people from ArcelorMittal Mazières, for giving me the opportunity of conducting an internship project; this time was crucial for determining the final direction of my research. A special thanks goes to Dr. Mingxin Huang (he is now at the University of Hong Kong), for his help and supervision during the experimental and modelling work; and to Dr. Astrid Perlade for her advice during the internship, for providing experimental data for validating the models in this thesis, and for always giving me positive feedback when I presented my work progress in ArcelorMittal.

I want to thank the Mexican Council of Science and Technology (CONACYT) for granting me a scholarship for my doctoral studies. I also want to thank the Roberto Rocca Education Program for awarding me a fellowship for supporting

my research stay at the University of Cambridge.

I would like to express my gratitude to Dr. Astrid Perlade (ArcelorMittal), Prof. Fionn Dunne (Imperial College London), Prof. Jeff Th. M. De Hosson (University of Groningen), Dr. Raymundo Arróyave (Texas A&M University), and Prof. Thijs Vlugt (TU Delft) for being members of the doctoral committee. I want to thank to all the people that offer me their friendship during this time. Special mention goes to my friends and officemates in Cambridge, Bijna Kim, Isaac Toda (and family), Kunio Hayashi (and family), Jerónimo Terrones and the people from SKF UTC.

I want to thank my family for their love and support during my whole life, without them I would not have made it this far. I would like to express my gratitude for teaching me to always pursue my dreams.

Last but not least, a very special acknowledgement goes to Daniela Lopez, my wife. I want to thank her, not only for the unconditional love and support, but also for the patience and understanding she had in these years. She made me feel like anything is possible, and to overcome difficulties during hard times. It is an honour for me to share this journey together. I love you!

List of publications

Journal publications:

1. E.I. Galindo-Nava, P.E.J. Rivera-Díaz-del-Castillo. Grain size evolution during discontinuous dynamic recrystallisation. *Under review*.
2. E.I. Galindo-Nava, G. Torres-Villaseñor, P.E.J. Rivera-Díaz-del-Castillo, A thermodynamic model for plastic deformation in superplastic alloys: Grain boundary sliding and cavitation effects. *Under review*.
3. E.I. Galindo-Nava, P.E.J. Rivera-Díaz-del-Castillo, Thermostatistical modelling of deformation twinning in HCP metals. *Under review*.
4. E.I. Galindo-Nava, A. Perlade, P.E.J. Rivera-Díaz-del-Castillo. A thermo-statistical theory for solid solution effects in hot deformation of alloys: An application to low alloy steels. *Under review*.
5. S. Neelakantan, E.I. Galindo-Nava, D. San Martin, J. Chao, P.E.J. Rivera-Díaz-del-Castillo. Modelling and design of transformation-induced-plasticity of a β titanium alloy. *Under review*.
6. E.I. Galindo-Nava, P.E.J. Rivera-Díaz-del-Castillo, Thermostatistical modelling of hot deformation in FCC metals, *International Journal of Plasticity* 47 (2013) 202-221
7. I. Toda-Caraballo, E.I. Galindo-Nava, P.E.J. Rivera-Díaz-del-Castillo, Unravelling the materials genome: symmetry relationships in alloy properties. *Journal of Alloys and Compounds* 566 (2013) 217-228
8. P.E.J. Rivera-Díaz-del-Castillo, K. Hayashi, E.I. Galindo-Nava, Design and modelling of nanostructured steels, *Materials Science and Technology*. Special issue article (2013).

9. E.I. Galindo-Nava, P.E.J. Rivera-Díaz-del-Castillo, Modelling multiscale plasticity: a thermostistical approach, *Scripta Materialia* 67 (2012) 915-918
10. E.I. Galindo-Nava, P.E.J. Rivera-Díaz-del-Castillo. Modelling plastic deformation in BCC metals: dynamic recovery and cell formation effects. *Materials Science and Engineering A* 558 (2012) 641-648
11. E.I. Galindo-Nava, P.E.J. Rivera-Díaz-del-Castillo, A thermodynamic theory for dislocation cell formation and misorientation in metals, *Acta Materialia* 60 (2012) 4370-4378
12. E.I. Galindo-Nava, P.E.J. Rivera-Díaz-del-Castillo. A thermostistical theory of low and high temperature deformation in metals. *Materials Science and Engineering A* 543 (2012) 110-116
13. E.I. Galindo-Nava, J. Sietsma, P.E.J. Rivera-Díaz-del-Castillo. Dislocation Annihilation in plastic deformation: II. Kocks-Mecking Analysis. *Acta Materialia* 60 (2012) 2615-2624.

Conference publications:

14. P.E.J. Rivera-Díaz-del-Castillo, E.I. Galindo-Nava, Tailoring dynamic recrystallization in Ni- and Fe-base high temperature alloys, *Materials Science Forum* 753 (2013) 427-430.
15. E.I. Galindo-Nava, P.E.J. Rivera-Díaz-del-Castillo, Modelling dynamic recrystallization in FCC metals employing thermostistics, *Materials Science Forum* 753 (2013) 153-156.
16. E.I. Galindo-Nava, I. Toda-Caraballo, P.E.J. Rivera-Díaz-del-Castillo, Strength/Elongation Optimisation in Materials: A Case for Accelerated Metallurgy Research. *TMS Annual Meeting* (2013) 319-326.
17. I. Toda-Caraballo, E.I. Galindo-Nava, P.E.J. Rivera-Díaz-del-Castillo, Symmetry in Material Property Relationships: A Tool for the Discovery of New Alloys. *TMS Annual Meeting* (2013) 312-318.
18. E.I. Galindo-Nava, J. Sietsma, P.E.J. Rivera-Díaz-del-Castillo, A thermostistical theory for plastic deformation, *Proceedings 4th International Conference on Fundamental Properties of Dislocations* (2012) 13-17.

Curriculum Vitae

Enrique I. Galindo Nava

born on 4th June 1984
in Mexico City, Mexico

2010 - 2013

PhD visiting student at the University of Cambridge, Cambridge, United Kingdom, under supervision of Dr. Pedro E.J. Rivera Díaz-del-Castillo.

2009 - 2013

PhD researcher at Delft University of Technology, Delft, The Netherlands, under supervision of Prof.dr.ir. Jilt Sietsma and Dr. Pedro E.J. Rivera Díaz-del-Castillo.

2004 - 2009

Bachelor of Science in Mathematics at National Autonomous University of Mexico, Mexico City, Mexico. Thesis under supervision of Prof. Jorge Ize: "Modern study of J.C. Maxwell's theory about Saturn Rings: Case of Rigid Body".

2002 - 2007

Bachelor of Science in Mechatronics Engineering at Panamerican University (*cum laude*), Mexico City, Mexico.